Author:
Zhang, Yichen

Title:
Sliding Keys on Inclined Deflecting-cantilevers (SKID) device for application with Post-Tensioned (PT) frames

Author:
Zhang, Yichen

Title:
Sliding Keys on Inclined Deflecting-cantilevers (SKID) device for application with Post-Tensioned (PT) frames

Sliding Keys on Inclined Deflecting-cantilevers (SKID) device for application with Post-Tensioned (PT) frames

By

Yichen Zhang

A dissertation submitted to the University of Bristol in accordance with
the requirements for award of the degree of
Doctor of Philosophy
in the Faculty of Engineering

June 2023

Word Count: 51619

“It can scarcely be denied that the supreme goal of all theory is to make the irreducible basic elements as simple and as few as possible without having to surrender the adequate representation of a single datum of experience.”

Albert Einstein

ABSTRACT

This thesis presents a novel frictional damping device for application with Post-Tensioned (PT) frames. A conceptual system named a Frictional Sliding on a Sprung Slope (FSSS) system is proposed first. Its mechanical schematisation is presented, and the theoretical hysteretic behaviour is discussed. The FSSS system has a triangular-shaped hysteretic curve with an amplitude-increasing resistance and a zero-activation threshold. Then, an innovative physical realisation of the conceptual FSSS system is presented and named a Sliding Keys on Inclined Deflecting-cantilevers (SKID) device. The device uses the end stiffness of cantilever bars as the "sprung-slope" for generating an amplitude-dependent normal force. The reliability of using cantilever bars is discussed. (Chapter 3)

To demonstrate the SKID device, two 1/4 scale-reduced prototypes are designed and manufactured. They have negative unloading stiffness (SKID A) and positive unloading stiffness (SKID B), respectively. By conducting quasi-static cyclic tests, it is found that they exhibited stable and repeatable triangular-shaped hysteretic curves, verifying a satisfactory consistency between the theoretical behaviour and the test results. In addition, SKID configurations having different manufacturing parameters (i.e., friction materials, cantilever bar stiffness and slope angle) are built and tested by both cyclic and fatigue tests to investigate the behaviour sensitivity. (Chapter 4)

Chapter 5 presents the application of the SKID device in PT frames (the PT-SKID frames). The theoretical hysteretic performance of the PT-SKID frame is discussed by deriving its analytical formulations. The PT-SKID frame has a dual-triangular-flag-shaped hysteretic curve, featuring a full self-centring capability. Then, three PT frames with and without the SKID device are analysed numerically using OpenSees as a numerical proof-of-concept. Incremental dynamic analyses (IDA) are carried out to explore the contribution of the SKID device. The results show that the device significantly reduces the seismic response of the PT frame and no residual deformations are observed after the earthquake excitations. Additionally, more than 700 one-story one-bay PT frames with different SKID devices (PT-SKID frames) are numerically tested to investigate the dynamic characteristics of the structural system affecting the seismic response.

Chapter 6 investigates the linear equivalence of the PT-SKID frames for estimating peak seismic displacement response. The linear equivalent system is constructed by its secant stiffness and the equivalent damping ratio estimated by Jacobsen's method. Such linearisation is the basis of Direct Displacement-Based Design (DDBD). Then, the accuracy of the linearisation to assess the peak seismic displacement response is evaluated by numerically testing 5,880 mid- to long-period PT-SKID frames. The results show that the linear equivalence frequently underestimated the peak displacement response, leading to an unconservative design in the DDBD. To eliminate the influence of this error, a correction factor is suggested for the design spectrum used in the DDBD of the PT-SKID frames.

Chapter 7 proposes a novel Post-Tensioned Precast Warehouse structure with the Sliding Keys on Inclined Deflecting-cantilevers Device (the PTPW-SKID Structure) following the concept of the PT-SKID frame for industrial buildings. The structure comprises a PT outer frame and a SKID inner frame. The PT outer frame supports the roof and cladding systems; and the SKID inner frame supports the SKID devices and crane system. The design and seismic performance of the PTPW-SKID structure are presented by a case frame located in L'Aquila, Italy. The Direct Displacement-Based Design (DDBD) method is utilised for the seismic design. A 3D numerical model is built in OpenSees. Both quasi-static and seismic dynamic analyses are carried out to investigate its hysteretic behaviour and the seismic response.

ACKNOWLEDGEMENT

I would like to express my sincere gratitude to my supervisors, Prof. Nicholas Alexander and Dr. Raffaele De Risi, for their insightful guidance, kind encouragement, and generous support throughout my PhD journey. The conversations I have had with them are not only informative and insightful, but also continuously inspiring. Their inspiration has been instrumental in enabling this innovative and exciting research project to be explored and then presented in this thesis.

I would like to thank Prof. Anastasios Sextos for his supportive suggestions and enlightening comments on my research during the entire process.

I would like to thank technicians Mr. Steve Harding, Mr. Pete Whereat, Mr. Guy Pearn, Mr. Mark Reed, and Mr. Mictroy Mitchell for their technical assistance during the conduction of the physical tests. I would like to thank the team of the Advanced Computing Research Centre (ACRC), University of Bristol, for providing access to their computational facilities (the High-Performance Computing machine, BlueCrystal) to carry out the numerical analysis.

I am supported by University of Bristol – China Scholarship Council Joint PhD Scholarship to participate in this research. I would acknowledge their financial support.

I sincerely express my warm gratitude to my parents for their unconditional support, encouragement and love.

AUTHOR'S DECLARATION

I declare that the work in this dissertation was carried out in accordance with the requirements of the University's *Regulations and Code of Practice for Research Degree Programmes* and that it has not been submitted for any other academic award. Except where indicated by specific reference in the text, the work is the candidate's own work. Work done in collaboration with, or with the assistance of, others, is indicated as such. Any views expressed in the dissertation are those of the author.

SIGNED: .....  ..... DATE:..23.06.2023.....

LIST OF PUBLICATIONS

This thesis is based on the work published in the following papers, all of which were authored by Yichen Zhang as the first author.

Peer reviewed journal papers:

1. Zhang, Y., De Risi, R., & Alexander, N. A. (2021). A frictional sliding on a sprung slope (FSSS) device that axiomatically confers energy dissipation with re-centring to post-tensioned (PT) frames: A conceptual study. *Engineering Structures*, 244, 112794.

2. Zhang, Y., De Risi, R., & Alexander, N. A. (2022). A novel seismic energy dissipating device, Sliding Keys on Inclined Deflecting-cantilevers (SKID): Theoretical and experimental evidence. *Engineering Structures*, 273, 115056.

3. Zhang, Y., De Risi, R., & Alexander, N. A. (2022). The Sliding Keys on Inclined Deflecting-cantilevers (SKID) device: Empirical and analytical sensitivity analysis with application in post-tensioned frames. *Earthquake Engineering & Structural Dynamics.*

Conference papers:

1. Zhang, Y., De Risi, R. & Alexander N.A. (2022). An Innovative Frictional Sliding on a Sprung Slope (FSSS) Device and Its Cyclic Test Demonstration. *The Third European Conference on Earthquake Engineering and Seismology*. Bucharest, Romania.

2. Zhang, Y., De Risi, R. & Alexander N.A. (2023). The seismic responses of the Post-Tensioned frame with Sliding Keys on Inclined Deflecting-cantilever device (the PT-SKID frame). *EURODYN 2023*. Delft, Netherlands.

TABLE OF CONTENTS

LIST OF FIGURES

LIST OF TABLES

NOMENCLATURE

Chapter 3

E_{FSSS}	Dissipated energy by the FSSS system
E_{L}	Dissipated energy by an equivalent linear viscous oscillator
F_{f}	Friction force
F_{FSSS}	Strength of the FSSS system
S_{F}	Factor of safety
$k/2$	Stiffness of one spring block
k_{FSSS}	Stiffness of the FSSS system
k_{L}	Linear stiffness
$k_{\mathrm{PT}}(x)$	Stiffness function of the PT frame
$\dot{x}$	Velocity of the sliding keys (slider)
β_{crit}	Critical slope angle
ζ_{eq}	Equivalent viscous damping ratio
c_{x} and c_{y}	Factors regarding the boundary conditions of the cantilever bars
E	Young's modulus of the material
F_{SKID}	Strength of the SKID device
I_{x} and I_{y}	Second moment of areas in the x and y directions
k_{SKID}	Sliding stiffness of the SKID device
K_{SKID}	Global stiffness of the SKID device
k_{x} and k_{y}	Cantilever flexural stiffnesses in the x and y directions
L	Length of the cantilever
n	Number of the slider-slope unit
R	Longitudinal constraining force
R_{s}	Spring reaction forces
x	Relative sliding displacement between the slope blocks and sliding keys (slider)
X	Total displacement of the sliding keys
x_{c} and y_{c}	Cantilever bar displacement in the x and y directions
Π	Normalised dissipated energy
α	Sliding displacement reduction factor
β	Angle of inclination of the sliding surface
μ	friction coefficient

ρ	Elastic deformation factor
M	Storey mass
N	Normal force
R'	Moment provided for moment equilibrium
η	Non-dimensional parameter determining the shape of hysteretic curve
λ	Inertial moment ratio

Chapter 4

Δ_y	Tip deflection of the cantilever bars
ε_i	Strain at *i* position of the cantilever bars
d_i	Distance from F_y to the measured *i* position
F_y	Resultant force in the *y* direction generated from sliding surfaces
k_{eff}	Effective tip cantilever stiffness
k_s	Cantilever stiffness
L	Cantilever bar length
t	Thickness of the cantilever bars
X	Actuator displacement
y_c	End deflection of the cantilever bars
α	Sliding displacement reduction factor
β	Slope angle
β_{eff}	Effective slope angle
β_{norm}	Nominal slope angle
η	Non-dimensional parameter determining the shape of hysteretic curve
μ	Friction coefficient
μ_{norm}	Nominal friction coefficient
ρ	Elastic deformation factor
ζ_{eq}	Equivalent damping ratio

Chapter 5

$\ddot{u}_g(t)$	Ground acceleration
$F_{PT}(\theta)$	Lateral strength of the PT frame
$F_{PT\text{-}SKID}(\theta)$	Lateral strength of the PT-SKID frame
$F_{SKID}(H\theta)$	Lateral strength of the SKID device
T_0	Linear Elastic Period
$f_d(u,\dot{u})$	Base share force of the FSSS part

$f_s(u, \dot{u})$	Base share force of the PT frame part
$\zeta_{\mathrm{eq},0}$	Elastic viscous damping ratio
$\zeta_{\mathrm{eq,hyst}}$	Equivalent viscous damping ratio of the hysteretic component
ζ_{eq}	Total equivalent damping ratio
b_i	Contact width of the *i*th joint
c	Viscous damping coefficient
$F_{0,i}$	Pre-tension force of the *i*th joint
F_{PT}	Base shear response of the PT part
F_{SKID}	Base shear response of the SKID part
H	Floor height
$k_{\mathrm{c,i}}$	Cable stiffness
k_{s}	Spring stiffness
$k_{\mathrm{s,i}}$	Contact stiffness
K_{SKID}	Lateral stiffness of the SKID device
m	Floor mass
M	Total weight of the frame
R_{epi}	Epicentre distance
S_{a}	Spectral acceleration
u	Relative roof drift response
γ	Post-opening joint stiffness ratio (the post-opening joint stiffness to initial stiffness of the PT-SKID frame)
λ_i	Non-dimensional moment
θ	Drift ratio
k	SKID cantilever bar stiffness
β	SKID Slope
μ	SKID Friction Coefficient

Chapter 6

$\ddot{x}_{\mathrm{g}}$	Ground acceleration
$\dot{x}_{\mathrm{norm}}$	Normalised velocity
$\Delta_{(T,\,\xi)}$	Displacement design spectrum
C_{ξ}	Reduction factor for the equivalent damping ratio greater than 5%
$F_{\mathrm{PT}}(\theta)$	Base shear of the PT frame
$F_{\mathrm{PT\text{-}SKID}}(\theta,\dot{\theta})$	Base shear of the PT-SKID frame
$F_{\mathrm{SKID}}(\theta,\dot{\theta})$	Base shear of the SKID device
ξ_0	Elastic viscus damping ratio

$\xi_{\text{eq, hyst, PT-SKID}}$	Hysteretic component of equivalent damping ratio of PT-SKID frame
T_e	Effective period
c	Damping coefficient
C_1, C_2, and γ	Factors defining C_ξ
C_e	Correction factor
$D_{\text{nonlinear}}$	Peak displacement response of the nonlinear hysteretic model
D_{spectrum}	Estimated peak displacement from the displacement spectrum
F_{PT}	Restoring force
$F_{\text{PT, norm}}$	Normalised shear force of the PT frame part
$F_{\text{PT-SKID}}$	Total stiffness force of the PT-SKID frame
F_{SKID}	Damping force
g	Gravity acceleration
$\text{H}(x_{\text{norm}})$	Heaviside formulation
k_e	Effective stiffness
k_{PT}	Initial stiffness of the PT frame
m	Mass
m_e	Effective mass
r	Stiffness ratio of PT frame
S_a	Spectral acceleration
S_d	Spectral displacement
T	Period of structure
x	Displacement
x_0	Gap opening displacement
x_{norm}	Normalised displacement
x_{peak}	Peak displacement
z	Stiffness ratio between the unloading and loading stiffness of the SKID device
α	Ratio between the SKID stiffness and PT frame initial stiffness
κ	Effective stiffness ratio
λ	Factor controlling the corner sharpness of the curve of $\text{H}(x_{\text{norm}})$
μ	Ductility level
ζ_{eq}	Equivalent damping ratio
$\zeta_{\text{eq, 0}}$	Elastic viscous damping ratio
$\zeta_{\text{eq, hyst}}$	Hysteretic component of equivalent damping ratio
$\zeta_{\text{eq, hyst, SKID}}$	Hysteretic component of equivalent damping ratio of SKID device
ω	Circular natural frequency

η	Displacement ratio
η_{ave}	Average displacement ratio

Chapter 7

F_{SKID}	Strength of the SKID device
E_{SKID}	Energy dissipated per cycle
$F_{PT\ outer\ frame}$	Strength of the PT outer frame
$F_{SKID\ inner\ frame}$	Strength of the SKID inner frame
K_{SKID}	Stiffness of the SKID device
$\dot{X}$	Velocity of the sliding keys
$\zeta_{eq.,\ SKID}$	Equivalent damping ratio of the SKID device
$\zeta_{SKID\ inner\ frame}$	Equivalent damping ratio of the SKID inner frame
$\xi_{eq.,\ hyst.,\ PTPW\text{-}SKID}$	Equivalent damping ratio of the PTPW-SKID inner frame
a_g, F_0, T_c^*	Parameters defining the seismic hazards of the site in the Italian National Annex of Eurocode 8
a_s	Site altitude above sea level
C_e	Exposure coefficient
C_t	Thermal coefficient
E	Young's modulus of the support column
$F_{SKID\text{-}support\ column}$	Global strength of a group of SKID-support column
H_{SC}	Hight of the support column
I_{SC}	Second moment of area of the support column section
K_{eff}	Effective stiffness
$K_{eff,\ PTPW\text{-}SKID}$	Effective stiffness of entire frame
$K_{eff.,\ PT\ outer\ frame}$	Effective stiffness of the PT outer frame
$K_{eff.,\ SKID\ inner\ frame}$	Effective stiffness of the SKID inner frame
$K_{PT\ outer\ frame}$	Stiffness of the PT outer frame
K_{SC}	Flexural stiffnesses of the support column
$K_{SKID\ inner\ frame}$	Lateral stiffness of the SKID inner frame
$K_{SKID\text{-}support\ column}$	Stiffness of one group of SKID-support column
m_e	Total seismic mass
n	Number of groups of SKID-support column
q_p	Peak velocity pressure
q_s	Characteristic value of snow on roof
q_{sk}	Characteristic value of snow on ground

R_{epi}	Epicentre distance
S_a	Spectral acceleration
T_{eff}	Effective period
T_R	Return period
$V_{b,0}$	Basic wind velocity
X	Displacement of sliding keys
X_{peak}	Peak displacement
$X_{reactivate}$	Displacement where the SKID device is reactivated
X_{SKID}	Displacement of sliding keys relevant to the SKID base
z	Stiffness ratio of the SKID device between loading and unloading stage
α	Ratio between the SKID device and support column
$\Delta_{est., SLS}$	Estimated drift ratio at SLS
$\Delta_{support\ column}$	Deformation of support column
β	Sliding slope angle
η	Non-dimensional parameter defining the shape pattern of hysteretic curve
μ	Friction coefficient
μ_1	Snow load shape coefficient
ρ	Deformation factor
ζ_0	Elastic equivalent damping ratio
ζ_{hyst}	Equivalent damping ratio of the hysteretic component
$\zeta_{PTPW\text{-}SKID}$	Equivalent damping ratio of the PTPW-SKID frame

Chapter 8

C_e	Correction factor
$D_{nonlinear}$	Peak displacement response of the nonlinear hysteretic model
$D_{spectrum}$	Estimated peak displacement from the displacement spectrum
k_s	Cantilever bar stiffness
K_{SKID}	Loading stiffness of the SKID device
T_e	Effective period
β	Slope angle
κ	Effective stiffness ratio
λ	Cantilever bar ratio of the second moments of area
μ	Friction coefficients
ζ_{eq}	Equivalent damping ratio

Chapter 1 Introduction

1.1 Motivation

On February 06, 2023, southern Turkey and Northern Syria were struck by a M_w 7.8 earthquake, followed by a series of aftershocks with the highest magnitude of M_w 7.7. As of June 01, over 50000 death were confirmed, and at least 2.3 million people left homeless, according to the United Nations (2023). Earthquake events like this have caused collapse of structures and consequently massive casualties and economic losses both in developing and developed countries. To improve the seismic resistance of structures, modern design codes have widely adopted ductile design logic. By introducing a reduction factor (a.k.a., the behaviour factor), the equivalent horizontal force considered in design is reduced, and plastic hinges are allowed to form at assigned positions to dissipate energy. This design method successfully balances the construction costs and life safety.

However, the structures following this design logic inevitably incur damage in structural components, even in earthquakes with low intensities. Most of them have been demolished after earthquakes because of the technical or economical issues of repair. According to McCormick et al. (2008), a residual drift ratio greater than 0.5% makes demolishing and rebuilding more economical than repairing damaged structures. In Christchurch earthquake of 2011, about 50% of buildings in central business district were identified to be unusable and 1000 buildings were demolished, resulting in an estimated cost of 40 billion dollars for reconstruction (Chancellor et al., 2014). The unavailability of such buildings led to stagnation of economic activities and further economic losses. A case is the Emilia earthquake of 2012, which caused direct losses of 1 billion Euros and additional 5 billion losses due to the interruption of production activities (Magliulo et al., 2014).

Improving seismic resilience of structures and making them operational in the aftermath of earthquakes have been identified as important targets in modern earthquake engineering. A pioneer work is the Precast Seismic Structural Systems (PRESSS) program carried out in 1990s (Priestley 1991). A self-centring precast moment-resisting concrete frame system was proposed and tested. The beams and columns were fastened to each other using prestressed cables, as were the columns to the foundations. Such connections were allowed to open (i.e., joint opening mechanics) when the frame was subjected to horizontal actions. The joint opening introduced a stiffness softening at large displacement, lengthening the structural period and capping the maximum loads accrued by the frame. In 2019, Obbdjornsson (2009) and Alexander et al., (2011) abstracted a one-story one-bay post-tensioned (PT) frame from the PRESSS structures. The quasi-

static properties and dynamic behaviours of the PT frame was systematically investigated by theoretical analysis and experimental shake-table tests. The research was then extended to multi-story buildings. Results indicated that damping devices are required in the PT frames as they do not provide any hysteretic damping.

The options for the damping devices can be friction based or hysteretic sacrificial-based. These devices perform a parallelogram-shaped hysteretic curve. Their energy dissipation capability is decided by the activation threshold, which is the frictional sliding activation force for frictional damping devices and the yield force of the hysteretic sacrificial devices. A greater activation threshold yields a better energy dissipation, however, requires a higher pre-tension force from the PT frame to make the damping device recentre. Additionally, the device with a greater activation threshold may not be triggered in low-intensity earthquakes, while a device with a low activation threshold may not dissipate sufficient energy in severe events. Therefore, these devices cannot satisfy all competing design criteria: (i) providing sufficient energy dissipation in severe earthquakes, (ii) dissipating energy in low-intensity events, and (iii) having a low activation threshold for re-centring. Besides, the hysteretic sacrificial devices may retain non-zero residual stresses and need repair after a strong event, raising health and safety concerns over the repair works. For frictional damping devices, measuring and ensuring the correct magnitude of the normal force is problematic.

This research aims to propose a novel device for providing large energy dissipation without an activation threshold. The device is intended for application within the PT frames to provide additional hysteretic damping but does not inhibit their self-centring. The mechanical schematisation is presented by proposing a conceptual Frictional Sliding on a Sprung Slope (FSSS) system. Then, a practical configuration is proposed and termed a Sliding Keys on Inclined Deflecting-cantilevers (SKID) device. The reliability and stability of the SKID device are physically demonstrated by carrying out quasi-static cyclic tests and fatigue tests. In addition, the study numerically investigates the application of the SKID device within the PT frames. The contributions of the SKID device to the seismic control of the PT frames are discussed. The influence of the SKID parameters on the dynamic performance of the PT-SKID frames is analysed. The reliability of the DDBD design with the linearisation based on Jacobsen's method is explored. Finally, a new Post-Tensioned Precast Warehouse structure with the SKID device (the PTPW-SKID structure) is proposed by following the PT-SKID conception for industrial buildings.

1.2 Objectives and scopes

The research presented in this thesis contributes to the solutions of the following issues:

1. Is it possible to propose a device for providing significant energy dissipation into a post-tensioned (PT) frame without inhibiting its self-centring? How does the device (the conceptual FSSS system) work? Can we achieve the proposed conception by a simple configuration?

2. Is the proposed physical configuration (the SKID device) stable? How consistent is the theory with empirical experience? How do the SKID parameters (friction coefficient, slope angle, and cantilever stiffness) affect its hysteretic behaviour?

3. What is the contributions of the SKID device to the dynamic control of the PT frames? What are the dynamic features of the PT-SKID frames? What is the sensitivity of the seismic responses of the PT-SKID frames to the SKID properties?

4. How is the accuracy of the linearisation based on Jacobsen's method to estimate peak drift ratio response of the PT-SKID frames subjected to earthquake ground motions? Does the DDBD method work well for the seismic design of the PT frames? Could we obtain a more reliable seismic design results?

5. Is it possible to propose a full self-centring industrial structure by following the PT-SKID conception? What is the structural arrangement and the load paths of the proposed structural system? How could we design the proposed system (the PTPW-SKID structure)? How well does it work in earthquakes?

1.3 Structure of thesis

The research in this thesis is presented in eight chapters as follows:

Chapter 2 presents a literature review regarding self-centring structures. A brief description of the rocking podium structures is presented, followed by a detailed introduction to the post-tensioned self-centring (PTSC) structures. Then, the damping device options for the PTSC structures are presented. The problems raised by existing damping devices on the performance of the PTSC structures are discussed. Finally, the seismic design methods of the PTSC structures are introduced.

Chapter 3 presents the conception and theoretical derivations of the FSSS system and the SKID device. The conception of the FSSS system and its mechanical schematisation are presented first. Analytical formulations are derived to estimate its hysteretic behaviours. Then, an innovative

physical realisation of the conceptual FSSS system is presented. The device uses the end stiffness of cantilever bars as the "sprung-slope" and is named a Sliding Keys on Inclined Deflecting-cantilevers (SKID) device. The reliability of using cantilever bars as a means of generating normal force is discussed.

Chapter 4 reports the physical demonstration of the SKID device. Two groups of tests are carried out. The first group consists of two 1/4 scale-reduced specimens having negative unloading stiffness (SKID A) and positive unloading stiffness (SKID B). Both specimens are subjected to the same quasi-static cyclic loading protocol. The aim of these tests is to verify the conception of the SKID device. The test results are compared with the theoretical hysteretic curves, verifying a satisfactory consistency between them. The second group has six SKID specimens having different manufacturing parameters (i.e., friction materials, cantilever bar stiffness and slope angle). They are tested to investigate the sensitivity of behaviour. Both cyclic and fatigue tests are conducted to assess SKID performance empirically.

Chapter 5 presents the application of the SKID device in the PT frames (the PT-SKID frames). The hysteretic performance of the PT-SKID frame is discussed by deriving the analytical formulations for estimating its hysteretic curve. Then, three heuristic PT frames with and without the SKID device are analysed numerically using OpenSees as a numerical proof-of-concept. Incremental dynamic analyses (IDA) are carried out for a set of ground motions. Additionally, more than 700 one-story one-bay PT frames with different SKID devices (PT-SKID frames) are numerically tested to investigate the dynamic characteristics of the structural system affecting the seismic response.

Chapter 6 investigates the linear equivalence of the PT-SKID frames based on Jacobsen's method for estimating peak seismic displacement response. Such linearisation is at the base of the Direct Displacement-Based Design (DDBD) of such structural systems. A simplified model capturing the hysteretic properties of the PT-SKID frames is proposed. Then, a linear equivalent system of the PT-SKID frame is constructed by its secant stiffness and the equivalent damping ratio estimated by Jacobsen's method. The accuracy of the linear equivalence to assess the peak seismic displacement response is evaluated by numerically testing 5,880 PT-SKID frames covering the most common range of parameters. The results show that the linear equivalence frequently underestimates the peak displacement response of the mid- to long-period PT-SKID frames, leading to an unconservative design in the DDBD. To eliminate the influence of this error, a correction factor is suggested for the design spectrum in the DDBD of the PT-SKID frames.

Chapter 7 proposes a novel Post-Tensioned Precast Warehouse structure with the Sliding Keys on Inclined Deflecting-cantilevers Device (the PTPW-SKID Structure) following the concept of

the PT-SKID frame for industrial buildings. The structural arrangement is presented and load paths are discussed first. Then, a case frame located in L'Aquila, Italy is designed to demonstrate its seismic performance. The Direct Displacement-Based Design (DDBD) method is utilised for the seismic design. Finally, a 3D numerical model is built in OpenSees. Both quasi-static and seismic dynamic analyses are carried out. The hysteretic behaviour and the seismic response of the case structure are investigated and discussed.

Chapter 2 Literature review

2.1 Introduction

Earthquakes, as one type of most severe natural disasters, have caused collapse of structures and consequently casualties and economic losses both in developing and developed countries. Design and construction technologies for improving the seismic resistance of structures have been developed by researchers for centuries. The early logic is increasing the stiffness and strength of structural components by using larger sections and stronger materials to control deformation and damage, commonly known as "stiff" design. However, this methodology requires a high demand for materials and limits the span and height of structures. Additionally, from a modern earthquake engineering perspective, high stiffness would increase the equivalent lateral forces accrued by structures.

In modern design codes (CEN 2004; SNZ 2004; ATC 2009; ASCE 2017; AISC 2010), ductile plastic zones are allowed to be formed at assigned positions in structures to dissipate seismic energy and lengthen the effective period. It is achieved by using a reduction factor (i.e., the behaviours factor in EC8) to reduce the considered equivalent lateral forces in design. This design logic has successfully balanced the trade-off between structural safety and construction costs, but it inevitably induces damage in structural components even in mild events. The damaged structure weakens its seismic performance in successive earthquake events (Freddi et al., 2021). Although this method has been recently improved by damage control and replaceable design technologies (Di Sarno and Elnasai, 2005, Freddi et al., 2021), the post-earthquake repair is still generally unadopted because of technical problems or exorbitant costs. Thousands of damaged structures have to be demolished after earthquakes, which leads to the stagnation of economic activities and further losses. A typical case is the Northridge earthquake in 1994, where considerable damaged structures were demolished after the earthquake because of the loss of resilience capability. This earthquake had a casualty of 57 but the economic losses were approximately 50 billion dollars (Porter et al., 2006). In 2011, the Christchurch earthquake (with a magnitude of 6.3) rendered about 50% of buildings in the central business district unusable because of severe damages, and 1000 buildings had to be demolished after the earthquake, which caused a cost of 40 billion dollars (NZD) (account for approximately 20% GDP of New Zealand) for reconstruction (Chancellor et al., 2014). In 2012, the Emilia earthquake caused direct losses of 1 billion Euros and an additional

5 billion induced by the stagnation of production activity (Magliulo, et al., 2014). Over 5000 jobs were at risk because of the cease of production (Bricco, 2012). One of the main reasons behind this is the residual deformation. According to McCormick et al. (2008a), a residual drift ratio of around 0.5% can be perceivable by occupants, while a ratio of around 1.0% can result in headaches and disrupt daily life for residents. Additionally, residual drifts after a mainshock may increase the seismic response during strong aftershocks (Erochko et al., 2011; Ruiz-Garcia and Aguilar, 2015) and impede escape from structures due to significant damage to non-structural elements (McCormick et al., 2008b). FEMA P58 suggests that a probability of demolition, given a residual drift ratio follows a lognormal distribution (ATC and NEHRP, 2012). Based on the field investigation of 12 steel moment resisting frame buildings after the Hyogoken-nanbu earthquake, Iwata et al. (2005) concluded that a residual inter-story drift ratio greater than 0.5% makes repairing structures unviable because of technical problems or high costs. McCormick et al. (2008a) suggested a 0.5% residual drift ratio as the threshold corresponding to building functionality, construction tolerance, and safety. Numerical results from Erochko et al. (2011) indicate that 6-storey structures with residual drift ratios greater than 0.5% no longer behave the way they were designed. The demarcation point for acceptable residual drift likely falls between 0.5% and 1.0 %. This reinforced the 0.5% limit suggested by McCormick et al. (2008a). According to Ramirez and Miranda (2012), economic losses in intermediate earthquakes are often dominated by losses due to residual drifts, especially for high-rise buildings designed with modern ductile methods. Obviously, larger residual drift ratios lead to higher repair costs (Dimopoulos et al., 2016). Thus, improving the resilience of structures to enable them operational after earthquakes has been widely seen as a significant goal.

The base isolation system effectively enhances structural resilience by limiting superstructure damage under design-level seismic intensities. By decoupling the motion of the superstructure from the ground shaking, the base isolation mitigates the forces and deformation accrued by the superstructure. Recent years have witnessed the development and broad utilisation of various base isolation systems, broadly categorised as elastomeric isolators (e.g., high-damping rubber isolators, lead rubber isolators) and sliding isolators (e.g., flat sliding isolators, friction-pendulum systems) (Di Sarno and Elnashai, 2005; Calviet at al., 2016; 2017). However, traditional base isolation systems entail high operating costs and maintenance requirements. To address this, a low-cost, easy-to-implement seismic base isolation system named PVC ‘sand-wich’ (PVC-s) was proposed recently (Tsiavos et al., 2020; 2021a; 2021b, Sextos, et al., 2022). As shown in Figure 2-1, the PVC-s system consists of two layers of polyvinyl chloride (PVC) positioned underneath the foundation, with said grains encapsulated between them. By allowing the PVC-s to slide, the seismic demand of the superstructure can be reduced by 30% to 70% in the design-level intensities (Sextos, et al., 2022). Generally, the base isolation systems work well under earthquakes with design-level intensities, where the superstructure is expected to be in the elastic stage and

possesses sufficient rigidity. However, the isolated structures may develop brittle failures under unexpected events, lacking robustness (Freddi et al., 2021).

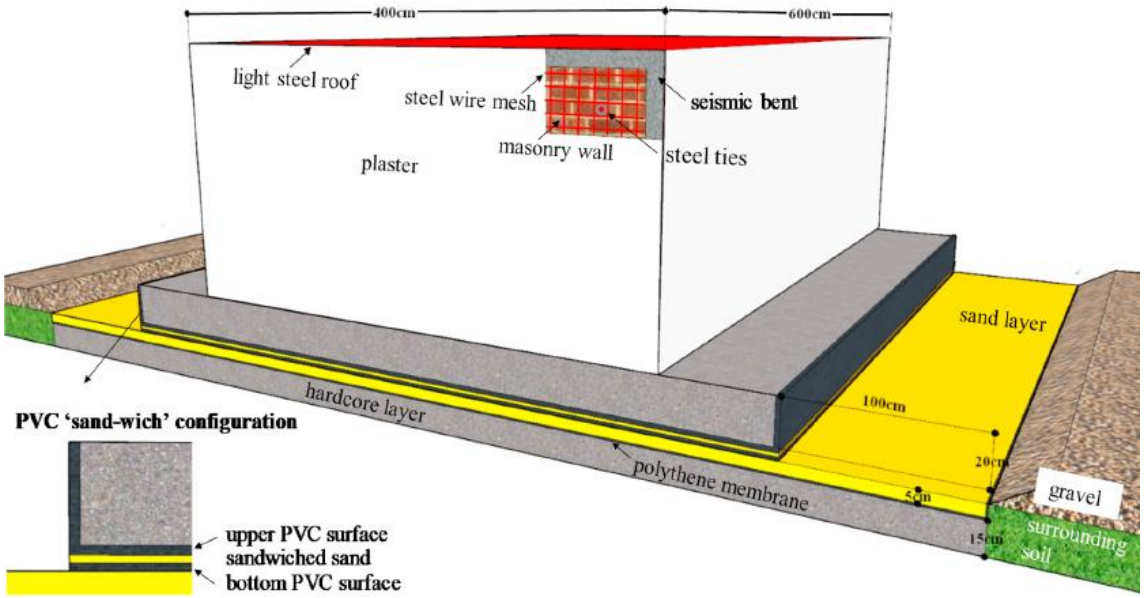

Figure 2-1 PVC 'sand-wich' (PVC's) isolation system (Tsiavos et al., 2021a).

Another viable option for enhancing structural resilience is self-centring structures. The self-centring structures are capable of automatically and promptly recovering back to their initial states by allowing certain members or subassemblies to lift or rock around a pivot point (Bachmann et al., 2017; Vassilion et al., 2017). These structures can be categorised into two groups: rocking podium structures and post-tensioned self-centring (PTSC) structures. Rocking podium structures permit superstructure to uplift freely by releasing whole vertical restrains, with their recentring capability ensured by gravity. PTSC structures allow gap-opening at beam-column or column-foundation connections. Post-tensioned cables are utilised to fasten structural components and provide recovery forces, with energy dissipation devices are normally required for additional damping.

The following sections focus on the historical development of self-centring structures. First, a brief description of rocking podium structures is presented, followed by a detailed introduction to PTSC structures. The PTSC structures covered in this literature review include self-centring moment-resisting frames, frames with PTSC braced, and PTSC rocking walls. Then, the damping devices used in PTSC structures are discussed, followed by an introduction to the design methods of these structures.

2.2 Rocking podium structures

As early as the mid-nineteenth century, researchers had realised the benefits of introducing rocking features into structures, although perhaps unconscious. One example is the amount of petroleum cracking towers that survived the Arvin-Tehachapi earthquake because they rocked on foundation pads under the earthquake events because of the lack of vertical restraints (Housner et al., 1956). In 1960, a study carried out by Muto et al. (1960) indicated that the overturning of slender structures requires ground motions possessing very long periods and large amplitudes, which are unlikely to occur in real earthquakes. This investigation demonstrated the theoretical feasibility of rocking podium structures.

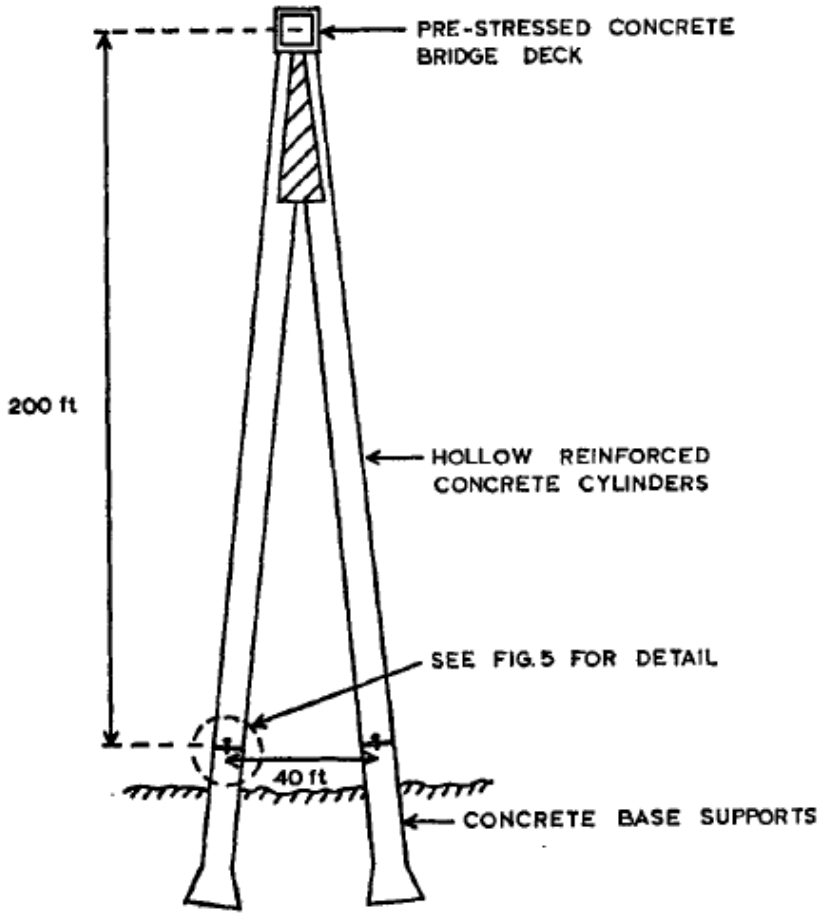

Figure 2-2 A typical A-frame pier for railway viaducts (Beck et al., 1973).

A pioneer work of rocking podium structures is the stepping pier for a railway viaduct in New Zealand proposed by Beck et al. (1973). As shown in Figure 2-2, the pier had an A-shaped configuration in elevation, with the top of the pier fixed rigidly to the deck and the feet connected with foundations using losing steel guide pins, allowing for uplifting. As the radiation damping (a form of energy dissipation that occurs in uplifting and dropping actions) provided by rocking mechanics is very limited (the equivalent viscous damping ratio is around 2%-6%) (Ajrab et al.,

2004), energy dissipation devices were utilised for additional damping to limit maximum lift. Computed lateral response of the pier under the EI Centro earthquake (1940) showed a substantial reduction in the equivalent horizontal force induced by the earthquake because of the existence of stepping action. Thus, the requirements for the sections and connections of the pier were reduced. Additionally, the pier could promptly recover back to its initial state after the excitation by the energy stored in the form of gravity.

In 1977, Huckelbridge et al. investigated a nine stories steel frame with rocking columns. A 1/3 scaled model was designed and manufactured. Its dynamic response was investigated by carrying out shake table tests, and the results indicated that the equivalent lateral loads accrued by the structure were reduced compared with its counterpart without the uplift feature. Additionally, storing seismic energy by gravitational potential energy was found more economical than dissipating it. Similar conclusions were also presented by (Clough, 1977; Meek, 1975; and Preistley et al., 1978). Based on the theoretical analysis and physical tests results, providing sufficient uplift limits for wind load and using a "shear key" to prevent walking off the foundation were suggested (Huchelbridge et al., 1977).

After the 1980s, Russia and the former USSR built over 400 buildings with rocking columns (Bachmann et al., 2017). Figure 2-3 shows a typical configuration of these systems, where the columns on the ground floor were permitted to rock freely. Figure 2-4 shows details of the rocking columns. The top and bottom of the columns were wrapped by steel caps to prevent concrete crushing induced by high stress in rocking. These rocking podium structures performed well in earthquakes, and the columns did not deteriorate over the years (Cherepinskiy, 2004; Uzdin et al., 2009). The design guidelines based on the elastic fixed-base cantilever SDOF model were proposed for this system (Polyakov 1974).

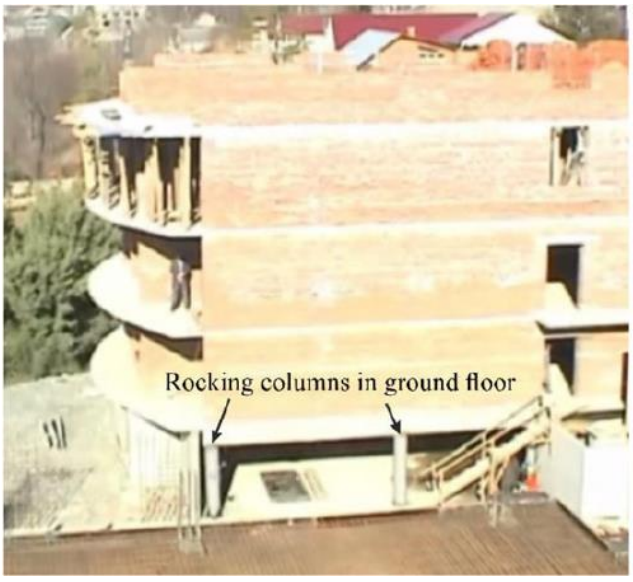

(a) (b)

Figure 2-3 Full-scale dynamic tests of a rocking podium structure: (a) the four-story masonry structure; and (b) rocking of a ‘kinematic bearing’ column (Bachmann et al., 2017).

(a) (b)

Figure 2-4 Rocking columns in bottom ‘kinematic bearing’ story: (a) completed (left) and unfinished (right) column; and (b) rocking of columns in a free-rocking-motion test (Bachmann et al., 2017).

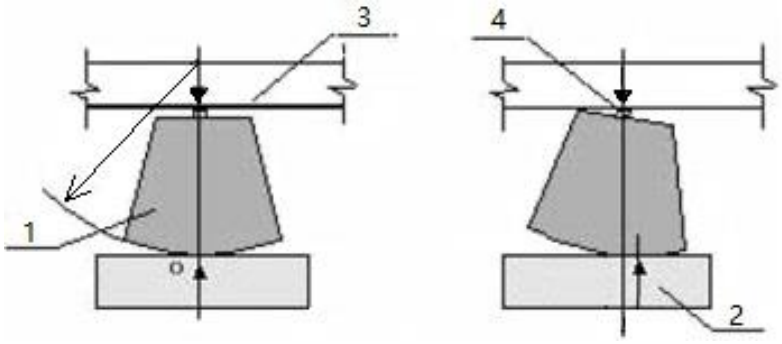

1-spherical abutment; 2-bedplate; 3-tie beam; 4-hinge junction

Figure 2-5 Configuration of the kinematics foundations (Cherepinskiy, 2004).

The concept of the rocking podium structures has been extended to wider structural systems (Sharp and Skinner, 1983; Cherepinskiy, 2004; Uzdin et al., 2009; Kelly, 1993; Savinov et al., 1995; and Dolgaya, 2002; Gelagoti et al., 2012; Kokkali et al., 2015). An example is kinematics foundations (KF) which were widely used in multi-store buildings (Cherepinskiy, 2004). The KF comprised a spherical abutment, a bedplate, a tie beam and a hinge junction, as shown in Figure 2-5. Investigations had shown that the KF was cost-effective and reliable to resist earthquake events. Then, the rocking shallow foundations were developed with the inspiration of the

nonlinear response of shallow foundations (where the failure of soil yielding and foundation uplifting accommodated the ductility demand and improved the safety of the entire structure) (Gelagoti et al., 2012; Kokkali et al., 2015). The structure with these foundations was found stable in strong seismic ground motions (Gelagoti et al., 2012). However, under poor soil conditions, the rocking shallow foundations may experience sinking dominant response instead of uplifting, which induced permanent rotations. This can be sorted out by using a compacted soil layer between shallow foundations and poor soil (Kokkali et al., 2015).

2.3 PTSC structures

The rocking podium structures rely on gravity to ensure the self-centring feature, which successfully balances the dynamic performance and construction costs. However, gravity alone cannot provide sufficient recovery force for lightweight structures, such as hospitals, multi-storey parking structures, and office buildings (Chancellor et al., 2014). Thus, post-tensioned cables are introduced into the system for additional recovery force, resulting in what is called post-tensioned self-centring (PTSC) structures.

PTSC structures can be conceptualised as comprising two main parts: a self-centring part and a damping device part. In the self-centring part, core members in certain structural components (e.g. braces) and/or assemblies (e.g. beam-column connections, column bases) are fastened by the post-tensioned cables, and the gap-opening is allowed between them, resulting in a nonlinear elastic backbone curve (the force – deflection curve) with a stiffness softening at large deformation. The stiffness softening effectively lengthens the period of the structure and limits the maximum equivalent lateral force that the structure can accrued. Figure 2-6 shows a typical hysteretic curve of the self-centring part of a post-tensioned moment-resisting steel frame (the PT frame) obtained from both quasi-static and dynamic numerical analysis (Oddbjornsson, 2009; Kibriya, et al., 2018). The equations for estimating the hysteretic behaviours of the PT frame and their verification can be found in (Alexander et al., 2011). The gap-opening feature of the self-centring part provides a chance for activating damping devices. As the damping provided by the gap-opening mechanics is insufficient (Kibriya, et al., 2018), damping devices are generally required in PTSC structures. The damping device could be hysteretic sacrificial devices (Xie et al., 2016; Nakaki et al., 1999; Qiu et al., 2019; Priestley et al., 1999) or frictional damping devices (Christopoulos et al., 2008; Tsai et al., 2008; Freddi et al., 2017; Pieroni et al., 2022). The traditional damping devices have a parallelogram-shaped hysteretic curve (Figure 2-7), requiring a recovery force to make them recentre. In PTSC structures, this recovery force is provided by the post-tensioned cables. Ideally, the pretension force should be greater than the activation

threshold (which is the yield force of the hysteretic sacrificial devices or the sliding activation force for the frictional damping devices) of the damping device to ensure self-centring.

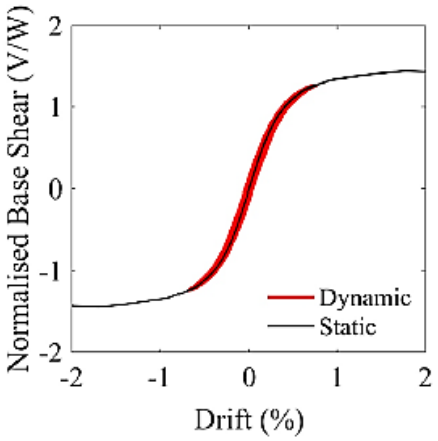

Figure 2-6 A typical hysteretic curve of the PT frame (Kibrya et al., 2018).

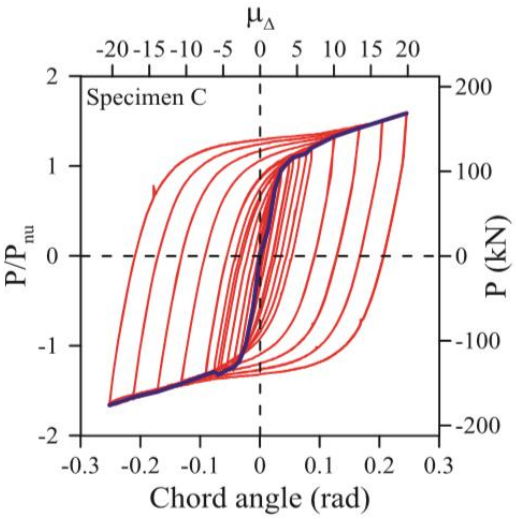

Figure 2-7 A typical hysteretic curve of the hysteretic damping device proposed by Qiu et al. (2019).

The pioneering work of PTSC systems was the Precast Seismic Structural Systems (PRESSS) program in the 1990s, where a five-storey precast moment-resisting concrete building was proposed and tested (Priestley, 1991; Priestley et al., 1999; Cheok, 1997). As shown in Figure 2-8, The beams and columns of the hybrid frame were fastened by unbonded pre-stressed cables. Mild steel reinforcements wrapped with solid grouted ducts were inserted into the top and bottom of the beams. The steel reinforcements could deform yield when they were subjected to tension or compression loads to dissipate seismic energy. The pre-tension force provided by the cables could make the frame re-centre by overcoming the resistance force of the reinforcements in the unloading stage. The dynamic results of a 60% scaled model showed that such a system could

perform a low residual drift ratio, while damage was limited to minor spalling and crushing in cover concrete and fibre grout pads (Priestley et al., 1999).

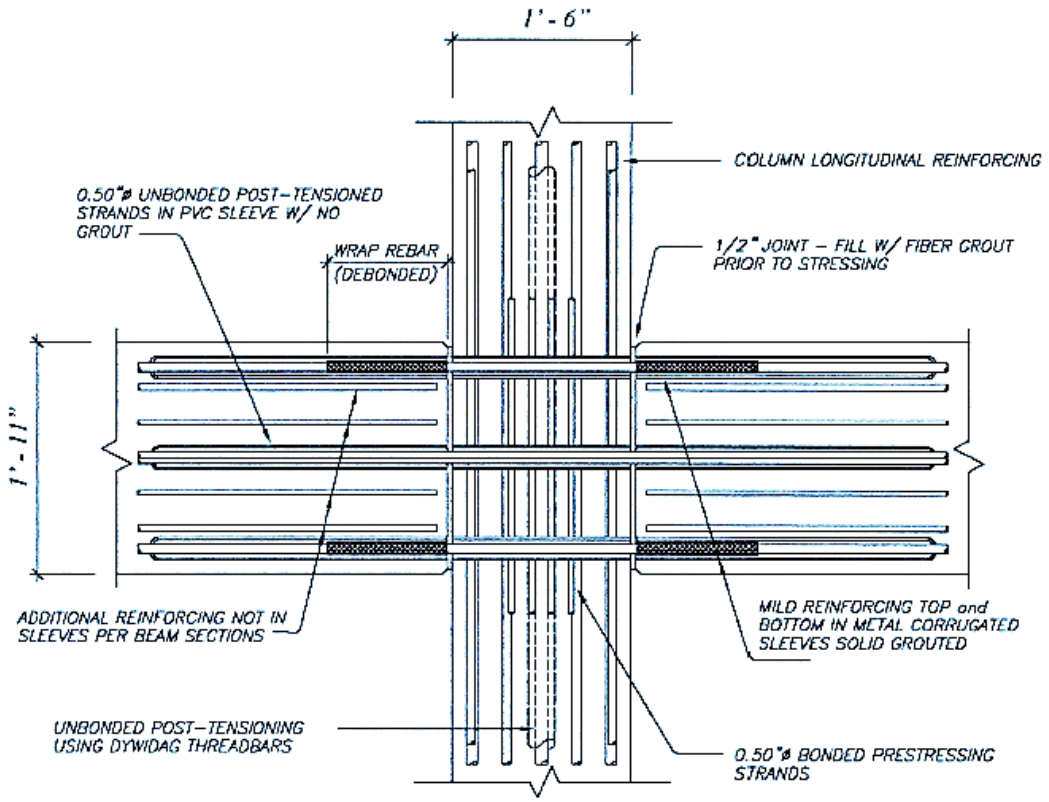

Figure 2-8 Configuration of the hybrid frame interior connection proposed by Nakaki et al. (1999).

The concept of the hybrid post-tensioned frames derived from the PRESSS program has been extended to wider structural systems, members, and assemblies, such as self-centring moment-resisting connections (Ricles et al., 2001; Christopoulos et al., 2002; Garlock et al., 2005; Chou et al., 2006; Garlock et al., 2005; Garlock et al., 2008; Tsai et al., 2008; Wolski et al., 2009; Chou and Chen, 2011; Dimopoulos et al., 2013; Vasdravellis and Karavasilis, 2013; Ralmzadeh and Alam, 2017), self-centring braces (Christopoulos et al., 2008; Xie et al., 2016; Chou et al., 2016; Wang et al., 2017; Moradi et al., 2018; Qiu et al., 2018), and self-centring rocking walls (Holden et al., 2003; Kurama et al., 2004; Marriott et al., 2008; Dowden et al., 2019; Dowden et al., 2012; Wu et al., 2019).

2.3.1 PTSC moment-resisting structures

The lateral resistance of the PTSC moment-resisting structures relies on the beam-column and column-foundation connections. The members in these connections are fastened by post-

tensioned cables, resulting in a high initial rotation stiffness. The Post-tensioned cables also provide recovery force for self-centring. Gap-opening is allowed in these connections, and members rotate around the flanges at the interface. Damping devices are installed and activated by the gap-opening. These connections avoid the brittle failure of traditional weld connections which were widely observed in the 1994 Northridge earthquake (Yussef et al., 1995). Additionally, the self-centring feature of these connections makes the structure promptly occupiable after earthquakes.

Both hysteretic sacrificial devices and frictional damping devices can be used for additional damping in the PTSC connections. Figure 2-9 shows a typical configuration of a PTSC connection where hysteretic sacrificial devices are used (Ricles et al., 2001). As shown, the top and bottom flanges of the beam are bolted with the inner flange of the column by angles. These angles could deform yielding with the rotation of the beam around the top or bottom pivot point (driven by the gap opening at the top or the bottom between the beam and the column flange). The schematics of the connection were physically demonstrated, and a six-story steel moment-resisting frame with this type of connection was numerically investigated. Then, nine large-scale and six full-scale interior connection subassemblies were physically tested by following cyclic protocols with a maximum drift ratio of 4% (Ricles et al., 2002; Garlock et al. 2005). The results showed that the connection could perform the compatible initial stiffness with a traditional welded connection. The connection could self-recentre promptly after excitations and concentrated damage in the angles (Ricles et al., 2001).

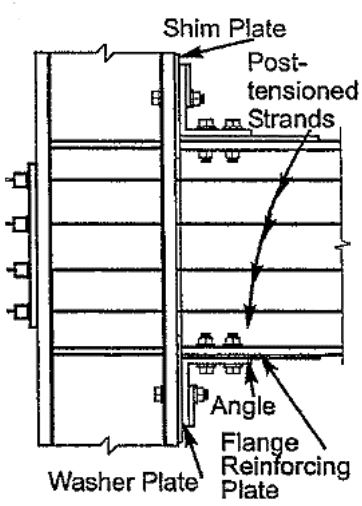

Figure 2-9 Configuration of the PTSC connection proposed by Ricles et al. (2001).

Figure 2-10 shows a PTSC connection with energy-dissipating bars (Christopoulos et al., 2002). Four buckling restrained bars were symmetrically welded inside of the beam flange and wrapped

by confining cylinders. The bars provide additional hysteretic damping through axial deformation under tension and compression, making it easier to estimate the strength and equivalent damping of this connection. The core member of hysteretic sacrificial devices could also be web hourglass pins (Vasdravellis and Karavasilis, 2013), reduced flange plates (Chou et al., 2006), or bolted T-stubs (Mirzaie Aliabadi et al., 2013).

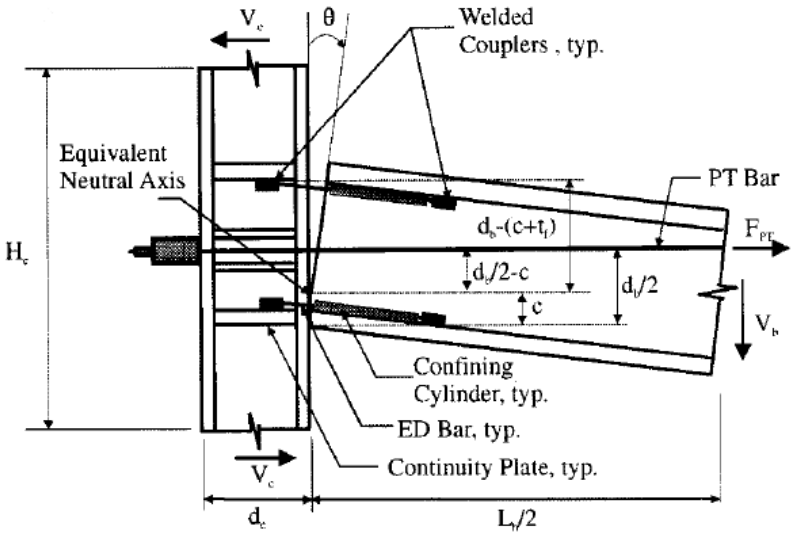

Figure 2-10 The PTSC connection proposed by Christopoulos et al. (2002).

Frictional damping devices dissipate energy through the frictional sliding between sliding pads. High-strength bolts with disc-spring washers are used to compress entire assemblies together and provide normal forces (Wolski et al., 2009). As shown in Figure 2-11, the frictional damping devices could be installed on the bottom and/or top flanges of beams (Figure 11 (a) and (b)) (Rojas et al., 2005; Wolski et al., 2009), or webs of beams (Figure 11 (c)) (Tsai et al., 2008), or both (Figure 11 (d)) (Pieroni et al., 2022). As the normal force applied by the high-strength bolts is constant, these connections perform a rectangular-shaped hysteretic curve. Frictional damping devices are normally repair-free after earthquakes.

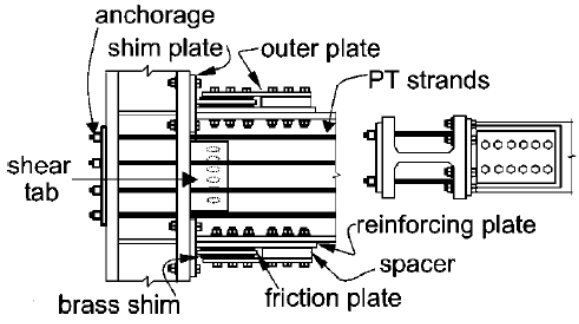

(a)

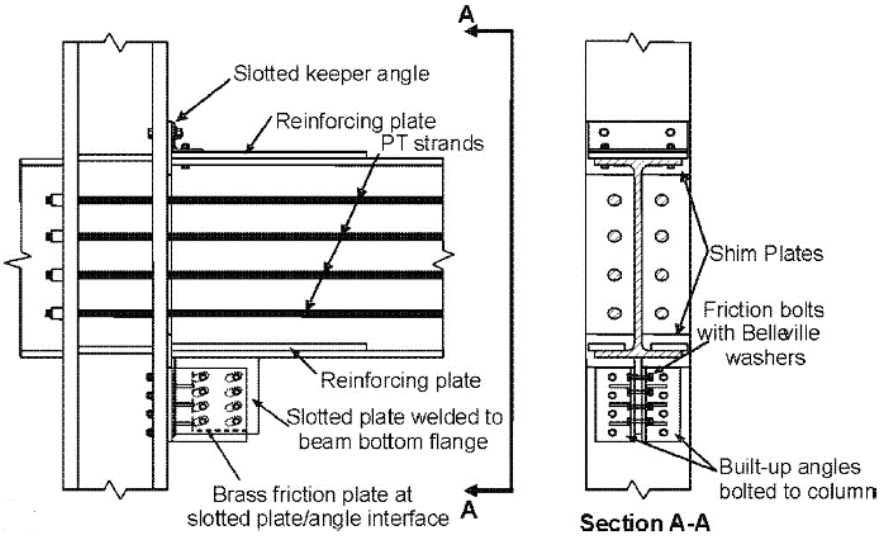

(b)

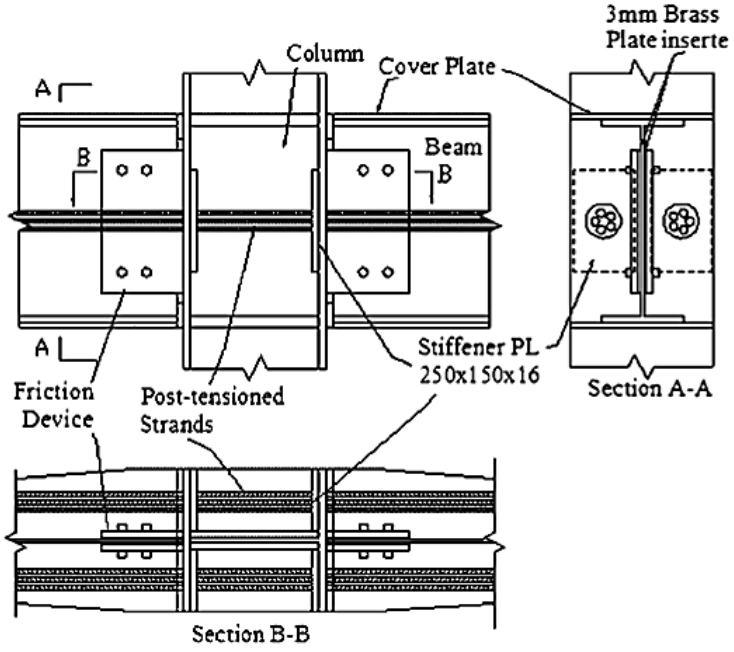

(c)

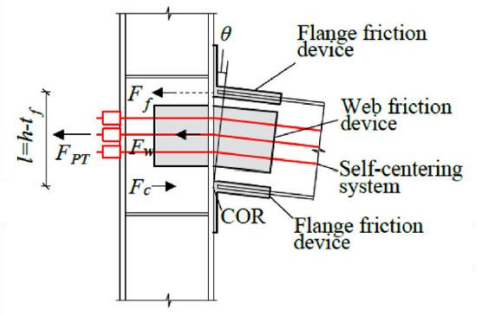

(d)

Figure 2-11 PTSC connections with frictional damping devices at: (a) both the top and bottom flanges (Rojas et al., 2005); (b) only bottom flange (Wolski et al., 2009); (c) the web of beam (Tsai et al., 2008) and (d) both the flanges and the web of beam (Pieroni et al., 2022).

The aforementioned connections allow the beam rotates around both the top and bottom pivot points to generate gap-opening, resulting in the expansion of frame. This expansion would be restrained by columns and slabs, leading to additional axial forces on the beam (Rahmzadeh and Alam, 2017). Additionally, this mechanism would affect the self-centring of the connection. Thus, measures have to be taken to accommodate the frame expansions raised by the PTSC connections, such as: (i) allocating floor slabs with collector beams (Garlock and Li, 2008; Garlock et al., 2006), or (ii) having discontinuous decks and unbonded slabs near columns (Rojas et al., 2005). These measures eliminate the interaction between the frame expansion and slabs (Chou and Chen, 2011). Alternatively, the frame expansion can be avoided by allowing the beam to rotate only around the top pivot point, as shown in Figure 2-12 (Dowden and Bruneau, 2011). In this case, the beam ends were cut out, and post-tensioned cables were eccentrically anchored. Two sets of cables must be used and anchored independently at two ends of the beam to achieve a self-centring feature.

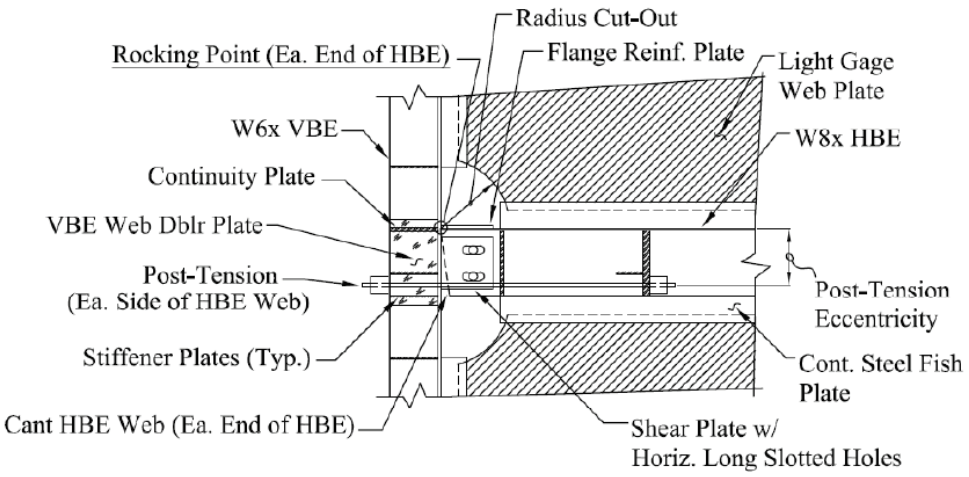

Figure 2-12 Configuration of the PTSC connection proposed by Dowdenet al. (2011).

2.3.2 Frames with PTSC braces

Braces can effectively increase the lateral stiffness of structures and achieve better drift response control. However, traditional steel braces perform stiffness and strength degradation in earthquake events, resulting in deformation concentration in certain stories. Buckling restrained braces (BRB) greatly improve the hysteretic behaviour of braces and concentrate damages (Qu et al., 2018), however, large residual deformation makes repairment of damaged braces impracticable or uneconomical (McCormick et al., 2008). Thus, PTSC braces have been proposed by many researchers. PTSC braces can be easily introduced into concentric braced frames by

replacing traditional braces. Compared with PTSC moment-resisting frames, PTSC braced frames avoid the challenge of frame expansion. (Chou et al., 2014).

As shown in Figure 2-13, PTSC braces comprise two bracing elements with a tension system and energy dissipating devices (Christopoulos et al., 2008). The bracing elements with the tension system perform a high initial stiffness and a stiffness softening feature by allowing gap-opening between two bracing elements. The gap-opening mechanism also provides a chance for activating the energy dissipating devices. The energy dissipating devices could be those based on frictional sliding (Christopoulos et al., 2008), hysteretic sacrificial (Xie et al., 2016), or viscous damping(Kitayama and Constantinou, 2017).

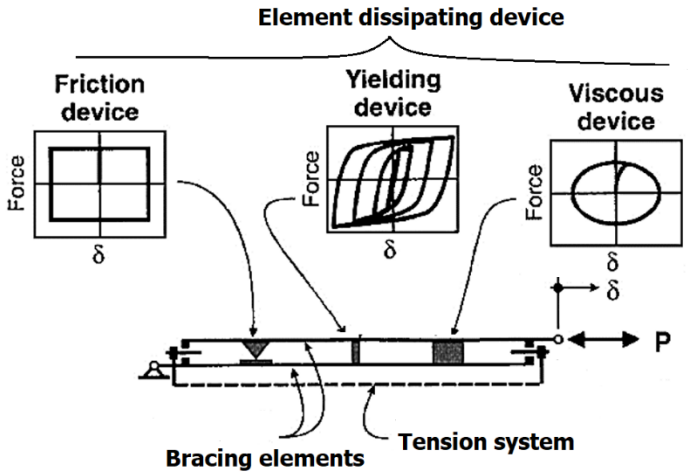

Figure 2-13 Conceptual configuration of the PTSC braces (Christopoulos et al., 2008).

Figure 2-14 (a) shows a typical configuration of the PTSC brace proposed by Christopoulos et al. (2008). The brace had two concentric rectangular steel tubes (an inner tube and an outer tube) with the same length but different diameters. Two end plates were fastened and firmly against two ends of the outer tube by post-tensioned cables. Aramid fibre-reinforced polymer (AFRP) strands were used as the post-tensioned cables. The elastic strain capability of the AFRP was up to 4%, which was much greater than that of steel cables (around 1%) (Ricles et al., 2001). The energy dissipating devices of the brace are friction-based, comprising two highly polished Type 304 stainless steel outer pads and a non-asbestos-organic inner friction pad. The inner tube and the outer tube were extended by end connections. When the brace was subjected to tensile or compression loads, a gap will be generated between the outer tube and the end plate at one end of the brace. The frictional damping device was activated by the malposition between two concentric tubes, and recovery force was generated by the elongation of the post-tensioned cables. In the unloading stage, the recovery force would overcome the resistant force of the frictional damping device to make the brace recentre. The ‘yield’ force (i.e., the gap opening force) of this brace was

decided by the pretension force. The hysteretic performance of the brace was physically demonstrated by Christopoulos et al. (2008) and shown in Figure 2-14 (b).

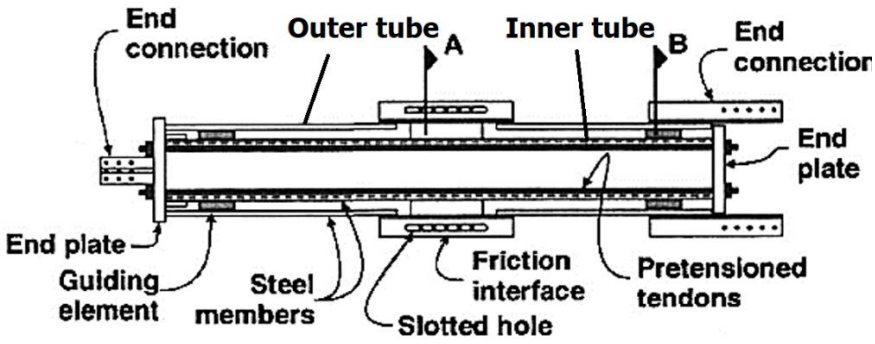

(a)

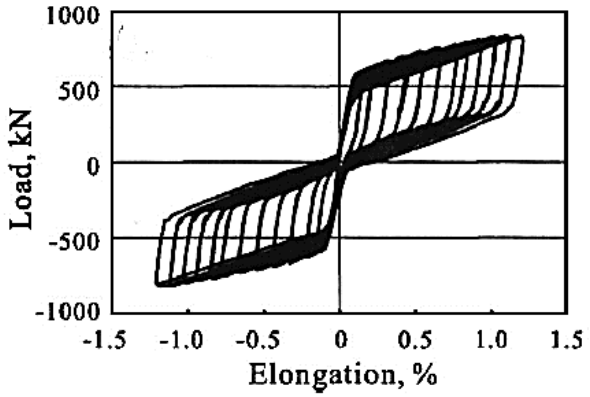

(b)

Figure 2-14 The PTSC brace proposed by Christopoulos et al. (2008): (a) the configuration and (b) the hysteretic curve.

Although AFRP strands have a larger elongation capability than steel cables, they were stretched at 84% of their ultimate strength when the brace reached a 1.3% elongation (which is corresponding to a 2% inter-story drift of the prototype structure) (Christopoulos et al., 2008). Thus, a friction fuse (Christopoulos et al., 2008) or buckling fuse (Lin et al., 2013) is required at the anchor ends of the strands to prevent their brittle failure. To reduce the elongation requirement on the post-tensioned cables, dual-core self-centring braces (DC-SCB) were proposed (Chou et al., 2014; Wang et al., 2017). Figure 2-15 shows the configuration of a DC-SCB proposed by Chou et al., (2014). The brace consisted of three sets of bracing elements, two sets of tensioning elements, and fiction devices. The three sets of bracing elements had a concentric layout and were denoted as the first core, second core and outer box, respectively. One end of the first core and the other end of the outer box were extended to form two ends of the brace. Adjacent bracing elements were cross-fastened at two ends with the inner end plate or the outer end plate by post-tensioned cables. E-glass fibre-reinforced polymer (EFRP) cables were used as the post-tensioned

cables. The energy dissipating device was frictional-based and activated by the malposition between the first core and the outer box. The special configuration successfully reduced the elongation requirement on the cables to half of the displacement between the two ends of the brace. The hysteretic performance of the DC-CSB was physically demonstrated, and its application in steel frames was numerically investigated in the following years (Chou et al., 2014; 2016; 2016a). The results indicated that the frame with the DC-SCB performed superior to traditional BRB frames both in transient inter-story drift ratio response and residual deformation (Chou et al., 2014).

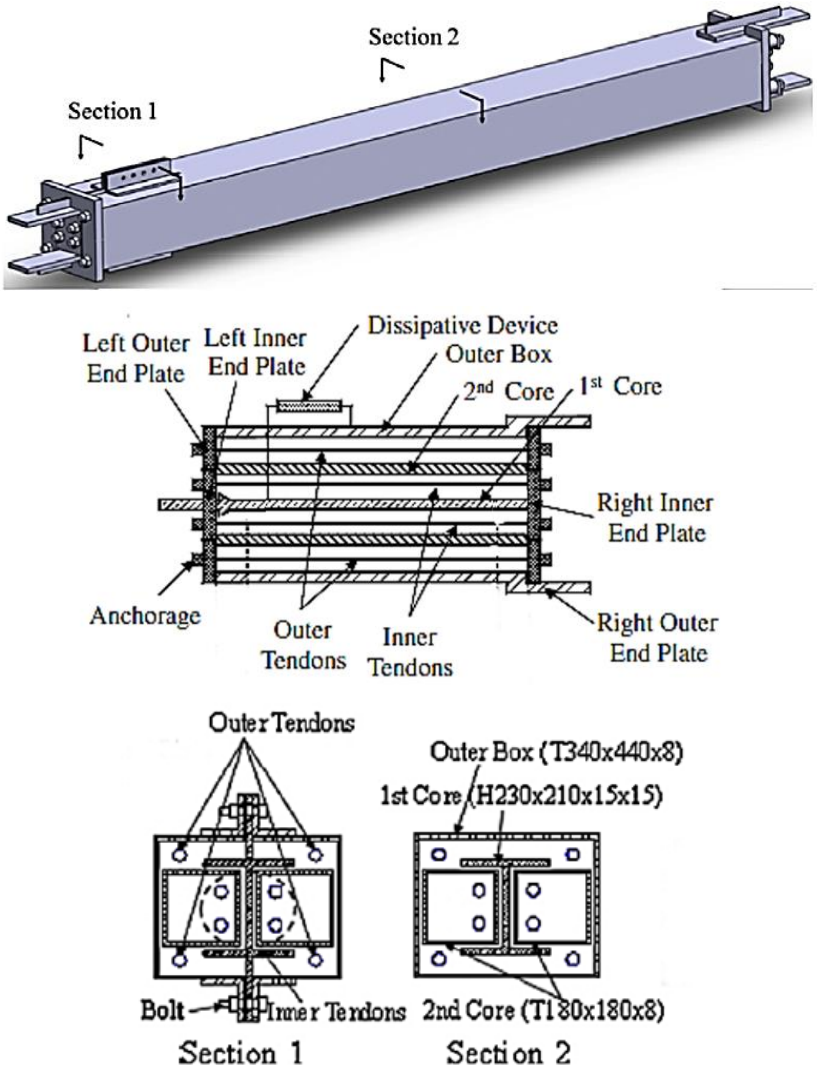

Figure 2-15 Configuration of the dual-core self-centring brace (DC-SCB) (Chou et al., 2014).

The dual-core configuration enables the utilisation of steel cables, which are seen as the most cost-effective and easy-anchored choice for post-tensioned cables. However, the physical test results showed that the initial stiffness of the DC-SCB was highly sensitive to the member length accuracy. Even a small member length error of 1/3000 could significantly reduce the initial stiffness of the brace, as reported by (Chou et al., 2014).

2.3.3 PTSC rocking walls

Steel plate shear wall (SPSW) has been widely used in steel frames to provide lateral stiffness and additional damping. It comprises a steel boundary frame and a thin steel infill plate or infill web strips that dissipate energy by the buckling tension field action. However, residual deformation is inevitable because of the buckling of the infill plate or web strips and the plastic hinges in steel boundary frames (Dowden et al., 2012). To reduce residual deformation, self-centring steel plate shear walls (SC-SPSWs) was proposed by integrating the rocking mechanism and post-tensioned moment-resisting connections with traditional SPSWs (Dowden et al., 2012). The connections used in the SC-SPSWs could be those rocking around the top beam flanges or the centreline (Clayton et al., 2012; Clayton et al., 2016; Dowden and Bruneau, 2019). The performance of SC-SPSWs has been systematically investigated by physical tests and numerical analysis (Dowden et al., 2012; Clayton et al., 2012; Clayton et al., 2016; Dowden and Bruneau, 2019; Clayton et al., 2013). The results indicated that this system could achieve a self-centring feature with stable energy dissipating capability and high initial stiffness.

Holden et al. (2003) proposed a post-tensioned concrete rocking wall for concrete structures, which allowed the concrete wall to rock around its bottom corners, generating a gap between the wall and its foundation. Mild steel bars were placed crossing the gap for additional damping. Post-tensioned cables passed through the gap to provide recovery force. Guide plates or thick reinforcement plates were set at the corners to prevent severe cracking. Physical tests of a half-scaled model indicated that visible damage could be successfully avoided under a cyclic loading drift of over 2.5%, and the self-centring was achieved (Holden et al. 2003; Retrepo et al., 2007). More PTSC shear walls can be found in (Marriott et al., 2009; Wu et al., 2019; Lu et al., 2017; Hassanli et al., 2017; Akbas et al., 2017).

The lateral stiffness and strength of structures can be significantly improved by coupling two or more walls utilising embedded steel beams, known as “hybrid” coupled wall systems. However, traditional "hybrid" coupled wall systems often experience residual deformation. To address this issue, post-tensioned self-centring devices can be used to connect the embedded steel beams with the walls (Aaleti and Sritharan, 2009; Huang et al., 2019; Sristharan et al., 2015). Kurama and Shen (2004) proposed a post-tensioned hybrid coupled wall system that allowed for free rocking at the foundation connections. Post-tensioned cables were horizontally anchored at two outer sides of the walls without any contact with link beams. Large-scale nonlinear cyclic tests were carried out, and the results indicated that this system achieved a coupling effect similar to traditional coupled wall systems and mitigated residual deformation. However, the energy dissipating capability of the system was limited (Kurama and Shen, 2004).

Similar concepts can also be applied to PTSC braced frames. Figure 2-16 shows a steel braced frame developed by Eatherton et al. (2014). The frame is allowed to rock around two column bases as a stiff vertical spine. A replaceable steel energy dissipating fuse was installed in the frame and activated by its rocking. The fuse compressed a set of mild steel plates with diamond-shaped holes, which optimised yielding distribution and achieved high ductility (Eatherton et al., 2014). Two post-tensioned cables were placed at the midspan of the frame and were anchored at the roof and the base. The recovery forces for self-centring were provided by the cables and gravity. Quasi-static cyclic tests and shake table tests indicated that this system could eliminate residual drift and concentrate damage into the replaceable fuses (Eatherton, 2010; Ma, 2010).

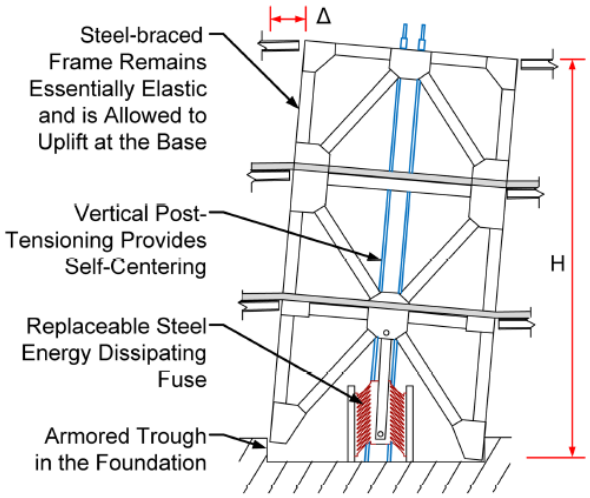

Figure 2-16 Configuration of the PTSC braced frame proposed by Eatherton et al., (2014).

2.4 Damping devices for PTSC structures

As mentioned, damping devices such as the hysteretic sacrificial devices and frictional damping devices are required in PTSC structures for additional damping. These devices have a parallelogram-shaped hysteretic curve with an activation threshold (the yield force of the hysteretic sacrificial devices as point B in Figure 2-17 (b) and the frictional sliding activation force for the frictional damping devices). With an increase of this activation threshold, the possible energy dissipation is increased (the area covered by the hysteretic curve is greater). However, a larger activation threshold requires larger earthquake magnitudes to trigger hysteretic damping, thus only protecting for large seismic events. Also, when used in combination with the PT frames, a large activation threshold (which is often the least required recovery force) will resist the re-centring of the PT frame after an earthquake ($M_{E,\,PTED}$ in Figure 2-17 (c), which decides the self-centring capability, is the sum of $M_{E,\,PT}$ in Figure 2-17 (a) and $M_{E,\,ED}$ in Figure 2-17 (b). Thus,

for the same self-centring capability, a greater $M_{E,ED}$ requires a higher $M_{E,PT}$.). On the contrary, low activation threshold devices, although can work in serviceability level events and contribute to better self-centring performance, will not be satisfactory in large seismic events. Even if the cables of the PT frame could provide sufficient post-tensioning forces to enforce frame re-centring, the hysteretic elements will contain non-zero residual stresses. If these elements need to be repaired/replaced, the potentially large residual stresses may raise health and safety concerns. For the frictional damping devices, although they can be designed as a repair-free device in the PTSC systems, measuring and ensuring the correct magnitude of the normal force is problematic.

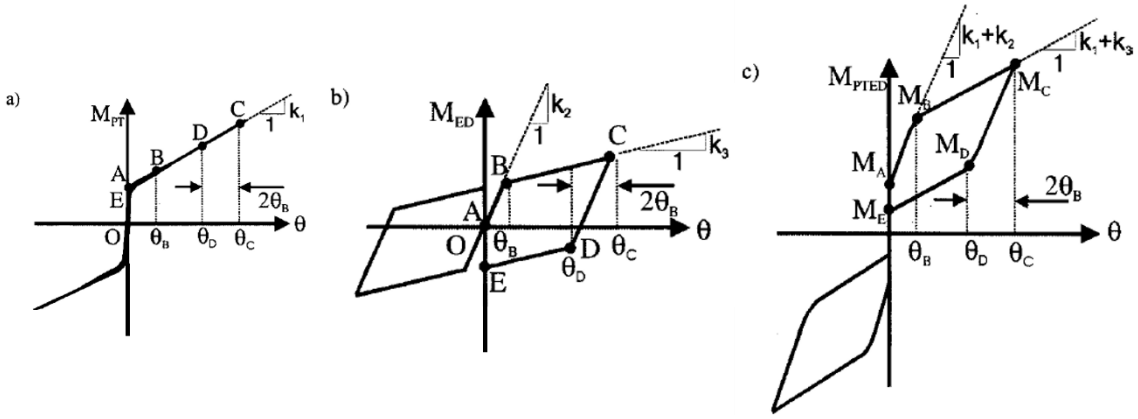

Figure 2-17 Application of hysteretic sacrificial device with PTSC frames: Hysteretic curve of (a) bared post-tensioned frame; (b) hysteretic sacrificial device; and (c) PTSC frame (Christopoulos et al., 2002).

There exists a type of damping device with a zero-activation threshold. These devices are based on the spring rings system and generate a triangular-shaped hysteretic curve. The spring rings are originally used as damping devices in drawbars and draft gears in railway systems (Hill, 1995) and missile shock isolation systems (Eshleman, 1972). They were introduced into structural systems in the 1980s for resisting earthquakes as braces (Shepherd and Erasmus, 1988; Issa ad Alam, 2019; Filiatrault et al, 2000; Wang et al., 2019; Hu et al., 2020), isolators (Hill, 1995), and beam-column joints (Khoo et al., 2012). The spring rings system is a set of separate inner rings and outer rings with tapered mating sliding surfaces in columnar form. When compressed, the inner rings and outer rings slide up against each other along the slopes, and the expansion/contraction of the rings generates a gradually increased normal force and consequentially amplitude-dependent friction force. This kinetic principle is the same as the wedge-lock mechanism used in coupon test wedge grips (De Baere et al., 2008), pneumatic wedge clampings (Tocut et al., 2021), cable anchors (Thompson, 2004; Motwani et al., 2020), and subsea pipeline recovery tools (Xing et al., 2019). In these applications, a set of wedge blocks is placed against sloped restraints (e.g. anchor pieces). The load born by the wedge blocks derives from the

friction forces generated along wedge-restrained sliding surfaces and increases with the sliding amplitude of the wedge blocks on the surface of the restraints. The gradual increase of load-bearing capability of these devices is because of the increased normal force from the minor compression deformation of the wedge blocks and the sloped restraints. The ring springs system adopts the amplitude-dependent force feature of the wedge-lock mechanism and dissipates energy by its frictional wedge sliding behaviour. The ring springs are driven by two endplates connected only with end rings. Therefore, only compression force can be carried by the spring rings systems. The continual work of such systems under cyclic loads (such as earthquakes) requires a self-recentre when the compression force unloads. This is achieved by ensuring a small friction coefficient and large slope angle for the sliding surfaces so that the potential energy stored in the rings from the sliding-up stage can start downward sliding automatically. The requirement of the self-driven sliding-down mechanic (limited by the mechanical principle of the spring rings system) places a constraint on its energy dissipation capability. A visual indicator of this behaviour is that the hysteretic curve of spring-ring devices is only located in the first and third quadrants of its force-deflection plot.

2.5 Seismic design methods for the PTSC structures

In current design codes (ECN, 2004; ASCE, 2017; NZS, 2004), the equivalent seismic lateral loads accrued by the frame are determined from a design acceleration spectrum with an estimated initial lateral stiffness. A reduction factor is used to consider ductile energy dissipation. This design logic (with capacity design principles) generally successfully prevents the collapse of the structures and saves lives in a relatively economical solution. However, such force-based design methods do not explicitly associate with damage level for this specific structural system. Although the peak displacement response (which is directly associated with damage level (Krawinkler, 1996; Priestley et al., 2007; Ghobarah et al., 2019) may be checked at the end of the design procedure by either nonlinear time history analysis method (Fajfar, 2000) or linear equivalence methods with the equal displacement (for medium- to long-period structures) or equal energy (for short-period structures) approximation, the code-defined displacement demand is deemed as a limit rather than a target. Thus, even if structures are designed based on the uniform seismic hazard spectrum, the seismic damage will vary from structure to structure. This failure in consistent damage design is inherent because, for example, (i) ductility capability (which determines the reduction factor) does not only depend on the structural type; (ii) equal displacement or equal energy may be invalid in structural equivalence; (iii) the force distribution among elements obtained from the structure analysis at the elastic conditions may differ from that in seismic events (Priestley and Grant, 2005; Priestley et al., 2007).

To achieve a uniform-damage seismic design, the maximum displacement can be defined as a target rather than a limit (Priestley, 1997; Eatherton et al., 2014; Bachmann and Dazio, 2019). As one type of displacement-based design method, the Direct Displacement-Based Design (DDBD, as shown in Figure 2-18) uses the secant stiffness (K_e in Figure 2-18 (b)) and the equivalent viscous damping (ζ in Figure 2-18 (c)) at the maximum response to construct the equivalent linear system (i.e., the substitute structure) (Priestley, 2002; Priestley et al., 2007; Priestley et al., 2007a). The equivalent linear system is used to estimate the nonlinear system dynamic response. The seismic response of the equivalent linear system can be easily obtained by spectrum analysis. The effective period associated with the secant stiffness is obtained from the code-defined displacement spectrum in this design procedure (Figure 2-18 (d). Then, the equivalent lateral force is calculated based on the effective period for structural analysis. Being different from the force-based design, where the structure analysis is carried out based on the elastic properties of elements, the structure analysis in the DDBD is carried out in the conditions at the target maximum displacement.

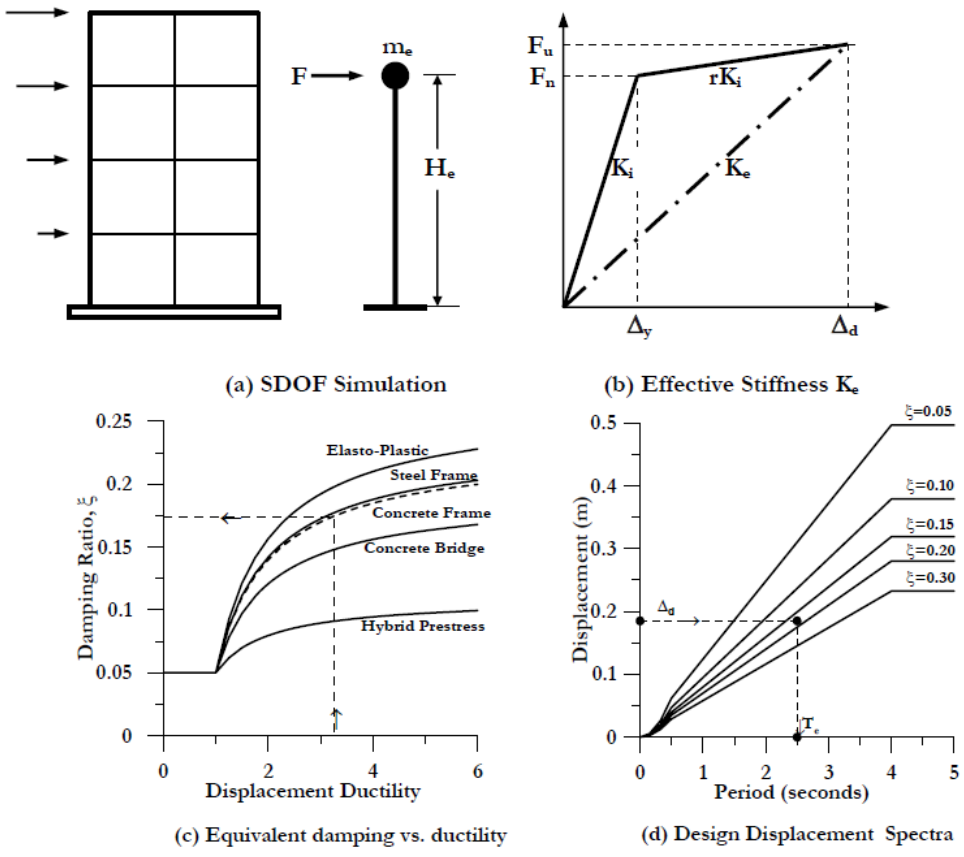

Figure 2-18 Foundations of DDBD: (a) SDOF simulation; (b) effective stiffness K_e; (c) equivalent damping vs. ductility; and (d) design displacement spectra (Priestley et al., 2007)

In the DDBD, the linear equivalence directly determines the design effectiveness (i.e., the closeness of design and effective performance of the system). Generally, the equivalent damping

ratio estimated by Jacobsen's method (Jacobsen, 1960) with the effective stiffness at the maximum displacement is utilised in the equivalence (Shibata and Sozen, 1976). This displacement-force relationship-based method can be easily incorporated with the capacity design of structural elements. However, the assumptions of Jacobsen's method cannot be met in a real earthquake. Thus, an unknown error is involved in estimating the peak displacement response. Blandon and Priestley (2005) evaluated the displacement estimation capability of this linear equivalence for different types of structures with various ductility demands. Six hysteretic models, including Modified Takeda Model, Bilinear Model, Elastic-perfectly-Plastic Model, Ramberg Osgood Model, and Ring Spring Model, were studied. The estimation accuracy was appraised by the ratio between the displacements obtained from the nonlinear system to their linear equivalence. The results showed that the linear equivalence based on Jacobsen's method frequently leads to an unconservative displacement estimation, especially for high-damping systems. Similar results were also reported by (Miranda and Ruiz-Garcia 2002; Dwairi and Kowalsky 2004; and Dwairi, et al., 2007).

2.6 Conclusion

Current seismic design methods rely on ductile plastic zones to dissipate earthquake energy, striking a balance between the structural safety and construction costs. However, damage is inevitable even after earthquakes with low intensity. These structures are normally demolished and rebuilt because their repair is unpracticable or uneconomical. The unavailability of these structures can induce long-term economic stagnation in the aftermath of earthquakes, resulting in further losses. Thus, self-centring structures have been proposed to improve the seismic resilience of structures.

Various self-centring structural systems have been proposed, such as rocking structures, PTSC moment-resisting frames, frames with PTSC braces, and PTSC rocking wall systems. The configuration of the self-centring structures can be conceptualised as two parts: a self-centring part and a damping device part. The self-centring part allows for gap opening at certain assemblages and performs a nonlinear elastic hysteretic behaviour, resulting in a high initial stiffness and stiffness softening at large deformations. The self-centring part also provides recovery forces for the self-centring capability.

The damping device part provides additional damping for the self-centring structures. It can be a hysteretic sacrificial device or a frictional damping device. These damping devices normally have a parallelogram-shaped hysteretic curve, with a non-zero activation threshold. The energy dissipation capability of these devices increases with the activation threshold. However, a large

activation threshold will inhibit the self-centring of the structure. Additionally, the device with a large activation threshold requires a large activation force to trigger the hysteretic damping, thus, cannot be activated in the serviceability limit state. On the contrary, the energy dissipation capability of the device with a low activation threshold may not be sufficient for large earthquake events. Although ring springs devices have a zero-activation threshold, their energy dissipation capability is limited because of their schematic mechanics. Thus, the design of traditional damping devices in self-centring structures must be a multi-objective compromise.

Therefore, a new damping device with both a zero-activation threshold (thus works at any event and does not inhibit self-centring capability) and satisfactory energy dissipation capability is required for the application within the self-centring structures. Once such a device is developed, it will be important to determine its optimal configuration for practical application. Additionally, the reliability and stability of its hysteretic performance should be demonstrated. The dynamic properties of the self-centring structures with this new device should be investigated. Furthermore, a design procedure should be developed for the self-centring structures with the new device.

Chapter 3 The conception of FSSS system and its engineering: The SKID device

The contents of this chapter have been adapted from the following publications:

1. Zhang, Y., De Risi, R., & Alexander, N. A. (2021) A frictional sliding on a sprung slope (FSSS) device that axiomatically confers energy dissipation with re-centring to post-tensioned (PT) frames: A conceptual study. *Engineering Structures*, 244, 112794.

2. Zhang, Y., De Risi, R., & Alexander, N. A. (2022) A novel seismic energy dissipating device, Sliding Keys on Inclined Deflecting-cantilevers (SKID): Theoretical and experimental evidence. *Engineering Structures*, 273, 115056.

3.1 Introduction

In this chapter, a conceptual novel progressive (amplitude-dependent) frictional energy dissipating device is proposed for post-tensioned (PT) frames. The device has a gradually increasing resistance and progressive energy dissipation capability, as sliding deformation increases in amplitude. This is achieved by a frictional sliding on a sprung slope (FSSS) system. These mechanical features, in combination with the PT frames, result in dual-triangular-flag-shaped hysteretic curve. This device is designed to axiomatically permit the self-centring features of PT frames while also providing good energy absorption for structures. It provides a 'repair-free state' for the main structural components after earthquakes since no residual stress remains (in FSSS and PT cables due to sway displacements) after it re-centres. The FSSS system has several advantages over traditional energy dissipating devices, namely, (1) energy dissipation capability in the serviceability performance level benefiting from no activation threshold, (2) customisable improvement in up-lift (post-yield) stiffness of frames, and (3) no impeding in the self-centring feature of PT frames. Compared with the spring-rings devices, the FSSS system can carry force both at the gap-opening and gap-closing stages, which leads to much more damping

in the second and fourth quadrants, in addition to that in the first and third quadrants. More hysteretic damping is significant for both controlling peak transient response (Di Cesare et al., 2020) and resisting progressive collapse (Qian et al., 2020). Besides, according to Hazaveh et al. (2020), the additional hysteretic damping in the second and fourth quadrants can reduce displacement response without increasing foundation demand.

The mechanical schematisation and design implementation of the FSSS system are first sketched. Then, theoretical analysis of the FSSS system was employed to quantitatively evaluate likely optimal properties of the device by deriving (a) its force-deformation relationship, (b) its energy-dissipative capabilities, (c) its estimated equivalent viscous damping ratios and (d) the influence of its core system parameters (such as slope angle, friction coefficient and spring stiffness) on performance.

This chapter also proposes an engineering development for the FSSS system. The device consists of three core components: (i) sliding keys, (ii) slope blocks, and (iii) deflecting-cantilever bars, and is termed a Sliding Keys on Inclined Deflecting-cantilevers (SKID) device. The configuration and the theoretical properties regarding the force-carrying capability and energy dissipation are presented in the chapter. In particular, the reliability of the cantilever bars is detailed.

The key research questions (aims) of this chapter are as follows:

1. Is it possible to add significant energy dissipation into post-tensioned (PT) frames, without compromising their self-centring?

2. What are the physically admissible configurations for this novel frictional sliding on a sprung slope (FSSS) system?

3. Can we propose a more rational configuration for the realisation of the FSSS conception?

3.2 The novel FSSS system: mechanical schematisation and design implementation

As a heuristic case, a one-storey one bay post-tensioned (PT) frame, experimentally tested by Oddbjornsson et al. (2012), is proposed. This provides both a simple proof-of-concept test of our FSSS system and an opportunity to benchmark the numerical models developed in this research against experimental results. Mechanically, this PT frame is schematised as a nonlinear spring-mass system (blue objects in Figure 3-1), where the nonlinear spring $k_{\mathrm{PT}}(x)$ is the stiffness

function (at sway displacement x) of the PT frame and M is the corresponding storey mass. Figure 3-1(b) also shows the kinematical schematic of the new FSSS system (red objects). The core assemblies of the FSSS system are (i) one slider block, (ii) two slope blocks and (iii) two compression spring blocks. The slider block (driven by the oscillating PT frame mass) is constrained to move in the same direction as the main sway motion of the PT frame while the slope block and compression spring blocks are constrained to move normal to the main sway motion of the PT frame. The arrangements of the device are symmetric such that its movement to the right and left produce identical behaviour. The sliding surfaces lie on an inclined plane of the sliding block and two slope blocks. The key feature of this system is that as the slider moves to the left the compression in the spring blocks increases gradually and this increases the normal contact force at the sliding interfaces. This is similar to the behaviour of a mechanical wedge grip used in standard tension tests. Hence, we have a system that progressively increases sliding resistance as the frame sway displacement increases. At a velocity sign reversal of the PT frame, the slider block moves back towards its initial position, and the friction force decreases with a gradual loosening of compression in the spring blocks. This process is repeated when the PT frame moves to the left. At the end of the exciting oscillations all loads remove from the compression spring blocks and hence the FSSS system return to their initial state and hence the PT frame re-centres.

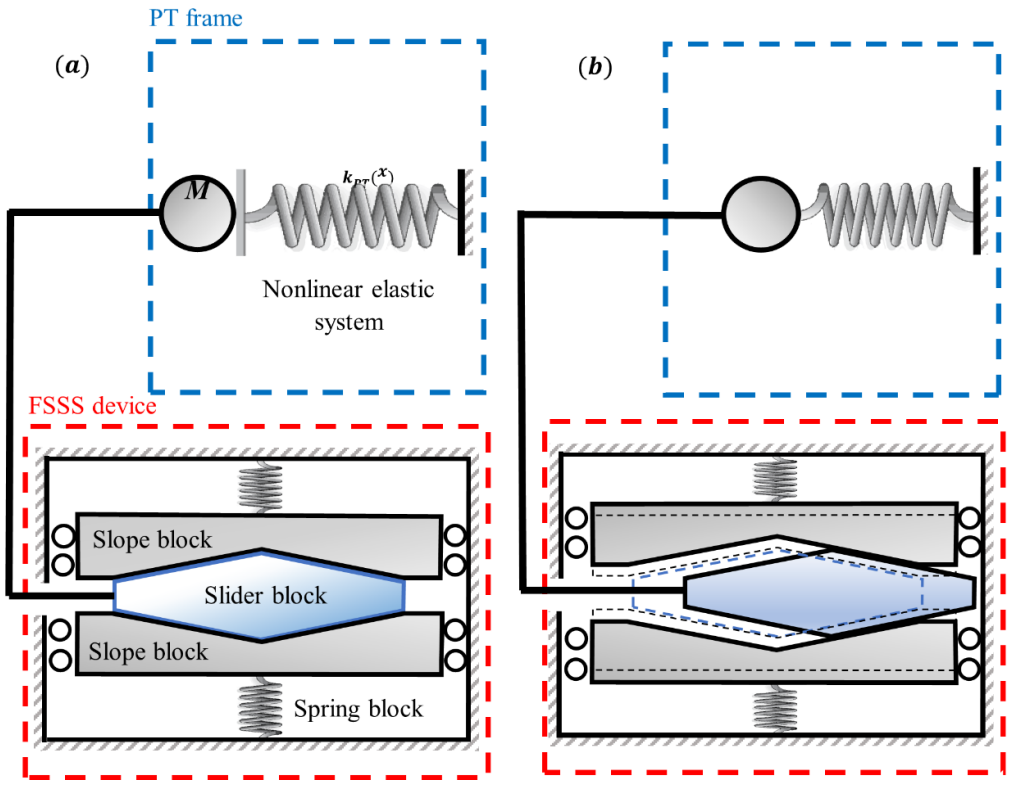

Figure 3-1 Kinematic schematic of the PT + FSSS system: (a) initial state, (b) when the mass moves right (spring blocks compress and slope blocks move normal to main sway motion of the PT frame).

In practice, there are many plausible design implementations of this device; Figure 3-2 shows an optional practical configuration that could be utilised in the PT frame. The FSSS system consists of a slider block, two slope blocks, two spring blocks, end roller bearings and a constraint container. The slider and the slope blocks of the device aggregate multiple inclined friction surfaces (a total of six in Figure 3-2), and are inserted into the constraint container. Two spring blocks are set between the slope blocks and the constraint container. Such a sandwich configuration ensures spring compression when the slider is sliding along the surfaces of the slope blocks. The friction surfaces between the slider and the slope blocks are expected to dissipate input energy in earthquake events. Roller bearings are placed between the ends of the slope blocks and the constraint container to eliminate any unwanted friction force at these edges. This may be achievable in practice using a low friction Teflon interface. The devices could be installed between the beam and a separate shear wall, and connected with them by the slider and the constraint container, respectively, as shown in Figure 3-2. The main in-plane sway motion of the PT frame drives the FSSS system in the plane, and it must be connected to the wall. We propose an indent/recess shown in Figure 3-2(a) to ensure this restraint. Any out-of-plane motions between the FSSS system and the 3D PT frame are not considered at the current research stage, although it is expected that these can be accommodated using a low-friction Teflon sliding surface underneath the device for out-of-plane sliding if this is necessary. The rocking of the PT frame about the pivot points, at the base of the columns, does require some vertical drop in the beam position as a second-order displacement. This can be accommodated by the vertical motion of the slider block and the slope blocks.

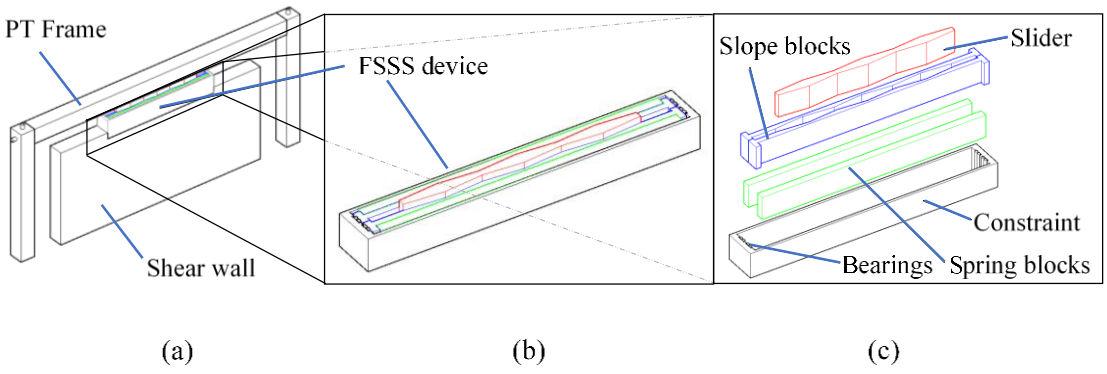

Figure 3-2 A design implementation of PT frame and FSSS system (a) PT frame and FSSS system connection (b) FSSS system components assembled (c) FSSS system components exploded view.

3.3 Theoretical hysteretic behaviour of the FSSS system

As shown in Figure 3-1, the horizontal component of the friction force along the inclined sliding planes are transferred to the PT frame by the slider. It is important to characterise the nature and magnitude of this resistive sliding force exerted on the PT frame. Therefore, a theoretical characterisation of the mechanical properties of the device is presented.

3.3.1 Force-displacement relationship of a FSSS system

The free-body diagram of the assemblage of a single slider block and two slope blocks is shown in Figure 3-3(a), when the slider moves toward the right-hand side as shown in Figure 3-1(b). In the figure, x is the displacement of the slider and is also the main sway degree of freedom (dof) of the PT frame. The angle of inclination of the sliding surface is given by β. F_{FSSS} is the force causing sliding induced by the seismic oscillations of the PT frame. R_s are spring reaction forces (which are due to the compression of the spring blocks); finally, R are the longitudinal constraining force applied by the external container and couple R' provide for moment equilibrium.

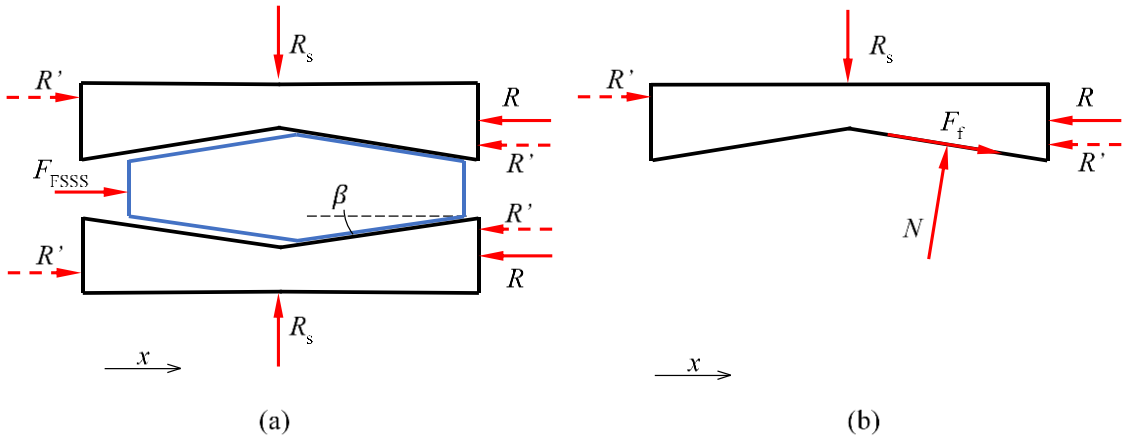

Figure 3-3 Free-body diagrams when the slider moves to the right for (a) the slider block and the slope blocks together; (b) the slope block alone.

Due to geometrical symmetry, the equilibrium of the free body diagram Figure 3-3(a) results in

$$F_{\mathrm{FSSS}} = 2R \qquad (3-1)$$

In Figure 3-3(b), the force equilibrium results in the following:

$$R = n(F_{\mathrm{f}}\cos\beta + N\sin\beta) \qquad (3-2)$$

$$R_{\mathrm{s}} = n(-F_{\mathrm{f}}\sin\beta + N\cos\beta) \qquad (3-3)$$

Where the integer *n* is due to the design case where there are multiple repeating units, in series, of up and down slopes. For example, in Figure 3-3(b) and Figure 3-1, the value of *n* should be taken as equal to 1. While in the design implementation shown in Figure 3-2, the integer *n=3* as there are three repeating units (up and down slopes) in series. In these equations, the relationship between the normal force *N* and the friction force F_{f} is assumed as:

$$F_{\mathrm{f}} = \mathrm{sgn}(\dot{x})\mu N \qquad (3-4)$$

where μ is friction coefficient, $\mathrm{sgn}(\dot{x})$ is a signum function. The relationship between the spring force and the longitudinal displacement of the slider block is:

$$R_{\mathrm{s}} = \frac{k}{2}\tan(\beta)x \qquad (3-5)$$

where $k/2$ is the stiffness of one spring block. By substituting Eq. (3-4) for *N* and Eq. (3-5) for R_{s} into Eq. (3-3) and solving for the sliding force F_{f} we obtain

$$F_f = \left(\frac{\tan(\beta)\,\mathrm{sgn}(\dot{x})\,\mu}{\cos(\beta) - \sin(\beta)\,\mathrm{sgn}(\dot{x})\,\mu}\right)\frac{k}{2n}x, \qquad \forall\ \beta < \beta_{\mathrm{crit}} \qquad (3-6)$$

where the critical slope angle β_{crit} is that value which causes the solution (3-6) to become singular, when $\dot{x} > 0$ and is defined as follows:

$$\beta_{\mathrm{crit}} = \arctan\left(\frac{1}{\mu}\right) \qquad (3-7)$$

This critical angle of slope is the maximum feasible value at which we can obtain a positive resistance while the FSSS system is loading and so should be considered a design limit, i.e. the angle employed should be $\beta < \beta_{crit}$.

By substituting Eq. (3-6) and Eq. (3-2) into Eq. (3-1), the expression of F_{FSSS} could be expressed as:

$$F_{\mathrm{FSSS}}(x,\dot{x}) = k_{\mathrm{FSSS}}x, \qquad k_{\mathrm{FSSS}} = \left\{\frac{(\mu\mathrm{sgn}(x\dot{x}) + \tan\beta))\tan\beta}{1 - \mu\tan\beta\mathrm{sgn}(x\dot{x})}\right\}k \qquad (3-8)$$

where k_{FSSS} is the stiffness of the FSSS system. Note that the number of multiple repeating units n plays no part in the final result. We replace $\dot{x}$ with $x\dot{x}$ so that the formulation above is generalised for both positive and negative x. This expression describes a piecewise linear (triangular-shaped) force-displacement relationship.

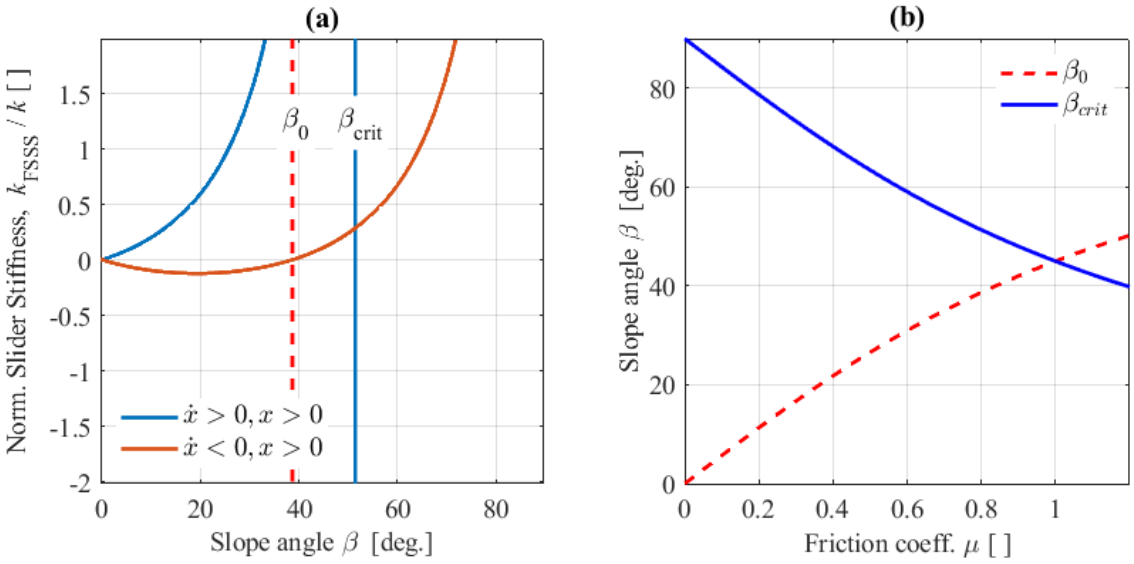

Figure 3-4 An example of FSSS stiffness vs. slope angle for loading (blue) and unloading (red) when the friction coefficient is μ=0.8; (b) generalised relationship between critical slope β_{crit}, β_0 and the friction coefficient μ.

Eq. (3-8) is displayed graphically in Figure 3-4(a). Figure 3-4(a) indicates that, while $\beta < \beta_{crit}$, the red unloading stiffness (when $\dot{x} < 0$ and $x > 0$, or similarly when $\dot{x} > 0$ and $x < 0$, although the equations for this case have not been presented for brevity's sake) can become negative for smaller values of slope angle β. This can also be observed directly by considering Eq. (3-8). In this case, the sign of the stiffness is driven by the sign of the numerator term and this sign changes from negative to positive when $-\mu\cos\beta + \sin\beta = 0$. Hence, the zero in this unloading FSSS stiffness occurs at the following angle β_0 defined as follows:

$$\beta_0 = \arctan(\mu) \qquad (3-9)$$

The relationship between angle β_0 and β_{crit} and the friction coefficient μ is displayed in Figure 3-4(b). This angle β_0 can be defined by the following non-dimensional parameter $\eta = 1$

$$\eta = \frac{\mu}{\tan\beta} \qquad (3-10)$$

Additionally, when $\eta > 1$ the unloading (red) FSSS stiffness is negative and when $\eta < 1$ the unloading (red) FSSS stiffness is positive. The device with positive unloading stiffness has a self-centring feature inherently but offers less damping. Conversely, negative stiffness makes the device have better energy dissipation capability but provides self-centring only when combined with a PT frame. Finally, in Figure 3-5, we can present the hypothetical form of the triangular shaped hysteretic loop which is based on Eq. (3-8).

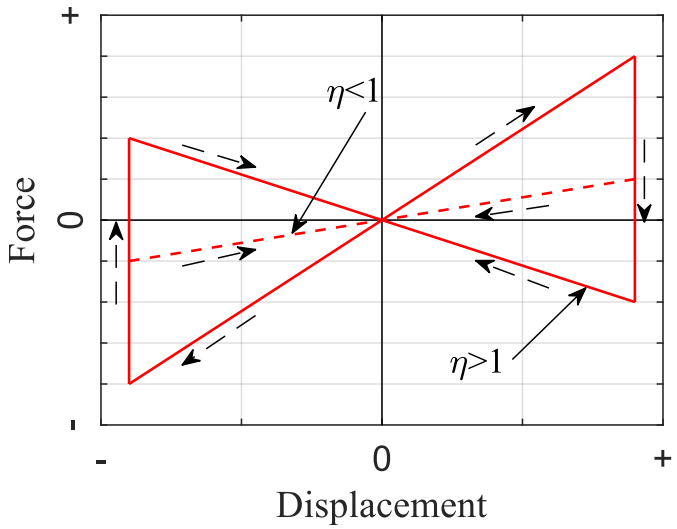

Figure 3-5 Shape of the hysteretic loop of the FSSS system: when η>1, the unloading stiffness is negative (red) and when η<1, the unloading stiffness is positive (dashed-red).

From a design perspective, it appears preferable to have a negative FSSS stiffness for unloading as this increases the area of the hysteretic loop, see Figure 3-4(b). Hence, an admissible design value for slope would be defined by the bound,

$$\beta < \frac{\min\{\beta_0,\, \beta_{\text{crit}}\}}{S_{\text{F}}} \qquad (3-11)$$

where a factor of safety $S_{\text{F}} > 1$ would allow for geometrical imperfections (i.e. fabrication and installation accuracy) in a physical FSSS system and limit excessively large stiffness of the device that could, in practice, completely negate the possibility of any significant sliding.

3.3.2 Estimating energy dissipation of the FSSS system

The energy dissipation capability of the FSSS system depends on the area within its hysteretic loop (shown in Figure 3-5). This energy dissipation E_{FSSS} in each complete cycle (for movement from the centre to the right and then to the left and back to the centre) is defined as follows:

$$E_{\mathrm{FSSS}} = \left(F_{\mathrm{FSSS}}(x, \dot{x} > 0) - F_{\mathrm{FSSS}}(x, \dot{x} < 0)\right) x \qquad (3-12)$$

Substituting Eq. (3-8) into Eq. (3-12), and rearranging we obtain the following:

$$\Pi = \frac{E_{\mathrm{FSSS}}}{kx^2} = \frac{2\mu\tan\beta(1+(\tan\beta)^2)}{1-(\mu\tan\beta)^2} \qquad (3-13)$$

where Π is the normalised energy dissipated per cycle. Figure 3-6 displays two examples of the normalised energy dissipation per cycle from Eq. (3-13). As the friction coefficient is increased, the normalised energy dissipation per cycle also increases. This is particularly apparent for larger slope angles. However, the design bound Eq. (3-11) limits excessively large slopes and in addition a designer must ensure that the stiffness force (provided by the FSSS system) from Eq. (3-8) is not so high that it effectively inhibits any meaningful sliding displacement in the case of a physical specimen.

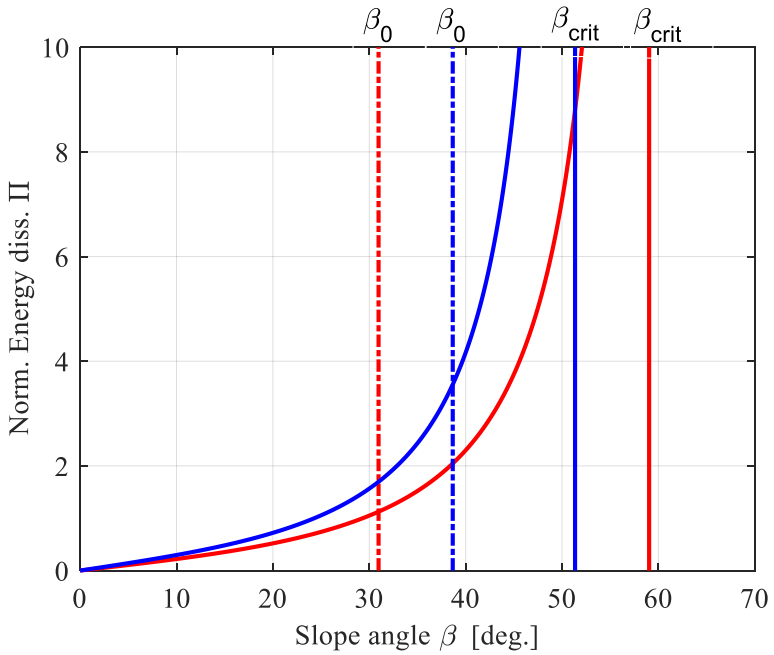

Figure 3-6 Examples of normalised energy dissipation per cycle for the FSSS system. Red lines (μ=0.6) , Blue lines (μ=0.8).

The work done E_{L} (per cycle) by an equivalent linear viscous oscillator is given by

$$E_{\mathrm{L}} = 2\pi\zeta_{\mathrm{eq}} k_{\mathrm{L}} x^2 \qquad (3-14)$$

where $k_{\mathrm{L}}$is the linear stiffness at the amplitude *x*. If we use the secant stiffness of the PT and FSSS system as our estimate of k_{L} then,

$$k_{\mathrm{L}} = k_{\mathrm{PT}}(x) + k_{\mathrm{FSSS}} \qquad (3-15)$$

Therefore, equating the energies Eq. (3-14) and Eq. (3-12), making use of Eq. (3-15), we can solve for the equivalent viscous damping ratio ζ_{eq} for the combined PT and FSSS system, which is defined as follows:

$$\zeta_{\mathrm{eq}} = \frac{k}{(k_{\mathrm{PT}}(x) + k_{\mathrm{FSSS}})} \frac{\Pi}{2\pi} \qquad (3-16)$$

Thus, the estimated equivalent damping ratio $\zeta_{\mathrm{eq}}$for the combined system appears proportional to sway displacement amplitude *x* due to the nonlinear elastic stiffness $k_{\mathrm{PT}}(x)$ of the PT frame. Additionally, $k_{\mathrm{PT}}(x)$ monotonically reduces with increasing sway displacement *x*; hence from Eq. (3-16) it is possible to conclude that the equivalent viscous damping ratio ζ_{eq} (of the combined PT and FSSS system) must monotonically increase with sway amplitude *x*.

3.4 A specific configuration choice of the FSSS system: SKID device

3.4.1 The configuration of SKID device

A new Sliding Keys on Inclined Deflecting-cantilevers Device (SKID) as a specific configuration choice of the Frictional Slider on a Sprung Slope (FSSS) conception is presented. By using the end stiffness of pairs of cantilever bars (columns), a few design problems existing in the configurations presented in Section 3.2 are avoided. These problems include: (i) the requirement of a shear wall within the PT frame bay, (ii) the practical difficulty in achieving a flexible layer and a very stiff box as "support" constraints for springs, and (iii) the requirement of roller sliding bearings for the orthogonal (the global *Y* direction in Figure 3-7) motion.

The device increases the lateral stiffness (of a PT frame) and dissipates input energy by the sliding motion of the sliding keys on the cantilever-supported slope blocks. As shown in Figure 3-7, the wedge-shaped inclined slope blocks (red objects) are mounted at the end of the deflecting cantilever bars (yellow column objects in Figure 3-7 (b) and 3-7 (c)). The cantilever bars have two functions when the device is loaded. Firstly, they provide resisting linearly elastic spring force (in the global *Y*-axis) that effectively increases with sliding displacement due to the geometry of the slope angle. This spring force is generated by the cantilevers bending about its

weak axis. A large range of cantilever cross-sections and lengths are available, which facilitates design optimisation of this spring stiffness. Secondly, the cantilevers carry a force component of the frictional force parallel to the PT frame motion by bending about its strong axis. Thus, a cross-section with a small inertial moment ratio (weak to strong axis) is highly recommended for the cantilever bar. The centroid of the sliding surface of the slope blocks should be positioned on the neutral axis of the cantilever bar to diminish the torsional moment, when the slope inclined normal forces and friction reaction forces are generated.

The sliding key(s) (cyan object(s)) contains one (for the monodirectional device Figure 3-7 (b)) or two (for the bidirectional devices Figure 3-7(c)) pairs of symmetric sliding surfaces with the same angle and friction coefficient. A pair of equal and opposite monodirectional SKID devices are theoretically equivalent to a single bidirectional SKID device. The slope blocks are designed to just touch the sliding keys with zero normal contact force for the initial zero sway displacement (global *X*) of the PT frame. In an assembled SKID device (Figure 3-7 (c)), the slope blocks, sliding keys, and cantilever bars are laid out symmetrically in terms of geometry and use identical materials for all slope blocks and cantilever bars. The sliding keys material may differ from the slope block to enable optimal frictional coefficient design choices. The sliding keys should be connected with the beams (that carry the story mass), and it is expected to be activated by the PT frame sway (horizontal) displacement during an earthquake event.

The support columns (shown in Figure 3-7 (a)) effectively provide an elevated rigid support restraint for the cantilever bars, thus enabling free choice of the length of the cantilever bar to the designer. This is important as we want to be free to assign the spring stiffness of the slope blocks, which is the tip stiffness of the cantilever bars, and this is predominantly governed by the length of the cantilever bar and its cross-section. The yielding of the support columns should be carefully avoided by design, ensuring it has appropriate stiffness and sufficient strength.

A flexible arrangement of the SKID device in a frame can be achieved depending on the architectural requirements; as in Figure 3-7, a pair of SKID devices with support columns installed separately at the two ends of the PT frame provides a large open and usable space below the beam. When the beam drifts in an earthquake event, the sliding keys move with the beam, slide on the slopes and enforce bending of the cantilever bars in the out-of-plane direction. As the sliding keys (the keys rigidly connected to the PT-frame) slide along the slope blocks, the normal force gradually develops, and hence the frictional force consequently increases. The magnitude of the normal force along the sliding interface depends on (i) the PT-frame sway displacement and (ii) the bending stiffness of the cantilever bars. It shall be demonstrated that the friction force that opposes the PT frame sway motion increases linearly during loading. After a velocity sign reversal (the unloading case) of the PT frame (sliding-down stage for the SKID device), the beam-driven

sliding keys move back to their initial position with a gradually decreased friction force. At the end of the exciting oscillation, frictional forces fade away, and the SKID device returns to the initial state without any residual deformation. This ensures that the PT frame is guaranteed to re-centre.

Note that any global out-of-plane motions (in the global *Y*-axis) between the SKID device and 3D PT frame are not considered at the current research stage, although they are expected to be accommodated using low-friction Teflon sliding surfaces or linear guide carriages between the beam and the top of the devices for out-of-plane sliding if this is necessary. In addition, the second-order vertical displacement drop of the beam induced by the rocking of the PT frame about the pivot points could be accommodated by permitting the sliding keys to slide vertically against the slope blocks. To achieve this, there is a need for a small gap between the bottom of the sliding keys and the top of the cantilever bars (see 'headroom' shown in Figure 3-7 (c)).

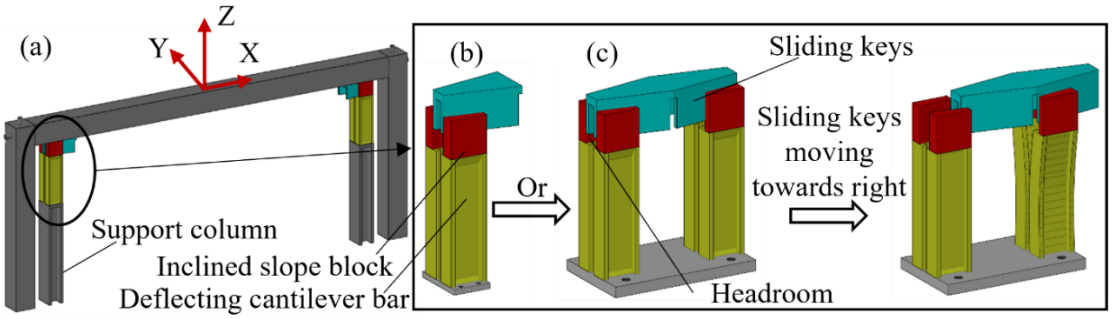

Figure 3-7 Configuration and kinematic of the SKID device: (a) positioning of a pair of SKID devices with PT-frame bay (b) single direction activation SKID device (c) bidirectional activation SKID device.

3.4.2 Force-displacement relationship between the sliding keys and slope blocks

Figure 3-8(a) shows the schematics of the SKID device, where the orange springs and the violet springs are the elastic flexural bending stiffness of the cantilever bars around their weak and strong axes, respectively. Figure 3-8(b) shows the free-body diagram of the sliding keys and slope blocks. In the figure, F_{SKID} is the force causing sliding induced by the seismic oscillation of the beam and applied to the sliding keys, x is the relative displacement between the slope blocks and the sliding keys in the longitudinal (local x) direction, β is the angle of slope blocks, F_s and R are the spring forces provided by the deflection of the cantilever bars around their weak and strong axes, respectively. The force-displacement relationship between the sliding keys and slope blocks complies the same derivation with that reported in Section 3.3.1, i.e., Eq. (3-8). Note that for the SKID device, k in Eq. (3-8) is the total bending stiffness of the cantilever bars around weak axes.

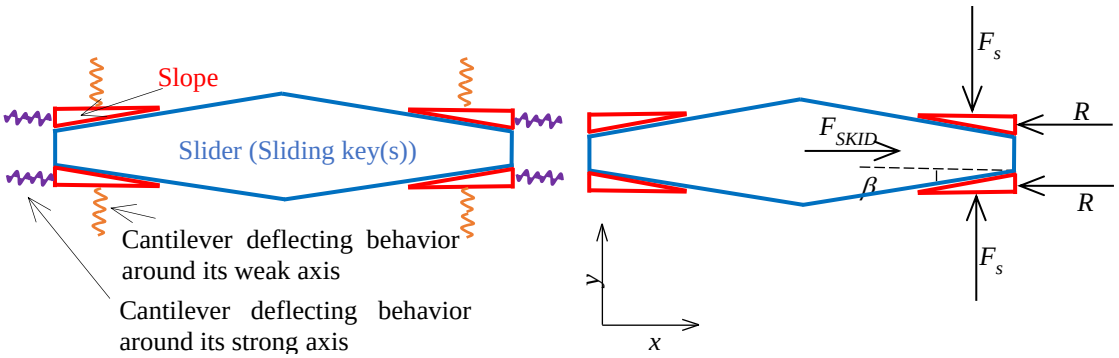

(a) (b)

Figure 3-8 Schematics of the SKID device: (a) schematics; (b) free-body diagram of sliding keys and slope blocks.

3.4.3 Influence of the cantilever bars

The cantilever bars are expected to deform by y_c about their weak axis as the sliding keys begin to slide (the deformation of the orange springs shown in Figure 3-8 (a)). The stiffness of the cantilever bar is specifically designed to ensure a triangular hysteretic property. In addition, the cantilever bar must deform by a smaller amount x_c by bending about its strong axis (the deformation of the violet springs in Figure 3-8 (a)).

The relative sliding displacement between slope blocks and sliding keys is defined by x (in Figure 3-8 and Eq. (3-8)), and hence the total displacement of the sliding keys (connected to the frame) is

$$X = x + x_c \tag{3-17}$$

Hence, the cantilever bar displacement x_c should be viewed, from a design perspective, as reducing the sliding displacement x compared to that of the frame displacement X.

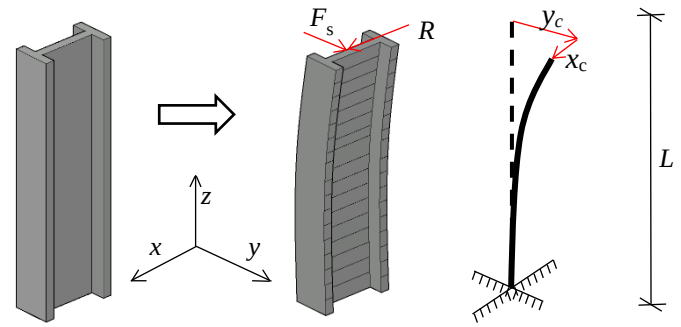

Figure 3-9 Deformation of the cantilever bar while the SKID device is active.

Figure 3-9 shows the deformation of a cantilever bar when the device moves from the initial condition to some arbitrary sliding relative displacement x. We assume small (linear elastic) displacements. The cantilever stiffness is assumed as follows

$$k_x = \frac{c_x E I_x}{L^3}, \qquad k_y = \frac{c_y E I_y}{L^3} = \frac{k}{2} \tag{3-18}$$

where k_x and k_y are the cantilever flexural stiffnesses in x and y directions, I_x and I_y are the second moment of areas in x and y directions, E is young's modulus of the material, L is the length of the cantilever, c_x and c_y are factors regarding the boundary conditions of the cantilever bars. In this case, both c_x and c_y can be assumed to be the value of 3. Note that it is slightly different in practice because the encastré boundary condition of the cantilever bars is difficult to achieve because of some flexibility in the foundation supports. Thus, the stiffness ratio of the cantilever bar in the x-axis to the y-axis is

$$\lambda = \frac{k_y}{k_x} = \frac{c_y I_y}{c_x I_x} \tag{3-19}$$

The displacement of the top point on the cantilever bar in the x direction relative to the fixed base is derived in the following

$$x_c = \frac{R}{k_x} = \frac{k_{SKID}}{2k_x} x \tag{3-20}$$

By substituting Eq. (3-19) for k_x to Eq. (3-20), the x_c can be rewritten as

$$x_c = \frac{k_{SKID}}{2k_y} \lambda x = \frac{k_{SKID}}{k} \lambda x \tag{3-21}$$

Note that, for the SKID device, k_y is the spring stiffness $k/2$ in Eq (3-8). Noting that x_c is, from a design perspective, a reduction (loss) in sliding displacement caused by deformation of the cantilever in the x-direction for a given frame displacement X.

Consider the relationship between frame displacement X, relative sliding displacement x and cantilever block displacement x_c, as follows

$$X = x + x_c = x\left(1 + \frac{k_{SKID}}{k}\lambda\right) \tag{3-22}$$

We can define the sliding displacement reduction factor, α, as

$$\alpha=\frac{x}{X} \qquad (3-23)$$

By substituting Eq. (3-8), Eq. (3-21) and Eq. (3-22) to Eq. (3-23), α can be rewritten as

$$\alpha=\left(1+\frac{(\mu\text{sgn}(x\dot{x})+\tan\beta))\tan\beta}{1-\mu\tan\beta\,\text{sgn}(x\dot{x})}\lambda\right)^{-1} \qquad (3-24)$$

According to Eq. (3-8), the resisting force of the SKID device is in the proportion of the relative displacement x and the stiffness k_{SKID}. Thus, the displacement reduction is equivalent to a stiffness reduction. The device strength expressed in Eq. (3-8), in terms of the sliding displacement between the slope and the sliding keys, can be rewritten in terms of PT frame displacement X as follows

$$F_{\text{SKID}}(X,\dot{X})=k_{\text{SKID}}\alpha X=K_{\text{SKID}}X, \qquad K_{\text{SKID}}=\alpha k_{\text{SKID}}=\alpha\left\{\frac{(\mu\text{sgn}(x\dot{x})+\tan\beta))\tan\beta}{1-\mu\tan\beta\,\text{sgn}(x\dot{x})}\right\}k \qquad (3-25)$$

where K_{SKID} is the SKID device stiffness that includes the reduction factor α caused by the bending of the cantilever bar about its major axis. The value of Eq. (3-24) is relative to a signum function, indicating that the stiffness reduction factor in Eq. (3-25) is different in the sliding-up and sliding-down phases. Figure 3-10 (a) presents the value of α both in the sliding-up (solid lines) and sliding-down (dashed lines) phases when different slope angle β and friction coefficient μ are utilised in the SKID device. The ratio of λ is set to be 0.1, which is a typical value of the I section. As shown, the deformation of the cantilever block in the strong axis has a more obvious effect on the sliding-up phase than the sliding-down phase. This deformation even 'increases' the sliding-down stiffness in the range of large μ and small β, as the value of α is greater than 1 in this range. This is because the SKID device with such parameters has a negative stiffness in the sliding-down phase, and this negative sliding-down stiffness is enlarged in its absolute value by the recovery of the elastic deformation of the cantilever bar about its strong axis. The different values of α in the sliding-up and sliding-down phases indicate that this reduction cannot be compensated by simply multiplying k with $1/\alpha$. Actually, the shape of the hysteretic curve is changed because of the existence of the α. Figure 3-11 shows the shape of the hysteretic curve of the SKID device considering this stiffness reduction. As shown in Figure 3-11, besides the reduction in sliding-up and sliding-down stiffness, the sliding-down begins later with an unloading stiffness induced by the deformation recovery of the cantilever bar. The beginning point of the sliding-down is expressed as ρX_{PT}, and the elastic deformation factor ρ is defined as

$$\rho = \frac{\alpha(x\dot{x} > 0)}{\alpha(x\dot{x} < 0)} \qquad (3-26)$$

where $\alpha(x\dot{x} > 0)$ and $\alpha(x\dot{x} < 0)$ are the α in the sliding-up and sliding-down phases, respectively.

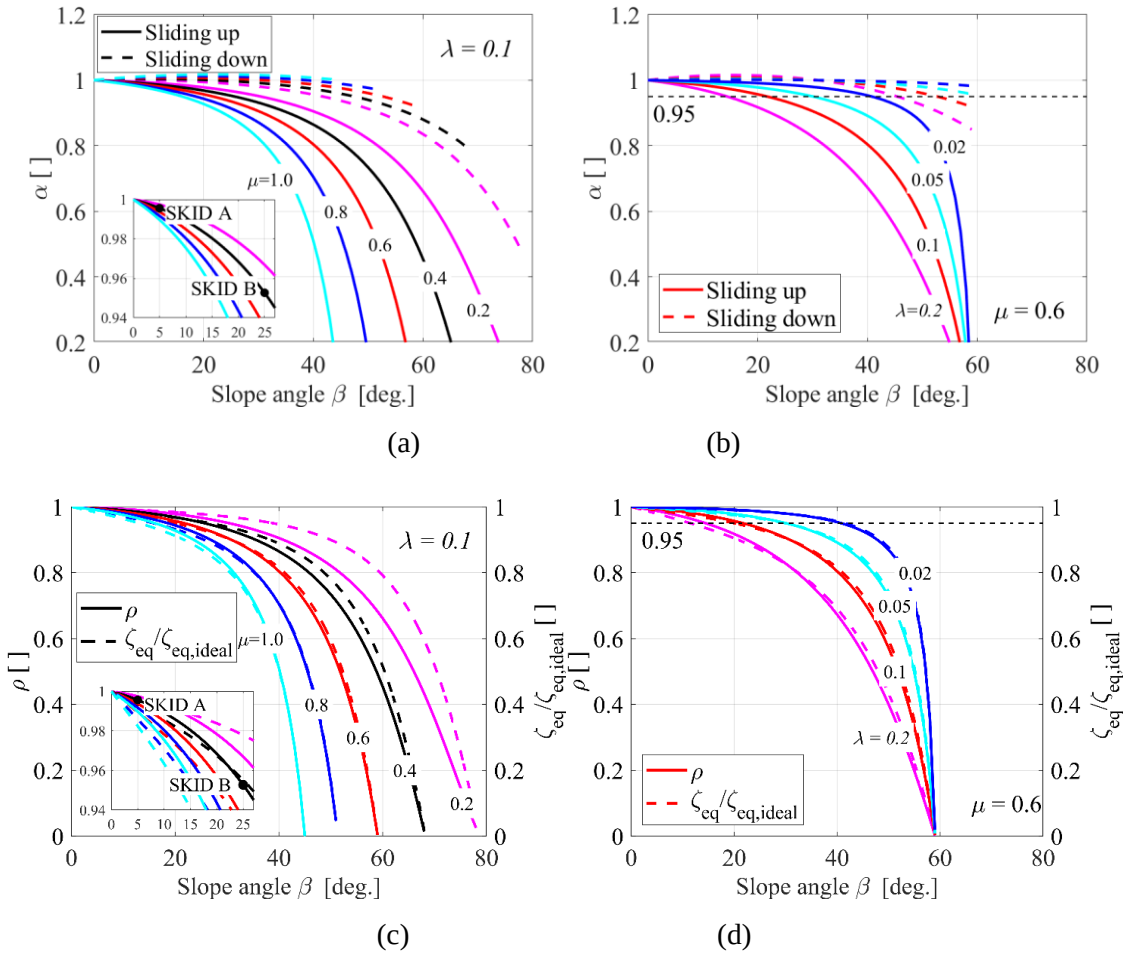

Figure 3-10 The values of: (a) α in different μ and β; (b) α in different μ and β; (c) ρ in different μ and β; (d) ρ in different μ and β.

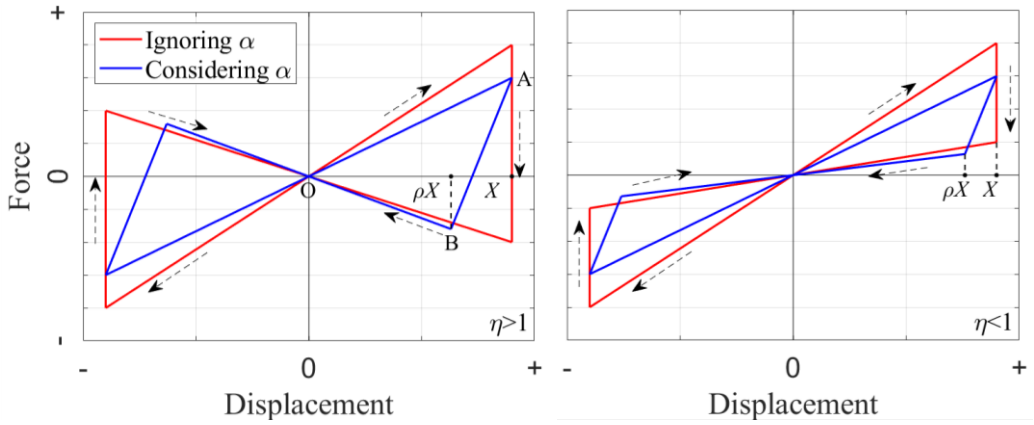

(a) (b)

Figure 3-11 Shape of the hysteretic loop of the SKID device: (a) when η>1, the sliding-down stiffness is negative; and (b) when η<1, the sliding-down stiffness is positive

Figure 3-10 (a) and (c) present the values of α and ρ when different μ and β are utilised in the SKID device. For the sliding-up phase, α and ρ decrease with friction coefficient μ and slope angle β, especially when a large β and μ are adopted, indicating a greater loss of the displacement apart from activating sliding. α and ρ could be tuned by the inertial moment ratio λ, as shown in Figure3-10 (b) and (d), where μ=0.6 is exampled. By avoiding large β and using small λ , the value of α and ρ can be limited to an acceptable range, such as 0.95 as shown in the figure.

3.4.4 Equivalent damping ratio of the SKID device considering the deformation of the cantilever bars

By evaluating the area of the hysteretic loop, for the SKID device (i.e. areas OAB and OAX shown in Figure 3-12), the equivalent damping ratio is defined as follows

$$\zeta_{\mathrm{eq}}=\frac{E_{\mathrm{SKID,\ per\ cycle}}}{4\pi F_{\mathrm{SKID}}(x\dot{x}\geqslant 0)}=\frac{S_{\mathrm{OAB}}}{2\pi S_{\mathrm{OAX}}} \qquad (3-27)$$

where ζ_{eq} is an equivalent ratio of critical viscous damping for the SKID device. By substituting Eq. (3-25) and Eq. (3-26) into Eq. (3-27) and rearranging, we obtain the following equation

$$\zeta_{\mathrm{eq}}=\frac{1}{2\pi}\left(\rho-\frac{(1-\mu\tan\beta)(\tan\beta-\mu)}{(1+\mu\tan\beta)(\tan\beta+\mu)}\right) \qquad (3-28)$$

If the deformation of the cantilever bar is ignored, i.e., ρ equals 1, Eq. (3-28) is the idealised equivalent damping ratio of the SKID device, $\zeta_{\mathrm{eq,ideal}}$. Figure 3-12 shows $\zeta_{\mathrm{eq,ideal}}$ of the SKID device with different μ and β. As shown, a greater μ but less β leads to a higher $\zeta_{\mathrm{eq,ideal}}$. Figure 3-10 (c) and (d) show the influence of the cantilever deformation on the equivalent damping ratio by deriving ζ_{eq} / $\zeta_{\mathrm{eq,ideal}}$. Similar to the stiffness of the SKID device, ζ_{eq} / $\zeta_{\mathrm{eq,ideal}}$ decreases with the increase of μ and β, indicating a severe reduction on the equivalent damping ratio ζ_{eq} . This reduction also can be mitigated by tuning λ (or I_y/I_x) as shown in Figure 3-10 (d).

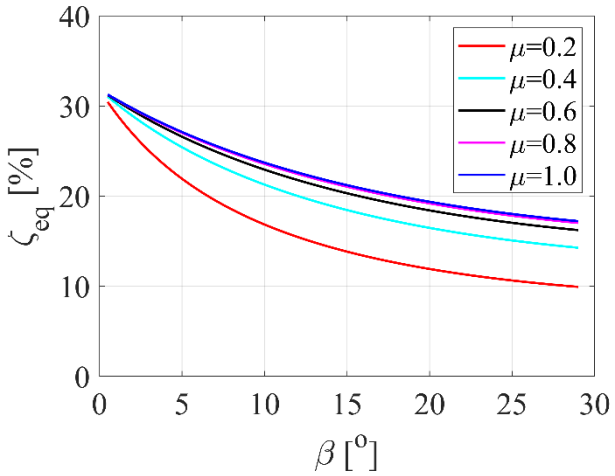

Figure 3-12 Equivalent damping ratio of the SKID device against β and μ.

3.5 Conclusion

This chapter presents a new conceptual FSSS system for application with geometrically nonlinear elastic PT frames. The mechanical schematisation and design implementation are described. The analytical expressions of the hysteretic curve and the equivalent damping ratios were derived to profile the properties of the FSSS system. Then, a novel practical configuration (the SKID device) for the conceptual frictional sliding on a sprung slope (FSSS) system is proposed by reposing frictional sliding keys on cantilever-supported slope blocks. The configuration of the device is presented, followed by a theoretical derivation of its global behaviour (hysteretic curves and equivalent damping ratios). Based on the investigation presented in this chapter, the following conclusions can be drawn:

1. The proposed FSSS conception performs a triangular-shaped hysteretic curve with a zero-activation threshold, leading to a full self-centring feature for PT frames. It can provide additional stiffness and frictional damping by the sliding of the slider against the slope blocks.

2. The FSSS system could perform two types of hysteretic curves featured by: (i) positive unloading stiffness, and (ii) negative unloading stiffness. The negative stiffness is achieved when the slope angle β is small and may be preferred because it makes the device having a greater damping ratio.

3. The loading stiffness of the FSSS system increases with slope angle β, friction coefficient μ, and spring stiffness k. But the slope angle β must be less than β_{crit} to ensure meaningful sliding displacement of the slider block.

4. The proposed SKID device realises the FSSS conception by avoiding using springs, stiff support constraints, and roller sliding bearing. It is achieved by using cantilever bars that perform two functions: (i) acting as a spring to generate the normal force on the sliding contact surface and (ii) carrying a lateral stiff support force to limit the motion of the bottom sliding surface.

5. The theoretical derivation regarding the global behaviours (hysteretic curve and equivalent damping ratio) and local performance (the reliability of the cantilever bar) of the SKID device verifies the realisation of the conceptual FSSS system with the innovative configuration. It should be noticed that the bending of the cantilever bar in the X direction (the frame sway direction) has some small adverse effects on the stiffness and the equivalent damping ratio of the SKID device. This small adverse effect is by a sliding displacement reduction factor α and can be mitigated by using a smaller slope angle β, friction coefficient μ and cantilever bar ratio of second moments of area λ.

Chapter 4 The physical demonstration of the SKID device

The contents of this chapter have been adapted from the following publications:

1. Zhang, Y., De Risi, R., & Alexander, N. A. (2022). A novel seismic energy dissipating device, Sliding Keys on Inclined Deflecting-cantilevers (SKID): Theoretical and experimental evidence. *Engineering Structures*, 273, 115056. 2022.

2. Zhang, Y., De Risi, R., & Alexander, N. A. (2022). The Sliding Keys on Inclined Deflecting-cantilevers (SKID) device: Empirical and analytical sensitivity analysis with application in post-tensioned frames. *Earthquake Engineering & Structural Dynamics.*

4.1 Introduction

To physically demonstrate the SKID device, two 1/4 reduced scaled prototypes, which corresponded to negative unloading stiffness (SKID A) and positive unloading stiffness (SKID B), were designed and manufactured. They were subjected to quasi-static amplitude varying cyclic load tests at the University of Bristol. The SKID A configurations were used to confirm and benchmark the theoretical analysis for the system mechanics of this device. A failure mode was identified from the physical tests of specimens in SKID B configurations. In addition, the mechanical behaviours of the SKID devices with six groups of different manufacturing parameters are tested and compared. Five different pads having different friction coefficients are tested.

The key research questions (aims) of this chapter are as follows:

1. Does the proposed SKID configuration work well in a stable movement?

2. How consistent is the theory with practice for the proposed configuration?

3. What is the sensitivity of the SKID device to different geometric configurations?

4. What is the sensitivity of the SKID device to the different friction coefficients?

4.2 The demonstration of the SKID device

4.2.1 Description of the prototype specimens

Two experimental specimens (designated SKID-A and SKID-B) were designed and manufactured to demonstrate both negative unloading slope case $\eta>1$ and positive unloading slope case $\eta<1$. For the sake of further investigation regarding the device in the prototypical scale-reduced PT frame (Oddbjornsson, 2009; Alexander et al., 2011), both specimens were designed as 1/4 scale (the same as the prototypical PT frame) in stroke and loading stiffness. The stroke was designed to allow for a ±40 mm displacement of the sliding keys on the slope blocks, corresponding to an approximately 4.5% drift ratio of the prototypical PT frame. It is worth noting that a 2% drift ratio is considered the target drift ratio of the prototypical frame at the Ultimate Limit State (i.e., Design Basis Earthquakes). The loading stiffness was limited by the permissible force of the floating joint of the actuator, but achieving a higher stiffness requirement can be easily done by using a larger section for the cantilever bars or installing multiple SKID devices in parallel within the PT frame. The dimensions of the specimens were decided by the grid of strong floor (see Figure 4-1 (b)), bolts spacing and edge distance demands, and required installation space. For example, the foot width for these specimens was 430 mm, which was determined by the grid of the strong floor in the laboratory. In practical applications, the foot width will be decided by the section width of the cantilever bars. The total width of sliding keys (equal to the bottom flange width of the 'I beam') was 400 mm. This dimension was designed to provide sufficient space for operating the sliding keys at 25° during experiments and to accommodate the position of the cantilever bars. As discussed in Section 3.4, a smaller angle is preferred in practice as it has a greater damping ratio and smaller stiffness reduction. For the devices using a small sliding angle, such as 5°, the total width of the sliding keys can be limited to 250 mm with the current configuration. If the sliding keys are manufactured through casting in a factory, their dimensions can be made more compatible. Please note that the primary purpose of these tests is conception validation. Devices for practical use need more detailed design and extensive research in configuration, especially in the connection methods capable of out-of-plane motion release. Figure 4-1 (a) shows SKID-A as an example. SKID-B had the same configuration as SKID-A and shared all the components apart from the cantilever bars and slope angles. SKID-A was a bidirectional device with two pairs of symmetric sliding surfaces. The sliding keys were made from angles and bolted under the I-beam flange. In the test, only the bottom half of the I beam was produced and replaced by two bolted angles, as shown in Figure 4-1 (b). The cantilevers were made from steel bars with a section of 25×100 mm. The slope blocks were cut from the cantilever bars directly, as shown in Figure 4-1

(c). The feet of every two cantilever bars were bolted with two angles and one hollow section tube to form a fixed connection to the lab strong floor. A balance stud at the foot connection shown in Figure 4-1 (c) was designed to balance the expansion force between the two cantilever bars to release the bending resistance requirement at the fixed floor support. An auxiliary angle was bolted on the top of each cantilever bar below its slope block to carry the self-weights of the beam and sliding keys in the installation stage. After the installation, the beam and sliding keys were lifted, leaving these auxiliary angles by the support system, as mentioned in the next paragraph, and these angles retired. The friction surfaces in both specimens were steel (slope blocks) against brake lining (pads on slider angles). All components of the specimens were designed to stay elastic and based on the capacity design philosophy.

In a real (prototype) PT frame system, the gravity load of the SKID sliding keys is carried by the PT frame beam and columns. Conversely, in this 1/4 scale test, the SKID system is tested (i.e. sub-structured) without the PT frame. Thus, a support system replicating the PT frame's gravity load transfer system was added below the I beam, as shown in Figure 4-1 (d). A linear array of ball bearings was installed on the top of the support to eliminate the unwanted friction force between the bottom of sliding keys and gravity load support system. Combining Teflon spray lubricant and ball bearings reduced the unwanted friction force to 0.05kN during the tests, representing about 1.4% of the total maximum frictional force of the SKID device.

All the components of both specimens were made of S355 steel. Mill processing was only required to manufacture the slope angles (as shown in Figure 4-1(c)). In addition, all the parts were bolted together (by Grade 8.8 high-strength bolts as shown in Figure 4-2) without any weld (apart from the ribs on the I beam, as shown in Figure 4-1(b)).

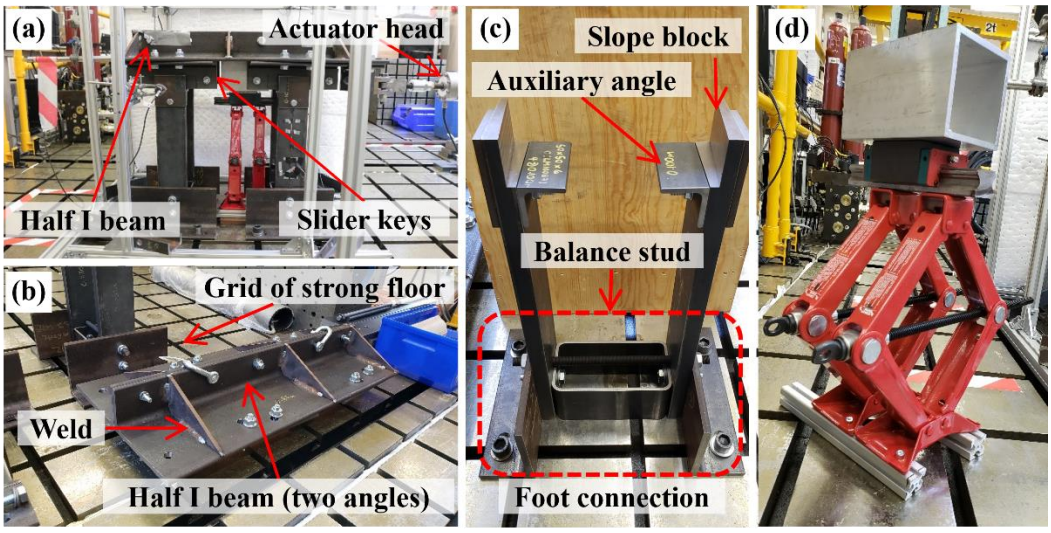

Figure 4-1 Finished product of SKID-A: (a) an overview; (b) the half I beam; (c) the cantilever bars with slope blocks; and (d) the weight support system.

4.2.2 Test setup, loading protocol, and instrumentations

As mentioned, SKID-A and SKID-B were designed corresponding to $\eta>1$ and $\eta<1$, respectively (see Table 4-1). According to Eq. (3-10), η is controlled by slope angle β and friction coefficient μ. A nominal slope angle β_{norm} of 5° and 25° were used for SKID-A and SKID-B, respectively, but keeping the same friction material (the same μ_{norm} of 0.4) to make $\eta_{SKID\text{-}A}>1$ and $\eta_{SKID\text{-}B}<1$. The nominal α and ρ of two specimens are dotted in Figure 3-10 (a) and (c), both are greater than 0.95. To accommodate different slider angles, long round holes were punched on the bottom flange of the I beam, as shown in Figure 4-2. The stiffness of SKID-B was limited such that the maximum loading range lay within the maximum loading capacity of the actuator. This was achieved by doubling the height of cantilever bars for SKID-B (887 mm) relative to SKID-A (480 mm). Figure 4-2 summarises the parameters of the two specimens and the positions of instrumentations. Six strain gauges were mounted on the cantilever bar, as shown in the figure. LVDT 1 and 2 were set beside the coworking cantilever bars to record their deformation. LVDT 3 were set to record the actuator displacement (which is equivalent to the PT frame displacement X in Eq. 3-25 in the prototype system).

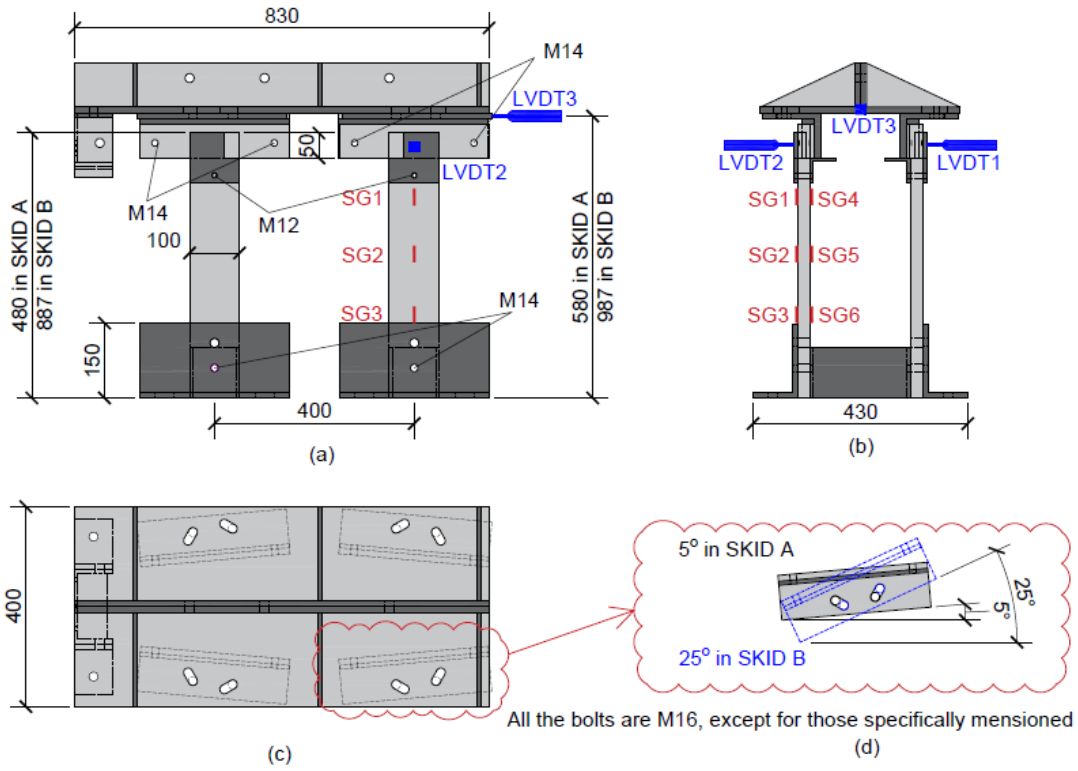

Figure 4-2 Drawings of specimens and positions of instrumentations.

Table 4-1 Information of specimens.

	β_{norm}	β_{eff}	μ_{norm}	Cantilever bar section	Cantilever bar length	k_{eff} N/mm	η
SKID-A	5°	3.9°	0.39	100×25 mm	480 mm	982.8	>1
SKID-B	25°	22.3°	0.39	100×25 mm	887 mm	146.3	<1

The tests were carried out at the Heavy & Light Structures Laboratory at the University of Bristol. An Instron servo-hydraulic actuator was utilised to apply horizontal displacements on the beam angles (see Figure 4-1(a)). The same cyclic displacement-controlled loading protocol was used for both specimens. Figure 4-3 shows the loading protocol where the pulling and pushing excursions (loading displacement X) were assigned with positive and negative signs, respectively. The loading rate was 0.05Hz, which can be viewed as a quasi-static load. There were nine loading steps in total, and the peak displacement were gradually increased with an increment of 4 mm. The maximum loading step had a peak loading displacement of 36 mm, corresponding to a 4% inter-story drift ratio of the prototypical scale-reduced structure (Oddbjorsson, 2009). Notably, a loading displacement of 18 mm corresponds to a 2% drift ratio of the prototypical frame, which is considered the target response at the Ultimate Limit State (ULS) and is marked in Figure 4-3. Additionally, each loading step included three repeat cycles to investigate the repeatability of the hysteresis. In the test, the load applied to each specimen was measured by the load cell mounted on the actuator, and the displacement was recorded by LVDT 3.

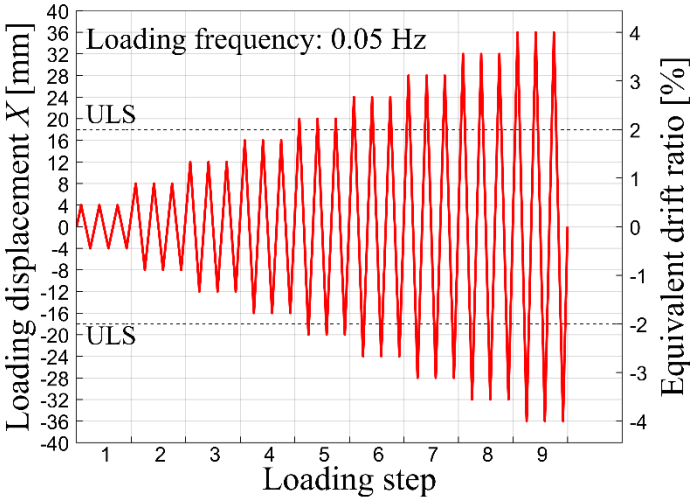

Figure 4-3 Test displacement-control loading protocol.

4.2.3 Test results

4.2.3.1 Global behaviour and failure mode

The SKID-A specimen exhibited a stable hysteretic behaviour during the test. Figure 4-4 (a) to (c) visually shows the device kinematics when it was at a negative, neutral, and positive position. As shown, throughout the entire experimental test, sliding only happened at the surfaces between the sliding keys and the slope blocks, and visible bending was only observed in the cantilever bars. All the other components, such as sliding keys, slope blocks, beam, and foot connections, did not develop any visible deformation or displacement. During the test, the sliding keys moving to the right made contact with the slope blocks on the right and thus pushed the right-side cantilever bars apart (Figure 4-4 (c)). During this process of right-side sliding contact, the sliding keys lost contact with the slope blocks on the left side (Figure 4-4 (e)). On the contrary, when the sliding keys moved to the left side, the left-side slope bocks were engaged, causing the left-side cantilever bars to be pushed apart. Abrasion was observed on the brake lining pads after the test (compare Figure 4-4 (f) and (g)). This abrasion only developed in the one side region of each pad adjacent to the position where the slope blocks were initially situated. This was because only this side of each pad touched with the slopes and worked to generate friction.

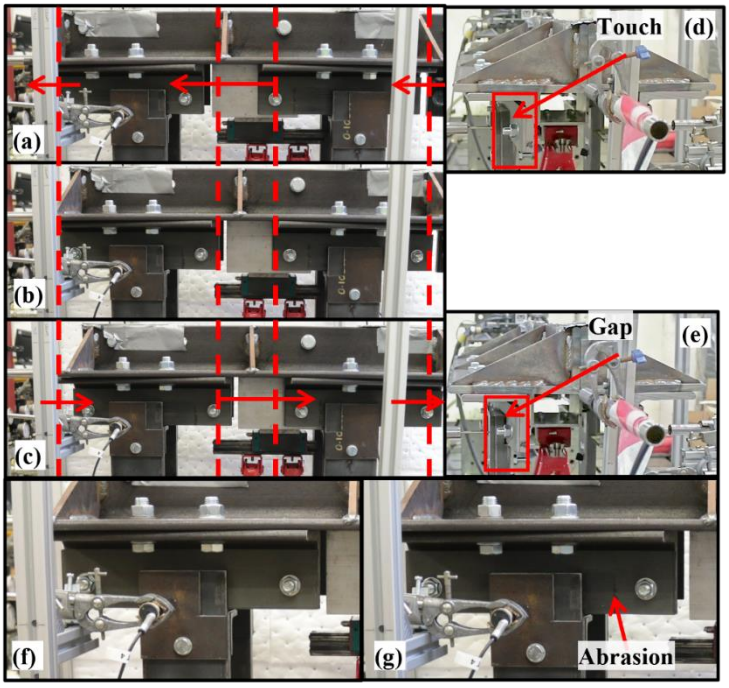

Figure 4-4 Global behaviour of SKID A: (a) front view when beam moving left, (b) front view at a neutral position, (c) front view when beam moving right, (d) side view when beam moving left, (e) side view when beam moving right, (f) the left brake lining pad before test, and (g) the left brake lining pad after test.

SKID-B was tested after the SKID-A by replacing the cantilever bars and adjusting the angle of the sliding keys from 5° to 25°. The specimen displayed the same global behaviour with SKID-A, but only up to an actuator displacement of around ±16mm. For larger actuator displacements, the bolted connection at the base of the cantilever bars (for SKID B) started to suffer from rotational frictional slippage (around the bolt), leading to some extra displacement at the top of the cantilever bars. Figure 4-5 shows the distance between the top ends of the two cantilever bars before and after the test. The distance was changed from 300mm before ±16mm excursion to around 309mm after the test, which corresponds to a cantilever bar rotation of around 0.01rad. Note that this rotation cannot be recovered once it happens. This rotational frictional sliding could be considered the first failure mode of the device. However, this failure mechanism could be avoided by a better-designed connection (at the base of the cantilever bars) that would prohibit this rotational sliding failure. The influence of this rotational slippage on the hysteretic response of SKID-B will be presented in the next section. Besides, the device may present other failure models in unexpected earthquakes, although they are not captured by the tests presented in this thesis. For example, a plastic bending deformation of cantilever bars along their weak axis may develop, resulting in idle running at the beginning of subsequent cycles. The displacement of sliding keys could exceed the stroke of the device, leading to a steep increase in loading stiffness. Yielding may also occur in other components, such as sliding keys or connections if they are not adequately designed. A presented failure mode is contingent on the design logic followed by the engineers. In other words, engineers can intentionally design or choose a preferable failure mode. The failure behaviours of the SKID device with different failure modes and their influence on the seismic performance of the PT-SKID frames need further investigations.

(a) (b)

Figure 4-5 Distance between the top ends of two cantilever bars: (a) before test, and (b) after test.

4.2.3.2 Hysteretic curves

Figure 4-6 presents the hysteretic curves of both specimens. In the figure, the measured strength of the specimens, *F*, is recorded by the load cell mounted on the actuator. The loading

displacement, X, (which would be the same as the beam displacement X in Eq. (3-25)) is recorded by LVDT 3.

Experimental results for the SKID A specimen, shown in Figure 4-6 (a), exhibited the same stable and repeatable triangular-shaped hysteretic curves without any in-cycle strength degradation. This performance is similar to what was predicted in the theoretical section 3.4.3. While the theoretical model captures the overall behaviour of the SKID system phenomenologically (as shown in Figure 3-5), the experimental results do deviate from the theoretical model at the beginning of the sliding-down stages of all cycles as shown in Figure 4-6. At these beginning points, small peaks exist in the experimental force-deflection data. This happened when the actuator velocity changes sign. This is where the friction sliding changes from a slip to a stick state and then again to a slip state. The introduction of a momentary stick and subsequent static friction phase induces a momentary higher frictional force. The hysteretic curves of SKID-A are in all four quadrants while SKID-B results only exist in the first and third quadrants. This verifies both $\eta>1$ and $\eta<1$ versions of the SKID devices as consistent with the theoretical predictions.

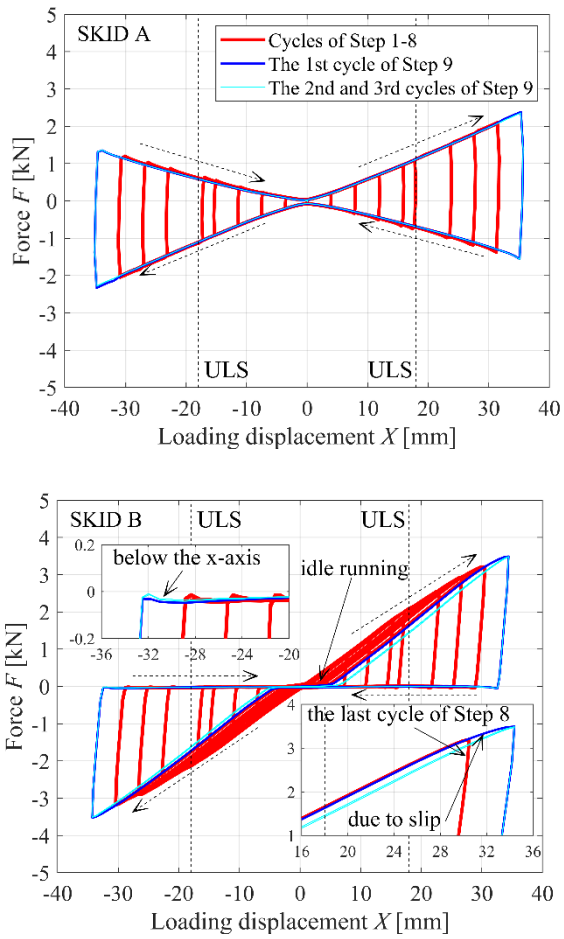

(a) (b)

Figure 4-6 Hysteretic curves of: (a) SKID-A, and (b) SKID-B.

As mentioned in section 4.2.3.1, the cantilever bars of SKID-B gradually slip, rotationally, at the support connection bolt at the base of the cantilevers with increased beam excursion after *X* over ±16mm. Figure 4-6 (b) depicts the influence of this rotational slippage (at the base of the cantilevers) on the hysteretic curves of SKID-B. As shown, the rotational slippage developed both in the push and pull phases at the first cycle of each loading step (exampled by the curves in Step 9 highlighted by the blue lines in the subplot of Figure 4-6 (b)). This leads to a small stiffness degradation at the sliding-up end corners in the hysteretic curves. The rotational slippage is because of the increased rotation moment at the base of the cantilever bars (which is proportional to the friction force generated on the sliding surfaces) which was greater than the moment capacity of the support connection. Because of this unrecoverable slippage, the distance between the top of the two cantilever bars was enlarged, and the position of slopes on the top of them no longer matched the position of the slider blocks. As a result, there was an idle running executed at the beginning of the subsequent cycles, where slope blocks on cantilever bars working in two directions changed shifts. Although the rotational slippage developed in the first cycles, the sliding-up and sliding-down stiffness did not degrade in the subsequent cycles once the sliding keys touched the slope blocks, until new rotational slippage developed because of larger displacement amplitude was introduced.

Figure 4-7 shows the backbone curve (the blue line) of each specimen. The backbone curve envelopes the strength of each specimen associated with the peak deformation in each cycle. As shown, the backbone curve of each specimen is linear before specimen failure, but softening after the rotational slippage of cantilever bars developed.

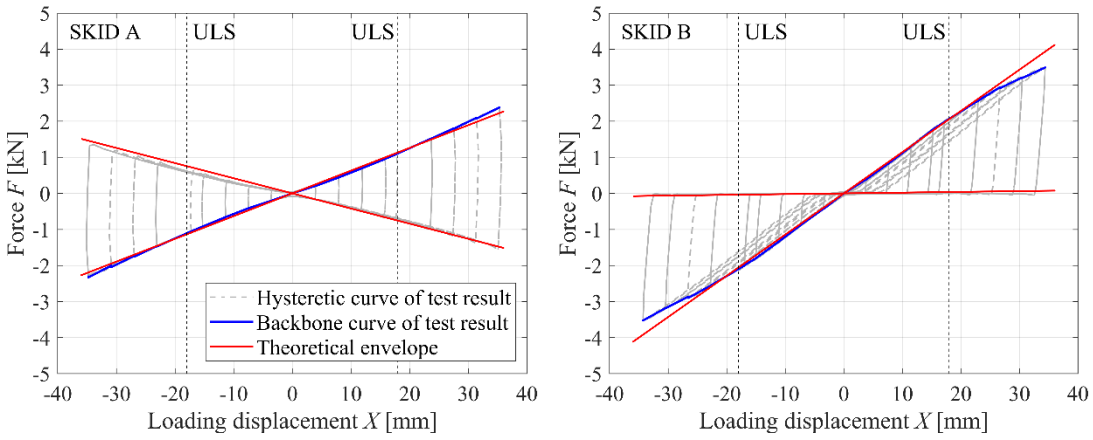

(a) (b)

Figure 4-7 Comparison between theoretical predictions and physical test results: (a) SKID A, and (b) SKID B.

The equivalent damping ratio, ζ_{eq}, of each specimen at each loading cycle is calculated based on Eq. (3-27). The progression of ζ_{eq} value with the increase of actuator amplitude (i.e. the PT frame sway displacement X) is shown in Figure 4-8. In this figure, the equivalent damping ratios ζ_{eq} of both specimens decreased with increased actuator displacement amplitude. The mean values of the experimentally measured equivalent damping ratios are similar to those predicted from theoretical Eq. (3-28).

The larger values of damping ratios at small actuator amplitudes (such as 0 to 8mm for SKID A) were due to the influence of the bearing friction force of the gravity load supporting system (i.e. the 0.05kN frictional force at the ball bearings) described previously. Note that this gravity load supporting system was necessary in the sub-structured test set-up employed. This unavoidable 0.05kN frictional force in the physical tests changed the shape of the force deflection loops from a triangle to that of a trapezium. Hence, large damping ratios ζ_{eq} were calculated erroneously. In the prototype system, this gravity load system is replaced by the PT-frame itself and hence these trapezium-shaped hysteretic curves should not be observed in practice. Therefore, we should discount the higher damping ratios at lower displacement amplitudes as an experimental test set-up artefact.

For the SKID B configuration, after the rotational slippage of the cantilever bars developed (loading displacement is over 16mm), the ζ_{eq} value decreased further, indicating a degraded energy dissipation capability. It is worth noting that once the failure (rotational slippage) developed in the first cycle of each loading step, ζ_{eq} values in subsequent cycles were less than the first cycle even having the same peak displacement as shown in the figure. This was because the rotational slippage gradually developed in the first cycle led to a larger idle running excursion in the subsequent cycles.

Comparing the energy dissipative capabilities of SKID A and SKID B configurations, it is clear that their ζ_{eq} values (in the stable moderate amplitudes >8mm) were around 25% and 15%, respectively. This demonstrates a better energy dissipation capability of the devices with $\eta>1$ than those with $\eta<1$.

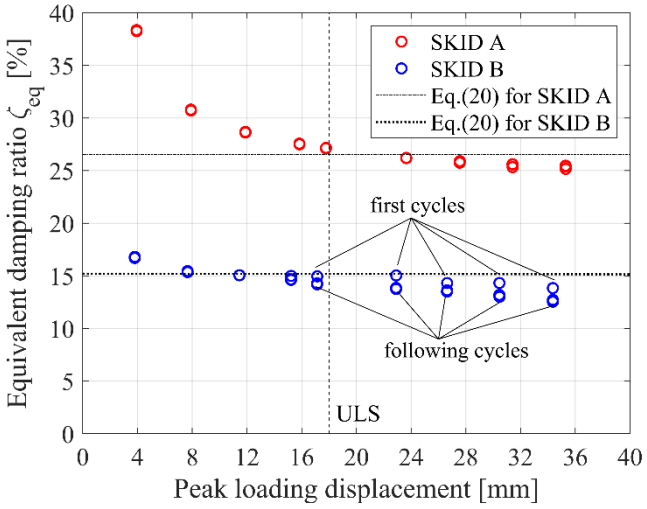

Figure 4-8 Equivalent damping ratio in each loading cycle.

4.2.3.3 Interpretation of representative strain gauges data and LVDTs data

As Figure 4-2 shows, Strain Gauges 1 to 6 and LVDTs 1 to 2 were set up to measure the deformation of the cantilever bars. For demonstration purposes, the data from SKID A are plotted in Figure 4-9. As shown, all the instrumentations recorded nonzero values only in the negative loading displacements, indicating the measured cantilever bars only work when the beam was pushed. The data recorded by two LVDTs almost overlap each other, revealing that the two measured symmetrical cantilever bars worked together with each carrying exactly half the total load. Both figures demonstrate a linear elastic behaviour of cantilever bars throughout the test.

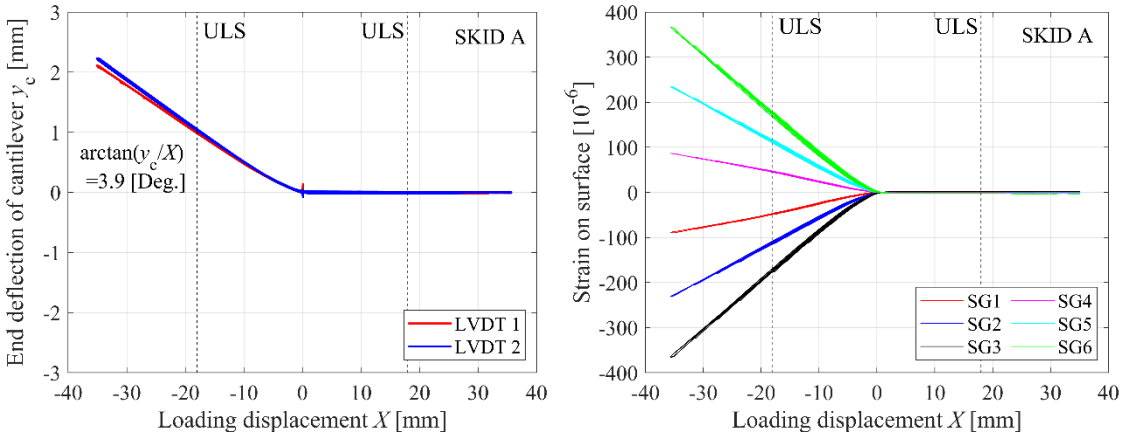

(a) (b)

Figure 4-9 Instrumentation data of SKID-A: (a) LVDTs, and (b) strain gauges.

4.2.3.4 Comparison between theoretical estimation and physical test behaviour

The effective sliding angle, β_{eff}, and effective tip stiffness of the cantilever bars, k_{eff}, can be obtained from the strain gauge data and LVDT data. The effective sliding angle, β_{eff}, can be calculated as follows:

$$\beta_{\text{eff}} = \arctan\left(\frac{y_{\text{c}}}{X}\right) \tag{4-1}$$

where y_{c} is the end deflection of the cantilever bars, X is the loading displacement (i.e., the beam excursion). The effective sliding angle β_{eff} actually involves manufacturing errors of slope blocks, installation errors of sliding keys, and kinematic compatibility adjustment between them.

The tip stiffness of the cantilever bars can be obtained from the LVDT data and the strain data. The strain ε_i at i position of the cantilever bars can be calculated by

$$\varepsilon_i = \frac{F_{\text{y}} d_{\text{i}} t}{2 I_{\text{y}} E} \tag{4-2}$$

where F_{y} is the resultant force in the y direction generated from sliding surfaces, d_{i} is the distance from F_{y} to the measured i position, and t is the thickness of the cantilever bars.

The effective tip stiffness of the cantilever bars in y direction, k_{eff}, can be expressed by

$$k_{\text{eff}} = \frac{F_{\text{y}}}{y_{\text{c}}} = \frac{X}{y_{\text{c}}}\frac{F_{\text{y}}}{X} \tag{4-3}$$

By substituting Eq. (4-2) to Eq. (4-3), the following expression can be obtained

$$k_{\text{eff,i}} = \frac{X}{y_{\text{c}}}\,\frac{2 I_{\text{y}} E \varepsilon_{\text{i}}}{t X d_{\text{i}}} \tag{4-4}$$

The first term in the right side of Eq. (4-4) can be calculated from the LVDT data shown in Figure 4-9 (a), and the second term can be obtained from the strain data shown in Figure 4-9 (b).

According to Figure 4-9 (a) and (b), β_{eff} of SKID-A and B are 3.9° and 22.3°, and k_{eff} are 982.8 N/mm and 146.3 N/mm, respectively. By substituting these values into Eq. (3-25) and Eq. (3-28), the theoretical envelopes (sliding-up strength and sliding-down strength), $F_{\text{SKID}}(X, \dot{X})$, and equivalent damping ratios of two specimens can be calculated. These estimations are shown in

Figure 4-7 (the red lines) and Figure 4-8 (the dashed and dotted black lines), respectively. Note that the friction coefficient μ between the brake lining and steel is sensitive to the surface temperature (0.4 (50°C) to 0.5 (150°C) (Bremskerl, 2007)) as stated in the datasheet from the manufacturer. Here, from physical lab tests (at the University of Bristol), a friction coefficient of 0.39 is adopted for both cases. As shown, the theoretical estimation of both ζ_{eq} and $F_{\mathrm{SKID}}(X, \dot{X})$ fit their physical test behaviour (before failure for SKID-B). It verifies a satisfactory consistency between the theory and practice of the SKID device.

4.3 The SKID device with various manufacturing parameters

4.3.1 The specimens

According to Eq. (3-25), the mechanical properties of the SKID device (i.e. loading stiffness, equivalent damping ratio) are controlled by three core manufacturing parameters: the friction coefficient μ, the sliding angle β, and the spring stiffness k_s. Additional six 1/4-scale SKID specimens with different manufacturing parameters were designed and built to assess the empirical performance experimentally. Specifically, the spring stiffness of the device is the flexural stiffness of the cantilever bars around their weak axis. Four specimens (S1 to S4) have shorter cantilever bars with the same stiffness of 982.8 N/mm and a sliding angle of 4°. The other two (T1 and T2) have a smaller stiffness of 146.3N/mm and a larger sliding angle of 23°. The friction coefficient was also changed using different materials for the friction pads. Specifically, two different brake linings (A and B) and three metals (bronze, copper, and steel) were utilised as friction pads. The estimated friction coefficients against steel (the material of slope blocks) were 0.4 (A), 0.2 (B), 0.5 (bronze), 0.55 (copper), and 0.6 (steel), respectively. The estimated friction coefficients were estimated by Eq. (3-25), after the loading stiffness k_{SKID}, slope angle β, cantilever stiffness k_s, and reduction factor α (assumed as 1 in these cases) were obtained. Note that the friction coefficient of materials can change with factors such as surface working temperature, contact pressure, and sliding velocity, which are challenging to measure during testing. Consequently, separate tests for determining the friction coefficient can be difficult to simulate the working conditions of the sliding surfaces. Given that changes in friction coefficient due to surface working conditions can impact the global behaviour of the SKID device (e.g., loading stiffness), as discussed in Section 4.3.3, it is meaningful to investigate further the tolerance of the friction coefficient for different materials. The core parameters of specimens and their identifiers are summarised in Table 4-2. It is worth mentioning that all the components of six specimens were designed remaining elastic in the tests, and the frictional sliding was designed only happening between the slope blocks and sliding keys.

Table 4-2 Summary of specimens.

Specimen identifier	Friction surface: Steel against	Thickness (mm)	Typical hardness	Estimated friction coefficient μ	Sliding angle β	Cantilever bar length L (mm)	Cantilever stiffness ks (N/mm)
S1	Brake lining A	3	20 N/mm^2 at 20°	0.4	4°	480	982.8
S2	Bronze	3	75-230 HV	0.5	4°	480	982.8
S3	Copper	3	40-110 HV	0.55	4°	480	982.8
S4	Steel	3	127-162 HV	0.6	4°	480	982.8
T1	Brake lining A	3	200 N/mm^2 at 20°	0.4	23°	887	146.3
T2	Brake lining B	8.4	3 N/mm^2 at 20°	0.2	23°	887	146.3

4.3.2 Test setup and loading protocols

Two quasi-static cyclic loading protocols (frequency of 0.05 Hz) with increasing amplitude and a fatigue test were conducted on six specimens using an Instron servo-hydraulic test machine. The amplitude-increasing test protocol (denoted as TP-A, Figure 4-10 (a)) had nine loading steps ranging from 4mm to 36mm with a single step increment of 4mm. The maximum loading displacement corresponds to a 4% drift ratio of the prototypical 1/4-scale PT frame abstracted by Oddbjornsson (2009). Three cycles are done for each displacement step to investigate the repeatability of the hysteresis. Only the first five loading steps (i.e. 4mm to 20mm) were applied on specimens T1 and T2 to limit the maximum reaction force. The fatigue test protocol (denoted as TP-B, Figure 4-10(b)) had 100 sinusoidal loops with a constant peak excursion at 18mm, corresponding to 2% drift ratio (which is considered the response target at ULS) of the prototypical PT frame to identify any possible fatigue damage. Besides, fifteen amplitude-increasing sinusoidal loops with peak excursion at 18mm, 24mm, and 36mm were added before and after the fatigue test loops to identify any influence of the fatigue damage at 18 mm on the behaviour at greater excursions. It is worth noting that new friction pads were used for each individual test to ensure reliable results. In the test, the strength of the specimens was recorded

by a load cell fixed to the actuator; an LVDT measured the displacement attached at one end of the I beam, as shown in Figures 4-2.

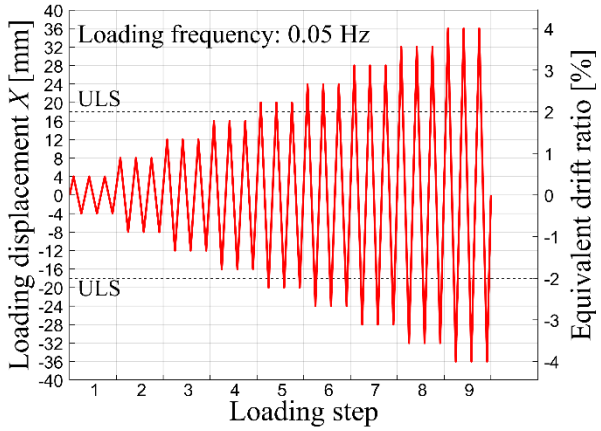

(a)

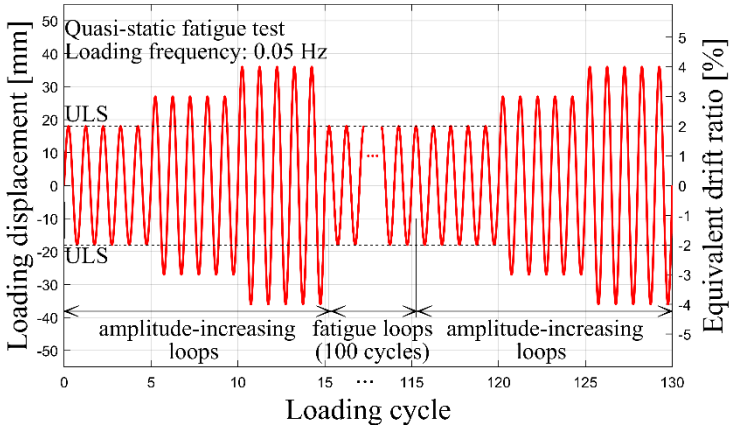

(b)

Figure 4-10 Test protocols: (a) test protocol A; and (b) test protocol B.

4.3.3 Hysteretic behaviours under TP-A

All the specimens exhibited stable hysteretic behaviours during the tests. With the excursion of the I beam, the sliding keys slide along the slope blocks and enforced cantilever bars bent. Only one pair of inclined cantilever bars activated when the beam moved in one direction. All the components moved back to their initial positions at the end of each loading loop. Audible noise was observed during all tests; such noise was generated from frictional surfaces, and it was light for brake lining pads and sharper for metal ones.

Figure 4-11 shows the hysteretic curves of specimens subjected to TP-A. Overall, all specimens exhibited triangular-shaped hysteretic curves. The curves of specimens S1 to S4 spread across all four quadrants (negative slope unloading), while T1 and T2 only exhibit behaviour in the first and

third quadrants (positive slope unloading). The negative slope unloading shapes of the hysteretic curves correspond to systems that are unable to re-centre on their own without the help of the PT-frame. While the systems with positive slope unloading shapes can re-centre, on their own without the help of the PT frame. Although there was a difference in the self-centring feature, both positive and negative unloading slope forms have zero activation force threshold (i.e. pass through the origin). The brake lining specimens (S1, T1, T2) show smooth hysteretic curves and overlapping each other for all loading loops. The devices with metal friction materials (S2, S3, S4) had hysteretic curves that were more unstable, especially the one with steel against steel friction surfaces (S4). For comparison, the hysteretic curves of S4 in different loading steps were shown with various colours in Figure 4-11 (d) and unfolded in time in Figure 4-12. A significant difference in stiffness and peak strength is observed among different loops in the same loading step. However, no clear trend of this variation in the loading cycle sequence was observed. In addition, Figure 4-13 summarises the backbone curves of the hysteretic curves of specimens. The results clearly show that the SKID loading stiffness increases with the friction coefficient μ.

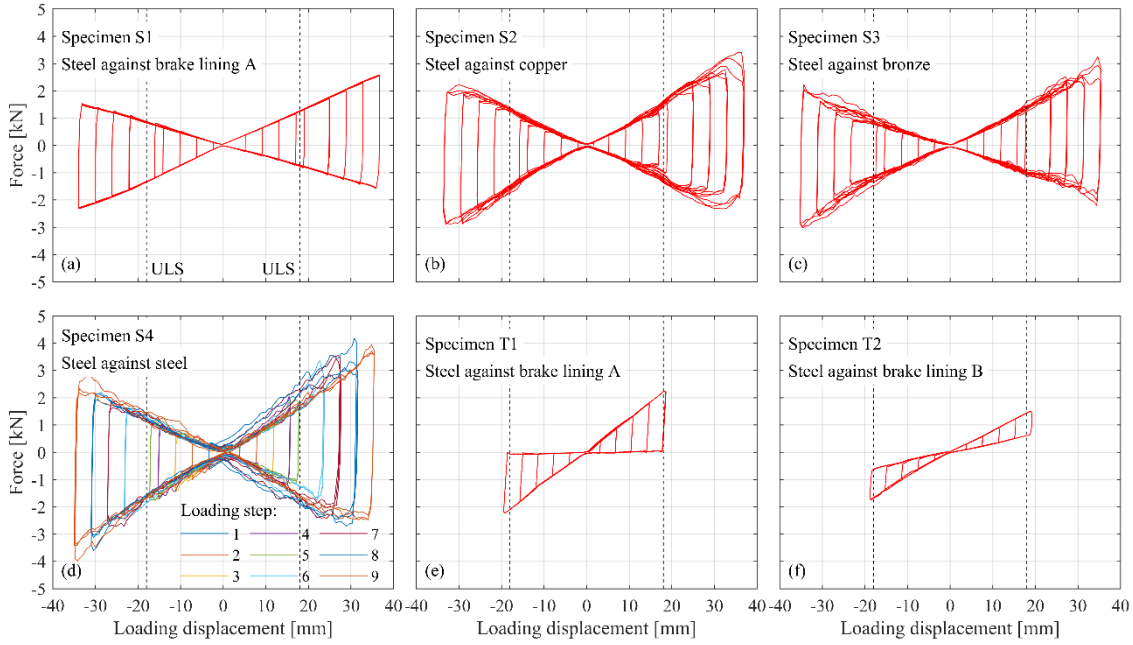

Figure 4-11 Hysteretic curve of (a) S1; (b) S2; (c) S3; (d) S4; (e) T1; and (f) T2.

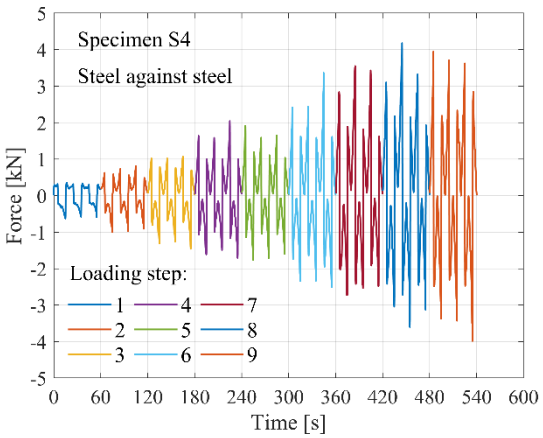

Figure 4-12 Force time history of S4 subjected to TP-A.

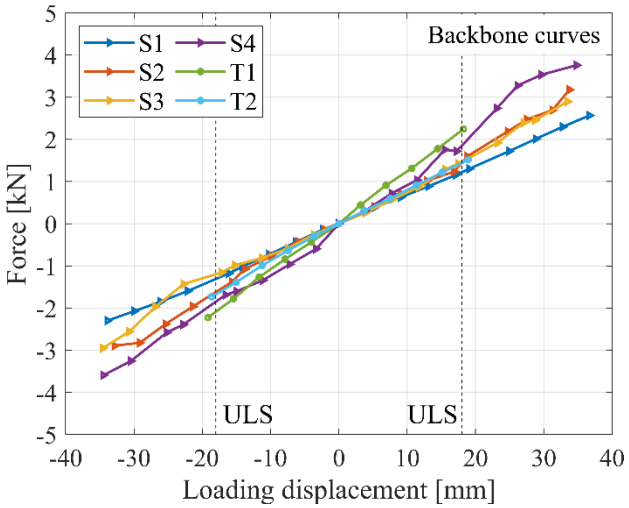

Figure 4-13 Backbone curves of the hysteretic curves of specimens.

Figure 4-14 shows the equivalent damping ratio ζ_{eq} for all specimens and for each loading step. For each loading step, the ζ_{eq} is the average of the values calculated for each of the three loops using Jacobsen's method (Jacobsen, 1960). The equivalent damping ratio is large for lower displacement (up to 8 mm) because more hysteretic damping was created from the friction of the self-weight support system and the relative movements of the components. Thus, the setup affects equivalent damping ratios for low displacement; the actual equivalent damping ratios of the specimens can be read for displacements larger than 8mm, where the trend stabilises. Comparing S1 and T1 (same μ and different β) as well as T1 and T2 (same β and different μ), it is clear that large friction coefficients and small sliding angles β lead to higher equivalent damping ratios. In addition, the specimens with brake lining pads (S1, T1, and T2) had a more stable equivalent damping ratio for increasing displacements. In contrast, specimens with metal pads exhibited a more significant fluctuation of the damping ratio. In addition, Specimen S2, S3, and T2 displayed

the same loading stiffness (Figure 4-13) but different damping ratios (Figure 4-14), exemplifying the SKID possibility of having the same strength properties but different damping behaviours.

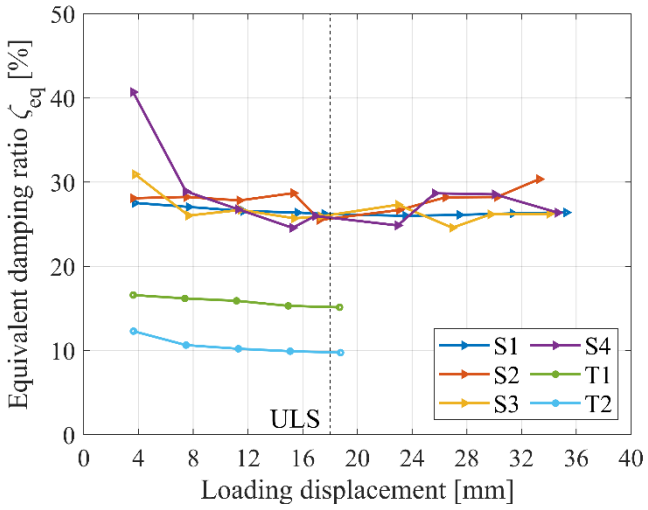

Figure 4-14 Equivalent damping ratios of specimens.

4.3.4 Fatigue behaviour of the SKID devices with different friction pads

In this Section, the fatigue behaviour of different friction materials used in the SKID device are investigated (protocol TP-B). The three specimens with brake linings exhibited the most stable hysteretic performance without any strength or stiffness degradation within the 100 cycles. Figure 4-15 shows the strength-displacement and the strength-time responses of S1, as an example. The hysteretic curves overlap each other, and the responses of the amplitude-increasing loops after the fatigue loops were the same as those before the fatigue loops, which indicates an excellent fatigue resistant capability. However, the specimens with metal pads (S2, S3, and S4) had much more irregularity in force and stiffness, forming a wide band in its strength response, as exampled by S4 in Figure 4-16. Although the irregularity, no stiffness degradation linked to the loading cycle sequence was observed. In addition, there were no significant changes in the responses due to the amplitude-increasing loops after the fatigue cycles (c.f. [0 to 400] cycles with [2100 to 2500] cycles). Figure 4-17 displays the comparison of the friction pads before and after the fatigue tests. As shown, different levels of abrasion were generated among six specimens after the same loading protocol. Among them, the steel pads in S4 displayed the most severe abrasion, as shown in Figures 4-17 (d) and (e). There was an increase in abrasions with the number of loading cycles. However, such abrasions did not lead to stiffness/strength degradation during the test.

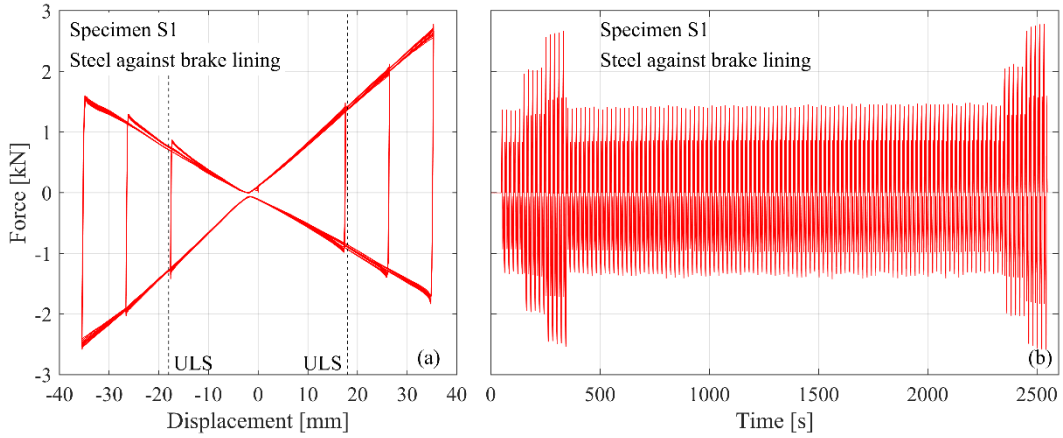

Figure 4-15 Behaviour of S1 subjected to TP-B: (a) hysteretic curve; and (b) force time history

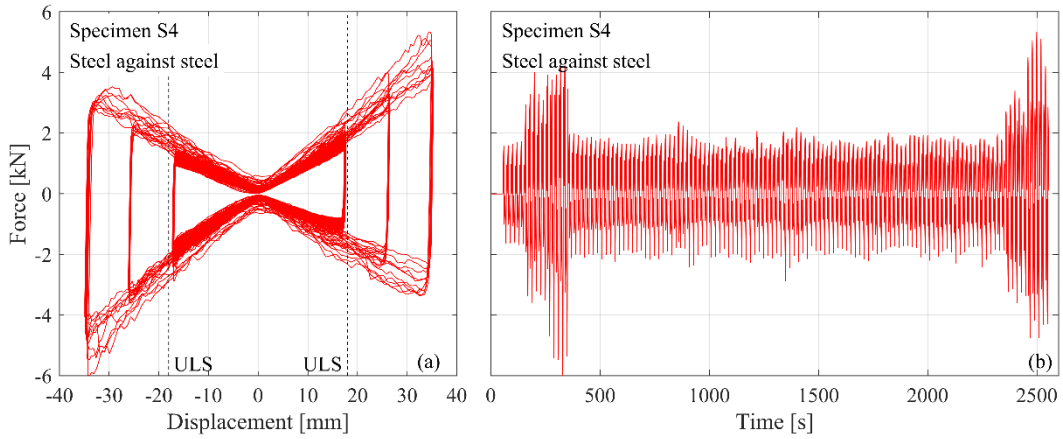

Figure 4-16 Behaviour of S4 subjected to TP-B: (a) hysteretic curve; and (b) force time history.

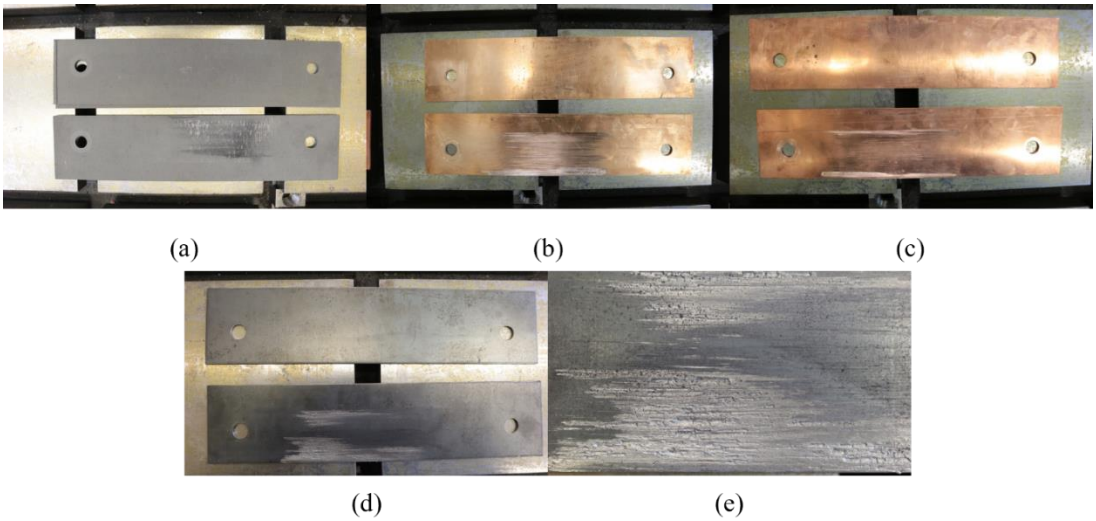

Figure 4-17 Abrasion of the friction pads of: (a) brake lining; (b) bronze; (c) copper; (d) steel; and (e) details of the steel pad.

4.3.5 Repairability of the SKID device

The SKID device was designed to be assembled and installed on-site only using bolted connections. The only expected damage is the abrasion on the friction pads. Any damage in other components should be avoided as a design target. As concluded in section 2.4, the development of these abrasions did not make any noticeable impact on the global behaviour of specimens, indicating that it is unnecessary to replace friction pads after earthquakes. However, a replacement of friction pads is still possibly required, for example, if the required mechanical properties of the device change due to a change of use of the structure (e.g., from residential to office spaces where different stiffness or damping may be required on the SKID device). This process of replacing friction pads was rehearsed between two consecutive tests, as shown in Figure 4-18, where new brake lining pads replaced the worn steel pads while all the other components were reused. The only operation was the removal of the old pads and the replacement of new ones, while all the other parts of the device were not touched at all; such an operation took one technician about a half-hour to complete the entire procedure.

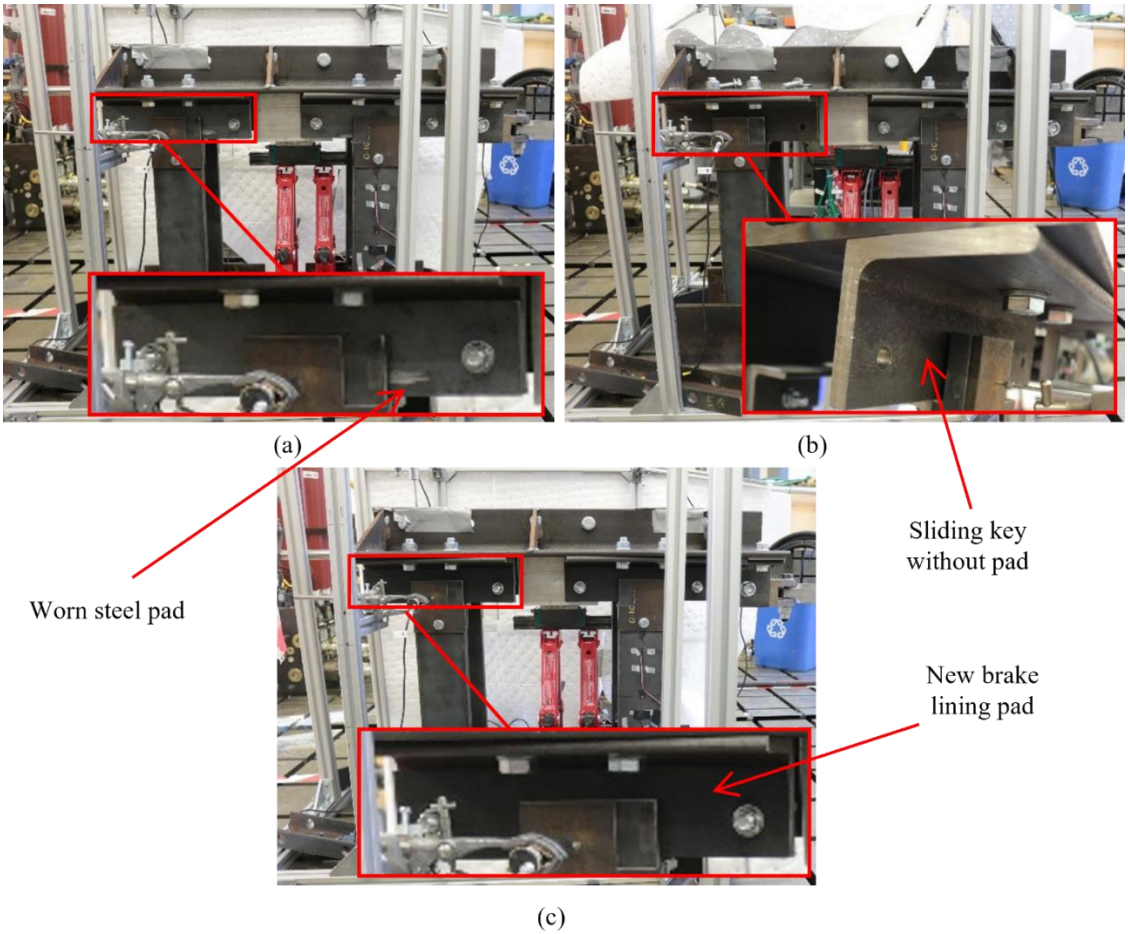

Figure 4-18 Replacement of friction pads: (a) the specimen with worn steel pads; (b) removing the worn pads and installing new pads; and (c) the specimen with new brake lining pads.

4.4 Conclusion

In this chapter, two 1/4 reduced scaled prototypes were manufactured and tested. Quasi-static cyclic tests were carried out to observe their hysteretic behaviour and failure mode. Their effective slope angles and cantilever bars tip stiffness were interpreted from their strain gauge and LVDT data and were substituted into the theoretical equations (derived in Chapter 3) to verify the consistency between the theory and practice of the proposed device. Then, six 1/4-scale physical specimens with different friction coefficients μ, slope angle β, and cantilever stiffness K_{SKID} were built and tested. Five materials were tested as friction pads by carrying out quasi-static amplitude-increasing cyclic tests and fatigue tests.

Based on the physical tests performed in this chapter, the following conclusions are drawn:

1. The cyclic tests reveal that the proposed SKID device can exhibit stable and repeatable triangular-shaped hysteretic behaviour and satisfactory energy dissipation capabilities, as theoretically expected in Chapter 3. In addition, the comparison of equivalent damping ratio, ζ_{eq}, between SKID-A and B demonstrates that the devices with negative unloading stiffnesses $\eta>1$ have a better energy dissipation capability than those with positive unloading stiffnesses $\eta<1$.

2. Rotational slippage of the cantilever bars can be seen as the first failure mode of the prototype in the SKID B configuration. This failure was developed gradually with the first loading cycle, leading to a stiffness degradation in the cycle. Subsequently, in the following cycles, an 'idle running' zone occurs around the point where a swap between the left and right sliding keys contact occurs. This is around the zero-displacement condition. This failure can be prevented by replacing the bolt connections with welded joints for the feet of the cantilever bars.

3. The strain gauge and LVDT data demonstrate the linear elastic performance of the cantilever bars as expected in theory. By substituting the equivalent slope angle, β_{eff}, and equivalent tip stiffness, k_{eff}, into Eq. (3-25) and Eq. (3-28), and comparing with the test-obtained results, a satisfactory consistency between theory and practice of the SKID device is verified.

4. Different mechanical properties (loading stiffness K_{SKID} and equivalent damping ratio ζ_{eq}) can be achieved on the SKID device by adjusting friction coefficient μ, slope angle β, and cantilever bar stiffness k_s. Specifically, large values for μ, β and k_s lead to a larger K_{SKID}; a large μ but low β lead to a higher ζ_{eq}. These are consistent with the theoretical results presented in Chapter 3. Although different parameters were utilised, all the specimens exhibited stable hysteretic behaviours with triangular-shaped hysteretic curves in general.

5. Although the cyclic response of all the specimens was generally stable, the specimen with metal pads (especially the steel pads) exhibited fluctuations in loading stiffness with severe abrasion. Meanwhile, the brake lining pads showed the most stable and repeatable hysteretic behaviour. Therefore, brake lining is recommended as a good material choice for the SKID sliding surfaces.

6. The steel friction pads experienced the most severe abrasion in 100 repeat loading cycles; however, no stiffness or strength degradation in the global behaviours of the specimen linked to the loading cycle numbers was observed.

7. The repair of the SKID device (by replacing friction pads) is straightforward and time-efficient.

Chapter 5 The Post-Tensioned frames with the Sliding Keys on Inclined Deflecting-cantilevers device (the PT-SKID frames)

The contents of this chapter have been adapted from the following publications:

1. Zhang, Y., De Risi, R., & Alexander, N. A. (2022). A novel seismic energy dissipating device, Sliding Keys on Inclined Deflecting-cantilevers (SKID): Theoretical and experimental evidence. *Engineering Structures*, 273, 115056.

2. Zhang, Y., De Risi, R., & Alexander, N. A. (2022). The Sliding Keys on Inclined Deflecting-cantilevers (SKID) device: Empirical and analytical sensitivity analysis with application in post-tensioned frames. *Earthquake Engineering & Structural Dynamics.*

3. Zhang, Y., De Risi, R., & Alexander, N. A. (2023). The seismic responses of the Post-Tensioned frame with Sliding Keys on Inclined Deflecting-cantilever device (the PT-SKID frame). *EURODYN 2023*. Delft.

5.1 Introduction

Zero activation threshold makes the SKID device suitable for various systems, especially those expecting considerable energy dissipation but in small vibration scenarios or requiring the self-centring feature. This chapter presents an application scenario of the SKID device used in a PT frame. The PT frame prototype exampled in this chapter is a one-storey one bay nonlinear elastic frame abstracted by Oddbjornsson (2009) from the PRESSS frames. Because of the lack of energy dissipation devices, the peak drift ratio of the bared PT frame could be significant in a large earthquake event. For this frame, there are many design options, such as the sacrificial re-bars in the original paper (Priestley, 1991). However, the inevitable damage leads to difficulty in its repair. Other solutions such as a metallic shear panel dissipator or traditional friction dampers (which typically have a parallelogram-shaped hysteretic curve) would result in either re-centring

inhibition or undesirable energy dissipation. In other words, the traditional damping 'devices' with a parallelogram-like hysteretic curve cannot permit both of these competing design criteria: (i) large energy dissipation and (ii) a low sliding activation force threshold and hence re-centring.

In this chapter, the Post-Tensioned frame with the Sliding Keys on Inclined Deflecting-cantilever device (the PT-SKID frame) is investigated. The hysteretic curve of the PT-SKID frame is estimated by equations and discussed. Then, a numerical model (in OpenSees) is developed for a heuristic case of a single storey PT frame with and without the SKID device. The model is benchmarked against the experimental results. Quasi-static cyclic tests were used to investigate the hysteretic behaviour of the frame models. Nonlinear time history analysis is also performed using incremental dynamic analysis (Vamvatsikos and Cornell, 2002; 2004) to explore the variability in system response with changes in earthquake time-series and magnitude. The dynamic benefits of the SKID device on the heuristic PT frame are explored by comparatively analysing both peak responses and the energy dissipating patterns among different frames. Finally, more than seven hundred one-story one-bay PT frames with different SKID devices (the PT-SKID systems) were numerically tested to investigate the influence of the SKID manufacturing parameters on the seismic responses. The basic dynamic features of the PT-SKID frame were also identified based on the frequency response functions generated from sin-sweep excitations.

The key research questions (aims) of this chapter are as follows:

1. How well do SKID devices (in conjunction with PT frames) work for a range of earthquakes and spectral acceleration intensities?

2. What are the dynamic features of the PT-SKID frames?

3. How do SKID manufacturing parameters affect the seismic response of the PT-SKID frames?

5.2 The application of the SKID device: the PT-SKID frames

Oddbjornsson (2009) abstracted a Post-Tensioned frame from the PRESSS frames (Priestley, 1991). The PT frame is a moment-resisting frame that uses pre-stressed cables to fasten the beam and columns, as well as the columns and foundations. The PT frame performs a nonlinear elastic hysteretic curve, presenting a high initial stiffness and a stiffness softening at large displacement. However, the PT frame does not involve any hysteretic damping. Thus, the SKID device is applied to the PT frame to provide additional damping while maintaining the full self-centring feature. In the PT frame, the SKID device is positioned below the beam and connected with it by

the sliding keys, as shown in Figure 3-7. A support column or shear wall may be required to support the cantilever bars if the SKID device is shorter than the floor height. Note that the SKID device is assumed to work in the plane of the frame. To accommodate the out-of-plane motions between the SKID device and the PT frame, low-friction Teflon sliding surfaces may be required to allow out-of-plane sliding between the beam and the devices.

As presented in (Alexander et al., 2011), the hysteretic curve of the bared PT frame could be expressed by the equation:

$$F_{\mathrm{PT}}(\theta) = \frac{\sum(\frac{1}{6} b_i F_{0,i})\lambda_i}{H} \qquad (5-1)$$

where H is the floor height, θ is the drift ratio, b_i and $F_{0,i}$ are the contact width and the pre-tension force of the ith joint, respectively, and the non-dimensional moment λ_i is defined by

$$\lambda_i = \begin{cases} \dfrac{b_i^2 k_{\mathrm{s},i}}{2F_{0,i}}\theta, & |\theta| \le \dfrac{2F_{0,i}}{b_i^2 k_{\mathrm{s},i}} \\ \left(\dfrac{3}{\omega_i} + \dfrac{12}{\omega_i^2} + \dfrac{8}{\omega_i^3}\right)\dfrac{b_i^2 k_{\mathrm{s},i}}{2F_{0,i}}\theta + \left(3 + \dfrac{9}{\omega_i} + \dfrac{6-6\sqrt{\psi_i}}{\omega_i^2} - \dfrac{6\sqrt{\psi_i}}{\omega_i^3} - \dfrac{2\psi_i^{3/2}}{\omega_i^3\left(\dfrac{b_i^2 k_{\mathrm{s},i}}{2F_{0,i}}\theta\right)^2}\right)\mathrm{sgn}(\theta), & |\theta| \ge \dfrac{2F_{0,i}}{b_i^2 k_{\mathrm{s},i}} \end{cases} \qquad (5-2)$$

and

$$\psi_i = (1+\omega_i)(\phi^2 + \omega_i|\phi|) \qquad (5-3)$$

$$\omega_i = \frac{k_{\mathrm{s},i} b_i}{k_{\mathrm{c},i}} \qquad (5-4)$$

where $k_{\mathrm{s,i}}$ and $k_{\mathrm{c,i}}$ are the contact and cable stiffness, respectively. The PT-SKID frame can be schematically seen as the combination of the PT frame and the SKID device in-parallel thus, the base shear-drift ratio relationship of the PT-SKID frame can be expressed as:

$$F_{\text{PT-SKID}}(\theta) = F_{\mathrm{PT}}(\theta) + F_{\mathrm{SKID}}(H\theta) \qquad (5-5)$$

Figure 5-1 shows the hysteretic curve of a 1/4 scaled case frame. The curve is based on Eq. (5-5). The height and the span of the frame are 900 mm and 2100 mm, respectively. The applied mass on the beam was 2 tons. The beam and column sections are RHS 100x40x3 mm. The areas of pre-stressed cables are 52 mm^2 and 38 mm^2 for beam-column and column-foundation connections, respectively. The corresponding pre-tension forces are 65 kN and 40 kN, respectively. The SKID device is assumed to have a slope angle of 3.9°, a friction coefficient of 0.4, and a cantilever bar stiffness of 258 N/mm. As shown, the PT-SKID frame has a dual-triangular-flag-shaped hysteretic curve. The curve is entirely in the first and third quadrants, indicating an inherently full self-centring capability.

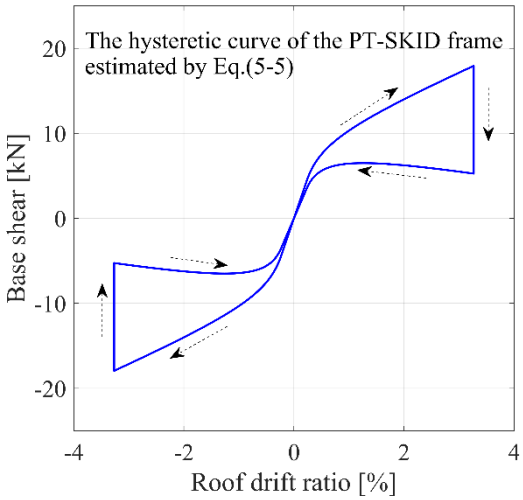

Figure 5-1 Hysteretic curve of the case PT-SKID frame.

5.3 The benefits of the SKID device on the PT frames

5.3.1 Details of OpenSees numerical model of the prototype PT frame and SKID device

In this section, quasi-static finite element analysis is carried out to evaluate benefits of the SKID device on the PT frame. The benchmark PT model is a quarter-scale one-storey one bay planar steel frame tested by Oddbjornsson et al. (2009), which was abstracted from the PRESSS post-tensioned self-centring prototype structure. The height of the frame was 900 mm, and the bay width was 2100 mm. The beam and columns were made of hollow steel tubes with a square section of 100×100×10 mm^3. The beam-column and column-foundation connections were fastened by pre-stressed cables with areas of 93 mm^2 and 52 mm^2, pre-tension forces of 115kN and 64 kN, respectively. The applied mass on the beam was 2 tons. The static and dynamic mechanical properties of the frame were theoretically analysed by Alexander et al. (2011), physically tested by Oddbjornsson et al. (2009), and numerically investigated by Kibriya et al. (2018). More details of the frame could be found in the above-mentioned literature. The benefits of adding the SKID device to the PT frame are compared using three heuristic frames denoted as Frame A, Frame B and Frame C described in Table 5-1.

Table 5-1 Description of three heuristic frames.

Frame	Description	Linear Elastic Period	SKID cantilever bar Stiffness	SKID Slope	SKID Friction Coeff.
		T_0	k	β	μ

		[s]	[kN/mm]	[deg]	[ ]
A	PT frame tested by Oddbjornsson et al. (2009)	0.135	NA	NA	NA
B	PT frame A stiffened by an equivalent stiffness due to that of the SKID but with no frictional dissipation	0.127	0.835	45	0
C	PT frame with SKID device	0.127	10	5	0.8

Frame A is the PT frame tested by Oddbjornsson et al. (2009) as mentioned above. Frame B is the PT frame A stiffened by an equivalent stiffness to that of the SKID but with no frictional dissipation. Frame C is the PT frame with the SKID device. The SKID device in Frame C is conceptionally designed based on the analysis in Section 3. The kinetic friction coefficient μ is 0.8, which is a typical value corresponding to rubber against rubber interface sliding. The sliding angle β and cantilever bar stiffness k are 5° and 10 kN/mm, respectively. According to Eq. (3-25), this SKID device has a loading stiffness of 0.835 kN/mm. The SKID device both (i) increases the lateral stiffness of the frame (especially the 'post-pseudo-yield' stiffness) and (ii) frictionally dissipates input energy. Note that Frame B is used to explore the effect of (i) the stiffness increases without the dissipative component. This is achieved in practice by applying the SKID device properties as described in Table 5-1 which results in a non-hysteretic stiffness increase to the PT frame of 0.835kN/mm.

OpenSees (McKenna, 2011) was employed to develop a two-dimensional planar model with three degrees of freedom nodes, as shown in Figure 5-2. The beam and columns were modelled by elastic beam-column elements with their respective material yield point of 275 MPa and elastic modulus of 210GPa. The pre-stressed cables were modelled by co-rotational truss elements, and their yield points were 1500 MPa. Rigid links were used to outline interfaces between different elements and ensure accurate anchor positions of cables. The stiffness and strength of each of the rocking connections were modelled by 100 (evenly spaced) compression-only springs, that are modelled by using zero-length elements with an elastic-perfectly plastic gap material. Note that the stiffness of springs located at the two exterior edges of the interfaces was half of the others. The influence length (which is used to determine the contact spring stiffnesses in the OpenSees model) of the members contributing to the rocking zone stiffness was set to approximately one-third of the storey height for the columns and one-sixth of the bay widths for the beams. The floor mass was applied to the beam as a uniformly distributed load. A Rayleigh damping ratio of 5% was specified for all elements. To account for geometric nonlinearities, the co-rotational geometric transformation was utilised for columns and beams. Results of Frame A have been benchmarked dynamically with those reported in Kibriya et al. (2018). The SKID device was modelled as two separate and independent devices (one for the motion to the right, and one for the motion to the left) with friction surfaces in only one direction, as shown in Figure 5-2. The

zero length 2D element was chosen to form the inclined sliding surface and simulate the loss of contact of the surfaces between the slider and the slope blocks. The spring blocks were modelled by zero-length elements to ensure that no force was generated on the loss of contact.

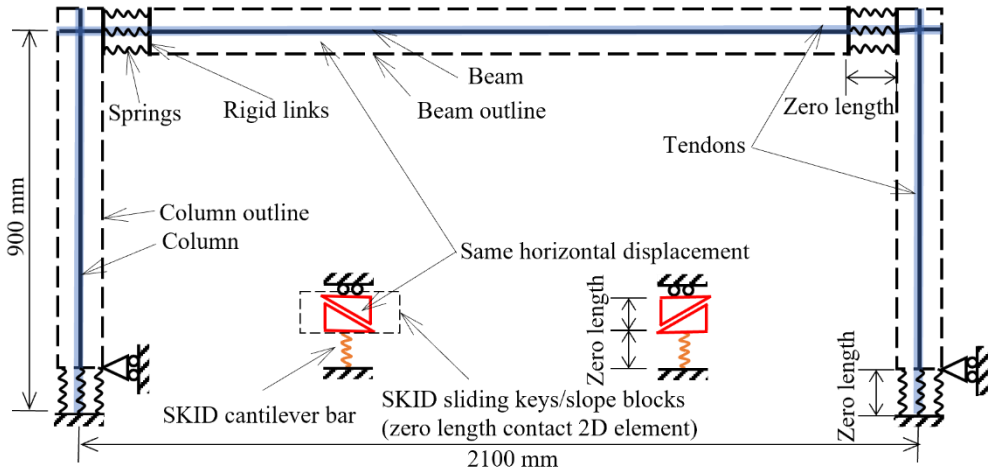

Figure 5-2 Details of the OpenSees model of the PT frame and SKID device.

5.3.2 Experimental benchmarking of OpenSees numerical model.

These numerical tests adopted a quasi-static cyclic constant amplitude (displacement control), and their peak drift ratio was set as 2%. Figure 5-3 (a) presents hysteretic results of Frame C with the non-hysteretic backbone curves of Frames A and B. Frame C exhibits a triangular flag-shaped hysteretic curve (a composite of the triangular shape of the SKID and the nonlinear elastic backbone of the PT frame). This contrasts with the parallelogram flag-shaped hysteretic curves of conventional self-centring systems. Frame B is still effectively a nonlinear elastic frame, albeit with a 14% increase in initial stiffness and a 321% increase in post-pseudo-yield stiffness of the frame. The term ‘pseudo-yield’ means here the cornering stiffness softening caused by geometrical nonlinearity rather than material inelasticity. Figure 5-3 (b) presents the force-deflection share taken by the PT frame components of the combined system. Experimental test results obtained by Oddbjornsson et al. (2009) are also plotted to benchmark the numerical model. The numerical (OpenSees) model (for the PT frame part) matches the form of the experimental results well, although the strength is slightly lower than the test results (around 9% at the drift ratio of 2%). This may have been induced by frictional forces parallel to the opening joints that have not been captured in the numerical models. Additionally, the numerical results of the SKID part perfectly match the mathematical prediction of Eq. (3-24). Therefore, we conclude that the OpenSees model of the PT frame and SKID device is reasonable and accurate.

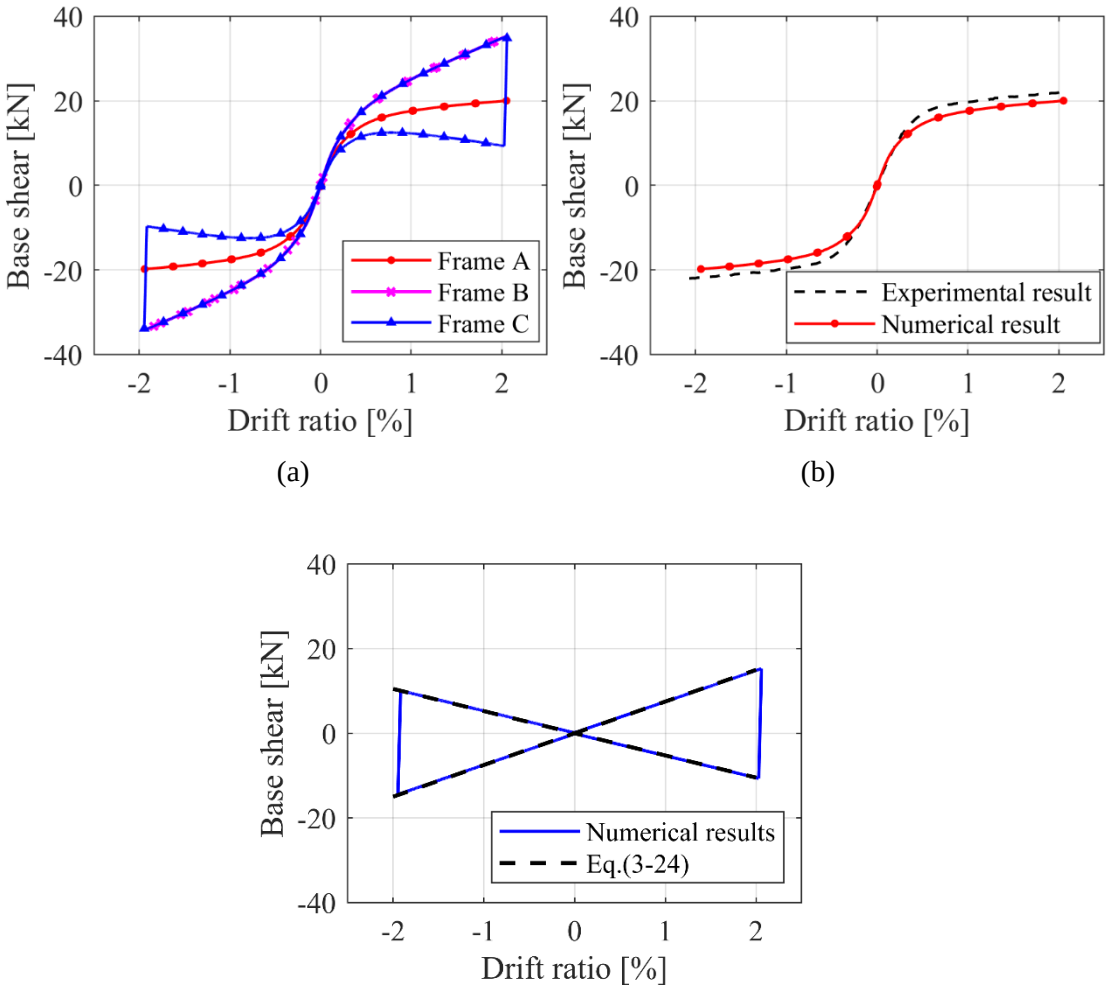

Figure 5-3 Hysteretic curves for cyclic tests of (a) PT Frame and SKID device, (b) PT frame parts alone with benchmarking against experimentally obtained push-over curves, and (c) SKID device part alone with benchmarking against theoretical envelope obtained from Eq.(3-24).

A pushover test was carried out on Frame A up to a drift ratio of 7% to identify the capability of the PT frame. The element for modelling the beam and columns were replaced with force-based beam-column elements with Steel 02 materials. Their respective material yield point is 275 MPa, and elastic modulus is 210GPa, as shown in Figure 5-4 (a). The element for the pre-stressed cables were replaced with co-rotational truss elements with Steel 02 and MinMax materials. The MinMax materials was used for modelling the broken of the cables at ultimate strain. Their strain-stress relationship was shown in Figure 5-4 (b). Because the real yield points of the cables were unknow, two yield strain values of 0.8% (which is normally the 0.1% proof load strain) and 0.9% (which was the results tested by Du et. al. (2018)) were assumed and shown in Figure 5-4 (b). Figure 5-4 (c) shows the pushover curves. As shown, the frame shows a stiffness softening at around 0.5% drift ratio. This stiffness softening was due to geometric nonlinearity. The stiffness of the frame reduced again after around 3.8% and 5.5% under the two yield strain assumptions,

respectively. This reduction was induced by the yield of the column cables. Figure 5-5 (d) shows the column cable force of Frame A. Please note that this OpenSees model of the PT part cannot capture the yield behaviour of the contact area where yield may happens within 7% drift ratio. No physical test data about the post-yield behaviours of this contact area is available in the literature. The physical test conducted at the University of Bristol in a previous study and used herein for the validation of this numerical model investigated only the elastic regime of the structural system. Thus, the current information about the bared Frame A cannot support a rational analysis with its post-yield behaviours. It is important to clarify that this research focuses on the behaviour of the PT-SKID frame rather than the bared PT frame. The following analysis is for supporting the design of the PT-SKID frames at a specific seismic level (i.e., the structural components are expected to remain elastic for self-recentre). Thus, the main point of this research is the behaviour of PT-SKID frame (especially the PT-SKID mechanism) before failure. Therefore, a model without including the plastic behaviour (or a model with an elastic assumption) is deemed sufficient for this research scope. In addition, an average dynamic responses of a model behaving elastically for some events and plastically for the others cannot represent the behaviour of the PT-SKID frame at the design earthquake level. The logic is not consistent if such a model is used for the analysis. However, the PT-SKID frame behaviour beyond the elastic range is important when, due the uncertainties on seismic actions, stronger earthquakes can occur. The failure mode of the PT-SKID frames in unexpectedly strong events should be properly considered in design. This is beyond the scope of this research but should be carried out in the next research stage.

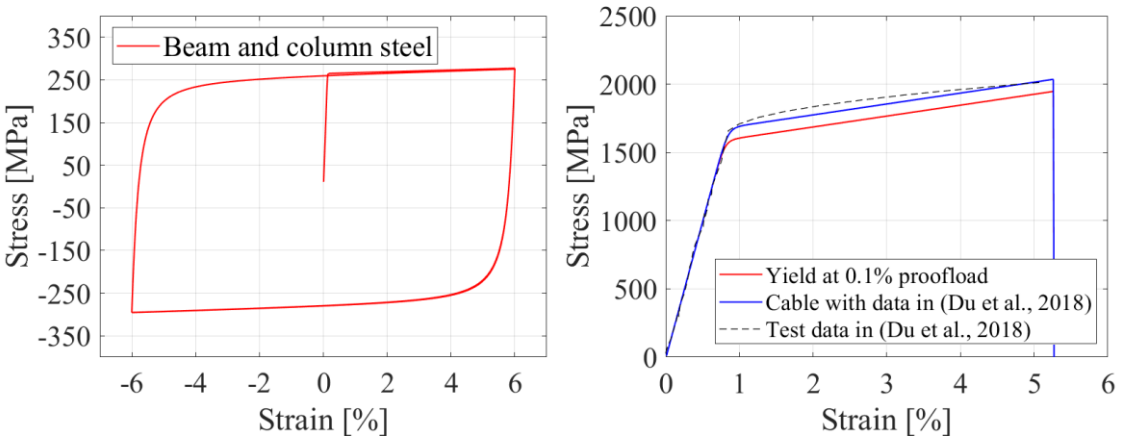

(a) (b)

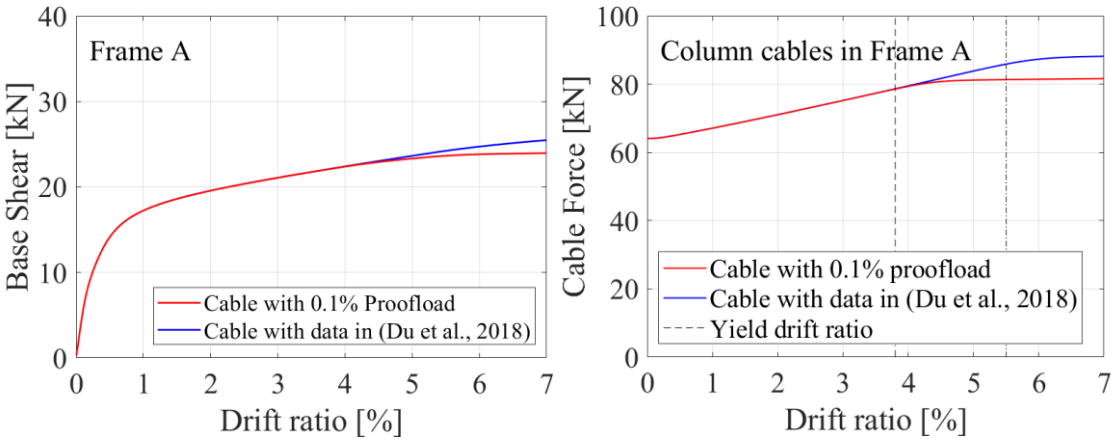

(c) (d)

Figure 5-4 The pushover results of Frame A: (a) the strain-stress relationship of the beam and column sections; (b) the strain-stress relationship of the cables; (c) the pushover curve of Frame A; and (d) the column cable force of Frame A.

5.3.3 Equivalent viscous damping ratio estimates

Figure 5-5 (b) presents an estimate of the equivalent viscous damping ratios of Frame C as the drift increases. The equivalent damping ratio of the SKID part of the frame also has been presented in Figure 5-5 (b). Here, the estimated equivalent viscous damping ratio (for the PT frame and SKID damper system), $\zeta_{\text{eq,hyst}}$, was calculated by the area-based approach proposed by Jacobson (1960):

$$\zeta_{\text{eq,hyst}} = \frac{S_1}{4\pi S_2} \qquad (5-6)$$

where S_1 and S_2 correspond to the areas illustrated in Figure 5-5 (a). Note that these damping ratios are only the hysteretic component. The total equivalent damping ratio, ζ_{eq}, of the frames should involve the damping from other sources (i.e., the elastic viscous damping component, $\zeta_{\text{eq,0}}$, including the flexure/friction of the non-structural elements and soil nonlinearity, etc) and is expressed as (Blandon and Priestley, 2005):

$$\zeta_{\text{eq}} = \zeta_{\text{eq,0}} + \zeta_{\text{eq,hyst}} \qquad (5-7)$$

It is worth mentioning that Jacobson's method expressed by Eq. (5-7) generally overestimates the hysteretic component of equivalent viscous damping ratio, induced by its approximations of harmonic excitation in the resonance condition and full cycles at the maximum amplitude (Blandon and Priestley, 2005; Dwairi and Kowalsky, 2004). In fact, the seismic energy dissipated

by the hysteretic behavior mainly depends on the characteristics of the earthquake excitation (Gentile and Galasso, 2021). Therefore, a more accurate approach for estimating the hysteretic equivalent damping ratio is expected in future research. Although these limitations exist, Jacobson's approach is useful in identifying the approximate hysteretic damping. Considering Figure 3-9, it is clear that the triangular-shaped hysteretic curve must give a constant damping ratio (for the SKID device alone) independent of drift ratio. However, in combination with the nonlinear elastic PT frame the effective system damping ratio (PT frame and SKID device) is dependent on drift (as stated in Eq. (3-16)), when calculated from the enclosed area of hysteretic loops shown in Figure 5-3 (a). These drift amplitude-dependent effective system damping ratios are displayed in Figure 5-5 (b). Thus, generally, the equivalent viscous damping ratios of Frame C increase as drift level increases.

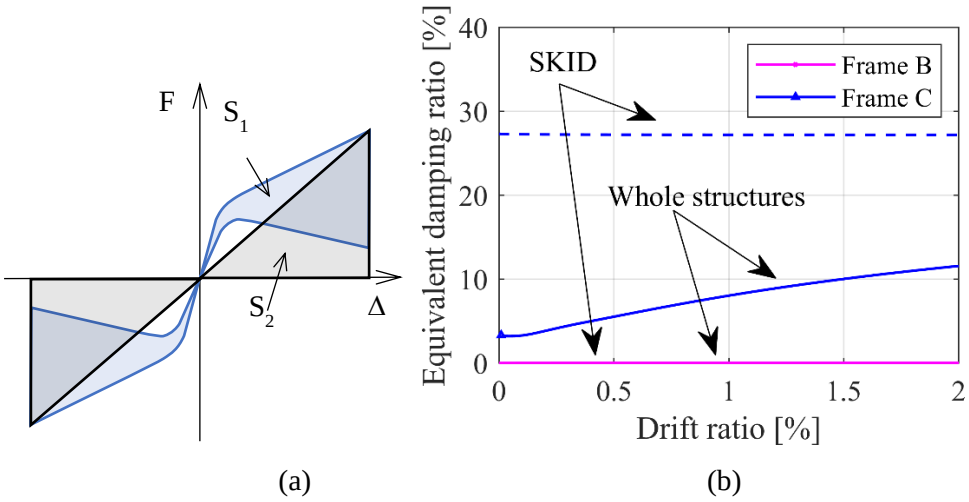

(a) (b)

Figure 5-5 (a) Hysteretic areas employed for the calculation of the equivalent viscous damping ratio; (b) equivalent damping ratios of Frame B and C.

5.4 Ground motion dynamic behaviour of the PT-SKID frames

5.4.1 Numerical analysis setup and ground motions

To comparatively investigate the benefits of the SKID device to the PT frames, three models described in Table 5-1 were subjected to earthquake ground motions. Seven pairs of ground motions selected by Lombardi et al. (2019) from the European Strong Motion Database were utilised in the analysis; they are spectrum-compatible for a high seismicity area in Italy (i.e. L'Aquila), where such a structural typology can be of interest. Table 5-2 summarises their characteristics, and Figure 5-6 shows the 5%-damped linearly elastic response spectrum of the ground motions (Average of original). The average acceleration response of them (the red dashed

line in Figure 5-6) matches well with the target code spectrum of the Life-Safety Limit-State (10% probability of exceedance in 50 years) for the sites (blue dashed line in Figure 5-6). An incremental dynamic analysis (IDA) was used to explore the sensitivity of the frame models to seismic excitations. The excitation intensity level in IDA was measured by the 5%-damped spectral acceleration (S_a) ranging from 0 to 3.5g with an increment of 0.05g.

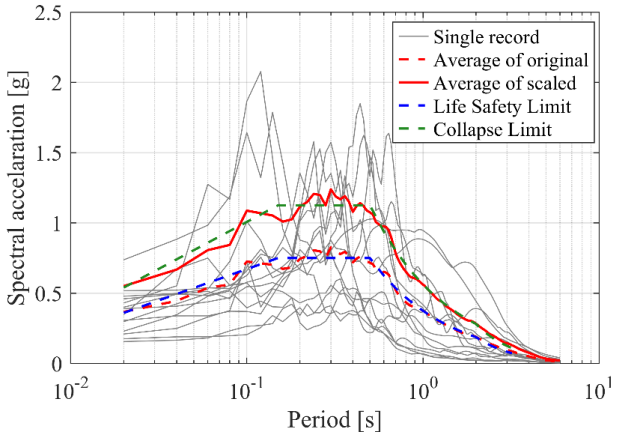

Figure 5-6 5%-damped linearly elastic response spectrum of the records in table 2.

Table 5-2 Characteristics of the considered ground motions (Lombardi et al. (2019)).

N	Earthquake Event	Station ID	Magnitude (Richter scale)	R_{epi} (km)	Duration (s)	EC8 Soil Class	Original PGA (g)	
							x	y
1	Montenegro (1979)	Petrovac-Hotel Oliva	6.9	25	48	B	-0.45	-0.31
2	Dursunbey (1979)	Dursunbey-Kandili	5.3	6	10	B	-0.22	-0.29
3	Campano-Lucano (1980)	Calitri	6.9	16	86	B	-0.16	-0.18
4	Erzincan (1992)	Erzincan	6.6	13	21	B	-0.39	0.51
5	South Iceland (2000)	Hella	6.5	15	81	B	-0.21	-0.48
6	South Iceland (2000)	Kaldarholt	6.4	12	51	B	0.33	0.39
7	South Iceland (2000)	Solheimar	6.4	11	55	B	0.42	0.72

5.4.2 Nonlinear dynamic time-history, IDA results.

Figure 5-7 summarises the average peak responses of Frames A, B and C in solid lines when subjected to the 14 records with the increasing spectral accelerations. According to Figure 5-7 (a), the SKID device would significantly reduce peak drift ratios of the PT frame, especially when the peak drift ratio exceeds 0.5% as this is where the system starts to exhibit pseudo-yielding. Results indicate that both stiffness increase (Frame B) and frictional energy dissipation (Frame C) contribute to this reduction. Specifically, the response difference between Frame A and B is due to the stiffness increase introduced by the SKID device (which is not active hysteretic damping). While the difference between Frame B and C exhibit the energy dissipation from the friction force in the SKID device. Furthermore, the responses of Frame A and B almost overlap when the S_a is less than 0.8g. This is where the PT frame parts deform with their initial stiffness. The reason is that the stiffness increase provided by the device only contributes significantly at post-pseudo-yield drift levels.

It is worth noting that the results are obtained under the hypothesis of elastic beams, columns, and cables. It is worth noting that the results are obtained under the hypothesis of elastic beams, columns, and cables. The numerical models based on the elastic elements have been validated numerically and theoretically. However, no physical test data or theoretical model was accessible for validating the mode when frame elements or assemblies (especially the contact surfaces) perform inelastically. To clarify this issue, the responses over a 2% drift ratio (peak displacement in the physical tests) are drawn by the dashed lines with hollow circle markers in the figures. Although a simplification, these results are sufficient to identify the benefits of introducing the new SKID device. As shown in the figure, even under the quite severe earthquake with a S_a of 3.5g, the mean performance of Frame C indicates its most probably still safe. According to Figure 5-7 (b), the average roof total acceleration response of Frame C is always the smallest among the three frames, but the difference between Frame A and C are not very large. This is due to the nature of the nonlinear elastic backbone curve of the PT frame, which effectively limits response accelerations.

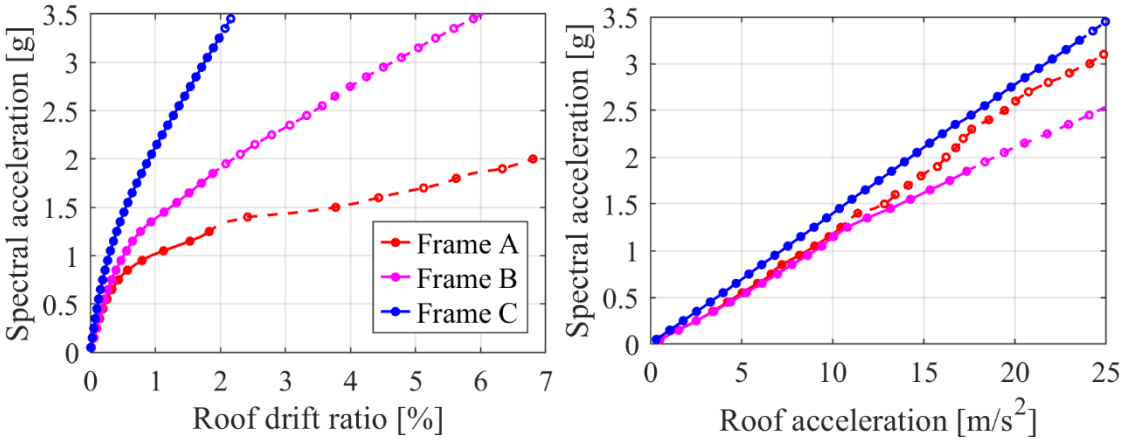

(a) (b)

Figure 5-7 IDA responses for Frames (Table 1, Frame A (red), Frame B (Cyan), Frame C (blue)) when subjected to ground motion (table 2) with incremental spectral accelerations: (a) roof drift ratio, (b) roof total acceleration.

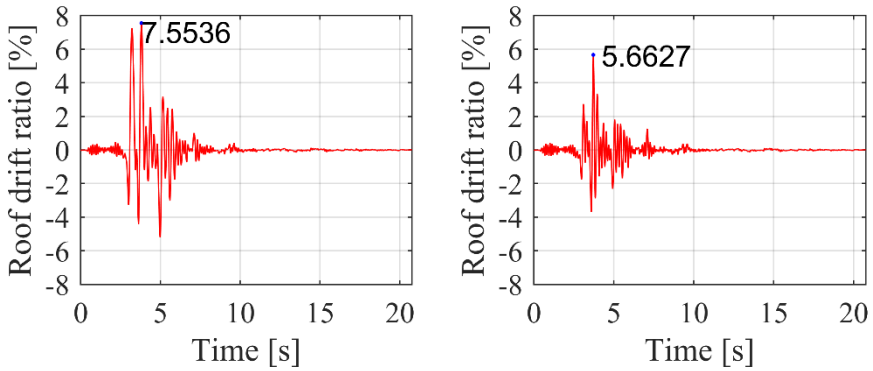

(a) (b)

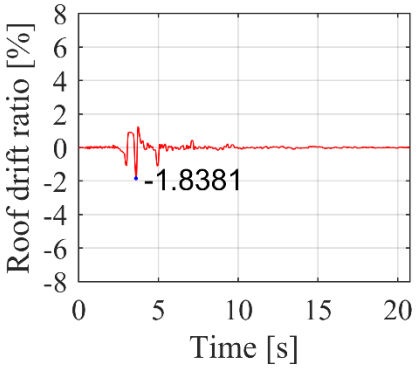

(c)

Figure 5-8 Roof drift ratio time history for Record 4 (y-direction) with a Sa of 2.5g for: (a) Frame A, (b) Frame B, (c) Frame C.

5.4.3 A forensic case study of an individual sample from the IDA results

The responses of three frames subjected to Record 4 (y-direction) with a S_a of 2.5g was selected to show how the frame responds to the severe earthquake excitation. This record with the S_a of 2.5g could be seen as a maximum considered earthquake (MCE) ground motion. Figure 5-8 shows the response time history of three frames in terms of the roof drift ratio. According to the figure, the peak drift ratio of the frame is reduced significantly after introducing the SKID device, by comparing the responses of Frame A and C. It is worth noting that Frame A and B have damaged and even collapsed when the drift ratio exceeds 3.8%. The results herein are obtained under the hypothesis of elastic beams, columns and cables. In addition, the residual drift ratio is negligible

in Frame C, which means the introduction of the SKID device does not compromise the self-centring feature of PT frame.

Figure 5-9 displays the force-deflection curves for the Frames. The force-deflection behaviour of the three frames under dynamic loads have a similar form to those under quasi-static cyclic loading, albeit the amplitude levels are determined by the dynamic performance of the entire nonlinear PT and SKID system.

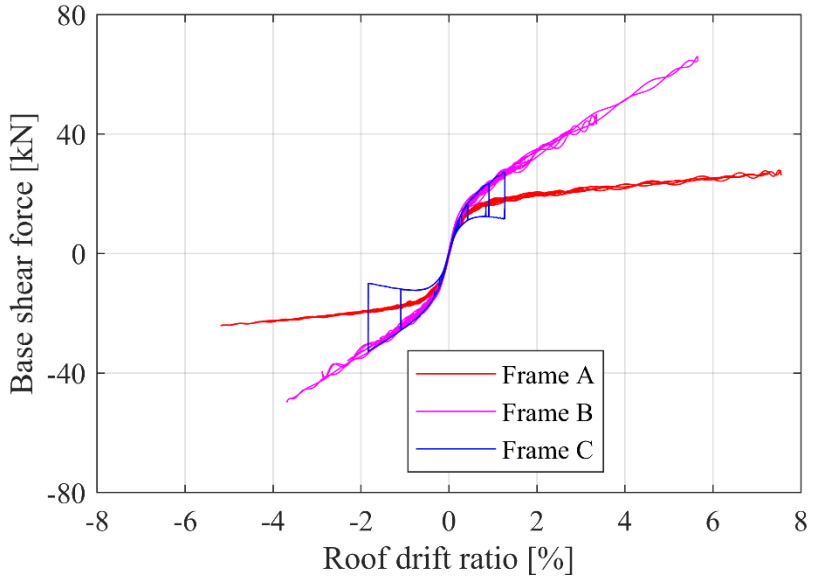

Figure 5-9 Hysteretic behaviour of the frames under Record 4 (y-direction) with a Sa of 2.5g.

Figure 5-10 shows the cumulative energy dissipated by the frames. The energy dissipated by each part is calculated from the integral of a nonlinear SDOF's system equation of motion, expressed as Eq. (5-8) given in Chopra (2007):

$$\int_0^u m\ddot{u}(t)du + \int_0^u c\dot{u}\,(t)du + \int_0^u f_s(u,\dot{u})du + \int_0^u f_d(u,\dot{u})du = -\int_0^u m\,\ddot{u}_g(t)du \quad (5-8)$$

where, in this case, m is the floor mass, u is the relative roof drift response, c is the viscous damping coefficient, and $\ddot{u}_g(t)$ is the ground acceleration, $f_s(u,\dot{u})$ and $f_d(u,\dot{u})$ are the base share force of the PT frame part and the SKID part, respectively. The right-hand side of the equation is the total energy input into the system. Four terms on the left are the kinetic energy of the mass, the energy dissipated by viscous damping, the recoverable strain energy in the PT frame part and the hysteretic energy dissipated by the SKID device, respectively. It is worth mentioning that the energy dissipated by viscous damping is calculated based on the equilibrium of Eq. (5-8) after obtaining the other four terms. As shown in Figure 5-10, the total dissipated energy is

reduced when the post-pseudo-yield stiffness is increased by the stiffness SKID device alone (Frame B). However, the reduction is far greater in Frame C as the SKID dissipates energy and reduces overall drift amplitude levels which inevitably results in far less total energy in the structural system.

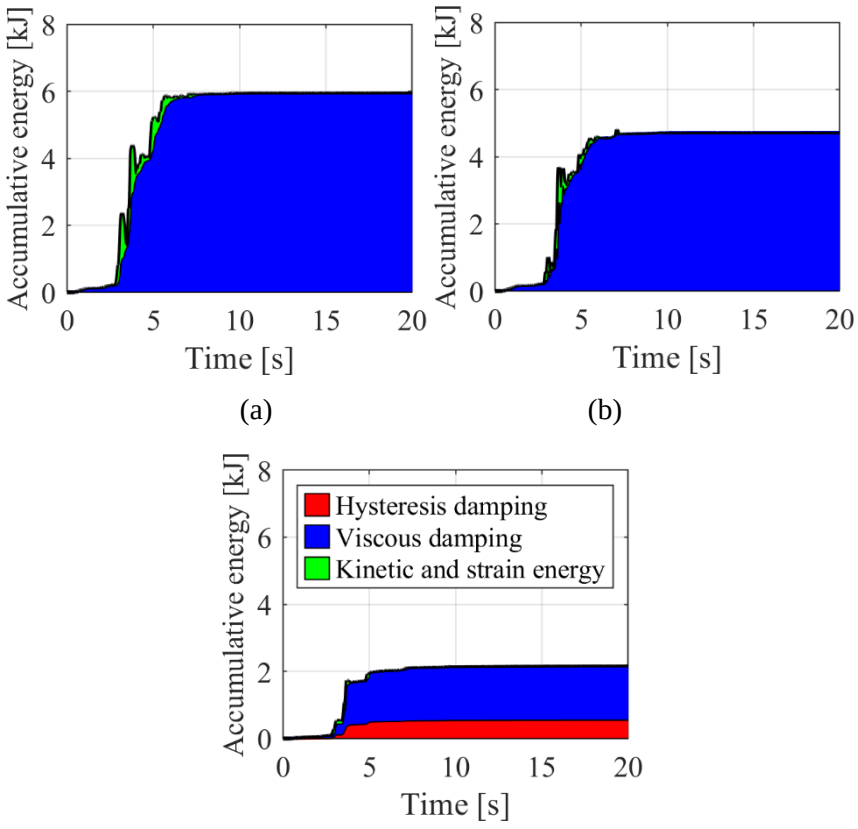

Figure 5-10 Cumulative energy dissipated by the each part of the system for Record 4 (y-direction) with a Sa of 2.5g (a) Frame A, (b) Frame B, and (c) Frame C.

5.5 The influence of manufacturing parameters of the SKID device on the dynamic behaviours of PT frames

Ihe influence of the SKID parameters on the dynamic response of PT frames has not been investigated yet. The following numerical analysis focuses on: (1) the dynamic characters of the PT-SKID frames using sine-sweep responses and (2) the influence of SKID manufacturing parameters on the earthquake responses of PT-SKID frames.

5.5.1 The prototype PT-SKID frames and their OpenSees numerical models

The same typical PT frame described in Section 5.3.1 is adopted. However, the cross-sections of the beam and columns have been redesigned into rectangular hollow sections of 100×40×3 mm^3 to consider the stiffness and damping contribution of the SKID device. The pre-stressed cables have also been modified with areas of 52 mm^2 and 38 mm^2 for beam-column and column-foundation connections, respectively, corresponding to pre-tension forces of 65kN and 40 kN.

Section 5.4 identifies two contributions of the SKID device to the response improvement in PT frames: (1) stiffness strengthening (mainly on post-opening joint stiffness) and (2) additional damping. These two effects from the SKID device can be reflected by two factors: the loading stiffness K_{SKID} and equivalent damping ratio ζ_{eq}, respectively. They are controlled by three independent manufacturing parameters: friction coefficient μ, slope angle β, and spring stiffness k_s. Jacobson's method suggests that the equivalent damping ratio of the SKID device is irrelevant to the spring stiffness k_s. Thus, we replace spring stiffness k_s with K_{SKID} (i.e. the loading stiffness) to reflect stiffness strengthening from the SKID device and keep friction coefficient μ and slope angle β as damping reflection parameters in the following analysis.

OpenSees is used to develop a two-dimensional planar model, as shown in Figure 5-11. The PT frame part was modelled the same as Figure 5-2. However, the model of the SKID device is refined in this section. The SKID devices are modelled as a simplified equivalent model (by replacing every two spring-slope sets with one set) to reduce numerical integrity complexity, as shown in Figure 5-11. The deflection cantilever bars were represented by the springs with twice the stiffness. The simple contact 2D element is chosen to model the sliding surfaces and to simulate the touch/separation of the surfaces. The sliding keys, slope blocks and springs are modelled by the quad and elastic beam-column elements, respectively.

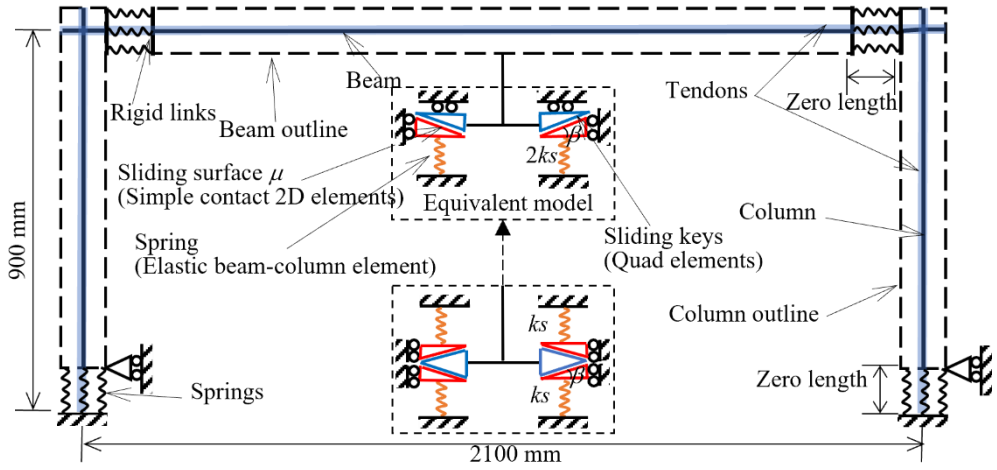

Figure 5-11 Details of the OpenSees model of the PT frame and the SKID device.

5.5.2 Benchmark of the OpenSees model of the SKID device

The equivalent model of the SKID device in OpenSees was benchmarked with the physical specimen S1. The numerical case frame (PT-S1) was assumed to be equipped with the SKID S1 and was subjected to the ground motion 4-y (see Table 5-1). Then the roof drift response of the frame from the numerical analysis was applied to the SKID physical model S1 as the excitation. By doing so, the physical model of the SKID S1 had the same loading protocol (i.e. pseudo-dynamic test) as its numerical counterpart in OpenSees. Note that, limited by the configurations of the actuator, the roof drift response from the numerical dynamic analysis was converted to a quasi-static signal by simply amplifying the time series with 10 in the physical test. Figures 5-12 (a) and (b) show the ground motion series and the physical test excitation series, respectively. The dynamic roof drift ratio response is expressed by the same line as the physical test excitation in Figure 5-12 (b) (please refer to the top axis). Figure 5-13 shows the force-response time history and hysteretic curve of the physical model S1 and its numerical counterpart. Empirical and numerical curves match each other, indicating a reliable and accurate reflection of the OpenSees model of the physical SKID device.

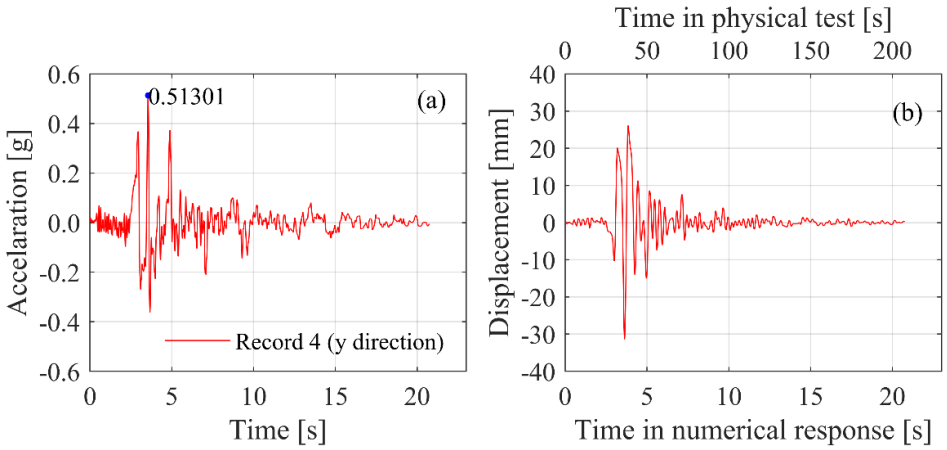

Figure 5-12 Time history of: (a) ground motion used in the numerical analysis; and (b) the dynamic response of the roof drift (beam excursion) in the numerical analysis and the converted quasi-static excitation used in the physical test.

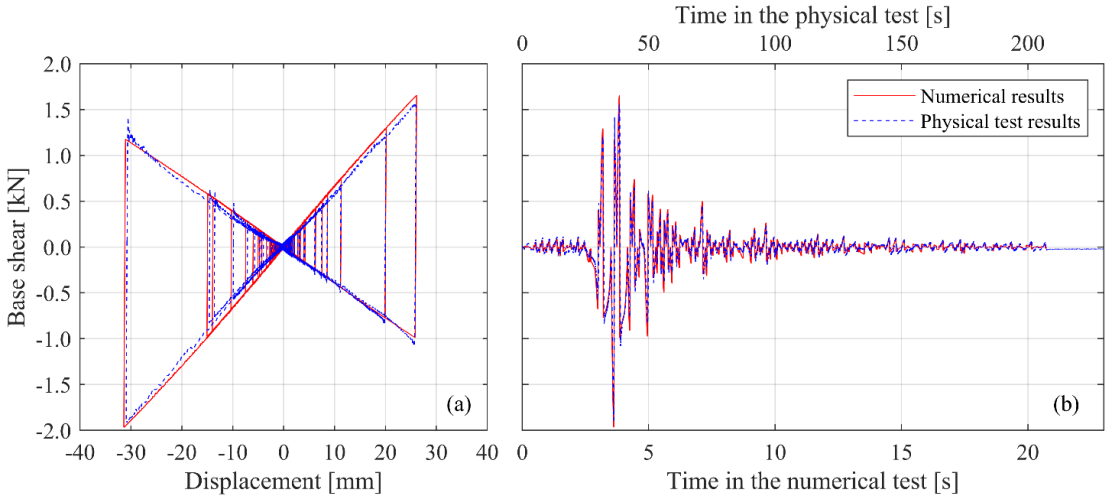

Figure 5-13 Response comparison between the physical test and its numerical counterpart: (a) SKID hysteretic curves; (b) base shear response time history.

5.5.3 Dynamic features of the PT-SKID frames: frequency response functions (FRFs)

First of all, the fundamental nonlinear features of the PT-SKID frames were investigated by focusing on the frequency response functions (resonance curves). The frames were subjected to sine-sweep excitations, including a series of amplitude-constant (in PGA) frequency-increasing and frequency-decreasing time series. Then, the response time histories were converted to the frequency domain and generated FRFs. The frequency range of sine-sweep excitations was from 1Hz to 5Hz and the time increment was 0.001s. A group of excitations with PGA from 0.01g to 0.20g was utilised to generate FRFs for each frame.

Three types of frames, denoted as Frame A, B and C, were designed as listed in Table 5-3. Frame A was a simple PT frame; the FRF of Frame A was reported in Alexander et al. (2011) and Kibriya et al. (2018). Frame C was generated by equipping Frame A with the SKID device. The device introduced additional damping and stiffness enhancement to the frames. Frame B was defined for separately identifying these two contributions. Frame B was provided with an equivalent stiffness of 400kN/m without frictional dissipation; a particular SKID device with negligible friction coefficient could conceptually achieve this characteristic. Besides, to unveil the influence of the slope angle of the SKID device on the FRFs of the PT-SKID frames, Frame C was split into four frames with the same K_{SKID} and μ, but different β ranging from 5° to 40°, and denoted as Frame C1 to C4, respectively. Additionally, the SKID devices with a smaller μ of 0.2 and a larger K_{SKID} of 600 kN/m were defined in Frame D and E to reveal the influence of the friction coefficient μ and sliding-up stiffness K_{SKID}. All members in the above-mentioned frames were designed and assumed as elastic in this paper.

Table 5-3. Description of five types of heuristic frames

Frame	Description	SKID lateral stiffness	SKID Slope	SKID Friction Coeff.
		K_{SKID} [s]	β [deg]	μ [ ]
A	Bared PT frame	NA	NA	NA
B	PT frame A stiffened by an equivalent stiffness but without frictional dissipation	400	45	0
C	PT-SKID frames where β is the variable	400	5 (C1); 15 (C2); 25 (C3); 40 (C4)	0.2
D	PT-SKID frames where μ is the variable	400	15	0.8
E	PT-SKID frames where K_{SKID} is the variable	600	15	0.2

The frequency response functions of Frame A, B, and C2 under the sine-sweep excitations with the PGA of 0.05g are plotted in Figures 5-14 (a), (b), and (c), respectively. The responses of all frames present typical features of nonlinear systems. The FRFs include two amplitude branches: the upper one (blue line in the figure) obtained from frequency-decreasing excitation and the lower one (black line) from frequency-increasing excitation, enveloping a coexisting solution region. By comparing the results of these three frames, it is clear that the SKID device considerably narrowed the coexisting solution region, thus, reducing the complexity of the nonlinear response. The backbone curve of the FRFs of each frame is constructed by following

peak values of their upper branches in different amplitude excitations, as shown in Figure 5-14 (red line). It is evident that the stiffness enhancement (by comparing Frame A and Frame B) and the additional damping (by comparing Frame B and Frame C2) introduced by the SKID device significantly reduced the peak drift ratio response of the frames.

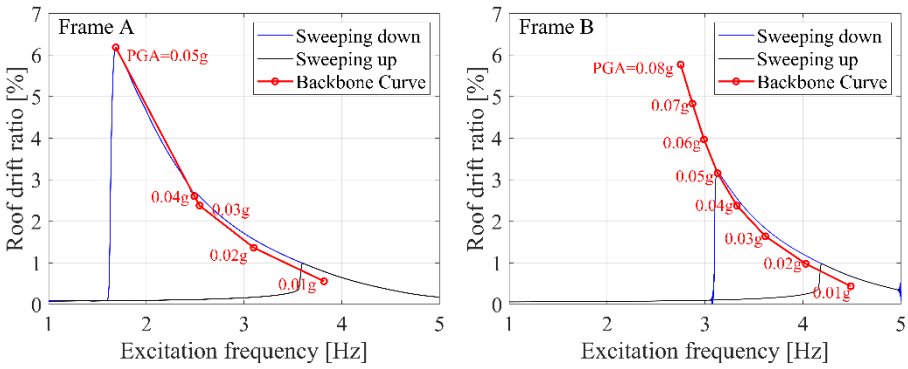

(a)

(b)

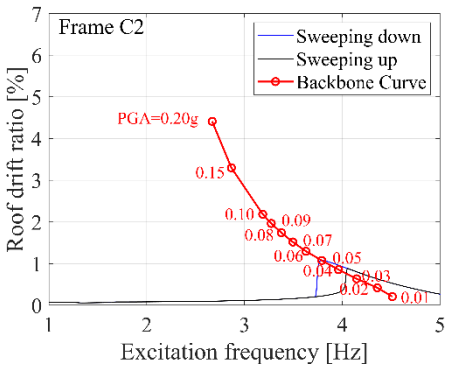

(c)

Figure 5-14 Frequency response functions in a wide range of excitation amplitudes (exampled by the case at the PGA of 0.05g) and their backbone curves of: (a) Frame A; (b) Frame B; and (c) Frame C2.

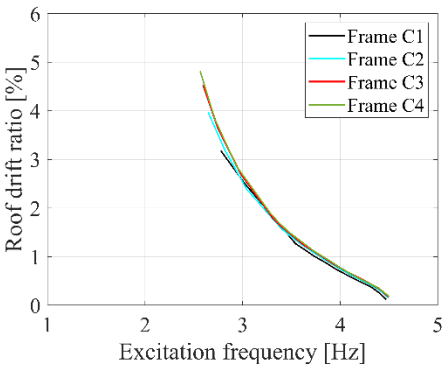

(a)

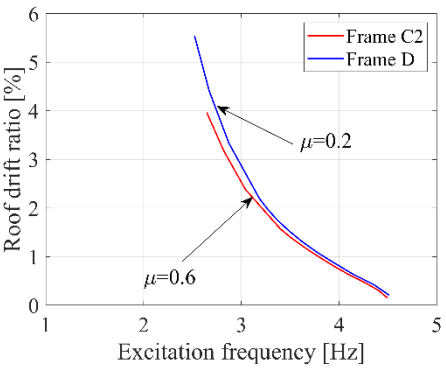

(b)

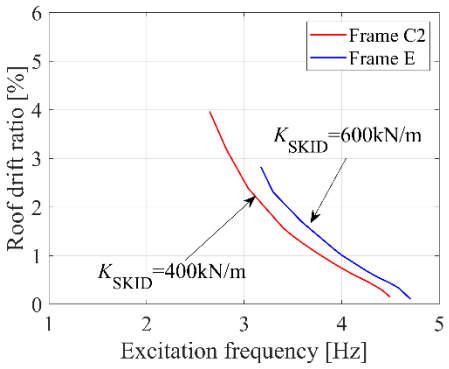

(c)

Figure 5-15 Comparison of FRF backbone curves among frames with SKID devices of: (a) different β; (b) different μ; and (c) different K_{SKID}.s

The backbone curves of FRFs belonging to Frame C1 to C4 (i.e. same K_{SKID} and μ but different β) are plotted in Figure 5-15 (a). The figure indicates that the drift ratio response rises with increasing β. Besides, a reduced trend in response with the increase μ can be observed from Figure 5-15 (b). These response trends with μ and β were in accordance with the estimated equivalent damping ratio ζ_{eq} using Jacobson's method, as shown in Figure 5-16. In addition, Figure 15 (c) shows the backbone curves of Frame C2 and Frame E, where the SKID devices possessed the same μ and β but different K_{SKID} of 400 kN/m and 600kN/m, respectively. The results show that frequency response amplitude reduces with the increasing K_{SKID}, similar to the response trends between Frame A and B where the same damping but different stiffness was conducted.

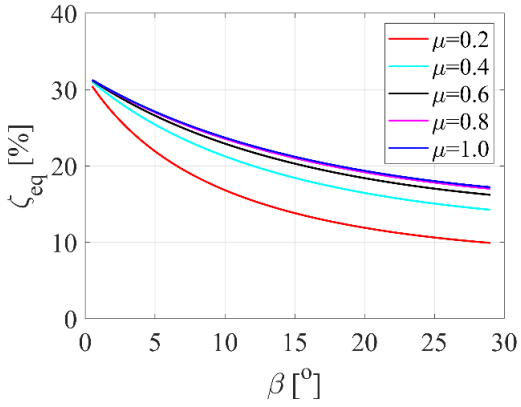

Figure 5-16 Equivalent damping ratio of the SKID device with various β and μ.

5.5.4 The influence of SKID device manufacturing parameters on the earthquake response of the PT-SKID frames

5.5.4.1 Numerical analysis setup and ground motions

In order to provide heuristic qualitative design suggestions for the SKID device, K_{SKID}, μ and β were chosen as variables to investigate their influence on the seismic response of the PT-SKID frames. The SKID devices considered in this paper cover a wide range of values of K_{SKID}, μ, and β. Specifically, K_{SKID} ranged from 200 to 2000 kN/m, corresponding to a post-opening joint stiffness ratio γ (the post-opening joint stiffness to initial stiffness of the PT-SKID frame) ranging from 0.21 to 0.61. μ was set from 0.2 to 1.0, comprising most of the usual friction interface. The range of β was up to 40°. Table 5-4 summarises the range and increment of each parameter. All the SKID devices were applied within the same PT frame, i.e., Frame A tested in section 3.2, in the analysis. Note that as the PT-SKID frame is expected to be a non-damage system (for a fully self-centring purpose) for conventional earthquakes. Therefore, all the components of the PT frames (i.e., beams, columns, and cables) and SKID devices (i.e., cantilevers) of the tested frames were assumed elastic in the numerical analysis. However, in practice, structural damage (e.g. plastic hinges) may be expected for some extreme earthquakes.

Table 5-4. The range and increment of parameters

parameters	Values
K_{SKID} (kN/m)	200 (γ = 0.21), 400 (γ = 0.29), 600 (γ = 0.36), 800 (γ = 0.42),1000 (γ = 0.46), 1500 (γ = 0.55), 2000 (γ = 0.61)
μ	0.2, 0.4, 0.6, 0.8, 1.0
β	From 2° to 40° with an increment of 2°

Seven pairs of ground motions listed in the Table 5-2 are used in the analysis. To highlight the seismic response under strong earthquakes, all the motions were scaled by 1.5 to make their average spectral acceleration (red solid line) match the target code spectrum of the Collapse Limit-State (2% probability of exceedance in 50 years, green dashed line) (see Figure 5-6). A 5-second time series with excitation of 0 was added at the end of each ground motion to observe residual deformation of the frames.

5.5.4.2 Sensitivity analysis results

Figure 5-17 presents the average drift ratio response of the PT-SKID specimens subjected to 7 pairs of ground motions in the form of contour plots. The response levels are expressed with different colours shown in the scaling bar. The specimens with the same μ are summarised into

the same plot because μ is a non-continuously selectable parameter in practice. Only the results for μ equal to 0.2, 0.6, and 1.0 are shown in the paper. The peak drift ratio response shows an obvious stiffness-dependent trend. With increasing K_{SKID}, the peak drift ratio reduces rapidly. Similar trends could be observed in Figure 5-18 in terms of the base shear response of the PT part (F_{PT}). However, large values of K_{SKID} lead to a large base shear response of the SKID part (F_{SKID}), as shown in Figure 5-19, which means larger sections are required in surrounding components and connections. Thus, the design of K_{SKID} should be considered a trade-off between the peak drift response (or the base shear of the PT part) and the base shear of the SKID part. Note that in Figures 5-18 and 5-19, the base shear is normalised by the total weight of the frame (M).

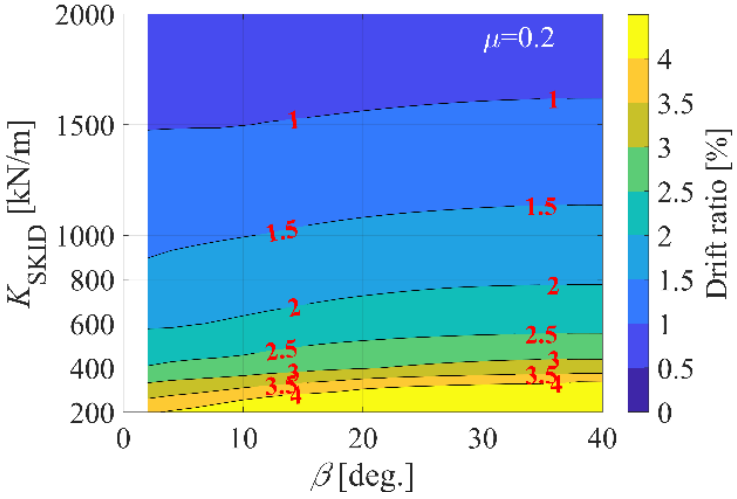

(a)

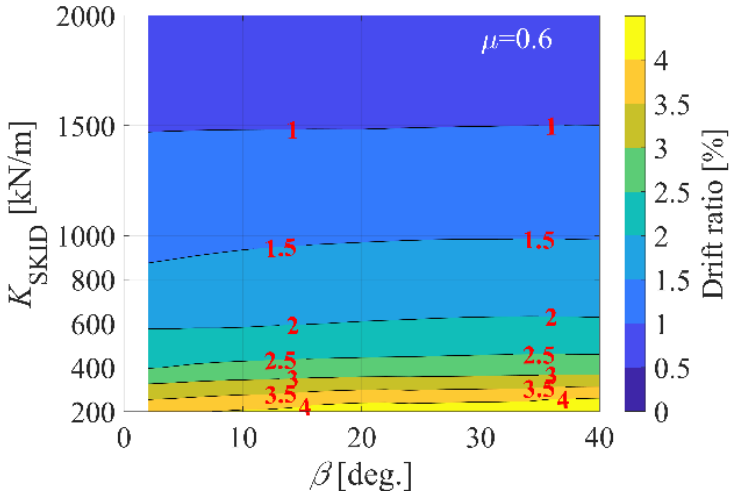

(b)

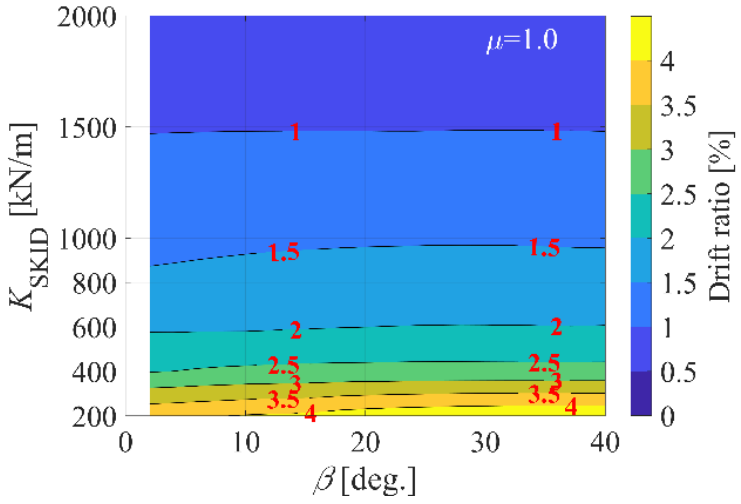

(c)

Figure 5-17 Peak drift ratios of the PT-SKID frames with different SKID parameters: (a) μ =0.2; (b) μ = 0.6; (c) μ =1.0.

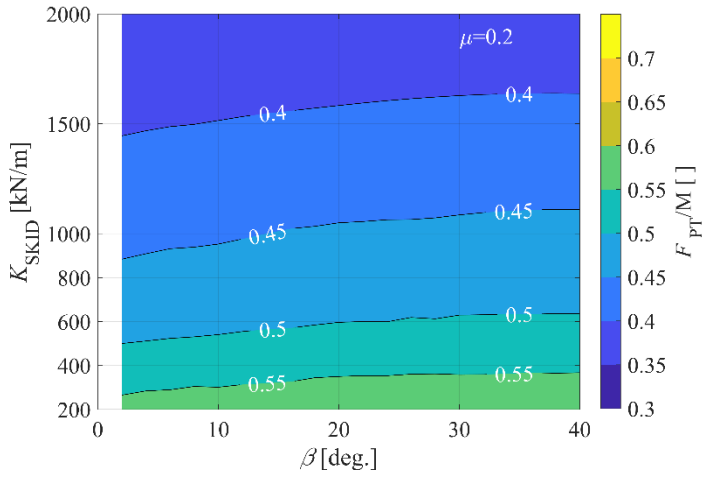

(a)

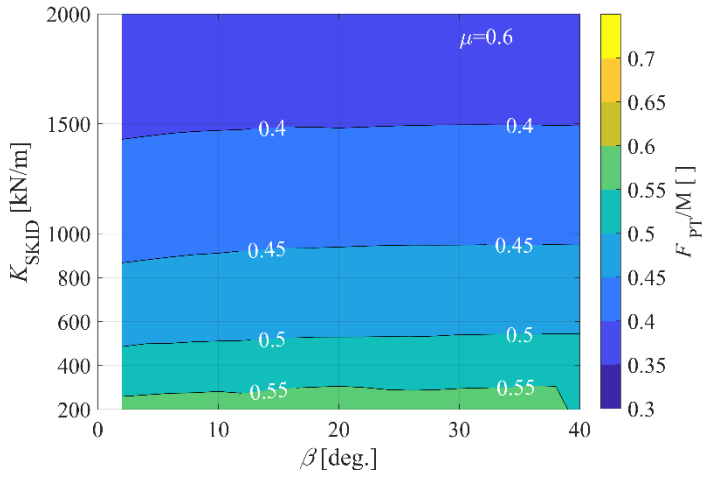

(b)

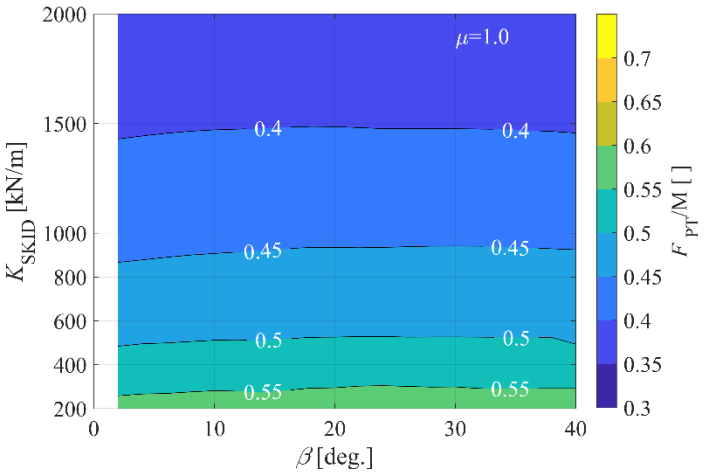

(c)

Figure 5-18 Peak base shears of the PT part of the PT-SKID frames with different SKID parameters: (a) μ =0.2; (b) μ =0.6; (c) μ =1.0.

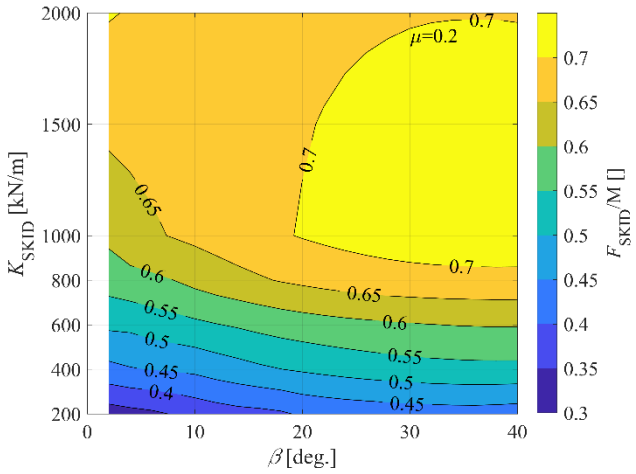

(a)

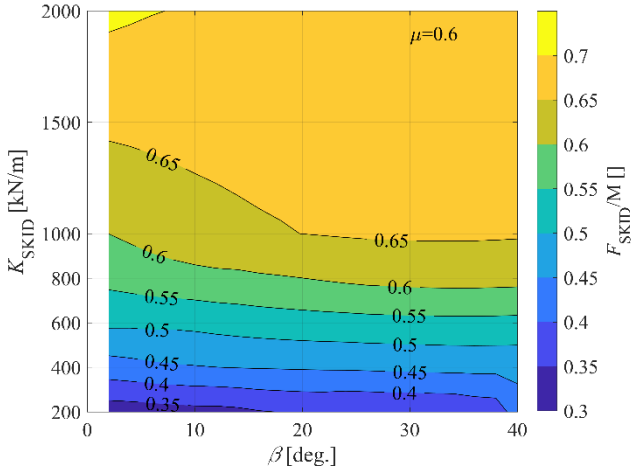

(b)

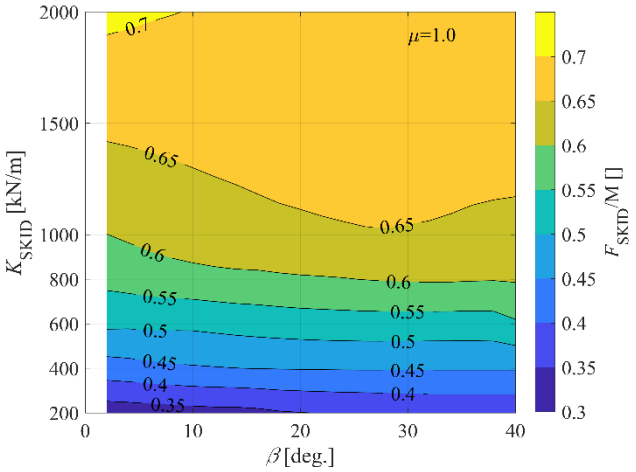

(c)

Figure 5-19 Peak base shears of the SKID part of the PT-SKID frames with different SKID parameters: (a) μ =0.2; (b) μ =0.6; (c) μ=1.0.

For the slope angle β, Figures 5-17 to 5-19 show that a small β leads to better seismic performance both in the drift ratio response and the base shear response (both the PT part and the SKID part). Additionally, the value of μ also makes a difference in the response. To make the comparison clearer, the response of the specimens with the same K_{SKID} of 600 kN/m but various μ and β are summarised in Figure 5-20. The figure indicates that improving the friction coefficient μ could reduce the earthquake response. Furthermore, a more obvious improvement is observed when the value of μ and β are low. The improvement in response control regarding β and μ coincides with their equivalent damping ratio calculated by Jacobson's method (Figure 5-16). Specifically, ζ_{eq} increases with smaller β and larger μ, but the trend becomes less evident around large β and μ.

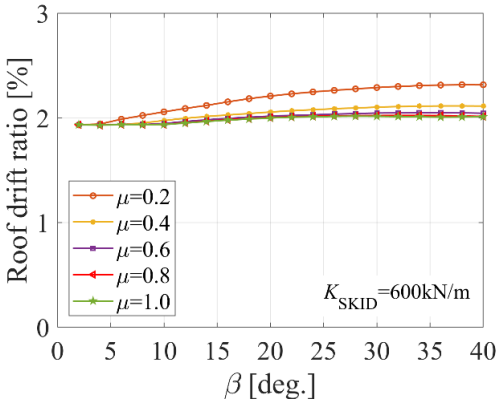

Figure 5-20 Peak drift ratio response of the PT-SKID frames with different μ and β.

The parameter analysis unveils a better dynamic control capability when large K_{SKID} and μ and small β are adopted in the SKID device. However, the response is more sensitive to the device loading stiffness K_{SKID}. This indicates that SKID should be produced with a discrete number of slope parameters (β and μ) for the market. A more restricted control target can be achieved by simply modularly using them in parallel in a PT-SKID frame.

5.5.4.3 The residual deformation of the PT-SKID frames

Conceptually, the self-centring frames can recentre after an earthquake because of their hysteretic curves in the first and third quadrants of the force-displacement space. Figure 5-21 shows the hysteretic response of a case PT-SKID frame subjected to Record 1-x. In this case, K_{SKID} was 800 kN/m, μ was 0.6, and β was 4°. As shown, for any response loop where the peak drift ratio was less than 1.8%, the hysteretic curve of the frame was entirely located at the first and third quadrants, indicating an inherent self-centring feature. Here, the drift ratio that guarantees a first and third quadrants hysteretic curve is termed a self-centring (quasi-static) threshold. In this case, some loops had a peak response over 1.8%, causing partially second or fourth quadrant hysteretic responses. In these over self-centring (quasi-static) threshold loops, the frame was conceptually not self-centring. In these loops, an external reactive force was required to make the frame recentre because the restoring force of the PT frame itself could not overcome the static friction force of the SKID device to trigger its sliding-down movement.

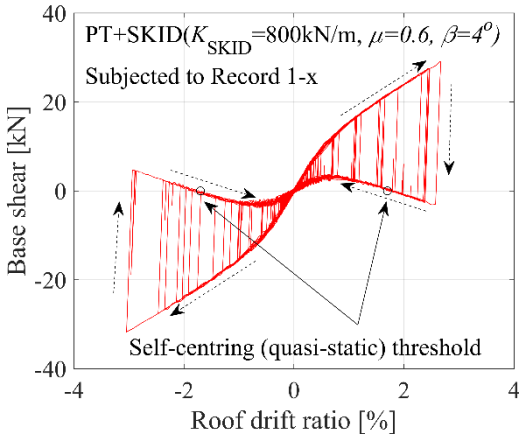

Figure 5-21 Hysteretic curves of the case model subjected to Record 1-x.

Free vibration response of the case PT-SKID frame is explored to help understand this self-centring mechanics. The free vibration was firstly activated by a small triangular pulse with a period of 0.12s and a peak at 3.0g (Excitation 1 in Figure 5-22(a)), and the corresponding response time history is shown in Figure 5-22(b). The initial drift ratio activated by the pulse was around 1% (which was less than its self-centring (quasi-static) threshold). The frame was damped to its

neutral position with a 0 drift ratio at 2.4s. Then, the acceleration of the pulse was scaled to 6.0g (Excitation 2) to make the initial drift ratio response exceed its self-centring (quasi-static) threshold (up to 2.2% in Figure 5-22(b)). The frame got stuck at the peak drift ratio after the excitation (0.1s to 5s in the figure) because the requirement of reactivating the sliding-down movement of the SKID device is greater than the maximum recovery force that the PT frame itself can provide. Finally, to demonstrate a successful reactive excitation to the frame, in Excitation 3, a reversal pulse with a peak at 2.0 g (1/3 scaled to the initial pulse)) was added after the initial excitation at 2s. This additional pulse successfully provided an inertial force for pushing the frame back into its self-centring (quasi-static) threshold, thus, the frame finally recentred at 5s.

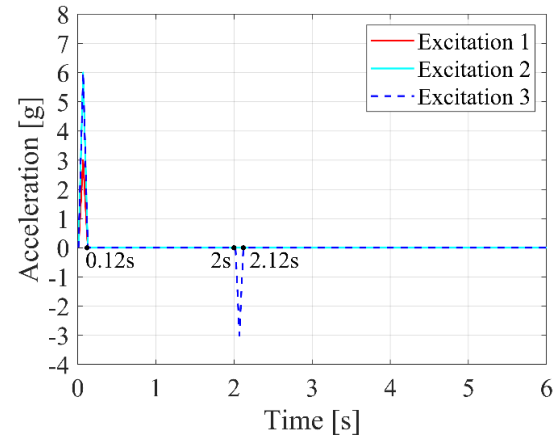

(a)

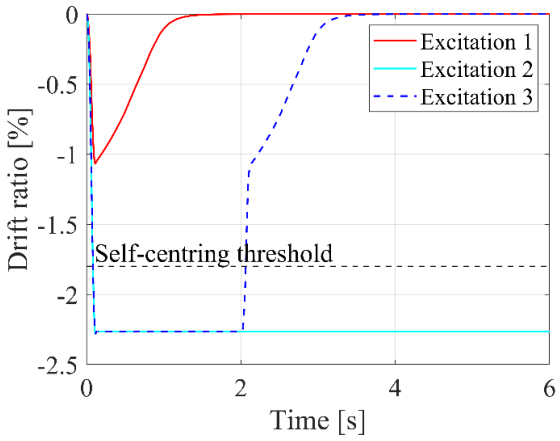

(b)

Figure 5-22 Free vibration of the case PT-SKID frame: (a) excitations; (b) drift ratio response.

Figure 5-23 shows the self-centring (quasi-static) thresholds of the PT-SKID frames tested in Section 5.5.4.2 in the form of a contour plot. Only the thresholds less than 5% are scaled in different colours, as a greater threshold exceeds the general drift ratio limit of preventing collapse. As shown in the figure, the threshold value (the self-centring-guaranteed peak drift ratio) is

reduced with an increasing K_{SKID} and μ, or a decreasing β. The cases where the peak drift ratio exceeds the self-centring (quasi-static) threshold in the tests are also dotted in Figure 5-23. In the figure, the red dots are the frames where the exceedance times over five in fourteen, and the white ones are those only exceeding the threshold once. It is clear that the frames with large K_{SKID} and μ or small β were easier to exceed the self-centring (quasi-static) threshold in earthquakes. In this research, 9800 cases in total (700 frames subjected to 14 ground motions) were conducted, and there were 869 cases where the transient peak drift ratio was over the self-centring (quasi-static) threshold. However, an ignorable residual drift ratio response of less than 0.1% was found in all cases (i.e., no case did not recentre). This is because the over-threshold peak response always happens before the end of the earthquake, and the following excitation of the earthquake itself actually could provide an activation force to make the frame recentre. These cases indicate that even if the peak drift ratio of PT-SKID frames exceeds their self-centring (quasi-static) thresholds, they still frequently recentre under the help of earthquakes themselves. Thus, the self-centring (quasi-static) threshold does not place a limitation on self-centring design. However, it needs further research on whether the earthquakes can always provide this sufficient reactivation excitation.

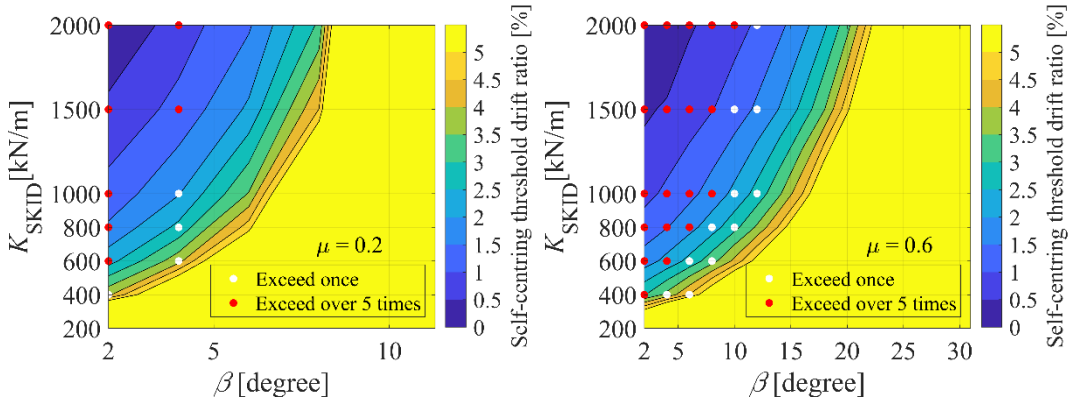

(a)

(b)

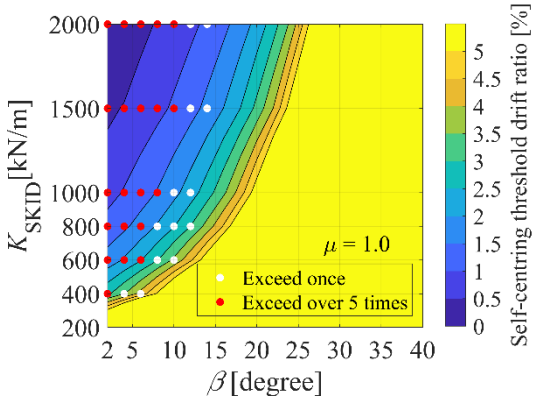

(c)

Figure 5-23 Values of self-centring threshold (in terms of drift ratio) of the PT frames with different SKID devices, and the cases where peak drift ratio exceeded the self-centring threshold in the tests: (a) μ =0.2; (b) μ =0.6; (c) μ =1.0.

5.6 Conclusion

This chapter presents an application of the SKID device in the PT frames. The PT-SKID frame performs a dual-triangular-flag-shaped hysteretic curve, indicating a full self-centring feature. The equations estimating the hysteretic curve of the PT-SKID frame are presented first. Then, three heuristic frames with and without the SKID device were designed and numerically tested as a proof-of-concept to investigate the benefits of the SKID device to the PT frame for resisting earthquake excitations. Both cyclic quasi-static analyses (which were benchmarked against experimental test results) and incremental dynamic analysis (IDA) using historically recorded ground motions were carried out. Finally, over seven hundred numerical models of PT-SKID frames were built and tested numerically in OpenSees to demonstrate the application of the SKID device in PT frames. The experimental results obtained in Chapter 4 are used to refine the finite element modelling of the SKID device in OpenSees. The dynamic characters of the PT-SKID frames and the influence of the SKID device on the seismic behaviours of PT-SKID frames were carefully analysed using sine-sweep excitations and earthquake ground motions, respectively. According to the theoretical and numerical works performed in this chapter, the following conclusions are drawn:

1. Analytical results indicate that the PT-SKID frame has a dual-triangular-flag-shaped hysteretic loop. According to the IDA analysis, the SKID device is demonstrated to act well at significantly reducing levels of drift in the system (PT frame and SKID device) considered. Hence, these devices are likely to produce a large reduction in structure/non-structural damage. Response base shear/acceleration levels are also reduced; however, this effect is more strongly influenced by the push-over characteristic of the PT frame. Analysis of estimated equivalent viscous damping ratios indicate that this system damping ratio (for PT frame and SKID device) is amplitude dependent, increasing with drift amplitude.

2. The FRFs obtained from the sin-sweep excitations indicate that the PT-SKID frames remain the typical dynamic characters of nonlinear systems, featuring two branches at higher and lower response levels with coexisting solutions. However, the improvement in post-opening joint stiffness and dissipation capability from the SKID devices considerably reduced the amplitude of responses and the range of the coexisting solutions. Specifically, the response amplitude was reduced with a greater K_{SKID} and μ but smaller β.

3. The seismic responses of the same PT frame equipped with different SKID devices indicate that large K_{SKID} and μ with a small β led to a small response amplitude. The trend regarding β and μ can be explained by their influence on the equivalent damping ratio calculated by Jacobson's method. However, blindly adjusting μ or β was less effective in tuning seismic response with respect K_{SKID}. This suggests designing and producing modular SKID products with specific slope parameters (μ and β) for the market. If needed, a higher K_{SKID} can be achieved by simply having more devices in parallel in a PT frame.

4. Although the transient response of over one in eleven cases surpassed their self-centring (quasi-static) threshold, all the cases recentred after earthquakes. This result indicates an excellent self-centring feature of the PT-SKID frames, and the self-centring (quasi-static) threshold does not place a limitation on self-centring design. The recentring for frames with small recentring threshold relies on a sufficient reactivation peak in the following excitations. The amplitude requirement of this 'following sufficient peak' and its existence in earthquakes need further investigation.

Chapter 6 The Direct Displacement-Based Design of the PT-SKID frame: the accuracy of the linear equivalence

6.1 Introduction

This chapter focuses on the linear equivalence of the PT-SKID system for the DDBD. The linear equivalence is employed for estimating the maximum displacement of the nonlinear system in earthquake events and is the fundamental principle of the DDBD. In this chapter, the linear equivalence of the PT-SKID frame is conducted using the effective stiffness and the equivalent damping ratio estimated by Jacobsen's method at the maximum response. First, a simplified model with five variables capturing hysteretic characters of the PT-SKID frame is proposed for more efficient analysis. The model is validated by the nonlinear analysis of a one-story one-bay case frame. Then, the accuracy of the linear equivalence in estimating the peak displacement response is evaluated. It is achieved by comparing the peak response displacement obtained from the nonlinear dynamic analysis on the PT-SKID hysteretic model with that estimated by the spectrum analysis on the equivalent linear system. A total of 5,880 PT-SKID hysteretic models covering the most common ranges of parameters are calibrated. Three types of earthquake records, i.e., far-field, near-field pulse-like, and near-field no-pulse, are used in the calibration. Finally, design suggestions are provided for the DDBD of the PT-SKID frames.

6.2. Simplified hysteretic model of the PT-SKID frames

6.2.1 The simplified hysteretic model

As discussed in Chapter 5, the total stiffness force of the PT-SKID frame, $F_{\text{PT-SKID}}$, is attributed to the sum of the restoring force, F_{PT}, and the damping force, F_{SKID}, which are provided by the PT frame part and the SKID device part, respectively, and is expressed as follows

$$F_{\text{PT-SKID}}=F_{\text{PT}}+F_{\text{SKID}} \tag{6-1}$$

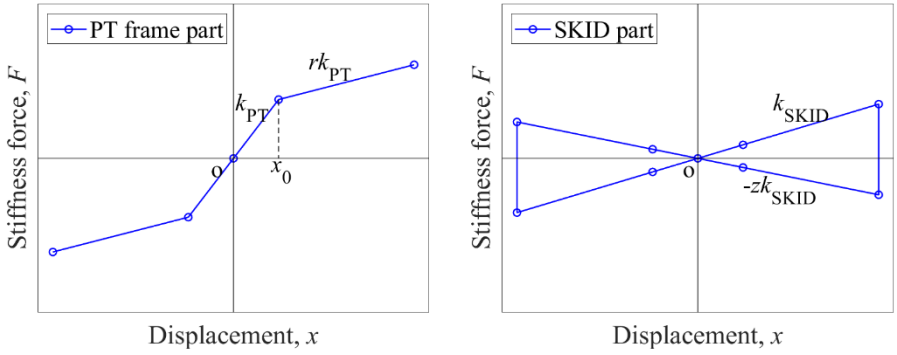

(a) (b)

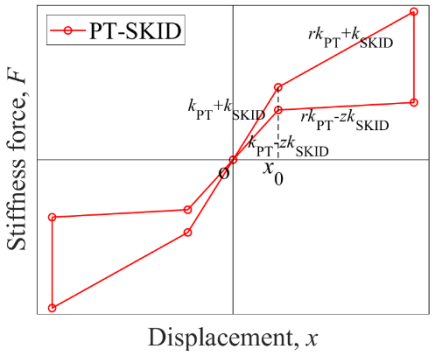

(c)

Figure 6-1 Definition of the simplified hysteretic model in (a) the PT frame part, (b) the SKID device part, and (c) the PT-SKID frame.

For the sake of simplification, the hysteretic behaviour of the PT frame part is represented by a bilinear model featured by its initial stiffness k_{PT} and stiffness ratio r, as shown in Figure 6-1 (a). Thus, the force-deflection function for the PT frame part is defined as follows

$$F_{PT,norm}=\begin{Bmatrix} x_{norm} & : & |x_{norm}|\leq 1 \\ rx_{norm}+(1-r) & : & x_{norm}>1 \\ rx_{norm}-(1-r) & : & x_{norm}<-1 \end{Bmatrix} \tag{6-2}$$

where x_{norm} is the normalised displacement which is defined by the ratio between the displacement (x) and the gap opening displacement ('pseudo-yield' displacement, x_0) as follows

$$x_{norm}=\frac{x}{x_0} \tag{6-3}$$

and $F_{PT,\,norm}$ is the shear force of the PT frame part (F_{PT}) normalised by the gap opening force ($F_{PT,\,gap\ opening}$) as follows

$$F_{\mathrm{PT,norm}}=\frac{F_{\mathrm{PT}}}{F_{\mathrm{PT,\ gap\ opening}}}=\frac{F_{\mathrm{PT}}}{k_{\mathrm{PT}}x_0} \tag{6-4}$$

The force-deflection function of the SKID device is defined as follows

$$F_{\mathrm{SKID,norm}}=\alpha\begin{Bmatrix} x_{\mathrm{norm}} & : & \dot{x}_{\mathrm{norm}}>0,\ x_{\mathrm{norm}}>0 \\ zx_{\mathrm{norm}} & : & \dot{x}_{\mathrm{norm}}<0,\ x_{\mathrm{norm}}>0 \\ x_{\mathrm{norm}} & : & \dot{x}_{\mathrm{norm}}<0,\ x_{\mathrm{norm}}<0 \\ zx_{\mathrm{norm}} & : & \dot{x}_{\mathrm{norm}}>0,\ x_{\mathrm{norm}}<0 \end{Bmatrix} \tag{6-5}$$

where

$$F_{\mathrm{SKID,norm}}=\frac{F_{\mathrm{SKID}}}{F_{\mathrm{PT,\ gap\ opening}}}=\frac{F_{\mathrm{SKID}}}{k_{\mathrm{PT}}x_0} \tag{6-6}$$

and

$$\alpha=\frac{k_{\mathrm{SKID}}}{k_{\mathrm{PT}}} \tag{6-7}$$

and z is the stiffness ratio between the unloading and the loading stiffness of the SKID device. The hysteretic curve captured by Eq. (6-5) is shown in Figure 6-1 (b).

To aid numerical stability, the Heaviside formulation is introduced into Eq. (6-2) and Eq. (6-5) to transform the piecewise functions to smooth approximation. Thus, Eq. (6-2) is re-expressed as follows

$$F_{\mathrm{PT,norm}}=x_{\mathrm{norm}}\,\mathrm{H}(1-|x_{\mathrm{norm}}|)+\left(rx_{\mathrm{norm}}+(1-r)\right)\mathrm{H}(x_{\mathrm{norm}}-1)+\left(rx_{\mathrm{norm}}-(1-r)\right)\mathrm{H}(-1-x_{\mathrm{norm}}) \tag{6-8}$$

where

$$\mathrm{H}(x_{\mathrm{norm}})\approx\frac{1}{2}+\frac{1}{2}\tanh(\lambda x_{\mathrm{norm}}) \tag{6-9}$$

λ controls the corner sharpness of the curve of $\mathrm{H}(x_{\mathrm{norm}})$. The accuracy of this estimation (Eq. 6-9) increases with λ.

Similarly, Eq. (6-5) is re-expressed in terms of the Heaviside function as follows

$$F_{\text{SKID,norm}}=\alpha\{\mathrm{H}(\dot{x}_{\text{norm}}x_{\text{norm}})-z\mathrm{H}(-\dot{x}_{\text{norm}}x_{\text{norm}})\}x_{\text{norm}} \tag{6-10}$$

Thus, the non-dimensional total stiffness force-deflection relationship of the PT-SKID frames is defined as follows

$$F_{\text{PT-SKID,norm}}(x_{\text{norm}},\dot{x}_{\text{norm}})=\left\{\begin{array}{c} x_{\text{norm}}\,\mathrm{H}(1-|x_{\text{norm}}|)+\big(rx_{\text{norm}}+(1-r)\big)\,\mathrm{H}(x_{\text{norm}}-1)+\dots \\ +\big(rx_{\text{norm}}-(1-r)\big)\,\mathrm{H}(-1-x_{\text{norm}})+\alpha\{\mathrm{H}(\dot{x}_{\text{norm}}x_{\text{norm}})-z\mathrm{H}(-\dot{x}_{\text{norm}}x_{\text{norm}})\}x_{\text{norm}} \end{array}\right\} \tag{6-11}$$

The hysteretic curve of the PT-SKID frame represented by Eq. (6-11) is shown in Figure 6-1 (c).

6.2.2 Validation of the simplified hysteretic model

The simplified hysteretic model is benchmarked by a one-story one-bay PT-SKID case frame. The PT frame is the same one used in Section 5.5. It is assumed to be located in L'Aquila, Italy and designed based on EC 8 (ECN 2004). The SKID device has a slope angle of 4° and a friction coefficient of 0.4 (steel against brake lining (Bremskerl 2021)). The section of the cantilever bars of the SKID device is 100x20 mm^2, and the length is 225 mm.

The numerical model shown in Figure 5-10 was used in analysis. The simplified hysteretic model of the PT-SKID frame was calibrated in Matlab. The parameters of the simplified model characterising the hysteretic properties of the case frame are summarised in Table 6-1. The OpenSees model and the simplified hysteretic model were subjected to the same ground motion time history. The information on the ground motions are summarised in Table 6-2. The seismic response of the simplified hysteretic model is obtained by solving the equation of the motion of the single degree of freedom oscillator expressed as follows

$$m\ddot{x}+c\dot{x}+F_{\text{PT-SKID}}(x,\dot{x})=-m\ddot{x}_{\text{g}} \tag{6-12}$$

Which, for the structural system at hand, can be re-expressed as follows

$$\ddot{x}_{\text{norm}}+2\xi_0\omega\dot{x}_{\text{norm}}+\frac{\omega^2}{1+\alpha}F_{\text{PT-SKID,norm}}(x_{\text{norm}},\dot{x}_{\text{norm}}:r,\alpha,z)=-\frac{\ddot{x}_{\text{g}}}{x_0} \tag{6-13}$$

where

$$\xi_0=\frac{c}{2m\omega},\quad \omega^2=\frac{k_{\text{PT}}(1+\alpha)}{m} \tag{6-14}$$

Table 6-1 Parameters of the simplified hysteretic model of the case frame.

k_{PT} (kN/m)	r	x_0 (mm)	α	z
1893.862	0.055	3.2	0.15	0.665

Table 6-2 Information of the ground motion.

Earthquake Event	Station ID	Magnitude (Richter scale)	EC8 Soil Class	PGA (g)
Erzincan (1992)	Erzincan	6.6	B	0.51

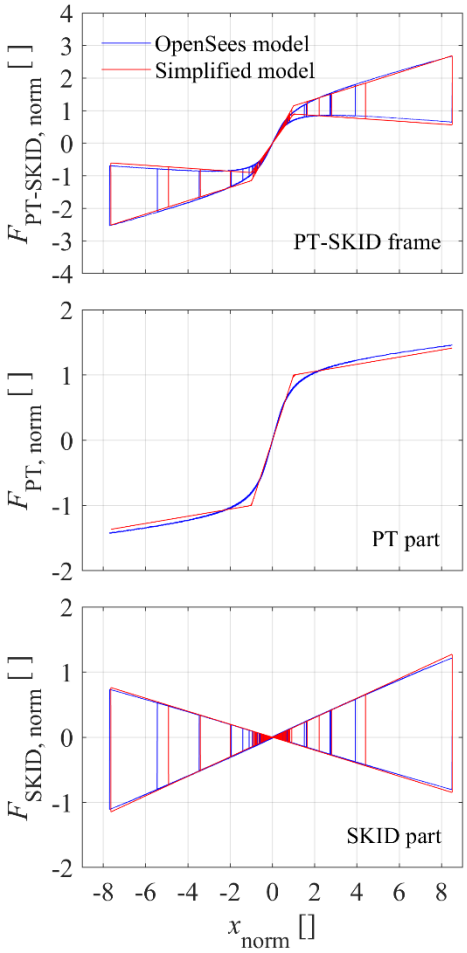

Figure 6-2 Hysteretic response of the case PT-SKID frame obtained from its OpenSees model and its simplified model.

Figure 6-2 presents the seismic hysteretic responses obtained from two models. The response obtained from the simplified hysteretic model matches well with that obtained from the OpenSees model in both stiffness and displacement. It indicates a good approximation of the simplified hysteretic model. It is worth noting that all the structural elements of the PT-SKID frame are

expected to stay elastic in design-level earthquakes to achieve self-centring. The proposed hysteretic model is intended to represent the hysteretic behaviour of this system before any failure occurs. Using this non-damage model for DDBD is reasonable, as DDBD primarily focuses on the system's behaviour at the design-level earthquakes. In earthquakes exceeding the design intensities, failures are expected to develop in certain elements of the PT-SKID frame; thus, a hysteretic model capable of capturing these failure behaviours is required. However, this exceeds the scope of this research.

6.3. Displacement estimation accuracy of the linear equivalence using Jacobsen's method

6.3.1 Evaluation procedure for the accuracy of the equivalent linear system

In the Direct Displacement-Based Design, the dynamic response of a nonlinear system is estimated by an equivalent linear system (the substitute structure) featured by effective mass (m_e), effective stiffness (k_e), and estimated equivalent damping (ζ_{eq}). In this paper, the effective mass is defined by the total seismic mass, and the equivalent stiffness is the secant stiffness at the peak displacement of the nonlinear system (Blandon and Priestley, 2005; Shibata et al., 1976). The hysteretic component of the equivalent damping ratio is estimated by Jacobsen's method (Jacobsen, 1960).

Jacobsen's estimation is based on the assumptions of (1) nonlinear and equivalent linear systems subjected to harmonic excitations and (2) peak response occurring exactly at the resonance steady state. However, these assumptions cannot be met for real earthquake ground motions (Blandon and Priestley, 2005). Thus, an unknown error is involved in displacement estimation. In this section, the error is identified by the ratio between the nonlinear displacement response of the PT-SKID hysteretic model and the estimated displacement of its linear counterpart. Because the PT-SKID frame aims to achieve self-centring after earthquakes, which requires no damage to all the structural components, the frames tested in the paper are assumed to have (1) no damage in structural components; and (2) non-structural components not interfering with the structural response. Figure 6-3 shows the accuracy evaluation procedure adopted in this research.

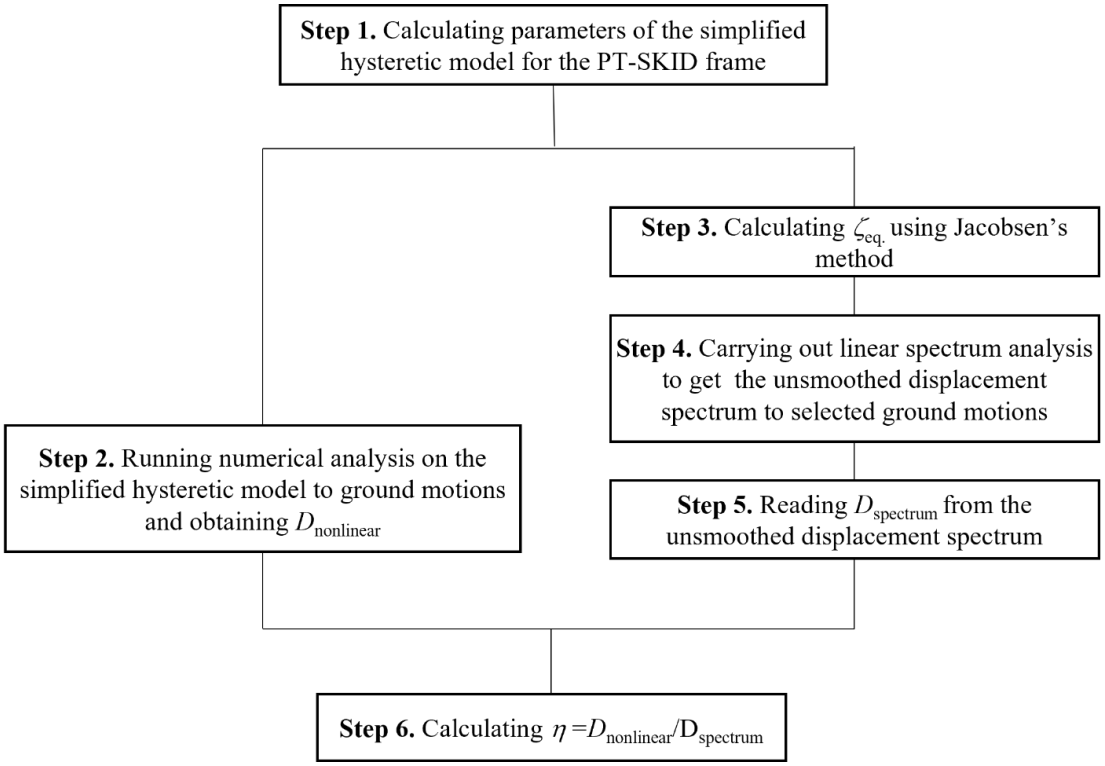

Figure 6-3 Procedure for the evaluation of Jacobsen's method accuracy.

Step 1: Computation of the parameters of the simplified hysteretic model proposed in Section 6.2 for the PT-SKID frame. A total of 5,880 PT-SKID models were tested in this study; more details about them will be discussed in Section 6.3.2.

Step 2: Calculation of the peak displacement response of the nonlinear hysteretic model, $D_{nonlinear}$, for each of the selected ground motions from nonlinear numerical analysis. In this study, the ground motions suggested by FEMA P695 are used. More details on the ground motions will be presented in Section 6.3.3. The nonlinear response is obtained by solving the equation of motion expressed by Eq. (6-13) in Matlab.

Step 3: Estimation of the equivalent damping ratio of the PT-SKID frame. The equivalent damping ratio involves the hysteretic component ($\zeta_{eq,\ hyst}$), and the elastic viscous damping component ($\zeta_{eq,\ 0}$). The hysteretic component is estimated by the area-based approach proposed by Jacobsen (Jecobsen 1960):

$$\xi_{eq,\ hyst,\ PT\text{-}SKID} = \frac{S1}{4\pi\, S2} \tag{15}$$

where $S1$ and $S2$ correspond to the areas illustrated in Figure 6-4. In this study, the elastic viscous damping component is specified as zero for both the nonlinear system and its linear equivalence

to eliminate the possible error introduced from this source, as suggested in Blandon and Priestley (2005).

Step 4: Computation of the unsmoothed displacement spectrum of the equivalent linear system to selected ground motions. The displacement response spectrum is obtained by carrying out linear spectrum analysis at considered equivalent damping for each of the selected ground motions.

Step 5: Assessment of the estimated peak displacement ($D_{spectrum}$) from the displacement spectrum. The effective period required in this step is calculated by :

$$T_e = \left(\frac{4\pi^2 m_e}{k_e}\right)^{0.5} \tag{16}$$

Step 6: Assessment of the displacement ratio between the nonlinear and the spectrum response, $\eta = D_{nonlinear}/D_{spectrum}$.

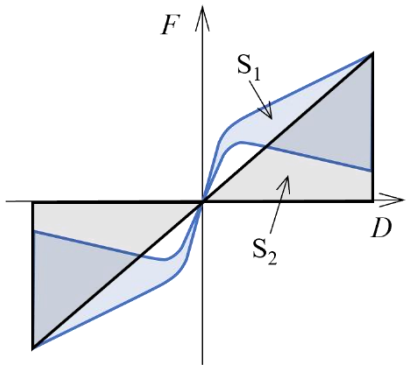

Figure 6-4 Hysteretic areas employed for the calculation of the equivalent damping ratio.

6.3.2 Considered PT-SKID frames

As presented in Section 6.2.1, the hysteretic properties of the PT-SKID frame are characterised by five variables in the simplified hysteretic model: (1) the initial lateral stiffness of the PT frame (k_{PT}), (2) the gap-opening displacement (x_0), (3) the stiffness ratio of the PT frame (r), (4) the ratio between the SKID stiffness and the PT frame initial stiffness (α), and (5) the stiffness ratio between the unloading and the loading stiffness of the SKID device (z). To be consistent with the DDBD procedure, these five variables are converted into an alternative set: effective period, T_e, ductility level, μ, PT stiffness ratio, r, effective stiffness ratio, κ, and equivalent damping ratio of PT-SKID frame, $\zeta_{eq,\ hyst,\ PT\text{-}SKID}$. Here, the effective period, T_e, is defined by Eq. (6-16), and k_e is defined as follows:

$$k_e = \frac{1-r+\mu r+\mu\alpha}{\mu} k_{PT} \tag{6-17}$$

The ductility level μ, is defined as

$$\mu = \frac{x_{peak}}{x_0} \tag{6-18}$$

where x_{peak} is the peak displacement. The effective stiffness ratio (κ), is defined as the ratio between the SKID stiffness and the effective stiffness of the PT part, and is calculated as follows:

$$\kappa = \frac{1}{r\left(1-\frac{1}{\mu}\right)+\frac{1}{\mu}}\alpha \tag{6-19}$$

The equivalent damping ratio of PT-SKID frame, $\zeta_{eq,\ hyst,\ PT\text{-}SKID}$, defined by Eq. (15) can be expressed by the equivalent damping ratio of the SKID device, $\zeta_{eq,\ hyst,\ SKID}$, as follows:

$$\xi_{eq,\ hyst,\ PTSKID} = \frac{1}{1+\frac{1}{\kappa}} \xi_{eq,\ hyst,SKID} \tag{6-20}$$

where $\xi_{eq,hyst,SKID}$ is calculated by Jacobsen's method. The derivation of Eq. (6-20) is presented as follows.

The hysteretic behaviour of the PT-SKID frame is the combination of its PT frame part and the SKID device part. The base shear - drift ratio relationship of a single DOF PT-SKID frame can be expressed as:

$$F_{PT\text{-}SKID}(\theta,\dot{\theta}) = F_{PT}(\theta) + F_{SKID}(\theta,\dot{\theta}) \tag{6-21}$$

where θ is the roof drift ratio and assumed to be equal to the joint rotations at the beam-column and the column-foundation joints, as the discrepancies induced by the geometric second-order effect are ignorable for simplicity. According to Eq. (6-15), the hysteretic component of equivalent damping ratio of the PT-SKID frame is:

$$\xi_{eq.,\ hyst.,\ PT\text{-}SKID} = \frac{F_{PT\text{-}SKID}(\theta,\dot{\theta}>0) - F_{PT\text{-}SKID}(\theta,\dot{\theta}<0)}{4\pi F_{PT+SKID}(\theta,\dot{\theta}>0)} \tag{6-22}$$

By substituting Eq. (6-21) into Eq. (6-22), the following expression is obtained:

$$\xi_{\text{eq., hyst., PT-SKID}}=\frac{F_{\text{SKID}}(\theta,\dot{\theta}>0)-F_{\text{SKID}}(\theta,\dot{\theta}<0)}{4\pi(F_{\text{PT}}(\theta)+F_{\text{SKID}}(\theta,\dot{\theta}>0))} \tag{6-23}$$

As the definition of κ can be expressed as

$$\kappa=\frac{F_{\text{SKID}}(\theta,\dot{\theta}>0)}{F_{\text{PT}}(\theta)} \tag{6-24}$$

By substituting Eq. (6-24) into Eq. (6-23), the following expression is obtained

$$\xi_{\text{eq., hyst., PT-SKID}}=\frac{1}{1+\frac{1}{\kappa}}\frac{F_{\text{SKID}}(\theta,\dot{\theta}>0)-F_{\text{SKID}}(\theta,\dot{\theta}<0)}{4\pi F_{\text{SKID}}(\theta,\dot{\theta}>0)}=\frac{1}{1+\frac{1}{\kappa}}\xi_{\text{eq., hyst., SKID}} \tag{6-25}$$

where $\zeta_{\text{eq., hyst.,SKID}}$ is the hysteretic component of equivalent damping ratio of the SKID device.

In this study, 5880 hysteretic models covering the most common ranges of parameters are tested. Specifically, μ ranges from 2.0 to 6.0 with an increment of 1.0; κ ranges from 0.4 to 1.0 with an increment of 0.1; r ranges from 0.05 to 0.30 with an increment of 0.05. The models are classified into (i) mid- to long-period frames, consisting of 3780 models, with a T_e between 0.6s and 4.0s with an increment of 0.2s, and (ii) short-period frames, consisting of 2100 models, with T_e between 0.1s to 0.6s with an increment of 0.05s. The equivalent damping ratio of the SKID device is fixed at 26.5%, which is obtained by the physical tests presented in Chapter 4. As indicated by Eq. (6-20), the hysteretic component of the equivalent damping ratio is only affected by κ when $\zeta_{\text{eq, hyst, SKID}}$ is fixed. The equivalent damping ratio of the cases considered in this study ranges between 7.57% and 13.25%. Note that the PT-SKID hysteretic model defined by any set of these variables is irrelevant to any specific k_{PT} and m_e. It represents a group of PT-SKID frames with different configurations.

6.3.3 The earthquake records

Both the far-field records and near-field records defined in FEMA P695 are considered in this research. The far-field records set includes 22 pairs of strong ground motions. The near-field records are categorised into the pulse-like set and the no-pulse set, with 14 pairs each. All the records are 'normalised' by their respective peak ground velocities to eliminate overall record-to-record variability due to inherent differences in event magnitude, distance to source, source type

and site conditions (Applied Technology Council, 2009). The 'normalisation' reduces the dispersion in PGV without significantly affecting the average values of PGA of the record sets. More details can be found in the Applied Technology Council (2009). Figure 6-5 presents their average acceleration spectra and unsmoothed average displacement spectra.

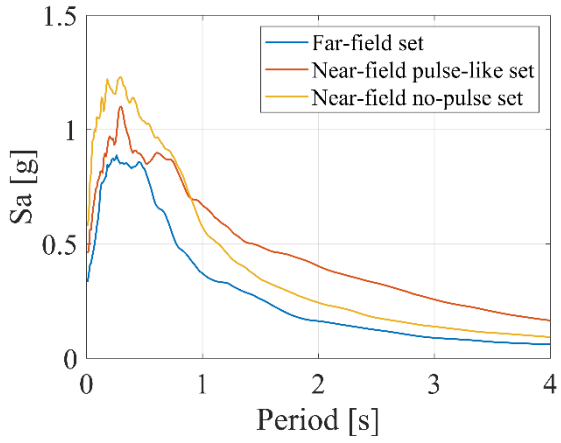

(a)

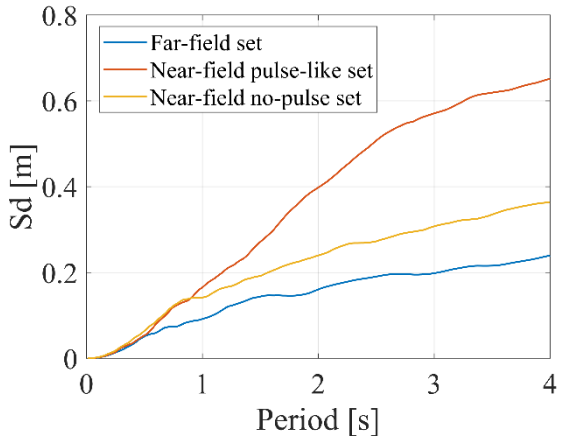

(b)

Figure 6-5 Average response spectra of each set of ground motions: (a) acceleration spectra; and (b) displacement response spectra.

6.3.4 The evaluation results of the mid- to long-period frames

First, the displacement ratio, η, of the mid- to long-period frames to each far-field ground motion is calculated by carrying out the procedure shown in Figure 6-3. As mentioned in Section 6.3.3, the hysteresis of the PT-SKID frame is controlled by five variables. To rank the contributions of variables to the variance of η, a variance-based global sensitivity analysis was carried out. The Matlab toolbox SAFE (Sensitivity Analysis For Everyone) (Pianosi et al., 2015) based on Sobol method (Solbol, 2001) was utilized. A uniform distribution in the range of each variable was

applied. The first-order effects (i.e., the main effects) of four variables (T_e, μ, r, κ) are shown in Table 6-3 (note that the $\zeta_{eq,\ hyst,\ SKID}$ is fixed in this study). A greater first-order effect indicates a great contribute to the variance of output (i.e., the variance of η in this study). According to the table, the effective stiffness ratio, κ, and the effective period, T_e, are identified as the most sensitive parameters because they have much higher first-order effects than the others. A visualized evidence is presented in Figure 6-6 (a), (b), and (c) in the form of contour plots, which shows η for the variable spaces of T_e and κ, T_e and μ, and T_e and r, with fixed values for the other two in each figure, respectively. It is obvious that η changes with T_e and κ, but is much less disturbed by μ and r in the considered ranges.

Table 6-3 The first-order effects of variables.

		T_e	r	μ	κ
Mid- to large-period frames	Far-field	0.13	0.03	0.01	0.26
Mid- to large-period frames	Near-field no-pulse	0.10	0.04	0.01	0.28
Mid- to large-period frames	Near-field pulse-like	0.12	0.11	0.01	0.31
Short-period frames	Far-field	0.16	0.15	0.01	0.46

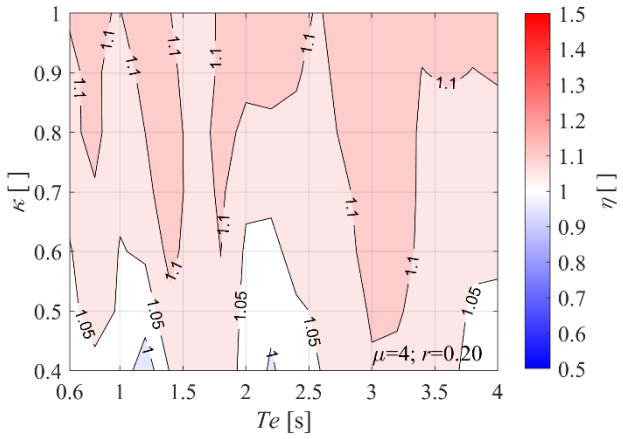

(a)

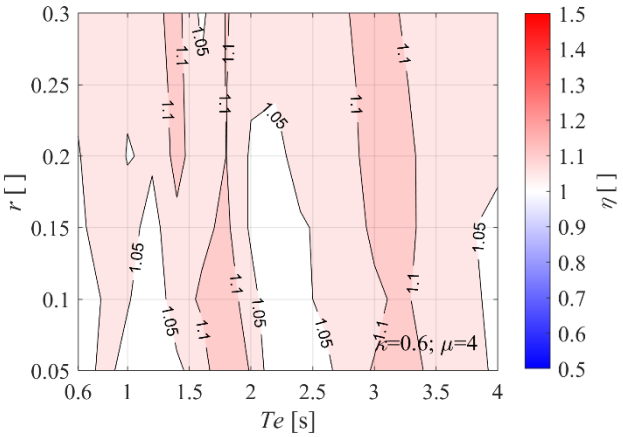

(b)

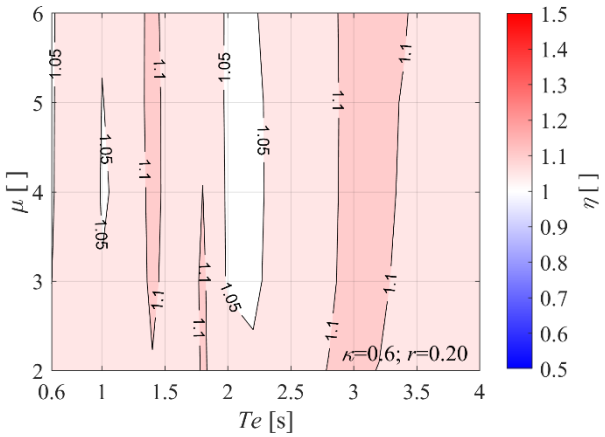

(c)

Figure 6-6. η value at the variable space of: (a) T_e and κ (μ=4, r=0.2), (b) T_e and μ (κ=0.6, μ=4), and (c) T_e and r (κ=0.6, r=0.2).

The results of global sensitivity analysis provide evidence for reducing the number of influential variables to η from four to two. The average displacement ratio, η_{ave}, for the domain T_e - κ are calculated and shown in Figure 6-7 (a). As shown, η_{ave} is greater than 1 for almost all the possible cases with an upper boundary of 1.15. Also, it can be observed that the error increases with κ. The variation trend of η_{ave} is less clear with T_e. The figure indicates that the linear equivalence based on Jacobsen's estimation always underestimates the seismic displacement response, leading to an unconservative design in the DDBD. Figure 6-7 (b) shows the C.O.V. of η_{ave} among the cases engaged in the average calculation. The C.O.V. is less than 3% for the most of cases.

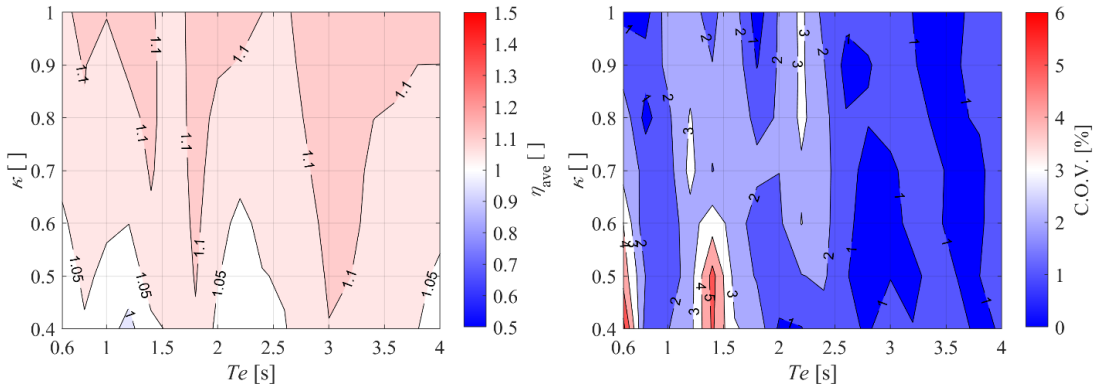

(a) (b)

Figure 6-7 η_{ave} of the cases with different μ or r: (a) η_{ave} value at the space of T_e and κ, and (b) the C.O.V. among the cases involved in the average calculation.

Similar results were observed in the cases subjected to near-field no-pulse records. As shown in Table 6-3, the effective period, T_e, and the effective stiffness ratio, κ, mainly contribute to the variation of η_{ave}, as the same results under the far-field records. Figure 6-8 shows η_{ave} of the cases with the same T_e and κ under the near-field no-pulse records. The trends of the variation of η_{ave} on T_e and κ are the same as those under the far-field records. In addition, η_{ave} at the same T_e and κ is not affected by the ground motion category of far-field or near-field no-pulse in general.

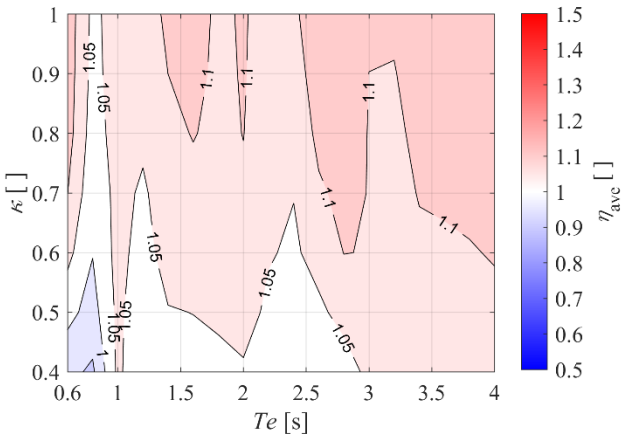

Figure 6-8 η_{ave} at the variables space of T_e and κ for the near-field no-pulse ground motions

According to the first-order index shown in Table 6-3, under the near-field pulse-like records, the PT stiffness ratio, r, also contributes to the variation of the displacement ratio, η. Only the effect of the ductility level, μ, can be ignored. Thus, the average displacement ratio, η_{ave}, is calculated among the ductility level, μ, only. Figure 6-9 shows η_{ave} at different T_e, κ, and r under the near-field pulse-like records. As shown, although η_{ave} is greater than 1 at most cases, it can be less than 1 when κ, r, and T_e are small. Compared with η_{ave} under far-field or near-field no-pulse records, η_{ave} under near-field pulse-like records shows a larger scatter to the variable T_e, κ, and r. Given that the upper boundary of η_{ave} is around 1.25, the effectiveness of the equivalence is deemed acceptable. In general, η_{ave} is greater with κ and r. The trends of the variation of η_{ave} on T_e is not clear.

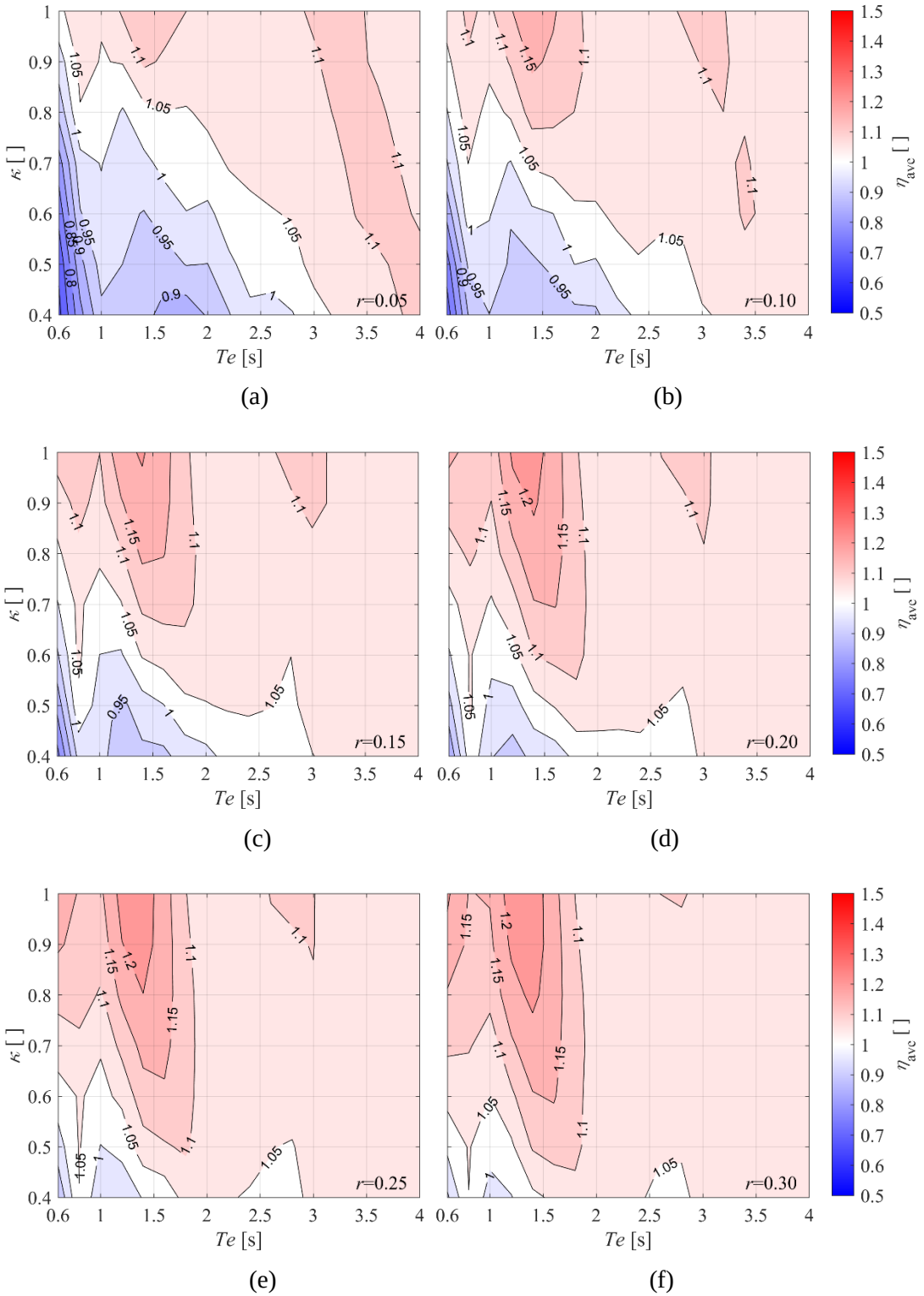

Figure 6-9 η_{ave} at the variables space of T_e and κ for the near-field pulse-like ground motions: (a) r=0.05; (b) r=0.10; (c) r=0.15; (d) r=0.20; (e) r=0.25; (f) r=0.30.

6.3.5 The evaluation results of short-period frames

The displacement estimation accuracy of the equivalence for the short-period PT-SKID frames is discussed in this section. Only far-field ground motions are considered. The first-order index of the variables to the variation of η is shown in Table 6-3. The effective period, T_e, is the most sensitive variable, followed by the PT stiffness ratio, r, and the effective stiffness ratio κ. The contribution of the ductility level μ can be ignored. Thus, the average displacement ratio, η_{ave}, among the ductility level are calculated and plotted in the space of T_e and κ in Figures 6-10 (a) to (d) (only r equal to 0.05, 0.15, 0.20 or 0.30 are used).

As shown in Figures 6-10 (a) to (c), η_{ave} increases with larger κ and r but smaller T_e. For large κ and r, η_{ave} is greater than 1, but when κ and r are small, the ratio can become smaller than 1. It is worth noting that η_{ave} can be high (greater than 1.5) when the frame has a small T_e with a large κ and r, indicating a significant error in the estimation. Thus, the effectiveness of the equivalence used in this paper for the short-period PT-SKID frames is questioned and requires further research.

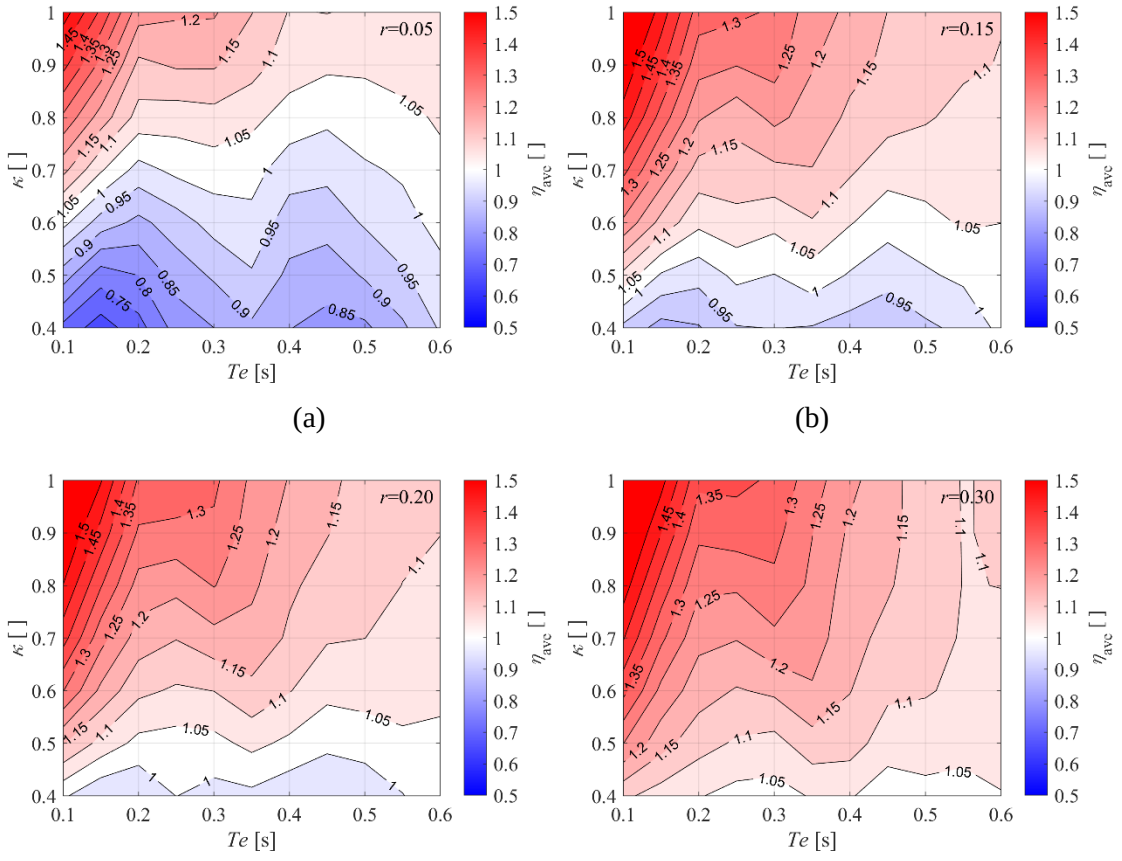

Figure 6-10 η_{ave} at the variables space of T_e and κ for: (a) r = 0.05; (b) r = 0.15; (c) r = 0.20; and (d) r = 0.30.

6.4. Suggestions for the Direct Displacement-Based Design (DDBD) of the mid- to long-period PT-SKID frames

6.4.1 Correction in the estimated displacement

The accuracy of the peak displacement estimation of the linear equivalence determines the effectiveness of the DDBD. As shown in Figures 6-7, 6-8 and 6-9, the equivalent linear system based on Jacobsen's method frequently leads to a smaller displacement response estimation ($D_{spectrum}$) for the mid- to long-period PT-SKID frames, which will lead to an unconservative design. The difference between $D_{nonlinear}$ and $D_{spectrum}$ indicates a failure in constructing an effective equivalent system (which should make $D_{nonlinear}$ the same as $D_{spectrum}$). Thus, a correction in $\zeta_{eq,\,hyst}$ or T_e is required for a more effective equivalence. Alternatively, a correction factor in the estimated displacement ($D_{spectrum}$) can be made and it is the ratio of $D_{nonlinear}$ to $D_{spectrum}$ at the corresponding group of parameters. As concluded in Section 6.3.4, for the sites where far-field or near-field no-pulse ground motions are considered, the accuracy of the linearisation is mainly affected by the effective stiffness ratio, κ, and effective period, T_e. Thus, these two parameters should be involved into the calculation of the correction factor. However, T_e is decided to be not involved as a variable in the correction factor because: (1) a correction factor involving T_e will lead to an iteration design in DDBD; (2) the actual effective stiffness of a structure is easy to be different with the design stiffness; (3) the influence of T_e is irregular. To consider the variation of η in T_e, a value of η with a 95% confidence at each κ is calculated. Figure 6-11 shows the estimated probability density functions (PDF) and the cumulative distribution functions (CDF) (Cao, 2010) of η at each κ under far-field ground motions as an example. Then, a polynomial correction factor function, $C_e(\kappa)$, is proposed by fitting the correction factor against the η values corresponding to a 95% confidence level at each κ for far-field or near-field no-pulse ground motions (please see Eq. (6-26 (a) and (b)), respectively. The least squares method is used for the fitting. C_e calculated by Eq. (6-26 (a) and (b)) at different κ are shown in Figure 6-12 (a) and (b) with η having a 95% confidence level. According to the figure, C_e increases with κ and ranges from 1.08 and 1.16. For the sites where near-field pulse-like ground motions are considered, the PT stiffness ratio, r, is involved into the determination of correction factor (C_e). The correction factor function $C_e(\kappa, r)$ has a cubic polynomial form (see Eq. (6-26 (c)). Figure 6-12 (c) shows C_e calculated by Eq. (6-26 (c)) and the η values corresponding to a 95% confidence level at each κ and r (the circles in the figure). As shown, the agreement is satisfactory. It is worth noting that the correction method presented in this section is proposed for applying to the mid- to long-period PT-SKID frames. For the frames with a short period, further investigation is required for a more effective linear equivalence.

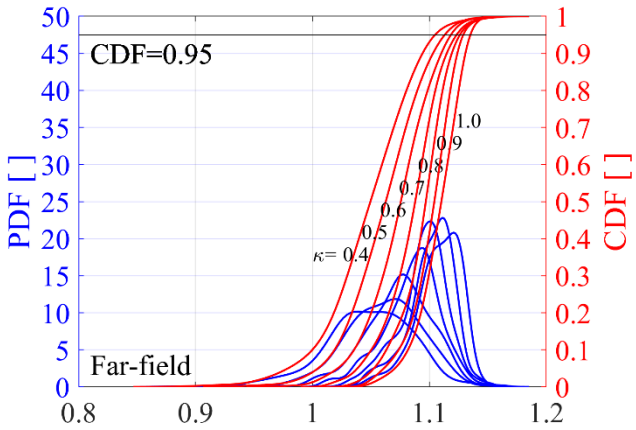

Figure 6-11 Estimated probability density functions (PDF) and the cumulative distribution functions (CDF) of the $D_{\text{nonlinear}}$ /D_{spectrum} at each κ.

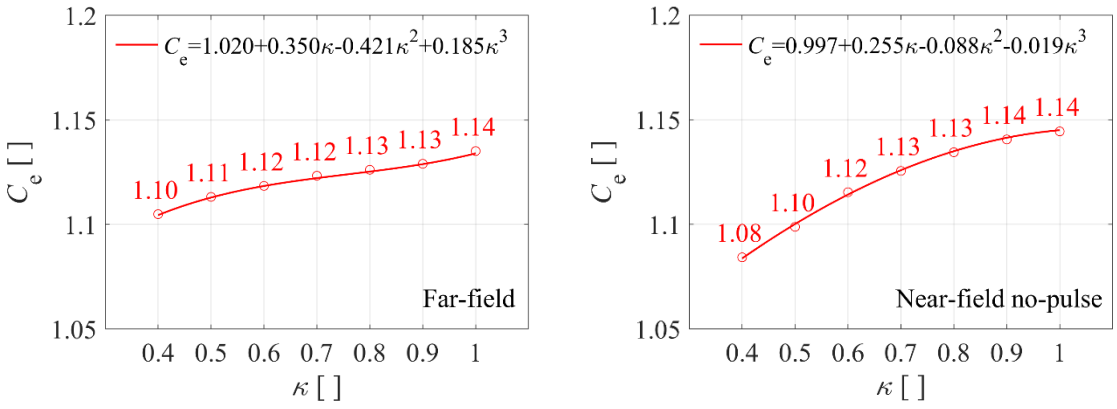

(a) (b)

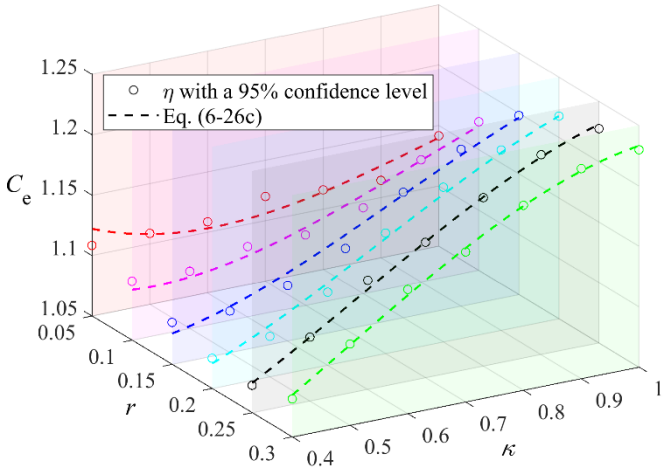

(c)

Figure 6-12 Correction factor (CF) with a 95% confidence at each κ for the sites with: (a) Far-field ground motions, (b) Near-field no-pulse ground motions, and (c) Near-field pulse-like ground motions.

$$C_e=0.938+0.615\kappa-0.648\kappa^2+0.250\kappa^3 \quad (6\text{-}26a)$$

$$C_e=1.004+0.165\kappa+0.087\kappa^2-0.094\kappa^3 \quad (6\text{-}26b)$$

$$C_e=1.447-1.059\kappa-3.047r+1.037\kappa^2+5.559\kappa r+6.175r^2-0.315\kappa^3-1.932\kappa^2 r-5.657\kappa r^2-3.603r^3 \quad (6\text{-}26c)$$

Alternatively, for the sites where far-field or near-field no-pulse records considered, as the variation of η on variables are at a narrow range, a uniform correction factor in $D_{spectrum}$ that can be applied to all the cases can be used. It is estimated based on η over all the cases regardless of T_e, κ, μ, r, or the ground motion feature considered at the site. The average and the standard variation of η sampled by this research are 1.08 and 0.05, respectively. The value with a 95% confidence is equal to 1.13, which can be deemed the uniform correction factor to make $D_{spectrum}$ equal to $D_{nonlinear}$.

6.4.2 The elastic design spectrum with the correction factor for the DDBD of the mid- to long-period PT-SKID frames

In the DDBD, the equivalent lateral force is determined by the product of the target peak displacement and the effective stiffness at the design earthquake intensity. The target displacement is the start point of the design and is determined by the expected damage level. The effective stiffness is calculated according to the effective period, which is obtained from the elastic displacement design spectrum. The displacement design spectrum can be those defined in codes and should be adjusted according to the equivalent damping ratio of the system as follows (Priestley et al., 2007):

$$\Delta_{(T,\,\xi)}=C_\xi \frac{T^2}{4\pi^2} S_{a(T,\,5)} g \quad (6\text{-}27)$$

where C_ζ is the reduction factor for the equivalent damping ratio greater than 5%, and it is defined as

$$C_\xi=\left(\frac{C_1}{C_2+\xi_{eq.,\,PT\text{-}SKID}}\right)^\gamma \quad (6\text{-}28)$$

where $\zeta_{eq,\,PT\text{-}SKID}$ is the equivalent damping ratio including the hysteretic component ($\zeta_{eq,\,hyst,\,PT\text{-}SKID}$) and the elastic viscous damping component ($\zeta_{eq,\,0,\,PT\text{-}SKID}$). For the site where far-field events considered, C_1, C_2, and γ in Eq. (6-28) is 0.10, 0.05, and 0.5, respectively (EC8 , 2004). For the site where near-filed events considered, a γ of 0.25 was suggested by (Priestley, 2003).

For the PT-SKID system, the effective stiffness and the equivalent damping ratio involved in the DDBD can be those defined by Eq.(6-17) and Eq.(6-20), respectively. The logic behind this design procedure is designing a nonlinear frame according to its linear equivalent system with the same displacement response. Because the linear equivalence based on Jacobsen's method frequently overestimates the displacement response of the PT-SKID system (see Section 3.4), a correction should be applied. For the PT-SKID frames with a mid- to long-period, a constant correction factor, C_e, is introduced to the displacement design spectrum to consider the error induced by the linear equivalence. Thus, Eq. (6-27) is corrected as follows:

$$\Delta_{(T,\,\xi)}=C_{\xi}C_{e}\frac{T^2}{4\pi^2}S_{a(T,\,5)}g \tag{6-29}$$

where C_e can be found from Figure 6-12 or calculated from Eq. (6-26).

Alternatively, for the sites where far-field or near-field no-pulse records considered, an uniform correction factor C_e of 1.13 can be used for all the cases.

6.4.3 The DDBD procedure using inelastic displacement spectrum

According to Eq. (6-20), the equivalent damping ratio of the PT-SKID frame is only determined by the effective stiffness ratio, κ, when the equivalent damping ratio of the SKID device is fixed. Thus, Eq. (6-27) can be expressed as follows by substituted with Eq. (6-18), Eq. (6-20), and Eq. (6-27)

$$\Delta_{(T,\,R)}=C_{e}\left(\frac{C_1}{C_2+\dfrac{0.265}{1+\dfrac{1}{\kappa}}+\xi_{0,\,\text{PT-SKID}}}\right)^{\gamma}\frac{T^2}{4\pi^2}S_{a(T,\,5)}g \tag{6-30}$$

where the equivalent damping ratio of the SKID device is assumed as 26.5%. The response spectrum defined by Eq. (6-30) is an inelastic displacement spectrum controlled by the effective stiffness ratio κ. Thus, the DDBD can be carried out for the PT-SKID frames by using the inelastic displacement spectrum defined by Eq. (6-30) and skipping the calculation of the equivalent damping ratio.

6.4.4 Summary of the DDBD procedure for the PT-SKID frame

This section briefly summarises the DDBD procedure, including the correction method proposed in previous sections, for the seismic design of the PT-SKID frame. The design procedure is shown in Figure 6-13. The first step is determining the design target, which is primarily the maximum displacement at the design-level earthquakes (Priestley et al., 2007). Then, the effective stiffness ratio κ (for all the cases) and stiffness ratio of the PT frame r (only for the site where near-field pulse-like ground motions are considered) need to be initiated; thus, the equivalent damping ratio of the frame and correction factor for the displacement spectra can be calculated. Note that the equivalent damping ratio should contain the elastic damping part and hysteretic part calculated by Eq. (6-20). The correction factor C_e should be calculated by Eq. (6-26) based on the specific earthquake characteristics under consideration. For the site where far-field or near-field no-pulse earthquakes are considered, a uniform correction factor of 1.13 can be used. This correction factor should be used to obtain the displacement response spectra according to Eq. (6-26) (for the area employing EuroCodes). The effective period of the PT-SKID frame can be read from the spectra at the target displacement, and subsequently, the effective stiffness of the frame can be calculated. After obtaining the effective stiffness, the target lateral strength of the frame at the design target displacement can be determined. The strength can be separated into the strength of the PT frame and that of the SKID device according to their effective stiffness ratio κ defined earlier. Then, the components of the PT frame and those of the SKID device can be designed based on capacity design logic. After the capacity design, a double-check in κ and r is required. If they do not meet the tolerance with the initiated values, an iteration is necessary.

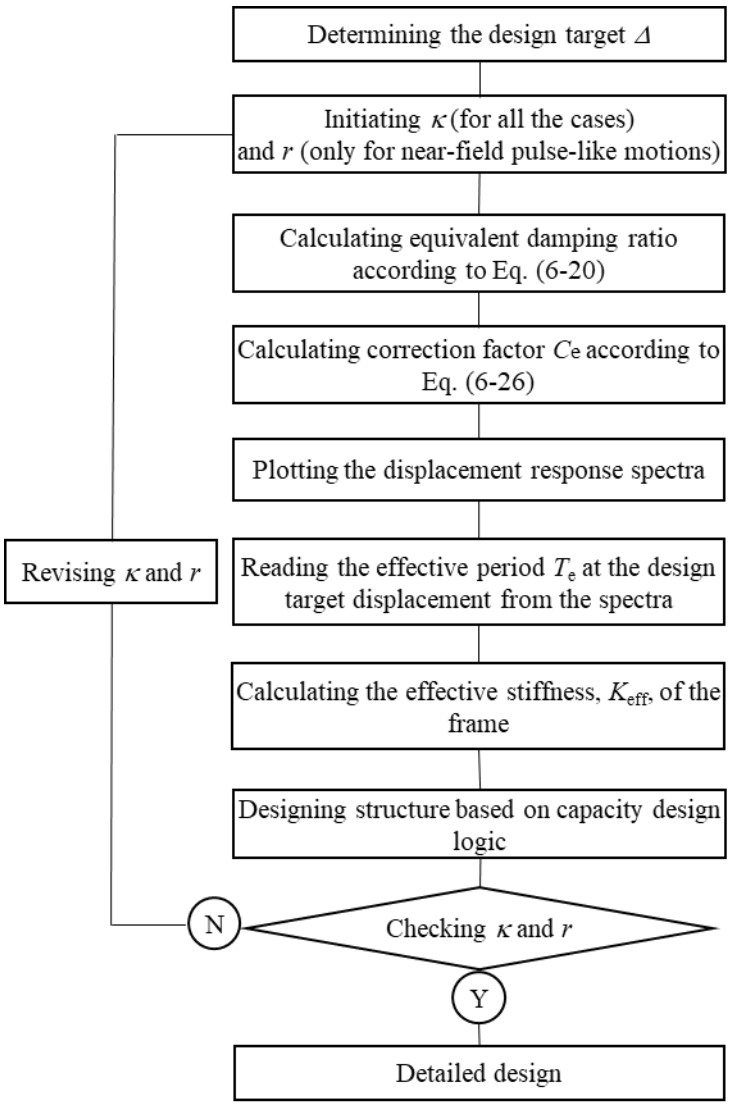

Figure 6-13 DDBD procedure for the PT-SKID frame

6.5 Conclusions

This chapter investigates the linear equivalence of the PT-SKID frames discussed in Chapter 5 for estimating their seismic response when designed according to DDBD. The equivalent system is constructed by the effective stiffness and the equivalent damping ratio estimated based on Jacobsen's method at the maximum displacement. First, a simplified model capturing the hysteretic properties of the PT-SKID frames was proposed. The model was calibrated using a one-story one-bay case frame from the literature. Then, the displacement estimation accuracy of the linear equivalence was evaluated considering a total of 5,880 models. The models used in the research covered the most common ranges of parameters of the PT-SKID frames. The accuracy was identified by the ratio between the seismic displacement response obtained from the simplified hysteretic model and that from its linear equivalence. Both far-field and near-field

record sets defined by FEMA P695 are utilised as seismic excitations. Based on the investigations performed in this research, the following conclusions are drawn:

1. The hysteretic property of the PT-SKID frame presented in Chapter 5 is characterised by five variables in the simplified hysteretic model: (i) initial lateral stiffness of the PT frame, k_{PT}, (ii) gap-opening displacement x_0, (iii) stiffness ratio of the PT frame, r, (iv) the ratio of the SKID stiffness to the PT frame initial stiffness, α, and (v) the stiffness ratio of the unloading stiffness to the loading stiffness of the SKID device, z. The first three parameters feature the property of the PT part. The last two parameters are the property of the SKID part and its combination factor with the PT part, respectively. The seismic hysteretic response obtained from the simplified hysteretic model matches well with that from the OpenSees model, indicating a good approximation of the simplified hysteretic model.

2. To be consistent with the DDBD, the parameters defined in the simplified hysteretic model (k_{PT}, x_0, α, r, and z) can be converted into an alternative set: effective period, T_e, ductility level, μ, PT stiffness ratio, r, effective stiffness ratio, κ, and equivalent damping ratio of PT-SKID frame, $\zeta_{eq, hyst, PT\text{-}SKID}$. By carrying out the procedure shown in Figure 6-3, $\eta = D_{nonlinear}/D_{spectrum}$ for each model and for each group of ground motions are obtained. According to the sensitivity analysis, the effective period, T_e, and the effective stiffness ratio, κ, are the most sensitive parameters to η of the mid to long-period PT-SKID frames when they are subjected to far-field or near-field no-pulse ground motions. For the near-field pulse-like ground motions, the PT stiffness ratio, r, also contributes. For the short-period frames, η is sensitive to T_e, κ, and r.

3. For the PT-SKID frames with a mid to long period, η_{ave} under far-field ground motions is greater than 1 for almost all the cases with a boundary of 1.15. This indicates that the linear equivalence based on Jacobsen's estimation always underestimates their seismic displacement response, which will lead to an unconservative design in the DDBD. With a more significant κ, a greater error is introduced. The variation of η_{ave} is less clear with T_e.

4. η_{ave} under the near-field no-pulse ground motions shows the similar results with that in the far-field events. However, under the near-field pulse-like ground motions, η_{ave} is more scatter to the variables, and may be slightly less than 1 when T_e, κ, and r are small. In general, η_{ave} is greater with κ and r.

5. For short-period frames, η_{ave} can be high (greater than 1.5) when the frame has a quite small T_e with a large κ and r, indicating a great error in estimation. Thus, the effectiveness of the

equivalence for the short-period PT-SKID frames is questioned. Further investigation is required for a more effective linear equivalence for these frames.

6. For the mid- to long-period PT-SKID frames, a correction factor (C_e) in the estimated displacement from the linearisation is proposed for a safer design using DDBD. The correction factor has a 95% confidence. For the sites were far-field or near-field no-pulse ground motions are considered, it is determined by the effective stiffness ratio κ of the frame. For the sites where the near-field pulse-like ground motions are considered, the PT stiffness ratio, r, is also affected. The correction factor can be found from the figure or calculated from the fitted functions and simply involved into the definition of the displacement design spectrum in the DDBD to consider the error raised by the linear equivalence. Alternatively, for the sites where far-field or near-field no-pulse records are considered, an uniformed correction factor of 1.13 can be used for all the cases without considering κ, r, or earthquake characters, resulting in an easier process.

Chapter 7 The PTPW-SKID structure: a case study

7.1 Introduction

This chapter proposes a one-story industrial structure following the PT-SKID concept, named as Post-Tensioned Precast Warehouse structure with the Sliding Keys on Inclined Deflecting-cantilever Device (the PTPW-SKID Structure). The precast reinforcement concrete one-story industrial structures were chosen as the object because: (1) their design is controlled by the seismic actions; (2) they are cost-effective and widely used in high seismic risk areas such as Italy and Slovenia (Ercolino et al., 2018); and (3) it has the potential to inform retrofit technology for the existing concrete one-story industrial structures in the future. The structure configuration is proposed, and the load path is analysed first. The structure comprises a PT outer frame and a SKID inner frame. The PT outer frame supports the roof and cladding systems and carries the loads applied to them. The SKID inner frame is composed of support columns, support beams, and SKID devices. The support columns are also the columns of the crane gantry frame and carry both the vertical and horizontal forces generated from the crane system. The horizontal forces are resisted by the PT outer frame and the SKID inner frame together. The PT outer frame provides parts of the lateral stiffness and stiffness softening feature, and the SKID inner frame contributes to the remaining lateral stiffness and provides additional hysteretic damping. The theoretic behaviours of the PTPW-SKID structure are investigated by focusing on the hysteretic curve of the SKID inner frame, where the SKID device is supported by high support columns. Then, a one-story industrial structure with the typical typologies in Italy is chosen as a case to demonstrate the design of the PTPW-SKID structure. The DDBD method is used for its seismic design. Finally, a 3D numerical model was built in OpenSees. Both quasi-static and seismic dynamic analyses were carried out to investigate the hysteretic behaviours and the seismic responses of the designed case structure. This chapter aims to explore the following questions:

1. Is it possible to propose a full self-centring industrial structure?

2. What is the structural arrangement of the PTPW-SKID structures?

3. How could we design the PTPW-SKID structure, and how well does it work in earthquakes?

7.2 The Post-Tensioned Precast Warehouse structures equipped with Sliding Keys on Inclined Deflecting-cantilevers Devices (PTPW-SKID structures)

7.2.1 The PTPW-SKID structure

A Post-Tensioned Precast Warehouse structure with the Sliding Keys on Inclined Deflecting-cantilever device (PTPW-SKID structure) is proposed. As shown in Figure 7-1, the structure consists of a Post-Tensioned (PT) outer frame (Figure 7-1 (c)) and a SKID inner frame (Figure 7-1 (d)). The PT outer frame comprises monolithic columns, prestressed primary beams with variable cross-sections, rectangular secondary beams, prestressed tee roof panels and vertical cladding panels (not shown in the figure). The columns are fastened to the foundations by prestressed cables and work as nonlinear elastic tied columns under horizontal actions. The columns have forks at their tops to support primary beams and restrain their torsional and lateral rotations. The horizontal shear forces from the primary beams are transferred to the columns by two vertical dowels protruding from the columns. This beam-column connection can be considered a pinned connection, as it provides limited rotational restraint when subjected to horizontal loads. tee panels are used as roof panels and connected with the primary beams with dowel connections (Magliulo et al., 2018). A 5 cm thick cast-in-situ concrete slab is cast on the top of roof panels and connected with tee panels using metallic systems. This roof can be assumed as a rigid diaphragm, according to Eurocode 8 (CEN, 2004). It is worth noting that the cast-in-situ concrete slab is necessary to achieve the design target of non-damage recentring behaviour at Design-Basis Earthquakes (e.g., with a return period of 475 years) because the primary beams cannot withstand large out-of-plane horizontal deformations imposed by non-damage panels without the diaphragm effect. The secondary beams are located overhead of the SKID device (in the longitudinal plane) and connected with the sliding keys to transfer the horizontal force carried by the SKID device. The tee panels with cast-in-situ concrete, primary and secondary beams form an integral roof system. The PT outer frame undertakes three roles: (1) supporting roof and wall cladding systems, (2) carrying the vertical loads applied to them, and (3) carrying part of the horizontal force by its lateral stiffness. The lateral stiffness of the PT outer frame is only provided by the non-linear elastic tied columns. The SKID device is necessary to provide additional hysteretic damping since the hysteretic damping of the PT outer frame is negligible. Figure 7-1 (d) shows that the SKID devices and their support columns and beams form the SKID inner frame. The support columns are a set of cantilever columns located in the plane of each transversal frame and connected with the support beams in the longitudinal direction. The SKID devices working in the transversal plane (denoted as the SKID in X in the figure) are installed between the support columns and the primary beams. As the SKID device works in only one direction, the other group

of SKID devices, which work in the longitudinal plane (denoted as the SKID in Y in the figure), is positioned between the support beams and secondary beams. The SKID inner frame carries the rest of the horizontal forces (wind loads and earthquake actions) and provides additional hysteretic damping. In addition, the SKID inner frame is designed to support the crane system. As shown in Figure 7-1 (b), the rail beams of a heavy crane are simply supported by the support columns. The support columns carry all the vertical loads regarding the crane system. Besides, almost all of the horizontal forces generated by the crane system (e.g., the serviceability horizontal actions at SLS and equivalent seismic actions at SLS and ULS) are expected to be carried by the support columns, while ignorable horizontal forces will be transferred to the primary beams (thus carried by the PT outer fame) via SKID devices. The force transferred to the PT outer frame is ignorable because the lateral stiffness provided by the SKID device is much smaller than that of the support columns, which will be demonstrated in the subsequent sections.

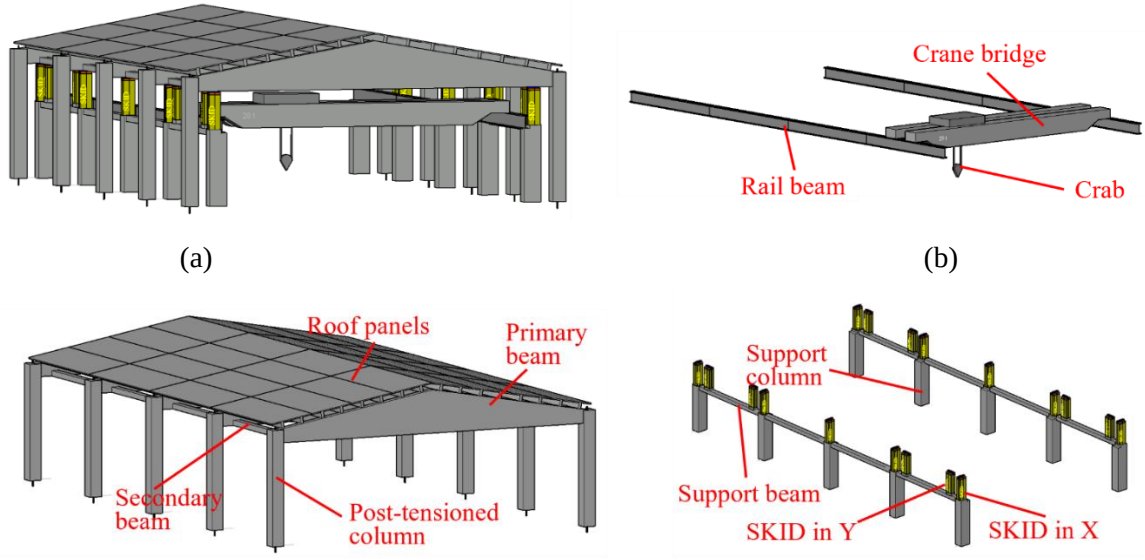

(a) (b)

(c) (d)

Figure 7-1 Post-Tensioned Precast Warehouse structure with the Sliding Keys on Inclined Deflecting-cantilever device (PTPW-SKID): (a) the whole structure; (b) the heavy crane system; (c) the PT outer frame; and (d) the SKID inner frame.

7.2.2 Global behaviour of the SKID inner frame: The influence of flexibility of support columns

Schematically, the lateral behaviour of the PTPW-SKID structure is the combination of the PT outer frame and the SKID inner frame in parallel. This section focuses on the hysteretic behaviour of the SKID inner frame. A planner SKID inner frame in the transversal plane is demonstrated.

The results are also valid for the SKID inner frame in the longitudinal plane. Considering the rigid roof diaphragm, the lateral stiffness of the SKID inner frame, $K_{\text{SKID inner frame}}$, is the total stiffness of groups of the SKID-support column as shown in Figure 7-1 (d):

$$K_{\text{SKID inner frame}}\left(X,\dot{X}\right)=nK_{\text{SKID-support column}}\left(X,\dot{X}\right) \qquad (7-1)$$

where $K_{\text{SKID-support column}}$ is the stiffness of one group of the SKID-support column, and n is the number of groups. Figure 7-2 shows a group of SKID-support column in the transversal plane.

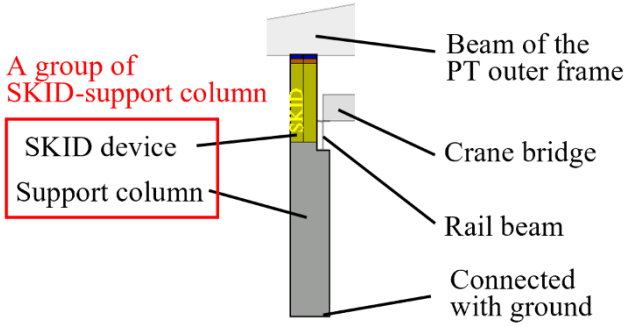

Figure 7-2 A group of SKID-support column in the transversal plane.

The stiffness of the SKID device alone is:

$$K_{\text{SKID}}\left(X,\dot{X}\right)=\left\{\frac{\left(\mu\text{sgn}(X\dot{X})+\tan\beta\right)\tan\beta}{1-\mu\tan\beta\,\text{sgn}\left(X\dot{X}\right)}\right\}k \qquad (7-2)$$

and its equivalent damping ratio is

$$\zeta_{\text{eq., SKID}}=\frac{1}{2\pi}\left(1-\frac{(1-\mu\tan\beta)(\tan\beta-\mu)}{(1+\mu\tan\beta)(\tan\beta+\mu)}\right) \qquad (7-3)$$

where μ is friction coefficient, and β is the slope angle. Note that the stiffness of the SKID device is relevant to the displacement, X, and velocity direction, $\dot{X}$, of the sliding keys. Because the SKID device is connected with the support column in line, the stiffness of a group of SKID-support column can be expressed as:

$$K_{\text{SKID-support column}}\left(X,\dot{X}\right)=\frac{1}{\dfrac{1}{K_{\text{SKID}}\left(X,\dot{X}\right)}+\dfrac{1}{K_{\text{SC}}}} \qquad (7-4)$$

where K_{SC} is the flexural stiffnesses of the support column:

$$K_{SC}=\frac{3EI_{SC}}{{H_{SC}}^3} \qquad (7-5)$$

where E and I_{SC} is the mean Young's modulus and the second moment of area of the support column section, respectively, and H_{SC} is the hight of the support column. By defining:

$$\alpha(X,\dot{X})=\frac{K_{SKID}(X,\dot{X})}{K_{SC}} \qquad (7-6)$$

and substituting Eq. (7-6) into (7-4), the following equation is derived:

$$K_{\text{SKID-support column}}(X,\dot{X})=\frac{1}{(1+\alpha)}K_{SKID}(X,\dot{X}) \qquad (7-7)$$

By substituting Eq. (7-7) into Eq. (7-1), $K_{\text{SKID inner frame}}(X,\dot{X})$ is expressed as:

$$K_{\text{SKID inner frame}}(X,\dot{X})=\frac{n}{(1+\alpha)}K_{SKID}(X,\dot{X}) \qquad (7-8)$$

and the lateral resistance of the SKID inner frame is:

$$F_{\text{SKID inner frame}}(X,\dot{X})=K_{\text{SKID inner frame}}(X,\dot{X})X \qquad (7-9)$$

Eq. (7-8) and (7-9) express the situation where the sliding keys are sliding up and sliding down against the slope blocks. However, the unloading stage of the SKID inner frame is more complex because the sliding keys will get stuck at the peak displacement for a short period after the displacement of the beam is reversed, until the applied force is sufficient to reactive the SKID device. During this period of the SKID being stuck, the stiffness of the inner frame only depends on the support columns. Thus, the difference between the frame peak displacement, X_{peak}, and the frame displacement where the SKID device is reactivated, $X_{reactivate}$, is equal to the difference of the support column deformation between these two status, $\Delta_{\text{support column}}$, (the definition of X_{peak} and $X_{reactivate}$ can be seen in Figure 7-3):

$$X_{peak}-X_{reactivate}=\Delta_{\text{support column}} \qquad (7-10)$$

where $\Delta_{\text{support column}}$ is calculated by:

$$\Delta_{\text{support column}} = F_{\text{SKID}}\left(X_{\text{peak}}, \dot{X_{\text{peak}}}\right)/K_{\text{SC}} - F_{\text{SKID}}\left(X_{\text{reactivate}}, \dot{X_{\text{reactivate}}}\right)/K_{\text{SC}} \qquad (7-11)$$

where $F_{\text{SKID}}\left(X_{\text{peak}}, \dot{X_{\text{peak}}}\right)$ and $F_{\text{SKID}}\left(X_{\text{reactivate}}, \dot{X_{\text{reactivate}}}\right)$ is:

$$F_{\text{SKID}}\left(X_{\text{peak}}, \dot{X_{\text{peak}}}\right) = K_{\text{SKID}}\left(X_{\text{peak}}, \dot{X_{\text{peak}}}\right) X_{\text{SKID}} \qquad (7-12a)$$

$$F_{\text{SKID}}\left(X_{\text{reactivate}}, \dot{X_{\text{reactivate}}}\right) = K_{\text{SKID}}\left(X_{\text{reactivate}}, \dot{X_{\text{reactivate}}}\right) X_{\text{SKID}} \qquad (7-12b)$$

where X_{SKID} is the displacement of the sliding keys relevant to the SKID base. As the SKID device get stuck at this moment, $F_{\text{SKID}}\left(X_{\text{peak}}, \dot{X_{\text{peak}}}\right)$ and $F_{\text{SKID}}\left(X_{\text{reactivate}}, \dot{X_{\text{reactivate}}}\right)$ have the following relationship:

$$\frac{F_{\text{SKID}}\left(X_{\text{reactivate}}, \dot{X_{\text{reactivate}}}\right)}{F_{\text{SKID}}\left(X_{\text{peak}}, \dot{X_{\text{peak}}}\right)} = \frac{K_{\text{SKID}}\left(X\dot{X} < 0\right)}{K_{\text{SKID}}\left(X\dot{X} > 0\right)} \qquad (7-13)$$

By defining a deformation factor, ρ, as:

$$\rho = \frac{X_{\text{reactive}}}{X_{\text{peak}}} \qquad (7-14)$$

and substituting Eq. (7-7), Eq. (7-10), Eq. (7-11) and Eq. (7-13) into Eq. (7-14), the following expression is obtained:

$$\rho = 1 - \frac{(1-z)\alpha\left(X\dot{X} > 0\right)}{1+\alpha\left(X\dot{X} > 0\right)} \qquad (7-15)$$

where z is

$$z = \frac{K_{\text{SKID}}\left(X\dot{X} < 0\right)}{K_{\text{SKID}}\left(X\dot{X} > 0\right)} \qquad (7-16)$$

The hysteretic curves of the SKID inner frame based on Eq. (7-8) and Eq. (7-15) are shown in Figure 7-3 (the blue lines). When α is infinitely small, the influence of the elastic deformation of the support columns can be ignored, as the red lines in Figure 7-3. This happens when a large section or a small height is used for the support columns. However, it is usually not the case in one-story industrial structures. It is worth to be mentioned that in Figure 7-3, the non-dimensional parameter η is introduced to identify the sign of the unloading stiffness of the system and defined as:

$$\eta=\frac{\mu}{\tan\beta} \tag{7-17}$$

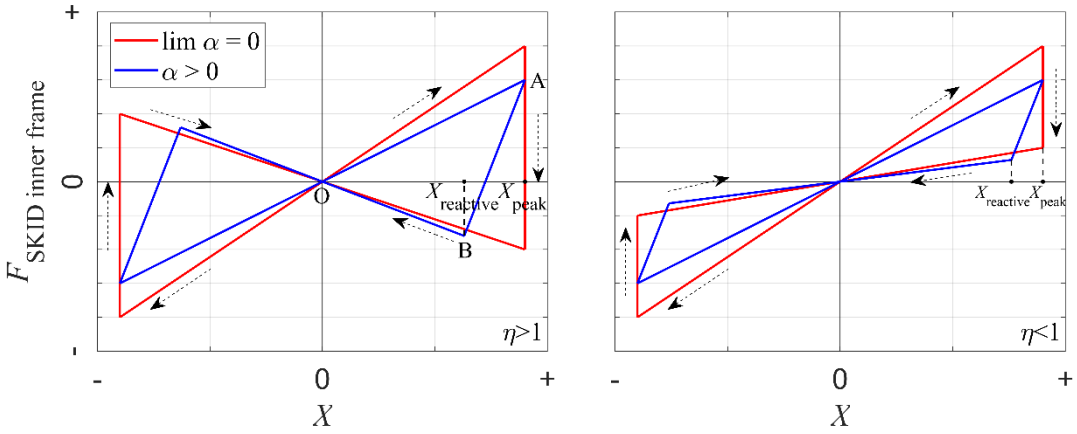

Figure 7-3 Hysteretic curve of the SKID inner frame.

In addition, the equivalent damping ratio of the SKID inner frame is derived based on Jacobsen's method (Jacobsen, 1960). It is defined as follows:

$$\zeta_{\text{SKID inner frame}}=\frac{S_{\text{OAB}}}{2\pi S_{\text{OAX}_{\text{peak}}}} \tag{7-18}$$

where areas OAB and OAX_{peak} are shown in Figure 7-3. Because the hysteretic damping of the SKID inner frame only derives from the SKID device, $\zeta_{\text{SKID inner frame}}$ can be expressed as:

$$\zeta_{\text{SKID inner frame}}=\frac{E_{\text{SKID}}}{\pi n F_{\text{SKID-support column}}(X\dot{X}>0)X} \tag{7-19}$$

where E_{SKID} is

$$E_{\text{SKID}}=n\frac{K_{\text{SKID}}(X\dot{X}>0)-K_{\text{SKID}}(X\dot{X}<0)}{2}X_{\text{SKID}}{}^{2} \tag{7-20}$$

$F_{\text{SKID-support column}}$ is

$$F_{\text{SKID-support column}}(X,\dot{X})=K_{\text{SKID-support column}}(X,\dot{X})X \tag{7-21}$$

As the SKID device is connected with the support columns in line:

$$F_{\text{SKID-support column}}(X\dot{X}>0) = F_{\text{SKID}}(X\dot{X}>0) \tag{22}$$

By substituting Eq. (7-7), Eq. (7-12), Eq. (7-20), Eq. (7-21) and Eq. (7-22) into Eq. (7-19) and rearranging, $\zeta_{\text{SKID inner frame}}$ can be expressed as:

$$\zeta_{\text{SKID inner frame}} = \frac{1}{2\pi}\rho(1\text{-}z) \tag{7-23}$$

7.3 The prototype structure and its seismic design

7.3.1 The prototype structure

A precast concrete one-story industrial structure featuring one of the most common typologies in Italy was abstracted by Ercolino et al. (2018) and Magliulo et al. (2018) and is selected for the case study. The one-story structure is designed with the PTPW-SKID structural system proposed in Section 7.2.1. Figure 7-4 shows the plan view and side elevation views of the structure. In the figure, the components of the PT outer frame are shown in bold black lines, the components of the SKID inner frame are in orange and yellow lines, and the rail beams that are parts of the crane system are shown in blue lines. The roof and wall panels and other components of the crane system are not shown in the figure. The SKID devices working in the transversal planes (the XZ plane in the figure) are carried by the support columns, and those working in the longitudinal plane (the YZ plane) are on the support beams. All the transversal frames (as shown in Figure 7-4 (b)) are equipped with two sets of SKID devices, while only the end bays of the longitudinal frames have SKID devices that work in the longitudinal direction (please see Figure 7-4 (d)). The structure has one bay with a span of 20 meters in the transversal direction and four bays with a span of 8 meters in the longitudinal direction. The height of the eave is 6 meters, and the clear height below the crane is 4.5 meters. The roof sloping is 10° and formed by the pediment-shaped primary beams. The structure is assumed to be located in L'Aquila, Italy, on Soil type C (CEN 2004).

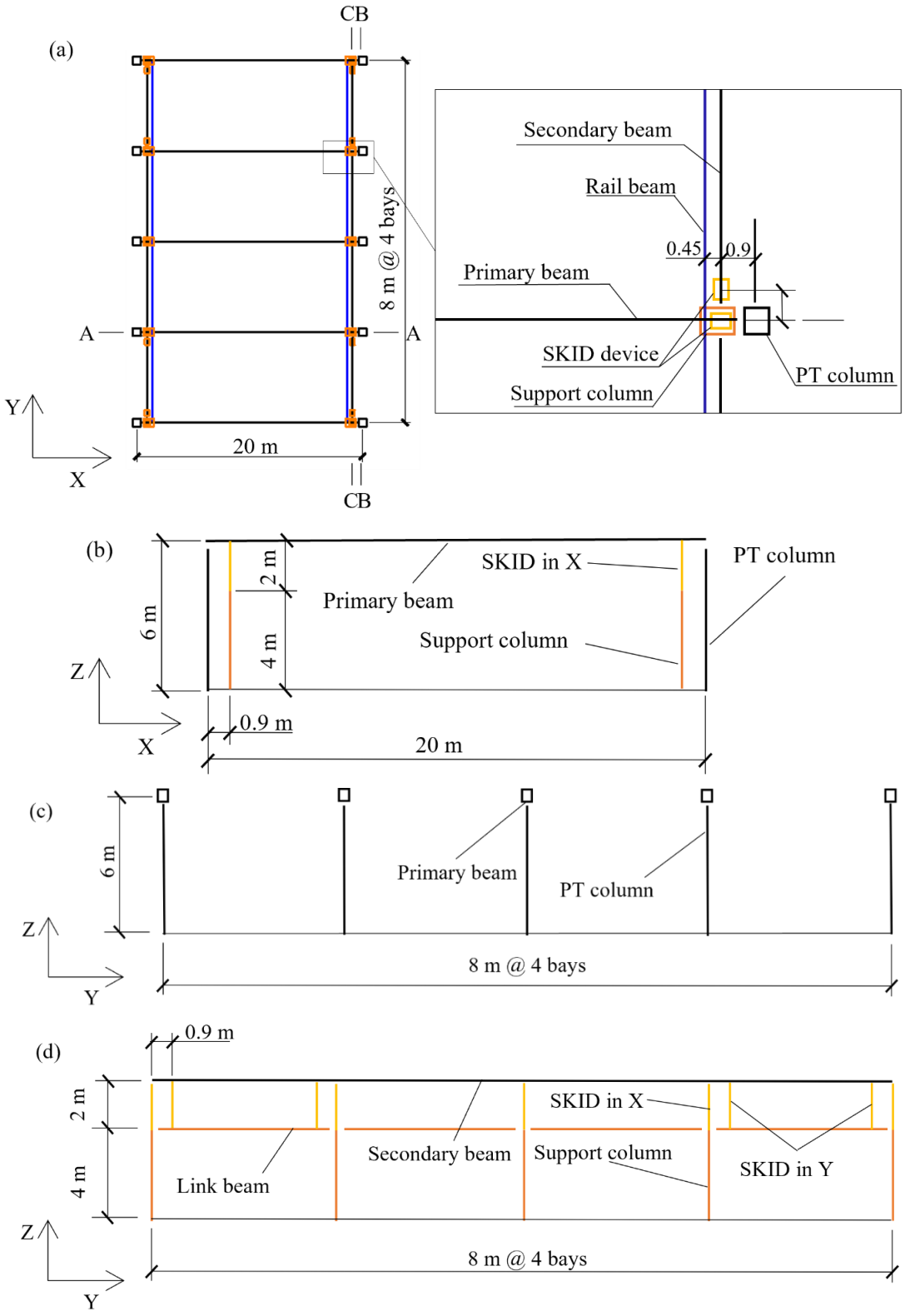

Figure 7-4 The case one-story industrial structure: (a) the plan view;(b) the transversal frame (A-A); (c) the longitudinal PT outer frame (B-B); and (d) the longitudinal SKID inner frame (C-C).

7.3.2 Loads considered in the design of the case structure and the load paths

The structure comprises the PT outer frame and the SKID inner frame with two corresponding load paths. The PT outer frame is designed to carry the vertical loads applied on the roof and wall cladding systems (their self-weights, the services, imposed roof loads, and snow loads) based on Eurocodes (CEN 2005). The concrete roof panels with a tee section as shown in Figure 7-5 are used and simply supported by the primary beams with a span of 8 meters. A 5 cm cast-in-situ concrete slab is placed on the panels, forming a rigid diaphragm. The self-weight of the roof panels is calculated as 2.26 kN/m^2, and a typical self-weight of 4 kN/m^2 is considered for the wall cladding system (Magliulo et al., 2018). The structure is assumed an industrial use with a service load of 3KN/m^2 and an imposed load of 0.5 kN/m^2 applied on the roof. According to the Italian National Annex of Eurocode 1, the structure is located in Climate Zone III, and the snow load is calculated as 1.31 kN/m^2. The critical parameters used to calculate the snow load is summarised in Table 7-1, where a_s is the site altitude above sea level, μ_1 is the snow load shape coefficient, C_e and C_t are the exposure coefficient and thermal coefficient, respectively, q_{sk} and q_s are the characteristic value of snow on the ground and the snow load on the roof, respectively.

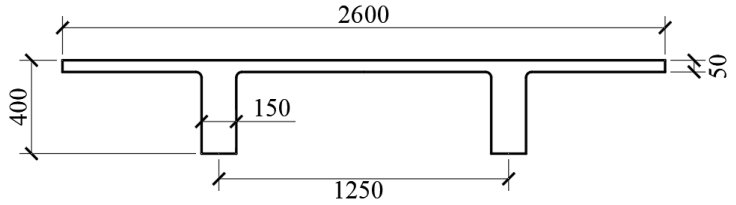

(a)

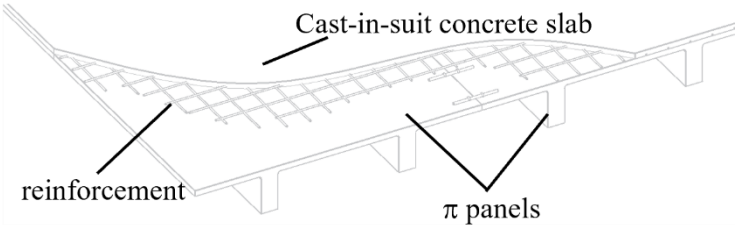

(b)

Figure 7-5 The roof system: (a) section (b) details.

Table 7-1 Snow loads on the structure.

Climate zone	a_s (m)	q_{sk} (kN/m^2)	μ_i	C_e	C_t	q_s (kN/m^2)
III	716	1.64	0.8	1.0	1.0	1.31

The horizontal loads (e.g., acceleration force, break force, skewing force) and vertical loads (e.g., self-weight of the crane system and service load on hook) generated by the crane system are

expected to be transferred to the ground by the support columns of the SKID inner frame. A heavy-duty crane with a service capability of 20 t is utilised in the case structure. The span of the crane bridge is 17 m, and the mass of the bridge with the crab is assumed as 20 t. The steel runway beams with a section of HEA 400 are used to meet the deflection requirement. As shown in Figures 7-1 (a) and 7-2, the horizontal forces generated by the crane in serviceability or earthquake events are applied on the top of the support columns. Although parts of the horizontal forces are transferred to the PT outer frame by the SKID device, because the stiffness of the SKID device is much lower than that of the cantilevered support columns, it can be considered negligible. The following section will demonstrate that less than 5% of the horizontal force generated by the crane system is transferred to the PT outer frame via the SKID device.

The wind actions and seismic actions are designed to be carried by the PT outer frame and SKID inner frame together. The equivalent wind loads are calculated based on Eurocode 1 and Italian National Annex. The location of the structure is identified at Wind Zone 3 with a terrain roughness of B and exposure class of IV. The fundamental value of the basic wind velocity, $V_{b,0}$, is 31.32 m/s, and the peak velocity pressure, q_p, is 1.00 kN/m^2. As the structure is located at a high seismic zone, both the horizontal and vertical seismic actions are considered in the design. The design spectra defined by the Italian National Annex of Eurocode 8 are utilised. The critical parameters defining the seismic hazards of the site at the Ultimate Limit State (ULS, with a return period, T_R, of 475 years) and the Serviceability Limit State (SLS, with a return period, T_R, of 30 years) are summarised in Table 7-2. The target design spectrum at ULS for the site is shown in Figure 7-12 (the blue dashed line).

Table 7-2 Parameters defining the seismic hazards of the site.

	a_g	F_0	T_c^*
ULS (T_R=475 yrs.)	2.610	2.36	0.35
SLS (T_R=30 yrs.)	0.789	2.40	0.27

7.3.3 The seismic design of the case structure

The structure is deigned according to EuroCode 2 (CEN 2004a) and 8 (CEN 2004) considering different load combinations. The design of the lateral capability of the case structure is dominated by the seismic actions combined with the permanent loads. This paper only reports the horizontal seismic design of the structure. The seismic actions and gravity loads generated by the crane system are ignored in the seismic design because: (1) they are transferred to the ground by the support columns, the part carried by the PT outer frame visa SKID is ignorable; (2) the mass of the crane system is small compared with the roof system; and (3) the seismic response of the

crane system does not induce any additional hysteretic oscillation on the global PTPW-SKID structure. It is worth to be noted that the section design of the support columns considered the force generated by the crane system, and the support columns were designed maintaining elastic at ULS. The total seismic mass of the structure is 504.126 t and is assumed to be concentrated on the roof. The seismic design is carried out by designing the planar transversal frame and the longitudinal frame, respectively. Direct Displacement-Based Design (DDBD) (Priestley et al. 2007) is used to make the frame performing the target responses in earthquake events. The drift ratio of 2% at ULS in two directions is set as the design target. Figure 7-6 briefly shows the design procedure. The equivalent damping ratio of the frame ($\zeta_{\text{PTPW-SKID}}$) involves the hysteretic component ($\zeta_{\text{hyst.}}$), and the elastic viscous damping component (ζ_0). The elastic viscous damping is assumed as 5% and the hysteretic component is estimated by the area-based approach proposed by Jacobsen (Jecobsen 1960) and calculated by:

$$\xi_{\text{hyst.}} = \frac{1}{1+\frac{1}{\kappa}} \xi_{\text{SKID inner frame}} \tag{7-24}$$

where κ is defined as:

$$\kappa = K_{\text{eff., SKID inner frame}} / K_{\text{eff., PT outer frame}} \tag{7-25}$$

and $\xi_{\text{SKID inner frame}}$ is calculated by Eq. (7-23). In Eq. (7-25), $K_{\text{eff., PT outer frame}}$ and $K_{\text{eff., SKID inner frame}}$ are the effective stiffness of the PT outer frame and the SKID inner frame at the target displacement, respectively. The derivation of the Eq. (7-24) is as follows.

The hysteretic behaviour of the planar PTPW-SKID frame is the combination of its PT outer frame and the SKID inner frame. The base shear - drift ratio relationship of a PTPW-SKID planar frame can be expressed as:

$$F_{\text{PTPW-SKID}}(X,\dot{X}) = F_{\text{PT outer frame}}(X) + F_{\text{SKID inner frame}}(X,\dot{X}) \tag{7-26}$$

According to the definition of Jacobsen's method, the hysteretic component of the equivalent damping ratio of the PTPW-SKID frame is:

$$\xi_{\text{hyst.}} = \frac{F_{\text{PTPW-SKID}}(X,\dot{X}>0) - F_{\text{PTPW-SKID}}(X,\dot{X}<0)}{4\pi F_{\text{PTPW-SKID}}(X,\dot{X}>0)} \tag{7-27}$$

By substituting Eq. (7-26) into Eq. (7-27), the following expression is obtained:

$$\xi_{\text{eq., hyst., PTPW-SKID}}=\frac{F_{\text{SKID inner frame}}(X,\dot{X}>0)-F_{\text{SKID inner frame}}(X,\dot{X}<0)}{\left(4\pi F_{\text{PT outer frame}}(X)+F_{\text{SKID inner frame}}(X,\dot{X}>0)\right)} \tag{7-28}$$

As the definition of κ can be expressed as

$$\kappa=\frac{F_{\text{SKID inner frame}}(X,\dot{X}>0)}{F_{\text{PT outer frame}}(X)} \tag{7-29}$$

By substituting Eq. (7-29) into Eq. (7-28), the following expression is obtained:

$$\xi_{\text{hyst.}}=\frac{1}{1+\frac{1}{\kappa}}\frac{F_{\text{SKID inner frame}}(X,\dot{X}>0)-F_{\text{SKID inner frame}}(X,\dot{X}<0)}{4\pi F_{\text{SKID inner frame}}(X,\dot{X}>0)}=\frac{1}{1+\frac{1}{\kappa}}\xi_{\text{SKID inner frame}} \tag{7-30}$$

where $\zeta_{\text{SKID inner frame}}$ is the hysteretic component of equivalent damping ratio of the SKID inner frame.

The displacement response spectra at the effective damping ratio, $\zeta_{\text{PTPW-SKID}}$, is generated by the method defined in EuroCode 8. The effective stiffness of the entire frame, $K_{\text{eff, PTPW-SKID}}$, is calculated by:

$$K_{\text{eff., PTPW-SKID}}=\frac{4\pi^2 m_{\text{e}}}{T_{\text{e}}{}^2} \tag{7-31}$$

where m_{e} is the total seismic mass in the case structure.

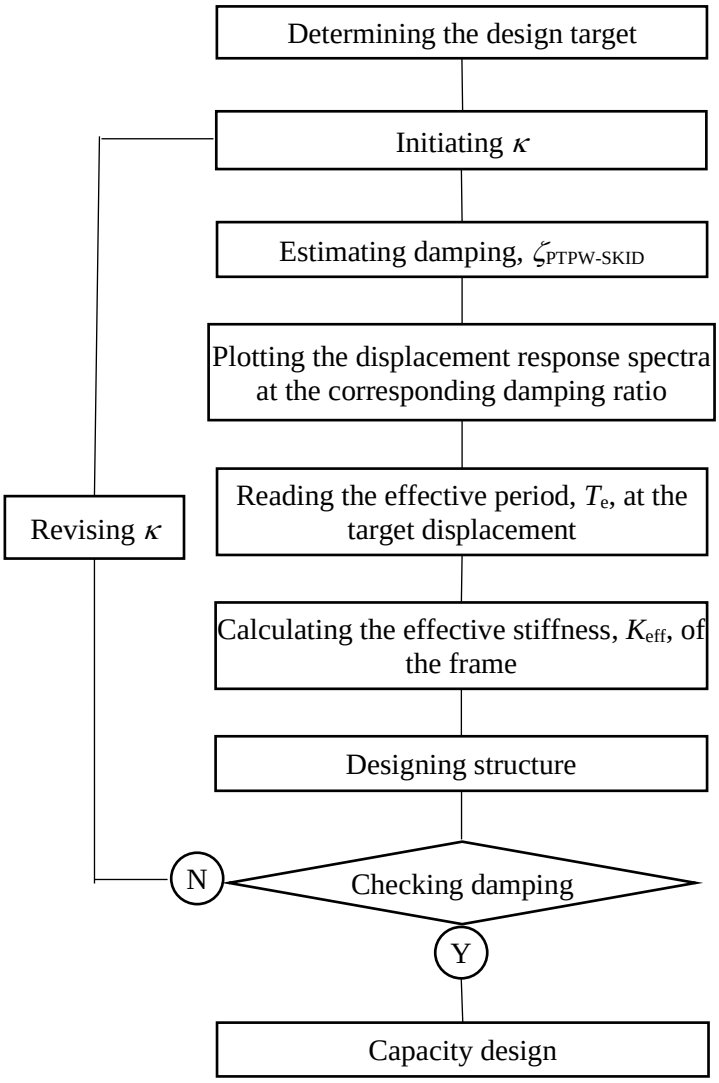

Figure 7-6 DDBD procedure used for the case structure.

After obtaining the effective stiffness, K_{eff}, the target lateral strength of the PTPW-SKID frame at the design target displacement can be calculated. The strength can be separated into the strength of the PT outer frame and that of the SKID inner frame according to their effective stiffness ratio κ defined earlier. Then, the components of the PT outer frame and those of the SKID inner frame can be designed based on capacity design logic according to EuroCode 2. For the design case, the internal forces of each component were determined using the OpenSees numerical model presented in the next section. All the structural components were designed maintain elastic at ULS, as the structure is expected to self-recentre after design earthquakes (T_R=475 years). The final κ, $\zeta_{hyst.}$, and $T_{eff.}$ of the planar transversal frame and the longitudinal frame of the case frame at ULS are summarized in Table 7-3. It is worth noting that the frame is design to possess the target strength at the target displacement at ULS, its strength at SLS is not directly considered at the DDBD design procedure. The performance of the frame at SLS is checked after the components determined. In the case study, a drift ratio limit of 0.5% at SLS is checked following the design logic of DDBD. Specifically, the effective stiffness and equivalent damping ratio of

the designed PTPW-SKID frame at 0.5% drift ratio was found by using the OpenSees numerical model. Then the drift ratio at SLS was estimated from the displacement response spectra at the corresponding equivalent damping ratio. Table 7-3 shows κ, $\zeta_{hyst.}$, and $T_{eff.}$, of the frame at SLS. The estimated drift ratios, $\Delta_{est., SLS}$, of the transversal frame and the longitudinal frame were 0.45% and 0.46%, respectively, which is less than the limit of 0.5%, indicates the design result is accepted.

Table 7-3 Target performance of the planar frame.

	ULS			SLS			
	κ	$\zeta_{hyst.}$	$T_{eff.}$	κ	$\zeta_{hyst.}$	$T_{eff.}$	$\Delta_{est., SLS}$
Transversal frame	0.91	11.4%	1.373 s	0.243	4.68 %	0.88 s	0.45 %
Longitudinal frame	1.00	10.5 %	1.344 s	0.272	4.49 %	0.88 s	0.46 %

Figure 7-7 shows the designed section of the precast PT columns, the profile of the principle beams, the section of the secondary beams, the support beams, and the support columns. The concrete with the Grade C35/45 and the reinforcement with characteristic yield strength of 500 MPa are used for all components. The reinforcement rate of the PT columns is 2.17%, and the applied post-tension force is 533 kN. A 7 strands of 15.7 mm diameter cable with the strength grade 1860 MPa is used to apply the pre-tension force. The contact between the PT columns and their foundations is enveloped by armour steel with grade of S355. Note that the columns are designed keeping elastic at the 2% drift ratio in one direction and simultaneously 0.6% drift ratio in the other. The principle beams have a variable section along span. The pre-tension force of 2200 kN is applied by a 12 strands of 15.7 mm diameter cable to control their deflection. The mid-section of the principle beams is shown in Figure 7-7 (d). The details of their profile are not designed in this study. The secondary beams and the support beams have the same section (Figure 7-7 (b)) and are designed to be easier to sit the SKID device (which has a width of 400 mm), thus the section is slightly greater than that required by strength. The section of the support columns (Figure 7-7 (c)) is designed considering the deformation requirement at the SLS of the crane system and has a reinforcement ratio of 1.02%. The SKID device used in the case study has a sliding slope angle, β, of 4° and a friction coefficient, μ, of 0.4, which are the same as the specimen demonstrated in Chapter 5. The cantilever bars of the SKID device are designed according to Eq. (7-2) to achieve the target stiffness obtained from the DDBD design procedure. The SKID device used in the transversal frames and in the longitudinal frames have a loading stiffness of 1068 kN/m and 1574 kN/m, respectively. A rectangular hollow section is selected for the cantilever bars, and the length of them are 1806 mm and 1696 mm for the SKID device in the transversal frames and the longitudinal frames, respectively. The connections among structural components

are not designed in this study but they are assumed having the sufficient strength to perform the corresponding connecting behaviour (pined or fixed) at ULS.

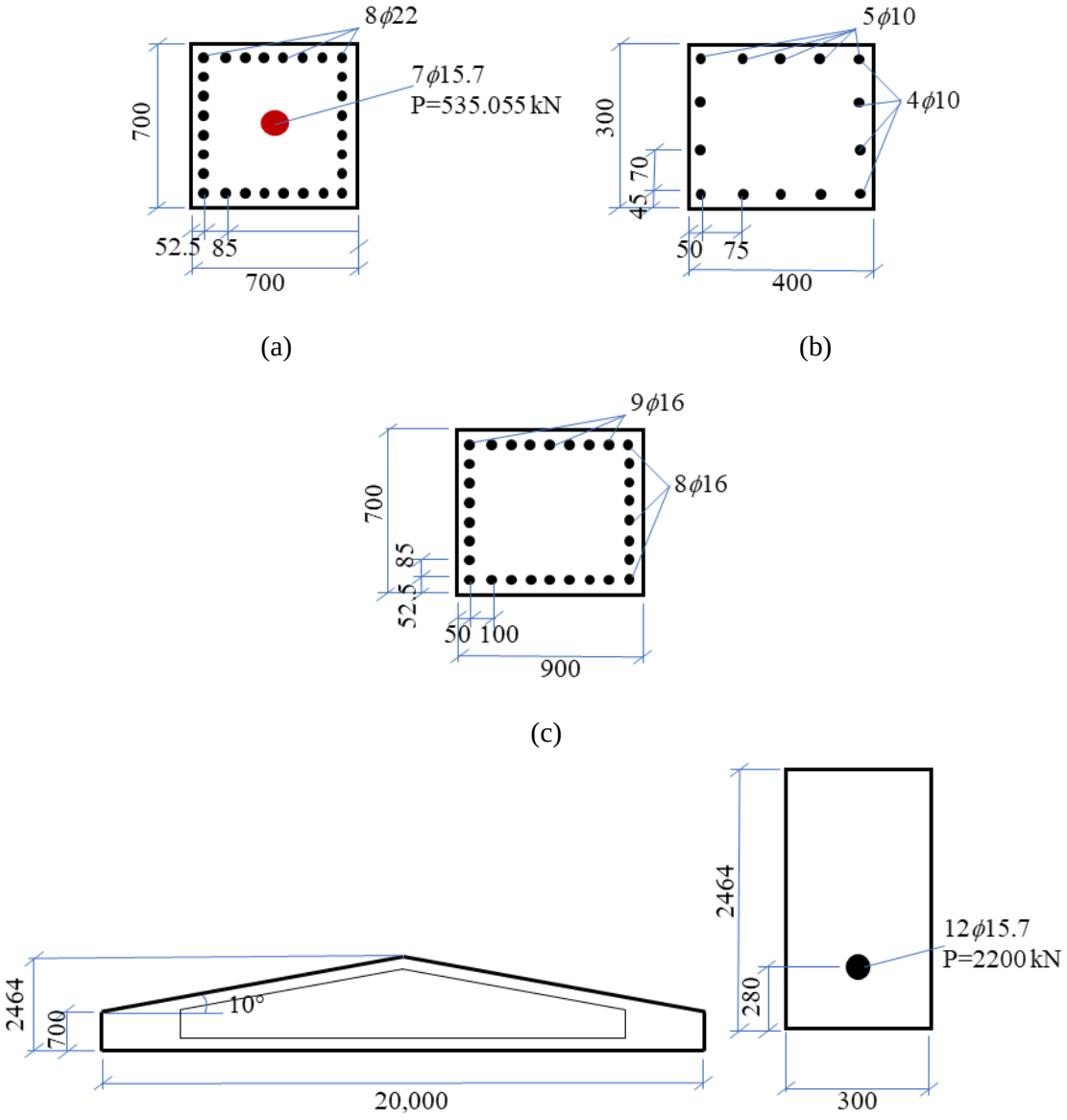

Figure 7-7 The section of: (a) the PT columns; (b) the secondary beams and support beams; (c) the support columns; and (d) the principle beams.

As mentioned, the horizontal force generated by the crane system is expected to be transferred to the ground by the cantilever columns. Figure 7-8 shows the schematic of a set of SKID-support column with its boundaries. In the figure, K_{SC}, K_{SKID}, and $K_{PT\ outer\ frame}$ are the stiffness of the support columns, the loading stiffness of the SKID device, and the lateral stiffness of the PT outer frame. It is worth to be noted that the horizontal force in the longitudinal direction is carried by all the support columns of the structure, and the lateral stiffness of the PT outer frame is that of

the whole structure because the rigid diaphragm is considered. The force generated by the crane system, F_{crane}, is applied at the top of the support column. The structural analysis results show that 96.6% and 99.9% of the F_{crane} are transferred to the fixed end (the ground) in the transversal direction and the longitudinal direction, respectively.

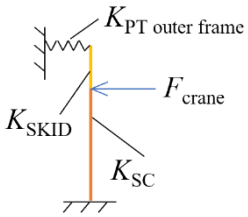

Figure 7-8 Schematics of a set of SKID-support column system with its boundaries.

7.4 Quasi-static and seismic performance of the PTPW-SKID case frame

7.4.1 The numerical model of the PTPW-SKID frame

A full-scale three-dimensional numerical model was built in OpenSees to investigate the static hysteretic behaviours and the seismic performance of the PTPW-SKID case structure, as shown in Figure 7-9 (McKenna, 2011). The rigid roof diaphragm system was simplified by a beam grid with fixed connections, as shown in Figure 7-9 (a). The crane system was not modelled because its influence on the global seismic behaviour of the PTPW-SKID frame is ignorable as stated in Section 3.3. As diaphragm effect of the roof system was considered, the positions of the SKID devices working in the Y direction were moved to align with the plane of the PT columns, as shown in Figure 7-9 (a). The roof panels and wall claddings were not modelled. The seismic mass of the structure was 504.126 t and assigned along the primary beams as uniformly distributed loads, which follows the real load path of the structure. The primary beams were pinned with the PT columns in the model. The beams and columns are modelled by elastic beam-column element with their elastic modulus and second moment of the area estimated by the section analysis. The linear and P-Delta geometric transformations are adopted for beams and columns. The corotational truss element modelled the cables with a yield point of 1860 MPa. The column-foundation interface was modelled by 100×100 evenly spaced compression-only springs, combined into a zero-length element with a fibre section and elastic-perfectly plastic gap material for each fibre, as shown in Figure 7-9 (a). The contact stiffness was set to one-third of the section height, according to Spieth et al. (2004). The yield point of each fibre was 355 MPa as the contact faces of the columns and foundations were covered by armour steel. Figure 7-9 (b) shows the

model's front view (the X-Z plane) where the SKID devices and support columns are detailed. The SKID devices were modelled by an equivalent method, in which every four groups of spring-slope blocks working in the same direction (two groups in each SKID and two SKID in each frame) were replaced by one group. Thus, the spring stiffness K_S was four times than designed tip stiffness of the cantilever bars of the SKID device, while the slope angle β and friction coefficient μ were the same as the design. This simplification was valid because the loading stiffness of the SKID device was proportional to the stiffness of the cantilever bars. The support columns were modelled by springs with their tip stiffness and simplified to be located between the beam and sliding blocks rather than between the slope blocks and the ground. This simplification was valid because the SKID device and the support column were connected in line between the beam and the ground; thus, their connection sequence did not affect the global behaviour in schematics. These simplifications were made to reduce numerical integrity complexity. It is worth to be noted that the simplified model was not centrosymmetric, which will raise torsion in the horizontal plane under seismic actions. Thus, the horizontal rotational degree of freedom of beams was restrained to avoid torsion of the structure to consider the centrosymmetric of the original structure. The sliding keys and slope blocks of the SKID device were modelled by the standard brick element, and the sliding surfaces were modelled by the simple contact 3D element with 3D contact material. A Rayleigh damping ratio of 5% was specified for all elements.

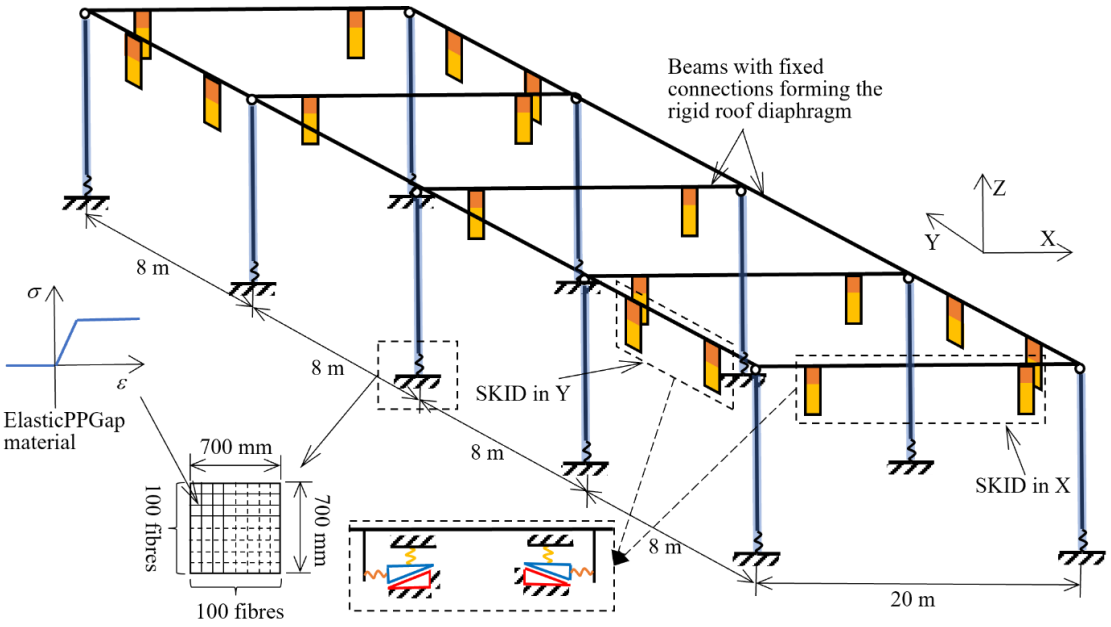

(a)

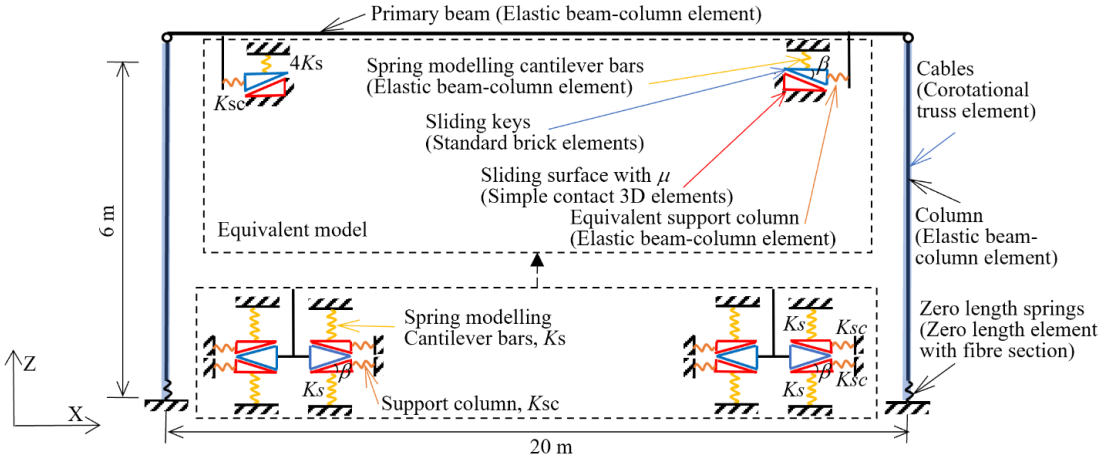

(b)

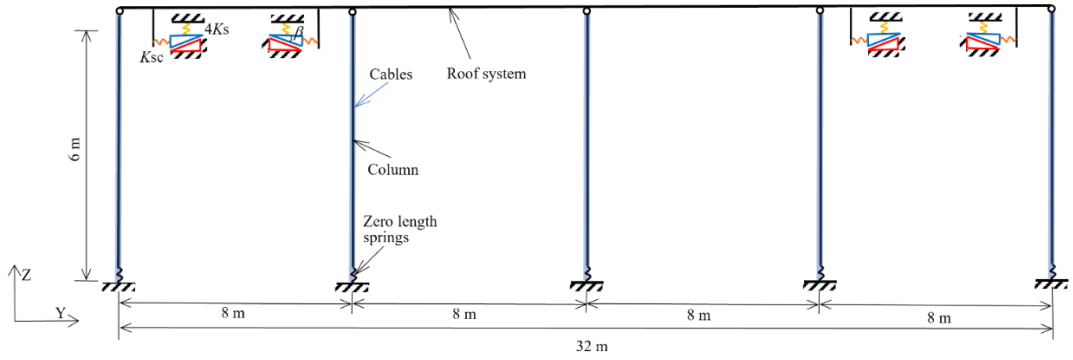

(c)

Figure 7-9 OpenSees model of the structure: (a) the 3D view; (b) the front view of the transversal frame in the X-Z plane; and (c) the side view of the longitudinal frame in Y-Z plane.

7.4.2 Quasi-static cyclic tests and the benchmark of the numerical model

Quasi-static cyclic tests with a peak amplitude of 2% drift ratio were carried out to present the hysteretic performance of the PTPW-SKID structure. In accordance with the actual seismic load path, the horizontal uniformly distributed loads were applied on the primary beams in the X direction, and horizontal point loads were applied on the top of columns in the Y direction. Displacement control was utilised in the numerical analysis. Figure 7-10 (a) shows the hysteretic curves of the structure drifting only in the transversal plane (the X-direction, with the loads in the Y-Z plane set to 0) or in the longitudinal plane (the Y-direction, with the loads in the X-Z plane set to 0). As shown, both hysteretic curves have a dual-triangular-flag shape. Figure 7-10 (b) shows the hysteretic curves of the middle transversal frame. As shown, the hysteretic curve of this subframe has the same shape as that of the whole structure, and its strength is one-fifth of the entire structure. The hysteretic curve of the frame is the composite of the nonlinear elastic backbone of the PT outer frame and the triangular-shaped hysteresis of the SKID inner frame, as shown in Figure 7-10 (b). In addition, the hysteretic curves of the SKID inner frame estimated by

Eq. (7-9) and Eq.(7-15) of the middle transversal frame are plotted in Figure 7-10 (b) to benchmark the numerical model. The curves obtained from the OpenSees model match well with that estimated by the equations.

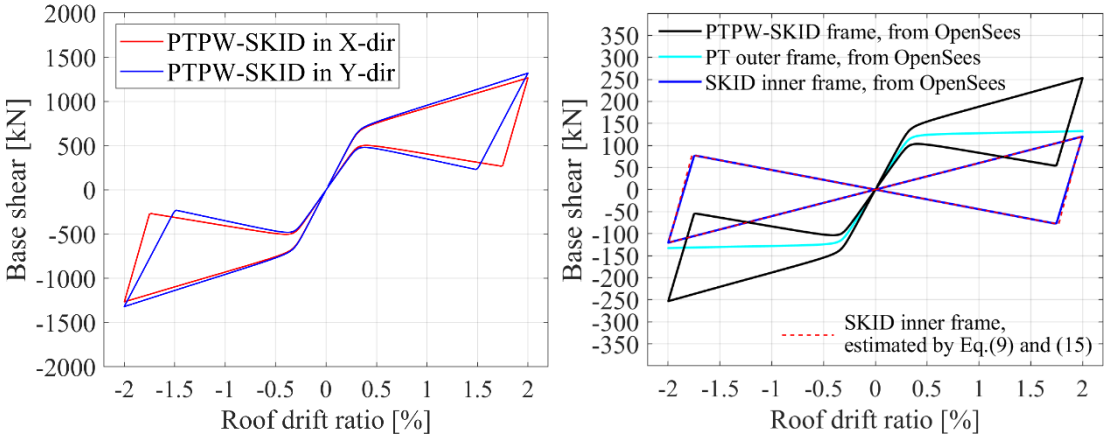

(a) (b)

Figure 7-10 Hysteretic curves of: (a) the structure when it drifts only in the X-direction or Y-direction; (b) the PT outer frame and SKID inner frame of the middle transversal frame when the structure drift only in the X-direction.

Figure 7-10 shows the hysteretic curves when the structure drifts in only one direction, where the PT column has a planar deformation. However, under seismic actions, the structure drifts in both directions, resulting in a 3D rocking motion of the PT columns. Figure 7-11 shows the hysteretic curves of the PT outer frame in the X direction when the structure was subjected to a cyclic load with a peak drift ratio of 2% in the X direction and a constant drift ratio (of 0%, 0.5%, 1.0%, 1.5% and 2%) in the Y direction. As shown, the initial stiffness of the structure in the X direction decreases with the drift ratio increase in the other direction, whereas the 'post-yield' stiffness and peak strength increase. Note that the hysteretic curve of the SKID inner frames does not affect by the 3D motion of the structure and is not presented in the figure.

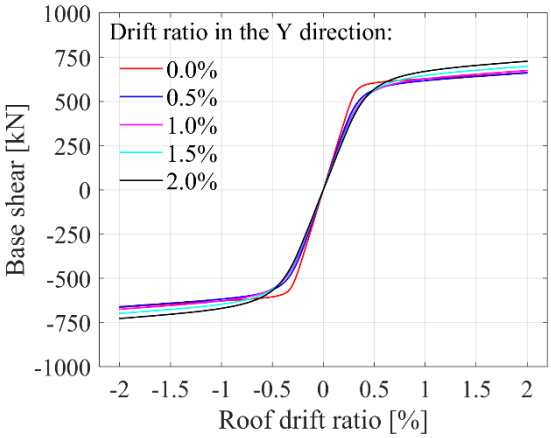

Figure 7-11 Hysteretic curves of the PT outer frame subjected to the cyclic load in the X direction when a constant drift ratio in the other.

7.4.2 Seismic performance of the PTPW-SKID case structure

Seven pairs of ground motions were selected from the European Strong-Motion Database to match the target acceleration code spectrum for the site (L'Aquila, Italy) at Ultimate Limit State (with a return period of 475 years) with an upper tolerance of 30% and a lower tolerance of 10% between 0.15s to 2s. All the ground motions were recorded at the sites of soil type C, and their distance to the source was between 0 to 60 km. The magnitudes of the events were between 4.5 to 8 M. The field conditions were unspecified in the selection. The information on the selected ground motions is summarised in Table 7-4. Figure 7-12 shows the 5%-damped linearly elastic response spectrum of the ground motions. The average acceleration response matches well with the target spectrum for the site.

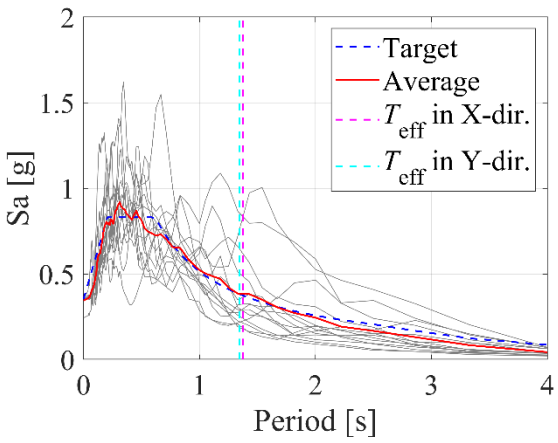

Figure 7-12 5%-damped linearly elastic spectrum of the ground motions.

Table 7-4 Information of the ground motions.

GM	Earthquake Event	Station ID	Magnitude (Richter scale)	Fault Mechanism	R_{epi} (km)	PGA (g)	
						X	Y
1	Friuli (aftershock), 1976	ST33	6	thrust	9	1.0686	0.9324
2	Ionian, 1973	ST8	5.8	thrust	15	5.1459	2.4983
3	Alkion, 1981	ST121	6.6	normal	20	2.2566	3.0363
4	Adana ,1998	ST549	6.3	strike slip	30	2.1575	2.6442
5	Ishakli (aftershock), 2002	ST856	5.8	normal	35	0.394	0.5069
6	Dinar, 1995	ST271	6.4	normal	8	2.6739	3.1306
7	Izmit, 1999	ST576	7.6	strike slip	39	0.8976	1.2659

The seismic performance of the structure subjected to the selected ground motions was investigated. The model was simultaneously activated in its *X* and *Y* direction by two horizontal components of each pair of ground motions. The peak drift ratio of the structure in each direction is shown in Figure 7-13 (a). The results on the left side of the figure represent the scenarios where the structure was subjected to seismic excitations in both the X and Y directions by the ground motion components with the same directional markers. Those on the right side are the scenarios where the activation direction of two components interchanged. The average peak drift ratios are also shown in the figure. As shown, the average peak drift ratio of the structure is 1.98% and 2.02% in the *X* and *Y* direction, respectively, which are around the design target drift ratio of 2.00%. In addition, the residual drift ratios of all the cases are negligible, which indicates the self-centring feature of the PTPW-SKID structure. The peak drift ratio and the residual drift ratio responses of the structure indicate that the PTPW-SKID structure met its design targets.

Then the structure was activated in two directions to compare the responses of planar and 3D motion. The peak drift ratio responses of the structure in each direction subjected to each component of ground motions are shown in Figure 7-13 (b). The average peak drift ratio in the X direction and the Y direction is 1.97% and 2.02%, respectively, which is close to the average response of the 3D motion, indicating the reliability of the seismic design based on planar frames. In addition, the peak drift ratio response in the two directions is almost the same for all ground motions. However, the structure has a different profile and hysteretic behaviours (see Figure 7-10 (a)) in two directions. This verifies the robustness of the DDBD design in achieving the design target. It is worth noting that all the elements were assumed elastic in the analysis, which aligns with the employed design logic at ULS. Figure 13(a) and (b) show that under Ground Motion 2,

3, and 5, the peak drift ratio may exceed 3.5%, potentially causing yielding in certain elements. However, this research focuses on the average peak drift ratio to evaluate the achievement of the design target at ULS. Thus, it is reasonable to use the hysteretic behaviour of the frame at ULS (i.e., a numerical model with elastic elements) in this research. The behaviour of the frame at significant events is beyond the scope of this research.

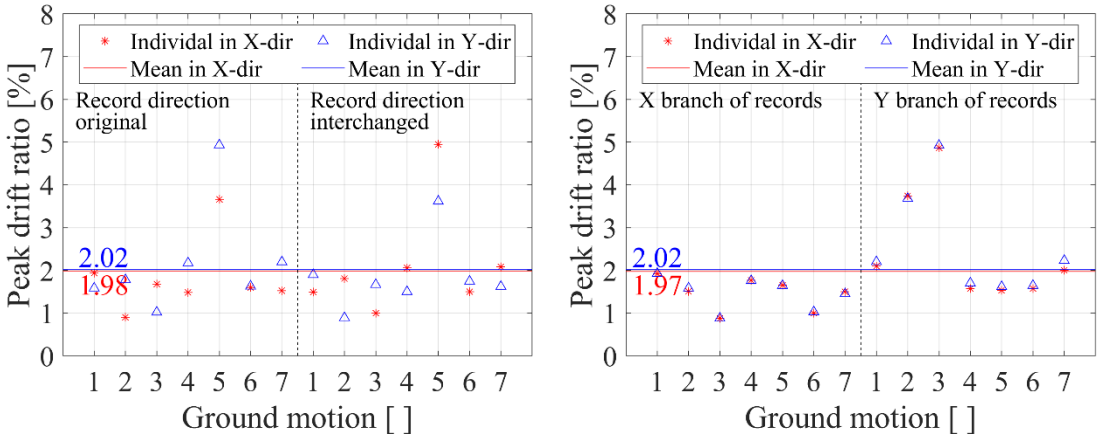

Figure 7-13 Individual and average peak drift ratio response of the structure subjected to the selected ground motions: (a) 3D motion; and (b) planar motion.

Figures 7-14 (a) and (b) show the hysteretic curves of the structure subjected to the Ground Motion 6 in the X and Y direction, respectively. The structure presents expected stable dual-triangular-flag-shaped hysteretic curves under earthquake excitations. The hysteretic curves of the PTPW-SKID structure are the combination of the PT outer frame and the SKID inner frame, as shown in Figures 7-14 (c) and (d). As shown, the hysteretic curves of the PT outer frame in different cycles are nonoverlapping and have various stiffness and gap-opening behaviours (stiffness softening). This is because the drifts that developed in the other direction were different for each cycle, as demonstrated in Figure 7-11.

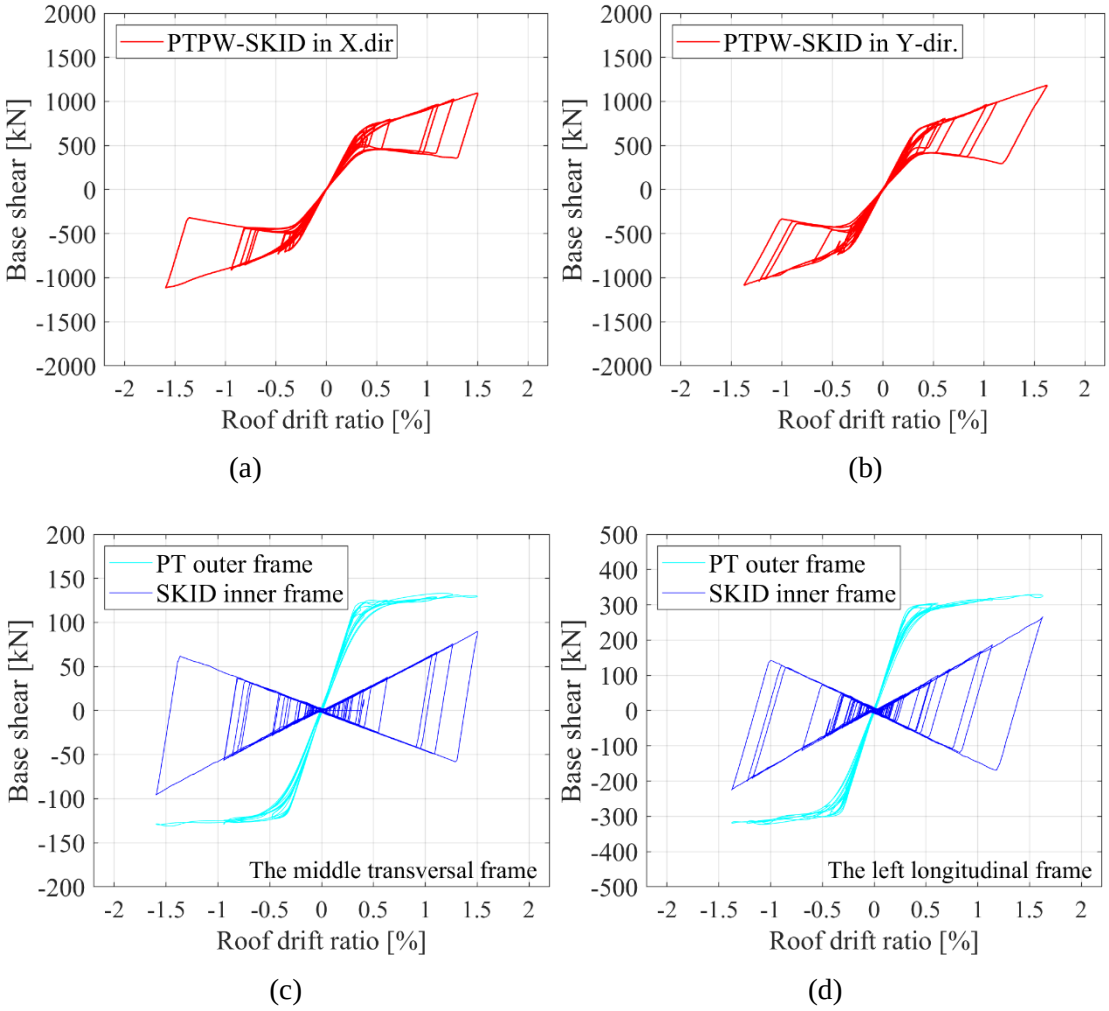

Figure 7-14 Hysteretic curve of: (a) the PTPW-SKID in the X direction, (b) the PTPW-SKID in the Y direction, (c) the PT outer frame and SKID inner frame in the X direction, and (d) the PT outer frame and SKID inner frame in the Y direction subjected to Ground Motion 6.

Finally, the peak drift ratio response of the structure at the SLS is double-checked. The selected ground motions were scaled to make their average match the design acceleration spectrum at SLS defined by the parameters listed in Table 7-2. The peak drift ratio of the structure in each direction under each ground motion is shown in Figure 7-15. The average peak drift ratio among cases is 0.31% and 0.32% in the X and Y direction, respectively, which meets the drift ratio limit of 0.5% at the SLS.

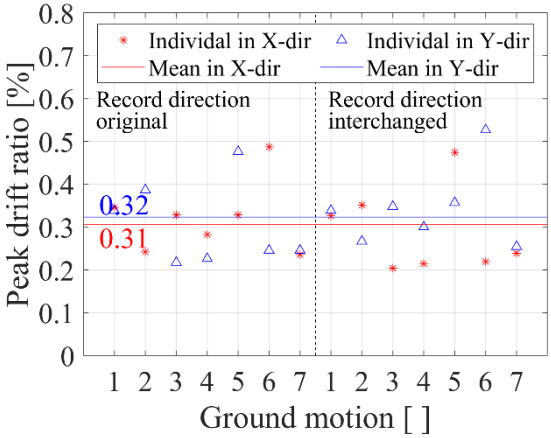

Figure 7-15 Individual and average peak drift ratio response of the structure subjected to the selected ground motions scaled to the SLS seismic hazard.

7.5 Conclusions

This chapter proposes a novel Post-Tensioned Precast Warehouse Structure with the Sliding Keys on Inclined Deflecting-cantilevers Device (the PTPW-SKID Structure) by following the concept of the PT-SKID frame (presented in Chapter 5 and 6). It is developed as a full self-centring structural system for industrial buildings. The structural arrangement and the load paths are discussed first. The theoretic properties of the PTPW-SKID structure are analysed by focusing on the hysteretic curve of its SKID inner frame. Then, a case-study structure was designed. The DDBD method is utilised in its seismic design. To investigate the quasi-static performance and seismic responses of the PTPW-SKID structure, a 3D numerical model was built in OpenSees. This research yields the following conclusions:

1. The PTPW-SKID structure consists of a Post-Tensioned (PT) outer frame and a SKID inner frame. The PT outer frame supports the roof and wall cladding panels and carries the force applied to them. The SKID inner frame carries the SKID devices and the crane system. The lateral stiffness of the PTPW-SKID frame is provided by both the PT outer frame and the SKID inner frame, while the hysteretic damping is only from the SKID inner frame.

2. High support columns are utilised to support the SKID devices to meet the clear height requirements below the crane system and the roof. The elastic deformation of the support columns reduces the lateral stiffness and the equivalent damping ratio of the SKID inner frame compared with the SKID device alone.

3. Most of the horizontal force generated by the crane system can be designed to be transferred to the ground by the support columns. The case study demonstrated that the support columns could carry over 96% of the crane horizontal force.

4. The quasi-static analysis indicates that the PTPW-SKID structure performs a dual-triangular-flag-shaped hysteretic curve in both directions. Its hysteretic behaviour combines the nonlinear elastic backbone of the PT outer frame and the triangular-shaped hysteresis of the SKID inner frame. It is similar as the PT-SKID frames discussed in Chapter 5 and 6, although distortions exist because of the elastic deformation of the support columns. The dual-triangular-flag-shaped hysteretic curve indicates a full self-centring property in earthquake events.

5. The hysteretic curve of the PTPW-SKID structure in one direction is affected by the drift in the other. Specifically, the initial stiffness of the structure in one direction decreases with the drift ratio in the other, whereas the 'post-yield' stiffness and peak strength have the opposite trends.

6. The seismic response of the PTPW-SKID structure subjected to seven pairs of spectrum-compatible ground motions indicates that the DDBD design method yields satisfactory results in achieving the drift ratio design target. The structure performs a stable hysteretic behaviour under the seismic excitations and an ignorable residual drift ratio after the excitations.

7. The average peak drift ratio response of the structure subjected to one-direction excitations (planar deformation motion) is almost the same as that under two-direction excitations (3D deformation motion), indicating the reliability of the seismic design based on planar frames. In addition, the peak drift ratio responses in two directions are almost the same as each other in all ground motions. However, the structure has a different profile and hysteretic behaviours in two directions. It verifies the robustness of the DDBD design in achieving the design target.

Chapter 8 Conclusions and future research

8.1 Summary

This thesis presents a frictional damping device for application with PT frames. The conceptual FSSS system is proposed first. Its mechanical schematisation and theoretical hysteretic behaviours are discussed. The analytical formulations are derived to estimate its hysteretic curve and equivalent damping ratio. The FSSS system has a triangular-shaped hysteretic curve, providing additional damping and lateral stiffness for the PT frames. The device has a zero-activation threshold without inhibiting the self-centring feature of the PT frame. Then, a novel practical configuration (the SKID device) for the conceptual FSSS system is proposed. The SKID device achieves the triangular-shaped hysteretic curve by reposing sliding keys on cantilever-supported slope blocks. The reliability of the novel configuration is discussed.

In Chapter 4, the SKID device is physically demonstrated by two 1/4 reduced scaled prototypes. Their hysteretic behaviour and failure mode are investigated by carrying out quasi-static cyclic tests. The test results verified its consistency with the theory. Then, six 1/4-scale physical specimens with different friction coefficients μ, slope angle β, and cantilever stiffness k_s are built and tested. Five materials are tested as friction pads by carrying out quasi-static amplitude-increasing cyclic tests and fatigue tests.

Chapter 5 presents an application of the SKID device in the PT frames. The equations estimating the hysteretic curve of the PT-SKID frame are presented first. The PT-SKID frame performs a dual-triangular-flag-shaped hysteretic curve, indicating a full self-centring feature. Then, three heuristic frames with and without the SKID device are designed and numerically tested as a proof-of-concept. The benefits of the SKID device to the PT frame for resisting earthquake excitations are identified by carrying out the incremental dynamic analysis (IDA). Finally, over seven hundred numerical models of the PT-SKID frames were tested numerically in OpenSees to investigate the dynamic characters of the PT-SKID frames and the influence of the SKID device on the seismic responses of the PT-SKID frames.

Chapter 6 investigates the linearisation of the PT-SKID frames for estimating their seismic response. The equivalent system is constructed by the effective stiffness and equivalent damping ratio estimated by Jacobsen's method. First, a simplified model capturing the hysteretic properties of the PT-SKID frames is proposed. Then, the displacement estimation accuracy of the linear equivalence is evaluated by numerically testing 5,880 PT-SKID frames. The frames tested in the research cover the most common ranges of parameters of the PT-SKID frames. Both far-field and near-field record sets defined by FEMA P695 are utilised as seismic excitations. The results indicate that the linearisation frequently underestimated the peak drift ratio response, leading to an unconservative design when it is used in DDBD. Thus, a correction factor is suggested for the DDBD of the PT-SKID frames.

Chapter 7 presents a novel Post-Tensioned Precast Warehouse Structure with the Sliding Keys on Inclined Deflecting-cantilevers Device (the PTPW-SKID Structure). The new structural system follows the concept of the PT-SKID frame. It is developed as a full self-centring structural system for industrial buildings. The structural arrangement and the load paths are discussed first. The theoretic properties of the PTPW-SKID structure are analysed by focusing on the hysteretic curve of its SKID inner frame. Then, a warehouse structure located in L'Aquila is chosen as a case to demonstrate the design of the PTPW-SKID structure. The DDBD method is utilised in its seismic design. A 3D numerical model is built in OpenSees to investigate the quasi-static performance and seismic responses of the case structure.

8.2 Conclusions

The research presented in this thesis yields the following conclusions:

1. The proposed FSSS conception performs a triangular-shaped hysteretic curve featuring a zero-activation threshold. It can provide additional stiffness and frictional damping for the application within PT frames without inhibiting their self-centring.

2. The proposed SKID device realises the FSSS conception in a simple configuration. The SKID device uses cantilever bars that perform two functions: (i) acting as a spring to generate the normal force on the sliding contact surface and (ii) carrying a lateral stiff support force. Although the flexibility of the cantilever bar has some small adverse effects on the stiffness and the equivalent damping ratio of the SKID device, these effects can be mitigated by selecting proper SKID parameters (a smaller slope angle β, friction coefficient μ and cantilever bar ratio of second moments of area λ).

3. The cyclic tests conducted on the physical prototypes of the SKID device demonstrate that the proposed device can exhibit stable and repeatable triangular-shaped hysteretic behaviour and satisfactory energy dissipation capabilities. In addition, the SKID devices with negative unloading stiffnesses have a better energy dissipation capability than those with positive unloading stiffnesses.

4. Different mechanical properties (loading stiffness K_{SKID} and equivalent damping ratio ζ_{eq}) can be achieved on the SKID device by adjusting friction coefficient μ, slope angle β, and cantilever bar stiffness k_s. Specifically, large values for μ, β and k_s lead to a larger K_{SKID}; a large μ but low β lead to a higher ζ_{eq}. The friction pads on the sliding keys can be steel, cooper, bronze or break lining. The brake lining pads showed the most stable and repeatable hysteretic behaviour, while the metal pads (especially the steel pads) exhibited fluctuations in loading stiffness with severe abrasion. Although the metal pads experienced severe abrasion, all the specimens performed stable hysteretic behaviours in general. No stiffness or strength degradation in the global behaviours of the specimen linked to the loading cycle numbers was observed.

5. The PT-SKID frame has a dual-triangular-flag-shaped hysteretic loop. Its equivalent damping ratio is amplitude dependent, increasing with drift. The IDA analysis indicates that the SKID device can significantly reduce the peak drift ratio response of the PT frame without inhibiting its self-centring.

6. The Frequency Response Functions (FRFs) obtained from the sin-sweep excitations indicate that the PT-SKID frames remain the typical dynamic characters of nonlinear systems, featuring two branches at higher and lower response levels with coexisting solutions. However, the SKID devices considerably reduced the amplitude of responses and the range of the coexisting solutions. Specifically, the response amplitude was reduced with a greater K_{SKID} and μ but smaller β.

7. The sensitivity analysis of the PT-SKID frames indicates that large K_{SKID} and μ with a small β lead to a small response amplitude. The trend regarding β and μ can be explained by their influence on the equivalent damping ratio calculated by Jacobson's method.

8. Although the transient response of over one in eleven cases surpassed their self-centring (quasi-static) threshold, all the cases recentred after earthquakes. This result indicates an excellent self-centring feature of the PT-SKID frames, and the self-centring (quasi-static) threshold does not place a limitation on self-centring design. However, the recentring for the frames with small recentring threshold relies on a sufficient reactivation peak in the following excitations. The

amplitude requirement of this ‘following sufficient peak’ and its existence in earthquakes need further investigation.

9. For the mid- to long- period PT-SKID frames, the linear equivalence based on Jacobsen’s estimation always underestimates their seismic displacement response (with η_{ave} greater than 1). This indicates that the linearisation will lead to an unconservative design in the DDBD. Thus, a correction factor (C_e) having a 95% confidence is suggested for the design spectrum used in the DDBD of the PT-SKID frames.

10. For the mid- to long- period PT-SKID frames, although η_{ave} may be slightly less than 1 under near-field ground motions when T_e and κ are small, the ground motion characters (far field or near field) do not have an obvious influence on η_{ave} in general.

11. The PTPW-SKID structure consists of a Post-Tensioned (PT) outer frame and a SKID inner frame. The PTPW-SKID structure performs a dual-triangular-flag-shaped hysteretic curve in both directions. Its hysteretic behaviour combines the nonlinear elastic backbone of the PT outer frame and the triangular-shaped hysteresis of the SKID inner frame. However, as a high support columns have to be used in the SKID inner frame, the effect of their elastic deformation cannot be neglected. Theoretical analysis indicates that the elastic deformation of the support columns reduces the lateral stiffness and the equivalent damping ratio of the SKID inner frame compared with the SKID device alone.

12. The results of the quasi-static analysis show that the hysteretic curve of the PTPW-SKID structure in one direction is affected by the drift in the other. Specifically, the initial stiffness of the structure in one direction decreases with the drift ratio in the other, whereas the 'post-yield' stiffness and peak strength have the opposite trends.

13. The seismic response of the PTPW-SKID structure subjected to seven pairs of spectrum-compatible ground motions indicates that the DDBD design method yields satisfactory results in achieving the drift ratio design target. The structure performs a stable hysteretic behaviour under the seismic excitations and an ignorable residual drift ratio after the excitations.

14. The average peak drift ratio response of the structure subjected to one-direction excitations (planar deformation motion) is almost the same as that under two-direction excitations (3D deformation motion), indicating the reliability of the seismic design based on planar frames. In addition, the peak drift ratio responses in two directions are almost the same as each other in all

ground motions, although different profiles are used in two directions. It verifies the robustness of the DDBD design in achieving the design target.

8.3 Contributions of the research

This thesis presents a novel Sliding Keys on Inclined Deflecting-cantilevers (SKID) device and its application in Post-Tensioned (PT) frames. The research makes the following contributions:

1. The research proposed a new schematic named a Frictional Sliding on a Spung Slope (FSSS) system. This schematic could achieve a triangular-shaped hysteretic curve in all four quadrants, giving the system have excellent energy dissipating capability without an activation threshold.

2. A novel Sliding Keys on Inclined Deflecting-cantilevers (SKID) device is proposed based on the FSSS conception. Its configuration reliability and hysteretic behaviour are investigated by theoretical analysis and physical demonstration. This research establishes the foundation for a practical SKID device and its further study.

3. The application of the SKID device in one-storey, one-bay PT frames is investigated. The dynamic properties and seismic behaviour of the PT-SKID frames are numerically analysed. The contributions of the SKID device to the seismic performance of the PT frames are identified. Design guidance for the DDBD method of the PT-SKID frames is provided based on the sensitivity analysis and linearisation accuracy analysis. This research delivers the basic dynamic performance of the PT-SKID frames and its seismic design logic.

4. Following the PT-SKID conception, a self-centring precast warehouse structure is proposed. Its hysteretic behaviour, especially the influence of high support columns, is theoretically investigated. This hysteretic character can be applied to other PT-SKID frames with high support columns below the SKID device. A case study is conducted based on the research outcomes presented in previous sections. This research can potentially inform retrofit technologies for existing precast one-storey industrial structures.

8.4 Limitations and future research

Further work is required to ensure SKID’s reliability in practical applications. This section lists possible limitations of the current work and suggestions for future research.

1. The configuration of the SKID device was proposed and physically demonstrated in this research. However, the configuration of the final products of the SKID device should be further detailed, such as its connections with the beam and support columns, the connection of the slope blocks to the cantilever bars, and the shape of sliding keys.

2. The physical tests carried out in this research were quasi-static cyclic tests. Dynamic tests are required to physically demonstrate stability of the SKID device in earthquakes. Shake-table tests for the PT-SKID frames are suggested.

3. Although the PT-SKID frames are expected to maintain elasticity during earthquakes, the failure modes of their structural components should be further investigated considering the unpredictability of earthquakes. A feasible failure behaviour can help mitigate the risks of structural collapse in an unexpected event. For the PT-SKID frames, 'designing' a proper failure mode is possible. For example, a failure sequence of components can be assigned by following capacity design logic.

4. This research proposed a novel PTPW-SKID structure system for industrial buildings and demonstrated its seismic design and performance by conducting a case study. However, further research is required, such as the reliability of connections among structural components, the 3D rocking behaviour of the PT outer frames, the possibility of the primary beams torsion, and the diaphragm effect of the cast-in-situ roof system. Additionally, application scenarios of the PTPW-SKID structure systems should be suggested based on life cycle costs analysis.

5. In this research, the application of the SKID device is within one-storey frames. Further efforts are needed to study the effectiveness of the SKID device in multi-storey buildings. This may include the reasonable load path for the building, the stiffness ratio between the SKID device and the PT frame, and the optimised distribution of the SKID stiffness along the building height.

REFERENCES

Aaleti, S., & Sritharan, S. (2009). A simplified analysis method for characterizing unbonded post-tensioned precast wall systems. *Engineering Structures*, *31*(12), 2966-2975.

American Institute of Steel Construction. (AISC). (2010). Seismic Provisions for Structural Steel Buildings, AISC 341-10, Chicago, IL: *American Institute of Steel Construction.*

Ajrab, J. J., Pekcan, G., & Mander, J. B. (2004). Rocking wall–frame structures with supplemental tendon systems. *Journal of Structural Engineering*, 130(6), 895-903..

Akbas, T., Sause, R., Ricles, J. M., Ganey, R., Berman, J., Loftus, S., ... & Blomgren, H. E. (2017). Analytical and experimental lateral-load response of self-centering posttensioned CLT walls. *Journal of Structural Engineering*, *143*(6), 04017019.

Alexander, N. A., Oddbjornsson, O., Taylor, C. A., Osinga, H. M., & Kelly, D. E. (2011). Exploring the dynamics of a class of post-tensioned, moment resisting frames. *Journal of sound and vibration*, 330(15), 3710-3728.

American Society of Civil Engineering (ASCE). (2017). Minimum design loads and associated criteria for buildings and other structures, ASCE/SEI 7-16. Reston, VA: *American Society of Civil Engineers*.

Applied Technology Council (ATC). (2009). Quantification of building seismic performance factors. US Department of Homeland Security. *Federal Emergency Management Agency*.

Applied Technology Council & National Earthquake Hazards Reduction Program (ATC & NEHRP), 2012. Seismic performance assessment of buildings. *Federal Emergency Management Agency*.

Bachmann, H., & Dazio, A. (2019). A deformation-based seismic design procedure for structural wall buildings. In *Seismic Design Methodologies for the Next Generation of Codes* (pp. 159-170). Routledge.

Bachmann J., Vassiliou M.F., & Stojadinović B. (2017). Dynamics of rocking podium structures, *Earthquake Engineering & Structural Dynamics*, 46 2499-2517.

Beck J., & Skinner R. (1973). The seismic response of a reinforced concrete bridge pier designed to step, *Earthquake Engineering & Structural Dynamics*, 2 343-358.

Blandon, C. A., & Priestley, M. J. N. (2005). Equivalent viscous damping equations for direct displacement-based design. *Journal of earthquake Engineering*, 9(sup2), 257-278.

Bremskerl. (2007). Datasheet of the braking lining BK5505. Available at: www.bremskerl.de/en/technical-datasheet/industrial_applications/bk6445/view (Accessed: June 2021).

Bricco. (2012) *A rischio settemila posti di lavoro*. II Sole 24 ore, 141:37.

Calvi, P.M., Moratti, M. and Calvi, G.M. (2016). Seismic isolation devices based on sliding between surfaces with variable friction coefficient. *Earthquake Spectra*, 32(4), pp.2291-2315.

Calvi, G.M., Calvi, P.M. and Moratti, M. (2017). Seismic isolation of buildings using devices based on sliding between surfaces with variable friction coefficient. *Innovative Infrastructure Solutions*, 2, pp.1-18.

Cao Y. (2010). Probability Density Function (PDF) Estimator (V3.2) (https://www.mathworks.com/matlabcentral/ fileexchange/19121-probability-density-function-pdf-estimator-v3-2), MATLAB Central File Exchange. Updated April 08, 2010. Retrieved January 11, 2023.

Chancellor N.B., Eatherton M.R., Roke D.A., & Akbaş T. (2014). Self-centering seismic lateral force resisting systems: High performance structures for the city of tomorrow. *Buildings*. 4 520-548.

Cheok, G. S. (1997). A hybrid reinforced precast frame for seismic regions. *PCI journal*, 42(2), 20-32.

Cherepinskiy, Y. (2004, August). Seismic isolation of buildings with application of the kinematics bases. In *13th world conference on earthquake engineering*.

Chopra, A. K. (2007). *Dynamics of Structures: Theory and Applications to Earthquake Engineering*, Prentice Hall. Inc., Upper Saddle River, NJ.

Chou, C. C., & Chen, J. H. (2011). Seismic design and shake table tests of a steel post-tensioned self-centering moment frame with a slab accommodating frame expansion. *Earthquake Engineering & Structural Dynamics*, *40*(11), 1241-1261.

Chou, C. C., Chen, J. H., Chen, Y. C., & Tsai, K. C. (2006). Evaluating performance of post-tensioned steel connections with strands and reduced flange plates. *Earthquake engineering & structural dynamics*, 35(9), 1167-1185.

Chou, C. C., Chen, Y. C., Pham, D. H., & Truong, V. M. (2014). Steel braced frames with dual-core SCBs and sandwiched BRBs: Mechanics, modeling and seismic demands. *Engineering Structures*, *72*, 26-40.

Chou, C. C., Chung, P. T., & Cheng, Y. T. (2016). Experimental evaluation of large-scale dual-core self-centering braces and sandwiched buckling-restrained braces. *Engineering Structures*, *116*, 12-25.

Chou, C. C., Wu, T. H., Beato, A. R. O., Chung, P. T., & Chen, Y. C. (2016a). Seismic design and tests of a full-scale one-story one-bay steel frame with a dual-core self-centering brace. *Engineering Structures*, *111*, 435-450.

Christopoulos, C., Filiatrault, A., Uang, C. M., & Folz, B. (2002). Posttensioned energy dissipating connections for moment-resisting steel frames. *Journal of Structural Engineering*, 128(9), 1111-1120.

Christopoulos, C., Tremblay, R., Kim, H. J., & Lacerte, M. (2008). Self-centering energy dissipative bracing system for the seismic resistance of structures: development and validation. *Journal of structural engineering*, 134(1), 96-107.

Clayton, P. M., Berman, J. W., & Lowes, L. N. (2012). Seismic design and performance of self-centering steel plate shear walls. *Journal of structural engineering*, *138*(1), 22-30.

Clayton, P. M., Berman, J. W., & Lowes, L. N. (2013). Subassembly testing and modeling of self-centering steel plate shear walls. *Engineering Structures*, *56*, 1848-1857.

Clayton, P. M., Dowden, D. M., Li, C. H., Berman, J. W., Bruneau, M., Lowes, L. N., & Tsai, K. C. (2016). Self-centering steel plate shear walls for improving seismic resilience. *Frontiers of Structural and Civil Engineering*, *10*, 283-290.

Clough, R. W., & Huckelbridge, A. A. (1977). *Preliminary experimental study of seismic uplift of a steel frame*. Earthquake Engineering Research Center, College of Engineering, University of California.

De Baere, I., Van Paepegem, W., & Degrieck, J. (2008). Design of mechanical clamps with extra long wedge grips for static and fatigue testing of composite materials in tension and compression. *Experimental Techniques*, *32*, 62-69.

Di Cesare, A., Ponzo, F. C., Lamarucciola, N., & Nigro, D. (2020). Experimental seismic response of a resilient 3-storey post-tensioned timber framed building with dissipative braces. *Bulletin of Earthquake Engineering*, *18*(15), 6825-6848.

Di Sarno, L. & Elnashai, A.S. (2005). Innovative strategies for seismic retrofitting of steel and composite structures. *Progress in Structural Engineering and Materials*, 7(3), pp.115-135.

Dimopoulos, A. I., Karavasilis, T. L., Vasdravellis, G., & Uy, B. (2013). Seismic design, modelling and assessment of self-centering steel frames using post-tensioned connections with web hourglass shape pins. *Bulletin of Earthquake Engineering*, 11(5), 1797-1816.

Dimopoulos, Athanasios I., Angelos S. Tzimas, Theodore L. Karavasilis, & Dimitrios Vamvatsikos. (2016) Probabilistic economic seismic loss estimation in steel buildings using post‐tensioned moment‐resisting frames and viscous dampers. *Earthquake Engineering & Structural Dynamics*, 45, no. 11: 1725-1741.

Dolgaya, A. A., & Indeikin, A. V. (2002). Statistical analysis of Arias intensity and velocity for actual earthquakes. *Seimostoikoe Stroit.*, 2, 32-33.

Dowden, D. M., & Bruneau, M. (2011). NewZ-BREAKSS: Post-tensioned rocking connection detail free of beam growth. *Engineering Journal(Chicago)*, *48*(2), 153-158.

Dowden, D. M., & Bruneau, M. (2019). Quasi-static cyclic testing and analytical investigation of steel plate shear walls with different post-tensioned beam-to-column rocking connections. *Engineering Structures*, *187*, 43-56.

Dowden, D. M., Purba, R., & Bruneau, M. (2012). Behavior of self-centering steel plate shear walls and design considerations. *Journal of Structural Engineering*, *138*(1), 11-21.

Du, Y., Peng, J. Z., Liew, J. R., & Li, G. Q. (2018). Mechanical properties of high tensile steel cables at elevated temperatures. *Construction and Building Materials, 182*, 52-65.

Dwairi, H., Kowalsky, M. J., & Nau, J. M. (2007). Equivalent damping in support of direct displacement-based design. *Journal of Earthquake Engineering*, *11*(4), 512-530.

Dwairi, H., & Kowalsky, M. J. (2004, August). Investigation of Jacobsen's equivalent viscous damping approach as applied to displacement-based seismic design. In *Proceeding of 13th World Conference on Earthquake Engineering* (pp. 1-6).

Eatherton, M. R. (2010). *Large-scale cyclic and hybrid simulation testing and development of a controlled-rocking steel building system with replaceable fuses*. University of Illinois at Urbana-Champaign.

Eatherton, M. R., Ma, X., Krawinkler, H., Mar, D., Billington, S., Hajjar, J. F., & Deierlein, G. G. (2014). Design concepts for controlled rocking of self-centering steel-braced frames. *Journal of Structural Engineering*, *140*(11), 04014082.

Ercolino, M., Bellotti, D., Magliulo, G., & Nascimbene, R. (2018). Vulnerability analysis of industrial RC precast buildings designed according to modern seismic codes. *Engineering Structures*, 158, 67-78.

Erochko, J., Christopoulos, C., Tremblay, R. & Choi, H., (2011). Residual drift response of SMRFs and BRB frames in steel buildings designed according to ASCE 7-05. *Journal of Structural Engineering*, 137(5), pp.589-599.

Eshleman, R. (1972). Dynamic Response of a ring spring. *The shock and vibration bulletin*, 42, 7.

European Committee for Standardization (CEN). (2004). Eurocode 8: Design of structures for earthquake resistance. *Brussels: European Committee for Standardization*.

European Committee for Standardization (CEN). (2004a). Eurocode 2: Design of concrete structures. *Brussels: European Committee for Standardization*.

European Committee for Standardization (CEN). (2005). Eurocode 1: Actions on structures. *Brussels: European Committee for Standardization*.

Fajfar, P. (2000). A nonlinear analysis method for performance-based seismic design. *Earthquake spectra*, *16*(3), 573-592.

Filiatrault, A., Tremblay, R., & Kar, R. (2000). Performance evaluation of friction spring seismic damper. *Journal of Structural Engineering*, 126(4), 491-499.

Freddi, F., Galasso, C., Cremen, G., Dall'Asta, A., Di Sarno, L., Giaralis, A., Gutiérrez-Urzúa, F., Málaga-Chuquitaype, C., Mitoulis, S.A., Petrone, C. & Sextos, A. (2021). Innovations in earthquake risk reduction for resilience: Recent advances and challenges. *International Journal of Disaster Risk Reduction*, 60, p.102267.

Freddi, F., Dimopoulos, C.A. & Karavasilis, T.L. (2017). Rocking damage-free steel column base with friction devices: design procedure and numerical evaluation. *Earthquake Engineering & Structural Dynamics*, 46(14), pp.2281-2300.

Garlock, M., & Li, J. (2008). Steel self-centering moment frames with collector beam floor diaphragms. *Journal of Constructional Steel Research*, *64*(5), 526-538.

Garlock, M., Ricles, J. M., & Sause, R. (2005). Experimental studies of full-scale posttensioned steel connections. *Journal of Structural Engineering*, 131(3), 438-448.

Garlock, M., Liu, J., & King, A. (2006, October). Construction details for self-centering moment resisting frame floor diaphragms. In *Proceedings, US-Taiwan Workshop on Self-Centering Structural Systems*.

Gelagoti, F., Kourkoulis, R., Anastasopoulos, I., & Gazetas, G. (2012). Rocking-isolated frame structures: Margins of safety against toppling collapse and simplified design approach. *Soil Dynamics and Earthquake Engineering*, 32(1), 87-102.

Gentile, R., & Galasso, C. (2021). Hysteretic energy-based state-dependent fragility for ground-motion sequences. *Earthquake Engineering & Structural Dynamics*, 50(4), 1187-1203.

Ghobarah, A., Aly, N. M., & El Attar, M. (2019). Performance level criteria and evaluation. In *Seismic Design Methodologies for the Next Generation of Codes* (pp. 207-215). Routledge.

Granello, G., & Palermo, A. (2020). Monitoring dynamic properties of a pres-lam structure: Trimble navigation office. *Journal of Performance of Constructed Facilities*, 34(1), 04019087.

Hassanli, R., ElGawady, M. A., & Mills, J. E. (2017). Simplified approach to predict the flexural strength of self-centering masonry walls. *Engineering Structures*, *142*, 255-271.

Hazaveh, N. K., Chase, J. G., Rodgers, G. W., Pampanin, S., & Kordani, R. (2020). Seismic behavior of a self-centering system with 2–4 viscous damper. *Journal of Earthquake Engineering*, 24(3), 470-484.

Hill, K. E. (1995). *The utility of ring springs in seismic isolation systems*. University of Canterbury.

Holden, T., Restrepo, J., & Mander, J. B. (2003). Seismic performance of precast reinforced and prestressed concrete walls. *Journal of Structural Engineering*, *129*(3), 286-296.

Housner G.W. (1956). Limit design of structures to resist earthquakes, in *Proc. of 1st WCEE*, pp. 5.1-5.13.

Hu, S., Wang, W., Qu, B., & Alam, M. S. (2020). Self-centering energy-absorbing rocking core system with friction spring damper: Experiments, modeling and design. *Engineering Structures*, 225, 111338.

Huang, X., Zhou, Z., & Zhu, D. (2019). Analytical investigation on lateral load responses of self-centering walls with distributed vertical dampers. *Structural Engineering and Mechanics*, *72*(3), 000-000.

Huckelbridge A.A., & Clough R. (1977). *Earthquake simulation tests of a nine story steel frame with columns allowed to uplift*, in, University of California, Berkeley.Issa, A. S., & Alam, M. S. (2019). Seismic performance of a novel single and double spring-based piston bracing. *Journal of Structural Engineering*, 145(2), 04018261.

Iwata, Y., Sugimoto, H. & Kuwamura, H., (2006). Reparability limit of steel structural buildings based on the actual data of the Hyogoken-Nanbu earthquake. In *Proceedings of the 38th Joint Panel. Wind and Seismic effects*. NIST Special Publication, 1057(23-32), p.30.

Jacobsen LS. (1960). Damping in composite structures. *Proc., 2nd World Conf. on Earthquake Engineering*, Vol. 2, Science Council of Japan, Tokyo, 1029-1044.

Kam, W. Y., Pampanin, S., Palermo, A., & Carr, A. J. (2010). Self-centring structural systems with combination of hysteretic and viscous energy dissipations. *Earthquake engineering & structural dynamics*, 39(10), 1083-1108.

Kelly, J. M. (1993). Earthquake-resistant design with rubber (Vol. 7). London: Springer-Verlag.

Khoo, H. H., Clifton, C., Butterworth, J., MacRae, G., Gledhill, S., & Sidwell, G. (2012). Development of the self-centering Sliding Hinge Joint with friction ring springs. *Journal of Constructional Steel Research*. 78, 201-211.

Kibriya, L. T., Málaga-Chuquitaype, C., Kashani, M. M., & Alexander, N. A. (2018). Nonlinear dynamics of self-centring rocking steel frames using finite element models. *Soil Dynamics and Earthquake Engineering*, 115, 826-837.

Kitayama, S., & Constantinou, M. C. (2017). Fluidic self-centering devices as elements of seismically resistant structures: description, testing, modeling, and model validation. *Journal of Structural Engineering*, *143*(7), 04017050.

Kokkali, P., Abdoun, T., & Anastasopoulos, I. (2015). Centrifuge modeling of rocking foundations on improved soil. *Journal of Geotechnical and Geoenvironmental Engineering*, 141(10), 04015041.

Krawinkler, H. (1996, June). A few basic concepts for performance based seismic design. In *Proceedings of 11th World Conference on Earthquake Engineering, Acapulco, Mexico. Paper* (No. 1133).

Kurama, Y. C., & Shen, Q. (2004). Posttensioned hybrid coupled walls under lateral loads. *Journal of Structural Engineering*, *130*(2), 297-309.

Lin, Y. C., Sause, R., & Ricles, J. (2013). Seismic performance of a large-scale steel self-centering moment-resisting frame: MCE hybrid simulations and quasi-static pushover tests. *Journal of Structural Engineering*, *139*(7), 1227-1236.

Lombardi, L., De Luca, F., & Macdonald, J. (2019). Design of buildings through linear time-history analysis optimising ground motion selection: a case study for RC-MRFs. *Engineering Structures*, 192, 279-295.

Lu, X., Dang, X., Qian, J., Zhou, Y., & Jiang, H. (2017). Experimental study of self-centering shear walls with horizontal bottom slits. *Journal of Structural Engineering*, *143*(3), 04016183.

Ma, X. (2010). *Seismic design and behavior of self-centering braced frame with controlled rocking and energy-dissipating fuses*. Stanford University.

Magliulo, G., Ercolino, M., Petrone, C., Coppola, O., & Manfredi, G. (2014). The Emilia earthquake: seismic performance of precast reinforced concrete buildings. *Earthquake Spectra*, 30(2), 891-912.

Magliulo, G., Bellotti, D., Cimmino, M., & Nascimbene, R. (2018) Modeling and seismic response analysis of RC precast Italian code-conforming buildings. *Journal of Earthquake Engineering*, **22**(sup2), 140-167.

Marriott, D., Pampanin, S., & Palermo, A. (2009). Quasi-static and pseudo-dynamic testing of unbonded post-tensioned rocking bridge piers with external replaceable dissipaters. *Earthquake engineering & structural dynamics*, *38*(3), 331-354.

Marriott, D., Pampanin, S., Bull, D., & Palermo, A. (2008). Dynamic testing of precast, post-tensioned rocking wall systems with alternative dissipating solutions. In *New Zealand Society for Earthquake Engineering (NZSEE) Conference*, Auckland.

McCormick J., Aburano H., Ikenaga M., & Nakashima M. (2008a). Permissible residual deformation levels for building structures considering both safety and human elements, in *Proceedings of the 14th world conference on earthquake engineering*, pp. 12-17.

McCormick, J., Matsuoka, Y., Pan, P. & Nakashima, M., (2008b). Evaluation of non-structural partition walls and suspended ceiling systems through a shake table study. In *ASCE Structures Congress 2008: Crossing Borders* (pp. 1-10).

McKenna, F. (2011). OpenSees: a framework for earthquake engineering simulation. *Computing in Science & Engineering*, 13(4), 58-66.

Meek, J. W. (1975). Effects of foundation tipping on dynamic response. *Journal of the Structural Division*, *101*(7), 1297-1311.

Miranda, E., & Ruiz-García, J. (2002). Evaluation of approximate methods to estimate maximum inelastic displacement demands. *Earthquake engineering & structural dynamics*, *31*(3), 539-560.

Mirzaie Aliabadi, M., Bahaari, M. R., & Torabian, S. (2013). Design and analytical evaluation of a new self-centering connection with bolted T-stub devices. *Advances in Materials Science and Engineering*, 2013, 1-12.

Moradi, S., & Burton, H. V. (2018). Response surface analysis and optimization of controlled rocking steel braced frames. *Bulletin of Earthquake Engineering*, 16(10), 4861-4892.

Motwani, P., Perogamvros, N., Taylor, S., & Laskar, A. (2020). Performance of industrial wedge-anchors for pre-stressing BFRP bars: Experimental and numerical studies. *Composite Structures*, *251*, 112592.

Muto K., Umemura H., & Sonobe Y. (1960). Study of the overturning vibrations of slender structures, in *Proc., 2nd World Conf. on Earthquake Engineering*, Association for Science Documents Information Tokyo, pp. 1239-1261.

Nakaki, S. D. (1999). An overview of the PRESSS five-story precast test building. *PCI journal*, 44(2), 26-29.

Oddbjornsson, O. (2009). *Dynamics of nonlinear elastic moment resisting frames*. University of Bristol.

Oddbjornsson, O., Alexander, N. A., Taylor, C. A., & Sigbjornsson, R. (2012). Numerical and experimental exploration of the fundamental nonlinear dynamics of self-centring damage resistant structures under seismic excitation. In *15th World Conference of Earthquake Engineering*, Lisbon, paper (Vol. 4670).

Pianosi F, Sarrazin F, & Wagener T. (2015). A Matlab toolbox for global sensitivity analysis. *Environmental Modelling & Software*. Aug 1;70:80-5.

Pieroni, L., Freddi, F. & Latour, M. (2022). Effective placement of self-centering damage-free connections for seismic-resilient steel moment resisting frames. *Earthquake Engineering & Structural Dynamics*, 51(5), pp.1292-1316.

Poliakov S. (1974). *Design of earthquake resistant structures*, Mir Publishers.

Porter K., Shoaf K., & Seligson H. (2006). Value of injuries in the Northridge earthquake, *Earthquake Spectra*, 22 555-563.

Priestley M. J. N., & Grant D. N. Viscous damping in seismic design and analysis. *Journal of earthquake engineering*. 2005;9(spec02):229-55.

Priestley M. J. N, Calvi G. M., and Kowalsky M. J. (2007). *Displacement-based seismic design of structures*. IUSS Press, Pavia, Italy, 721pp.

Priestley M. J. N. (2003). *Myths and fallacies in earthquake engineering, revisited: The ninth mallet Milne lecture*. Pavia, Italy: IUSS press.

Priestley, M. J. N. (1997). Displacement-based seismic assessment of reinforced concrete buildings. *Journal of earthquake engineering*, 1(01), 157-192.

Priestley, M. J. N., & Grant, D. N. (2005). Viscous damping in seismic design and analysis. *Journal of earthquake engineering***,** 9(spec02), 229-255.

Priestley, M. J. N., Calvi, G. M., & Kowalsky, M. J. (2007, March). Direct displacement-based seismic design of structures. In *NZSEE conference* (pp. 1-23).

Priestley, M. J. N., Evison, R. J., & Carr, A. J. (1978). Seismic response of structures free to rock on their foundations. *Bulletin of the New Zealand Society for Earthquake Engineering*, 11(3), 141-150.

Priestley, M. J. N. (1991). Overview of PRESSS research program. *PCI journal*, 36(4), 50-57.

Priestley, M. J. N. (2002). Direct displacement-based design of precast/prestressed concrete buildings. *PCI journal*, *47*(6), 66-79.

Priestley, M. J. N., Sritharan, S., Conley, J. R., & Pampanin, S. (1999). Preliminary results and conclusions from the PRESSS five-story precast concrete test building. *PCI journal*, 44(6), 42-67.

Qian, K., Liang, S. L., Xiong, X. Y., Fu, F., & Fang, Q. (2020). Quasi-static and dynamic behavior of precast concrete frames with high performance dry connections subjected to loss of a penultimate column scenario. *Engineering Structures*, 205, 110115.

Qiu, C., Zhang, Y., Li, H., Qu, B., Hou, H., & Tian, L. (2018). Seismic performance of concentrically braced frames with non-buckling braces: a comparative study. *Engineering Structures*, 154, 93-102.

Qiu, C., Zhang, Y., Qu, B., Dai, C., Hou, H., & Li, H. (2019). Cyclic testing of seismic dampers consisting of multiple energy absorbing steel plate clusters. *Engineering Structures*, *183*, 255-264.

Qu, B., Liu, X., Hou, H., Qiu, C., & Hu, D. (2018). Testing of buckling-restrained braces with replaceable steel angle fuses. *Journal of Structural Engineering*, *144*(3), 04018001.

Rahmzadeh, A., & Alam, M. S. (2017, October). Cyclic behavior of post-tensioned steel connections with shape memory alloy angles. In *Proc., 6th Int. Conf. on Engineering Mechanics and Materials. Vancouver, BC, Canada: Canadian Society for Civil Engineering*.

Ramirez, C. M., & Miranda, E. (2012). Significance of residual drifts in building earthquake loss estimation. *Earthquake Engineering & Structural Dynamics*, 41(11), 1477-1493.

Restrepo, J. I., & Rahman, A. (2007). Seismic performance of self-centering structural walls incorporating energy dissipators. *Journal of Structural Engineering*, *133*(11), 1560-1570.

Ricles, J. M., Sause, R., Garlock, M. M., & Zhao, C. (2001). Posttensioned seismic-resistant connections for steel frames. *Journal of Structural Engineering*, 127(2), 113-121.

Ricles, J. M., Sause, R., Peng, S. W., & Lu, L. W. (2002). Experimental evaluation of earthquake resistant posttensioned steel connections. *Journal of Structural Engineering*, 128(7), 850-859.

Rojas, P., Ricles, J. M., & Sause, R. (2005). Seismic performance of post-tensioned steel moment resisting frames with friction devices. *Journal of structural engineering*, *131*(4), 529-540.

Ruiz‐García, J. & Aguilar, J.D., (2015). Aftershock seismic assessment taking into account postmainshock residual drifts. *Earthquake Engineering & Structural Dynamics*, 44(9), pp.1391-1407.

Savinov, O. A., Uzdin, A. M., Sandovich, T. A., & Dolgaya, A. A. (1995). Consideration of seismic-effect characteristics in selecting parameters for earthquake-insulating foundation designs. *Osn., Fundam. Mekh. Gruntov*, (4), 9-13.

Sextos, A. G., Zhang, Z. and Alexander, N. A. (2022). Large-Scale Testing for Enhancing the Resilience of Schools in Seismic Regions: Challenges and Cost-Efficient Solutions. In *Progresses in European Earthquake Engineering and Seismology: Third European Conference on Earthquake Engineering and Seismology–Bucharest*, pp. 433-448. Cham: Springer International Publishing.

Sharpe, R. D., & Skinner, R. I. (1983). The seismic design of an industrial chimney with rocking base. *Bulletin of the New Zealand Society for Earthquake Engineering*, 16(2), 98-106.

Shepherd, R., & Erasmus, L. A. (1988). Ring spring energy dissipators in seismic resistant structures. In *Ninth World Conference on Earthquake Engineering*. Japan, Vol 5, pp 767-772.

Shibata, A., & Sozen, M. A. (1976). Substitute-structure method for seismic design in R/C. *Journal of the structural division*, *102*(1), 1-18.

Sobol IM. (2001). Global sensitivity indices for nonlinear mathematical models and their Monte Carlo estimates. *Mathematics and computers in simulation*. Feb 15;55(1-3):271-80.

Spieth, H. A., Carr, A. J., Murahidy, A. G., Arnolds, D., Davies, M., & Mander, J. B. (2004). Modelling of post-tensioned precast reinforced concrete frame structures with rocking beam-column connections. In *2004 NZSEE conference*.

Sritharan, S., Aaleti, S., Henry, R. S., Liu, K. Y., & Tsai, K. C. (2015). Precast concrete wall with end columns (PreWEC) for earthquake resistant design. *Earthquake Engineering & Structural Dynamics*, *44*(12), 2075-2092.

Standards New Zealand (NZS). (2004). Structural design actions - Part 5: Earthquake actions New Zealand. *NZS* 1170.5.

Thompson, A. G. (2004). Performance of cable bolt anchors–An Update. *MassMin2004, Instituto de Ingenerios de Chile Santiago*, 317-323.

Tocuţ, P. D., Stanasel, I., & Avram, F. T. (2021, August). Study of the clamping force in a pneumatic wedge device. In *IOP Conference Series: Materials Science and Engineering* (Vol. 1169, No. 1, p. 012022). IOP Publishing.

Tsai, K. C., Chou, C. C., Lin, C. L., Chen, P. C., & Jhang, S. J. (2008). Seismic self-centering steel beam-to-column moment connections using bolted friction devices. *Earthquake Engineering & Structural Dynamics*, *37*(4), 627-645.

Tsiavos, A., Sextos, A., Stavridis, A., Dietz, M., Dihoru, L. and Alexander, N.A. (2020). Large-scale experimental investigation of a low-cost PVC 'sand-wich'(PVC-s) seismic isolation for developing countries. *Earthquake Spectra*, 36(4), pp.1886-1911.

Tsiavos, A., Sextos, A., Stavridis, A., Dietz, M., Dihoru, L. and Alexander, N.A. (2021a). Experimental investigation of a highly efficient, low-cost PVC-Rollers Sandwich (PVC-RS) seismic isolation. *Structures*, 33, pp. 1590-1602. Elsevier.

Tsiavos, A., Sextos, A., Stavridis, A., Dietz, M., Dihoru, L., Di Michele, F., & Alexander, N. A. (2021bs). Low-cost hybrid design of masonry structures for developing countries: Shaking table tests. Soil Dynamics and Earthquake Engineering, 146, 106675.

United Nations. (2023). UNDP's response: Turkey-Syria Earthquakes. (https://www.undp.org/turkiye-syria-earthquakes). United Nations Development Programme. Retrieved 01 June 2023.

Uzdin, A. M., Doronin, F. A., Davydova, G. V., Avidon, G. E., & Karlina, E. A. (2009). Performance analysis of seismic-insulating kinematic foundations on support elements with negative stiffness. *Soil Mechanics and Foundation Engineering*, 46(3), 99-107.

Vamvatsikos, D., & Cornell, C. A. (2002). Incremental dynamic analysis. *Earthquake engineering & structural dynamics*, 31(3), 491-514.

Vamvatsikos, D., & Cornell, C. A. (2004). Applied incremental dynamic analysis. *Earthquake Spectra*, 20(2), 523-553.

Vasdravellis, G., Karavasilis, T. L., & Uy, B. (2013). Large-scale experimental validation of steel posttensioned connections with web hourglass pins. *Journal of Structural Engineering*, 139(6), 1033-1042.

Vassiliou M.F., Mackie K.R., & Stojadinović B. (2017). A finite element model for seismic response analysis of deformable rocking frames, *Earthquake Engineering & Structural Dynamics*, 46 447-466.

Wang, H., Nie, X., & Pan, P. (2017). Development of a self-centering buckling restrained brace using cross-anchored pre-stressed steel strands. *Journal of Constructional Steel Research*, *138*, 621-632.

Wang, W., Fang, C., Zhao, Y., Sause, R., Hu, S., & Ricles, J. (2019). Self-centering friction spring dampers for seismic resilience. *Earthquake Engineering & Structural Dynamics*, 48(9), 1045-1065.

Wolski, M., Ricles, J. M., & Sause, R. (2009). Experimental study of a self-centring beam-column connection with bottom flange friction device. *Journal of Structural Engineering*, 135(5), 479-488.

Wu, D., Lu, X., & Zhao, B. (2019). Parametric study of rocking cores-moment frames with supplemental viscous damping and self-centering devices using a distributed parameter model. *Soil Dynamics and Earthquake Engineering*, *123*, 304-319.

X. Lu, X. Dang, J. Qian, Y. Zhou, & H. Jiang, Experimental study of self-centering shear walls with horizontal bottom slits, *Journal of Structural Engineering*, 143 (2017) 04016183.

Xie, Q., Zhou, Z., Huang, J. H., & Meng, S. P. (2016). Influence of tube length tolerance on seismic responses of multi-storey buildings with dual-tube self-centring buckling-restrained braces. *Engineering Structures*, 116, 26-39.

Xing, Y., Eriksson, N. B., Ong, M. C., & Knutsen, C. (2019, November). Contact stresses associated with the wedge-lock mechanism in a prototype subsea pipeline recovery tool. In *IOP Conference Series: Materials Science and Engineering* (Vol. 700, No. 1, p. 012020). IOP Publishing.

Youssef, N. F., Bonowitz, D., & Gross, J. L. (1995). A survey of steel moment-resisting frame buildings affected by the 1994 Northridge earthquake. *US National Institute of Standards and Technology*.